GEOPHYSICAL STUDIES OF PLATE-BOUNDARY EARTHQUAKES AND MID-PLATE VOLCANISM IN THE OCEAN BASINS

by

CECILY JO WOLFE

SUBMITTED IN PARTIAL FULFILLMENT OF THE REQUIREMENTS
FOR THE DEGREE OF
DOCTOR OF PHILOSOPHY

at the
MASSACHUSETTS INSTITUTE OF TECHNOLOGY
and the
WOODS HOLE OCEANOGRAPHIC INSTITUTION

May 1994

© 1994 Massachusetts Institute of Technology

Signature of Author____
Joint Program in Oceanography, Massachusetts Institute of
Technology and Woods Hole Oceanographic Institution, April 1994

Certified by____
Marcia K. McNutt, Thesis Co-Supervisor

Certified by____
Sean C. Solomon, Thesis Co-Supervisor

Accepted by____
Chairman, Joint Committee for Marine Geology and Geophysics,
Massachusetts Institute of Technology/Woods Hole Oceanographic Institution

Lindgren

MASSACHUSETTS INSTITUTE OF TECHNOLOGY
MAY 18 1994
LIBRARIES

WITHDRAWN
FROM
MIT LIBRARIES

GEOPHYSICAL STUDIES OF PLATE-BOUNDARY EARTHQUAKES AND MID-PLATE VOLCANISM IN THE OCEAN BASINS

by

Cecily Jo Wolfe

Submitted to the Department of Earth, Atmospheric, and Planetary Sciences
Massachusetts Institute of Technology
and
the Department of Geology and Geophysics
Woods Hole Oceanographic Institution
on April 1994
in partial fulfillment of the requirements
for the degree Doctor of Philosophy

ABSTRACT

Chapter 1 presents evidence that elastic plate thicknesses are anomalously low beneath seamounts of the Darwin Rise, suggesting that the Japanese and Wake seamounts formed on thermally anomalous lithosphere, such as that which is thought to exist presently beneath volcanoes of French Polynesia. In Chapter 2, multichannel seismic lines, sonobuoy and gravity data across the Marquesas Islands are used to study volcano growth, island mass-wasting, and crustal underplating at island chains with overfilled moats. Plate-flexure models require broad underplating of the crust by low density (crustal?) material at the Marquesas Islands to explain the depth to volcanic basement and gravity data. On oceanic transforms, earthquakes are expected to occur on the principal transform displacement zone (PTDZ) and have strike-slip mechanisms consistent with transform-parallel motion. Chapter 3 is a study of oceanic transform earthquakes departing from this pattern. Much of the anomalous earthquake activity is associated with complexities in the geometry of the principal transform displacement zone or the presence of large structural features that may influence slip on the fault. Chapter 4 describes microearthquake and seismic structural characteristics along a segment at 29°N on the Mid-Atlantic Ridge. While tomographic images are supportive of a simple spreading-cell model, microearthquakes suggest complexities related to the small-scale variability of magmatic and hydrothermal processes.

Thesis Co-Supervisors:	Dr. Marcia K. McNutt Professor of Geophysics, MIT
	Dr. Sean C. Solomon Director, Department of Terrestrial Magnetism Carnegie Institution of Washington

ACKNOWLEDGEMENTS

My tenure in the Joint Program has been one rich in experience. Opportunities were given to participate on research cruises, attend conferences, travel on geological field trips, and, of course, work on research. The atmosphere at MIT and WHOI encouraged interaction between students and faculty, and the door was always open when I needed to stop by with questions. But just as important was the influence of friends and peers, first the older students who helped initiate me when I began graduate school, and now the younger students who provide support as I prepare to finish. I am grateful to those both at MIT and WHOI whose efforts have helped to maintain the program's values and standards.

I thank my advisors Sean Solomon and Marcia McNutt for providing guidance and supervision. I also thank collaborators Eric Bergman, Bob Detrick, Mike Purdy, and Doug Toomey for contributing to my education. The geodynamics seminar and field trips organized by Henry Dick helped broaden my interest in the world of geology. Tom Jordan deserves credit for first encouraging me to come to MIT as a special student.

For friendship and inspiration, I acknowledge past and present students: Chris Bradley, Gail Christeson, Matt Cordery, Javier Escartin, Carl Friedrichs, Jim Gaherty, John Goff, Emilie Hooft, Gary Jaraslow, Rafi Katzman, Pete Kaufmann, Sarah Kruse, Garrett Ito, Dan Lizzaralde, Peter Puster, Carolyn Ruppel, Mark Simons, Steve Shapiro, Anne Sheehan, Paula Waschbusch, Will Wilcock, and others. I give special recognition to my housemates Greg Cohen and Connie Hart and my officemate Emilie Hooft for helping me get through this past year.

I thank my committee, Bob Detrick, Marcia McNutt, Mike Purdy, and Sean Solomon, and my defense chairman, Kathy Gillis, for their advice and comments..

Finally, this thesis would not have been possible without the support of my family.

TABLE OF CONTENTS

INTRODUCTION

This thesis focuses on two areas: 1) earthquake characteristics at mid-ocean ridges and oceanic transforms, and tectonic implications; and 2) processes at oceanic volcanoes, such as lithospheric flexure, island mass-wasting, and controls on the stratigraphy of island moats. Each chapter is a distinct research paper meant to be read independently of the other chapters.

Beneath oceanic volcanoes, elastic thickness of the lithosphere T_e is thought to represent the depth to an isotherm (about 450°-600°C) marking the elastic/ductile boundary at the time of volcanism. In accordance with this simple model, the observed thickness of the elastic plate beneath midplate volcanoes increases with the square root of the age of the lithosphere at the time of loading [*Watts et al.*, 1980], just as isotherms in a conductively cooling plate deepen with time [*Parsons and Sclater*, 1977]. In chapter 1, I analyze satellite gravity and deflection-of-the-vertical and shipborne gravity collected during the *Roundabout* leg 10 expedition to determine T_e values for Cretaceous seamounts of the Darwin Rise. Elastic plate thicknesses beneath the Japanese and Wake seamount groups are found to be remarkably low given their age at the time of loading, which is consistent with formation of these seamounts on thermally anomalous lithosphere, such as suggested to presently exist beneath the volcanoes of French Polynesia.

Menard [1956] first proposed the term "archipelagic apron" to describe the smooth seafloor around island chains that is the result of material infilling the flexural moat. In Chapter 2, seismic stratigraphy and quantitative flexural and sedimentation models are used to learn more about the processes that form the Marquesas apron and make it different from that at Hawaii. The seismic velocities and seismic stratigraphy indicate that the Marquesas apron is mostly debris from island mass wasting. Plate-flexure models require broad underplating of the crust by low density (crustal?) material to explain the depth to volcanic basement and gravity observations. Three-dimensional diffusion models of sedimentation suggest that three main factors make the observed moat stratigraphy at the Marquesas different from that at Hawaii: (1) the Marquesas moat is overfilled, while the Hawaiian moat is underfilled, (2) sediment diffusivities are lower at the Marquesas, and (3) the Marquesas islands are separated by deep sedimentary basins, in contrast to Hawaii, where islands are separated by a shallow ridge. The lower sediment diffusivity at the Marquesas may reflect a larger proportion of "blocky", massive material in the central Marquesas moat or alternatively a change in the dominant processes of sediment transport. While there is similar sediment supply for a given along-moat distance at both the Marquesas and Hawaii, the underfilled moat at Hawaii is apparently a consequence of greater moat volumes due to the larger size of the Hawaiian volcanoes, and possibly variations in underplating, that load the plate. The difference in sediment/edifice ratios is likely related to the larger eruption rates at Hawaii and different styles of volcano construction between Hawaii and the Marquesas.

On oceanic transforms, earthquakes are expected to occur on the principal transform displacement zone (PTDZ) and have strike-slip mechanisms consistent with transform-parallel motion [*Sykes*, 1967]. Chapter 3 demonstrates the existence of transform earthquakes departing from this pattern. Much of the anomalous earthquake activity on oceanic transforms is associated with complexities in the geometry of the PTDZ or the presence of large structural features that may influence slip on the fault. Reverse-faulting earthquakes occur at a compressional bend in the Owen transform in the area of Mount Error and at the St. Paul's transform near St. Peter's and St. Paul's Rocks. A normal-faulting earthquake on the Heezen transform is located at the edge of a pull-apart basin marking an extensional offset of the fault. Some events with unusual mechanisms occur outside of the transform fault zone and do not appear to be related to fault zone geometry. Possible additional contributors to the occurrence of anomalous earthquakes include recent changes in plate motion, differential lithospheric cooling, and the development of a zone of weakness along the fault zone, but we do not find strong evidence to confirm the influence of these processes.

Microearthquake studies provide direct information on the depth distribution, mechanism, and moment release of seismic faulting at mid-ocean ridges, and are thus important for constraining the mechanical structure of the lithosphere, which is primarily dependent on temperature and rheology, and understanding the active tectonics of ridge segments [e.g., *Toomey et al.*, 1985, 1988; *Kong et al.*, 1991]. Chapter 4 discusses the results of a microearthquake and tomography experiment conducted at a segment at 29°N on the Mid-Atlantic Ridge and implications for a spreading cell model. Earthquakes clustered in three separate along-axis regions: (1) the southern deep, (2) the central high, slightly north of the Broken Spur hydrothermal vent field, and (3) a region midway between, beneath an along-axis volcano. In agreement with a spreading cell model and gravity observations [c.f., *Lin et al.*, 1990], 3-dimensional delay time tomography suggests that crustal velocities in the lower crust are heterogeneous, with higher velocities and thin crust occurring near the southern deep, and lower velocities and a thickened layer 3 occurring towards the central bathymetric high. The thickness of the lower crust at the segment end is also asymmetric across axis, with lesser thickness beneath the inside corner.

However, microearthquake characteristics show complexities not explained by a spreading cell model. Along axis, well-resolved focal depths determined with a 3-D velocity model range from 3 to 6 km beneath the seafloor and do not shoal from the segment end to the segment center. The significant seismicity at the segment center is likely associated with volcanic and hydrothermal processes at the axial volcanic ridge (the largest microearthquake is located 4 km beneath Broken Spur). Microearthquakes with anomalous focal mechanisms beneath an along-axis volcano may be the result of stresses related to magma migration or thermal cooling. The microearthquakes in this study have rupture lengths on the order of only 100 m and therefore are sensitive to small scale variability in the influence of magmatism and hydrothermal circulation. The characteristics of large ($m_b > 4.5$) earthquakes on the MAR, in contrast, may behave more nearly in accordance with a spreading cell model because of larger rupture lengths, on the order of 10 km, that sample structure on the segment scale.

The research presented in chapter 1 was conducted with Marcia McNutt and was published in *Journal of Geophysical Research* in 1991. Chapter 2 is presently in press in *Journal of Geophysical Research* with Marcia McNutt and Robert Detrick as coauthors. Eric Bergman and Sean Solomon are coauthors on chapter 3, which was published in *Journal of Geophysical Research* in 1993. Chapter 4 consists of work done in collaboration with Mike Purdy, and Sean Solomon, Doug Toomey, and will hopefully result in an eventual publication.

REFERENCES

Kong, L. S. L., S. C. Solomon, and G. M. Purdy, Microearthquake characteristics of a mid-ocean ridge along-axis high, *J. Geophys. Res.*, *97*, 1659-1685, 1992.

Lin, J., G. M. Purdy, H. Schouten, J.-C. Sempere, and C. Zervas, Evidence from gravity data for focused magmatic accretion along the Mid-Atlantic Ridge, *Nature, 344*, 627-632, 1990.

Menard, H.W., Archipelagic aprons, *Bull. Amer. Assoc. Petrol. Geol.*, *40*, 2195-2210, 1956.

Parsons, B., and J. G. Sclater, An analysis of the variation of ocean floor bathymetry and heat flow with age, *J. Geophys. Res.*, *82*, 803-827, 1977.

Sykes, L. R., Mechanism of earthquakes and nature of faulting on the mid-oceanic ridges, *J. Geophys. Res.*, *72*, 2131-2153, 1967.

Toomey, D. R., S. C. Solomon, G. M. Purdy, and M. H. Murray, Microearthquakes beneath the median valley of the Mid-Atlantic Ridge near 23°N: Hypocenters and focal mechanisms, *J. Geophys. Res., 90*, 5443-5458, 1985.

Toomey, D. R., S. C. Solomon, and G. M. Purdy, Microearthquakes beneath the median valley of the Mid-Atlantic Ridge near 23°N: Tomography and tectonics, *J. Geophys. Res., 93*, 9093-9112, 1988.

Watts, A. B., J. H. Bodine, and N. R. Ribe, Observations of flexure and the geological evolution of the Pacific ocean basin, *Nature, 283*, 532-537, 1980.

CHAPTER 1

COMPENSATION OF CRETACEOUS SEAMOUNTS OF THE DARWIN RISE, NORTHWEST PACIFIC OCEAN

JOURNAL OF GEOPHYSICAL RESEARCH, VOL. 96, NO. B2, PAGES 2363–2374, FEBRUARY 10, 1991

Compensation of Cretaceous Seamounts of the Darwin Rise, Northwest Pacific Ocean

CECILY J. WOLFE AND MARCIA K. MCNUTT

Department of Earth, Atmospheric, and Planetary Sciences, Massachusetts Institute of Technology, Cambridge

We estimate the elastic thickness T_e for the Pacific plate at the time of volcanism for approximately 60 guyots of Cretaceous age in the Japanese, Wake, and Mid-Pacific Mountain seamount groups of the northwest Pacific. The values of T_e are constrained by comparing synthetic gravity and deflection of the vertical computed from digital bathymetry assuming regional compensation models to potential field data derived from Seasat radar altimetry. The amplitude of the gridded Seasat gravity field over the seamounts is consistent with T_e values between 5 and 15 km, but these values represent only lower bounds since the 100-km spacing of satellite tracks may undersample the gravity for seamounts lying between adjacent passes. Direct modeling of the deflection of the vertical along individual satellite tracks avoids this distribution bias but can lead to errors if the bathymetric feature is mislocated with respect to the satellite coordinate system. Nevertheless, for no seamount does the root-mean-square (RMS) difference between observed and predicted deflection of the vertical show a distinct minimum for elastic plate thickness greater than 15 km. However, for some features the RMS minimum is unconstrained, allowing T_e greater than 15 km. Given the possible bias in the modeling of satellite data, the low values for elastic plate thickness were confirmed for the Japanese and Wake group using shipborne gravity data and multibeam bathymetry collected during the *Roundabout* leg 10 expedition, supplemented with published Navy sonar array sounding system (SASS) bathymetry. The analysis of shipborne data constrains most elastic plate thickness values to between 10 and 15 km for crustal densities between 2600 and 2800 kg/m^3. The low values for elastic plate thickness for these Cretaceous guyots that formed in the area of the "Darwin Rise" suggest either that they formed on lithosphere less than 40 m.y. old or that older lithosphere was reheated near the time of volcanism. While the first possibility is permitted by age data from the Mid-Pacific Mountains, radiometric dates and magnetic lineations from the Japanese and Wakes are more consistent with formation of these seamount groups on older, thermally anomalous lithosphere, such as that which is thought to exist presently beneath the volcanoes of French Polynesia.

INTRODUCTION

Modeling oceanic lithosphere as a thin elastic plate overlying a fluid substratum has been extremely successful in explaining its mechanical response to seamount loads formed in a midplate setting. Although the thin elastic plate model is just a first approximation to the true rheology of the lithosphere, which includes brittle failure at the surface and ductile creep at depth [*Goetze and Evans*, 1979], for the small deviatoric stresses induced by volcanic loading the flexure of a purely elastic plate closely resembles the true deformation of the lithosphere. Because the creep rate for rocks depends exponentially on temperature, the effective elastic thickness of the plate T_e is thought to represent the depth to an isotherm marking the elastic/ductile boundary. Based on the extrapolation of results from laboratory experiments to geologic strain rates, the isotherm at the base of the elastic plate may be as high as 800°C [*Kirby*, 1980], but lower temperatures (450°-600°C) are implied from a comparison of geotherms from the thermal plate model [*Parsons and Sclater*, 1977] with observed values for elastic plate thickness estimated from the wavelength of bathymetric moats and arches surrounding volcanoes [*Walcott*, 1970; *McNutt and Menard*, 1978] or from geoid, gravity, or deflection-of-the-vertical data over the loads [*Watts and Cochran*, 1974; *Watts and Ribe*, 1984; *Cazenave et al.*, 1980]. As the oceanic lithosphere continues to cool after emplacement of the load, the flexure of the elastic plate is frozen in, and thus T_e marks the depth to the isotherm at the elastic/ductile transition at the time of volcanism. In accordance with the prediction of this simple model, the observed thickness of the elastic plate beneath midplate volcanoes increases with the square root of the age of the lithosphere at time of loading [*Watts et al.*, 1980], just as isotherms in a conductively cooling plate deepen with time [*Parsons and Sclater*, 1977].

In general, volcanoes which form on lithosphere between 50 and 90 m.y. old show elastic plate thickness values between 20 and 40 km, except in the area of French Polynesia where T_e values are anomalously low, as shown in Figure 1 [*Calmant and Cazenave*, 1987]. *McNutt and Fischer* [1987] designated this region the South Pacific Superswell and have noted that the coincidence of shallow bathymetry, low Love wave phase velocities, and low elastic plate thicknesses on the superswell can all be explained by an unusually warm lithosphere given its age from magnetic lineations. They further speculated that the area now in the North Pacific known as the Darwin Rise [*Menard*, 1964] is an ancient example of a superswell, based on identical depth/age relationships [*Menard*, 1984; *McNutt et al.*, 1990], similar isotopic enrichment of hot spot lavas [*Hart*, 1984; *Natland and Wright*, 1984; *Staudigel et al.*, 1990], and plate motion models, which place the Darwin Rise over French Polynesia in Cretaceous time when the volcanoes erupted (R. G. Gordon and L. J. Henderson, Pacific plate hot spot tracks, preprint, 1985). *Smith et al.* [1989] extended the list of similarities between the superswell and Darwin Rise by finding T_e values of 10 and 15 km for two Cretaceous seamounts of the Darwin Rise that formed on lithosphere approximately 42 and 65 m.y. old, respectively, at the time of volcanism. The purpose of this study is to examine whether there is widespread evidence for low elastic-plate thicknesses for a much larger number of Darwin Rise volcanoes using both readily available digital data sets and recently acquired shipborne data from our 1988 expedition, *Roundabout* leg 10, to the northwest Pacific.

Copyright 1991 by the American Geophysical Union.

Paper number 90JB01893.
0148-0227/91/90JB-01893$05.00

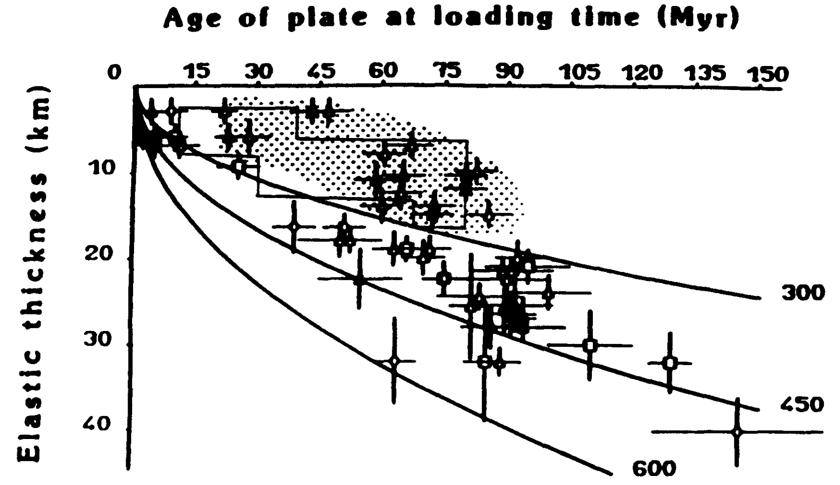

Fig. 1. Figure adapted from *Calmont and Cazanave* [1987]. Elastic plate thicknesses from volcanoes in the Atlantic (squares), Pacific (triangles), and Indian (diamonds) oceans plotted against estimated age at the time of loading. Isotherms calculated from *Parsons and Sclater* [1977]. Stippled area outlines the superswell volcanoes. The polygon represents the range of values derived from modeling shipborne gravity over the Japanese and Wake seamounts.

ANALYSIS OF SEASAT ALTIMETRY DATA

One of the goals of the *Roundabout* leg 10 expedition was to determine whether the volcanoes of the Darwin Rise are compensated by an anomalously weak elastic plate, consistent with formation on superswell-type lithosphere. It is not possible to prove that the volcanoes of the Darwin Rise formed on a superswell based on elastic plate thickness data alone, since the volcanoes might simply have formed on young lithosphere. On the other hand, it would be possible to disprove the superswell hypothesis by demonstrating that a number of Darwin Rise volcanoes are compensated by elastic plates more than 15 km thick. Because there are literally thousands of major volcanoes on the Darwin Rise and we could only survey about 2 dozen during a 1-month expedition, our strategy was to obtain preliminary estimates of elastic plate thickness for a large number of potential survey targets using digital dbdb5 bathymetry from the U.S. Navy and Seasat altimetry in the form of both digital gravity [*Haxby*, 1983] and along-track deflection of the vertical [*Sandwell*, 1984]. Those volcanoes that showed the greatest likelihood of being supported by a stiff elastic plate would be high-priority candidates for the shipborne survey. The regions of the Darwin Rise we examined include the Japanese Seamounts, the Wake Seamounts, and the Mid-Pacific Mountains (Figure 2).

Forward Modeling of Satellite Gravity

Two-dimensional maps of synthetic gravity were compared to gridded satellite gravity maps [*Haxby*, 1983] in order to constrain elastic plate thickness over seamounts of the Darwin Rise using a method similar to that of *Freedman and Parsons* [1986]. Digital bathymetric data (dbdb5) were first interpolated onto a 9x9 km grid using an Airy's minimum distortion projection, padded along the margins to avoid edge effects in the spectral domain, and Fourier transformed. With uppercase variables denoting the Fourier transforms of lowercase counterparts, the deflection of the elastic plate W beneath topography H was calculated from

$$W(k_x,k_y) = -\left(\frac{\rho_c-\rho_w}{\rho_m-\rho_c}\right)\left[1+\frac{(2\pi k)^4 D}{(\rho_m-\rho_c)g}\right]^{-1} H(k_x,k_y) \qquad (1)$$

in which k_x, k_y are the horizontal wavenumbers, ρ_c, ρ_w, and ρ_m are the densities of the crust, water, and mantle, respectively, D is the flexural rigidity of the plate, which depends on the cube of the plate thickness, g is the acceleration of gravity, and k is the modulus of the horizontal wavenumber vector. Values chosen for variables are given in Table 1. The gravity field $\Delta G(k_x, k_y)$ resulting from the topography h and the relief w on the Moho due to plate flexure was then calculated via *Parker*'s [1973] method:

$$\Delta G(k_x,k_y) = 2\pi G \left\{ (\rho_c-\rho_w)e^{-2\pi k z_t} \sum_{n=1}^{N}\left(\frac{(2\pi k)^{n-1}}{n!} F[h^n(x,y)]\right) + (\rho_m-\rho_c)e^{-2\pi k z_m} F[w(x,y)] \right\} \qquad (2)$$

in which z_t and z_m are the average regional depths from the sea surface for the topography and Moho, respectively, and $F[f]$ denotes Fourier transformation of the function f. The expansion for the gravity field from the topography converged after about N=5 terms. For the deeper, smoother Moho relief, one term in the expansion was sufficient, in keeping with the linear approximation in (1).

Contoured maps of satellite-derived gravity in each of the three seamount groups were compared with predicted gravity from (2) assuming T_e values of 0, 5, 10, 15, and 20 km. Because *Haxby*'s [1983] gravity data set is calculated using interpolated geoid data from satellite passes with variable track spacing (Figure 3), the synthetic gravity values were smoothed by a running filter with form $\exp(-r^2/R^2)$, where r is the distance to neighboring values and

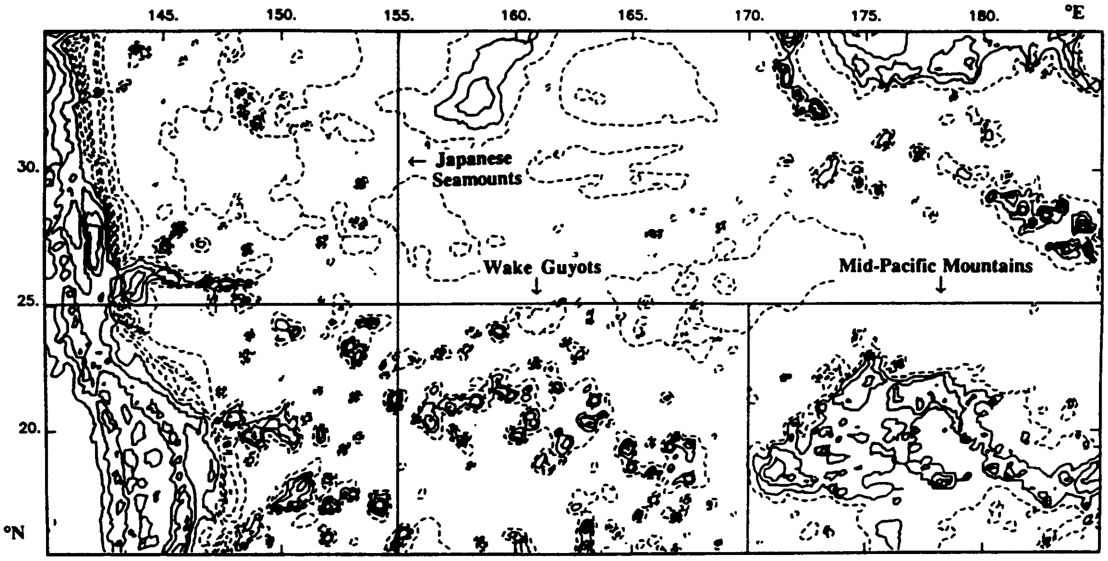

Fig. 2. Bathymetry of the Darwin Rise, taken from dbdb5 data, showing the location of the Japanese Seamounts, Wake Guyots, and Mid-Pacific Mountains. Contour interval is 1 km. Dashed contours show depths equal to and below 5 km.

TABLE 1. Symbols in Equations (1)-(4)

Parameter	Value or Definition
ρ_w	1000 kg/m^3
ρ_c	2800 kg/m^3
ρ_m	3300 kg/m^3
z_m-z_c (crustal thickness)	6 km
D	$\frac{ET_e^3}{12(1-\nu^2)}$
ν	0.25
E	8.0x10^{10} N/m
g	9.8 m/sec^2
G	6.67x10^{-11} N-m^2/kg^2
k_x , k_y	$\frac{1}{\lambda_x}, \frac{1}{\lambda_y}$
k	$\sqrt{k_x^2+k_y^2}$
λ_x , λ_y	wavelengths in x and y directions

R=27 km, to remove the higher frequencies for better comparison to the low-frequency satellite maps. For example, Figure 4 shows the satellite gravity map for the Wake group along with sample synthetic maps for T_e values of 5, 10 and 15 km. In the observed gravity (Figure 4*a*), anomalies over major volcanoes peak at about 75 mGal for features adequately sampled by the satellite passes. The model for T_e = 5 km produces too little gravity signal, while the model for T_e = 15 km produces gravity anomalies with too large an amplitude. On average for the Wake group, an elastic plate thickness of approximately 10 km is the best fit to the satellite gravity field. Based on comparing the amplitude of the gravity signature with that predicted by the different elastic plate models on a feature-by-feature basis, we assigned an elastic plate thickness to the lithosphere compensating each of the major seamounts in the Japanese, Wake, and Mid-Pacific areas.

Forward Modeling of Satellite Deflection of the Vertical

Since gridded two-dimensional contour maps contain a sampling bias from uneven track spacing, we compared directly profiles of Seasat data with the predicted signal from the seamount and its compensation along that same track. The most convenient form for the potential field data is deflection of the vertical, which is the along-track derivative of the geoid data observed by the altimeter. Like other derivatives of the geopotential, such as gravity, deflection of the vertical does not contain extraneous long-wavelength information arising from geoid anomalies of deep-Earth origin or errors in satellite altitude. Because deflection of the vertical is a horizontal gradient, it can be simply obtained for an individual satellite pass, unlike the case for computing gravity.

Both ascending (southeast to northwest) and descending (northeast to southwest) geoid data were edited, differentiated with respect to time, and converted to deflection angles in units of microradians using the satellite's ground speed as described by *Sandwell* [1984]. Longer-wavelength deflections of the vertical from geoid undulations have only a minor influence over the length of a seamount signal and were not removed. Profiles were projected onto the 9x9 km grid using the Airy's minimum distortion algorithm. Satellite values were smoothed along track by a running filter exp $(-r^2/2\sigma^2)$, where r is distance along track and σ=14, in order to reduce noise amplified by differentiation [*Sandwell*, 1984]. Typically, profiles extending 140 km on either side of a volcanic feature were retained, but in some cases, profiles had to be

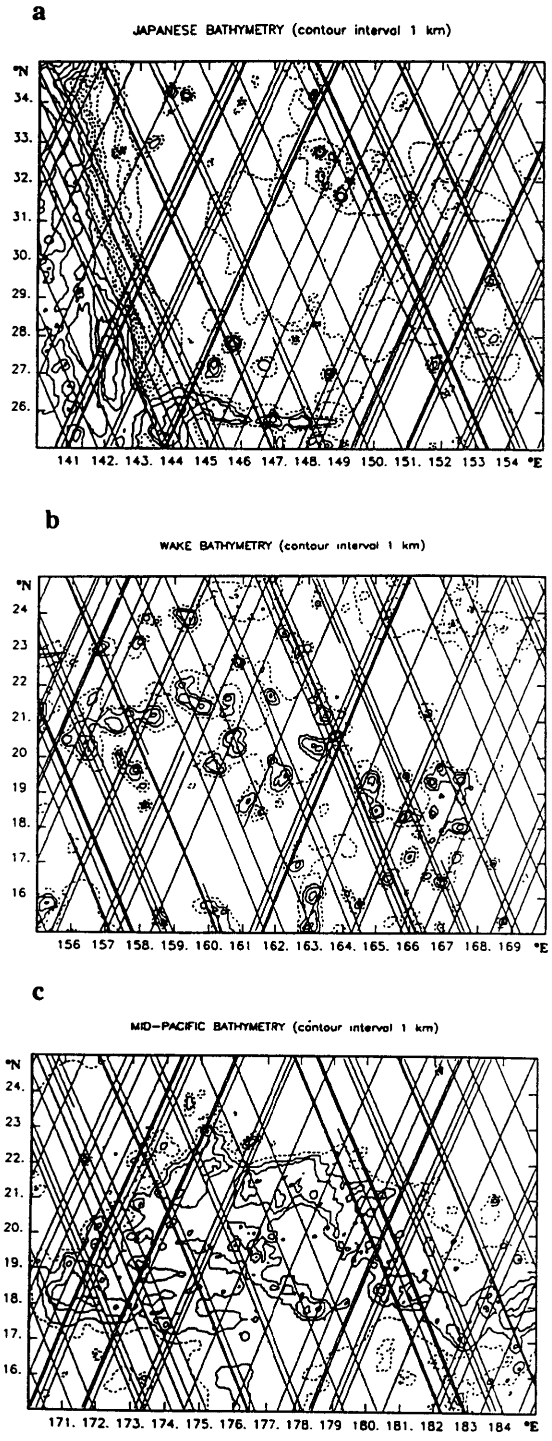

Fig. 3. Seasat tracks over the Darwin Rise. Dashed contours show depths equal to and below 5 km. (*a*) Japanese Seamounts. (*b*) Wake Guyots. (*c*) Mid-Pacific Mountains.

shortened to avoid interference from neighboring features. It was necessary to have at least one side of the profile extend for 100 km or more in order to observe the entire signal from the seamount and its compensation.

The gravity field predicted from (2) can be converted to eastern, E and northern, N, components in the wave number domain of deflection of the vertical via

$$E = \frac{-ik_x}{k\,g}\,\Delta G \tag{3}$$

$$N = \frac{-ik_y}{k\,g}\,\Delta G \tag{4}$$

in which $i=\sqrt{-1}$. For the deflection calculation, only one term was used in the gravity expansion. Synthetic grids were calculated for elastic plate thicknesses of 0, 5, 10, 15, 20, and 25 km and interpolated onto the satellite tracks. A vector sum of the north and east components was taken along the azimuth of the satellite track to obtain the final along-track deflection, which was then compared with the Seasat data.

Figure 5*a* shows an example of a descending satellite pass and the synthetic passes (dashed lines) over Scripps seamount in the Wake group. Deflection is positive and increasing as the seamount is approached, falls to zero immediately over the summit, and is negative and increasing on the outbound segment. A best fitting value for elastic plate thickness was chosen by searching for the minimum root-mean-square (RMS) misfit between observed and synthetic deflection-of-the-vertical profiles as T_e varies (Figure 5*b*). In some cases, mislocation of a bathymetric feature with respect to the satellite coordinate system caused a systematic offset between data and theory of the zero point at the closest approach to the seamount's summit. To correct for this error, we shifted the predicted traces horizontally by 15 km or less before computing the RMS. For some seamounts, such as Scripps, the shape of the RMS misfit as a function of T_e shows a well defined minimum (Figure 5*b*) that allowed us to chose a preferred elastic plate thickness with small uncertainty. Other seamounts displayed a broader, but still defined, minimum. For some seamounts, regardless of assumed density ρ_c, the RMS plots show a very gradual slope downwards toward larger T_e values, which allowed us to rule out weak plates but not define a best fitting plate thickness. Part of the lack of resolution at high T_e values results from the fact that the deflection of the plate does not change much once a certain strength is reached for such small seamounts. It can thus be difficult to distinguish the thickness of a strong plate using the potential field, especially given the existence of bathymetric errors or noise.

Figure 6 shows that results from comparing observed and predicted deflection of the vertical are generally consistent with the satellite gravity study, although slightly higher average values are obtained since the deflection data are not biased by track spacing. We believe that most errors in derived values are a function of either poor knowledge of the size or mislocation of bathymetric features in the dbdb5 data. Some satellite passes record the existence of features not included in the dbdb5 data set. For example, signals from nearby satellite seamounts, such as Vibelius seamount surveyed during *Roundabout* leg 10, are apparent in the ascending pass over Wilde seamount, but these features are not shown in the dbdb5 bathymetry. In such cases, the synthetic models provided such a poor fit to the shape of the Seasat profiles

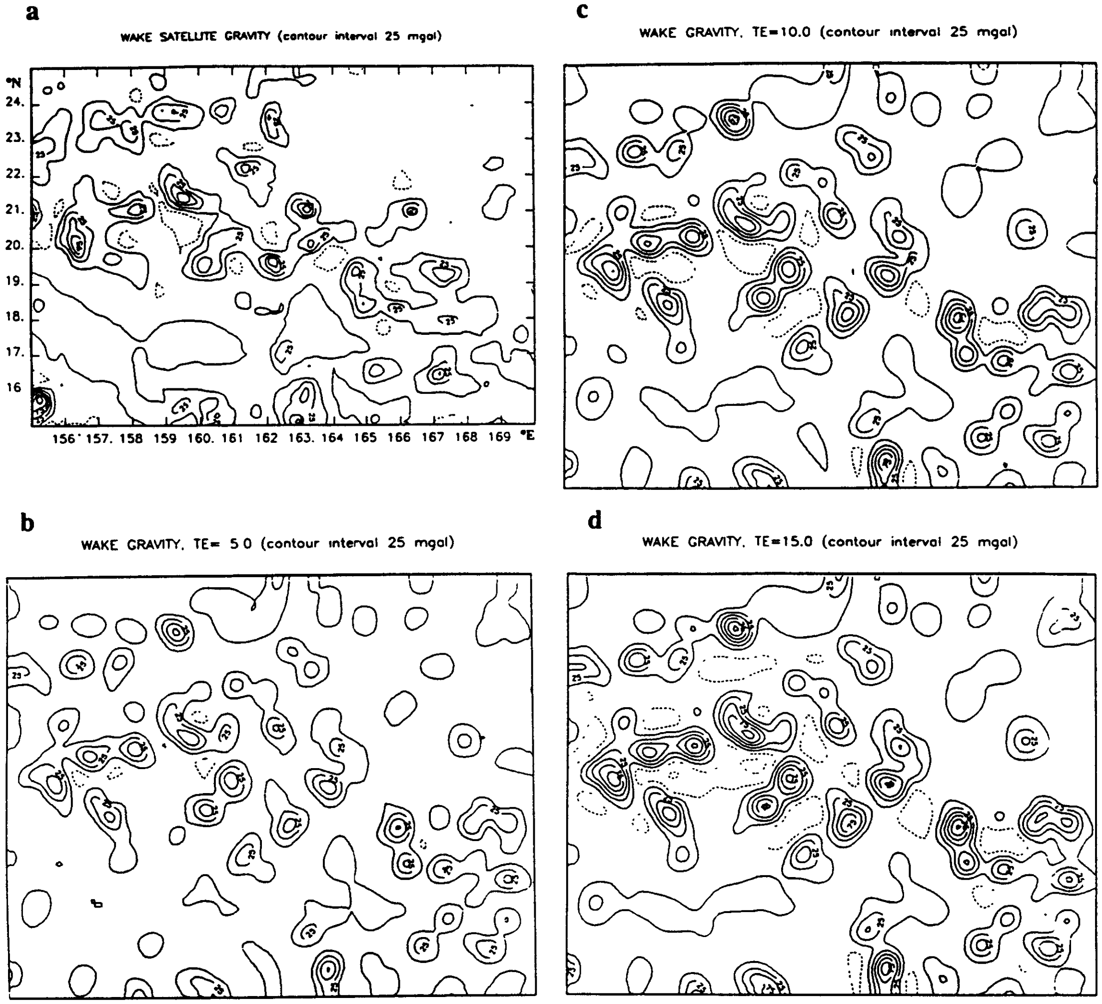

Fig. 4. Gravity over the Wake Guyots. Dashed contours show negative values. (*a*) Haxby's [1983] interpolated gravity. (*b*) Synthetic gravity, $T_e = 5$ km. (*c*) Synthetic gravity, $T_e = 10$ km. (*d*) Synthetic gravity, T_e=15 km.

that those passes could not be used to constrain elastic plate thickness.

ANALYSIS OF SHIPBORNE GRAVITY FROM THE JAPANESE AND WAKE SEAMOUNTS

Although the analysis of the satellite data suggested that the compensation of volcanoes in all three seamount groups is via flexure of plates thinner than 15 km, the poor quality of the bathymetry data and the inability of the satellite altimetry to distinguish 10- to 15-km-thick plates from thicker ones allows the possibility that some of the Darwin Rise volcanoes did not form on anomalously weak lithosphere. To better constrain the compensation of these volcanoes, we acquired high-resolution bathymetric data and shipborne gravity data during the *Roundabout* leg 10 expedition, along with single-channel seismic data, marine magnetics, and dredge samples, as part of a survey in support of possible ocean drilling of Cretaceous guyots. Here we focus on results from modeling the gravity data acquired for the Japanese Seamounts and the Wake Guyots along the track line given in Figures 7*a* and 7*b*.

We found that modeling the shipborne gravity over the seamounts required precise knowledge of bathymetry for the entire seamount, not just beneath the ship tracks. We were fortunate to have Navy multibeam sonar array sounding system (SASS) bathymetry [e.g.,*Vogt and Smoot*, 1984; *Smoot*, 1989] covering the flanks of the seamounts we surveyed in the Japanese and Wake groups to supplement our long ship tracks across the seamounts and detailed summit surveys. Experiments in modeling the gravity data without using any off-track information, via assuming that the bathymetry was circularly symmetric about its summit, produced poor agreement compared to models incorporating the actual, often complex, shape of the volcanoes.

Previously compiled SASS maps were digitized and projected onto grids with spacing between 1.0 and 1.4 km, which is

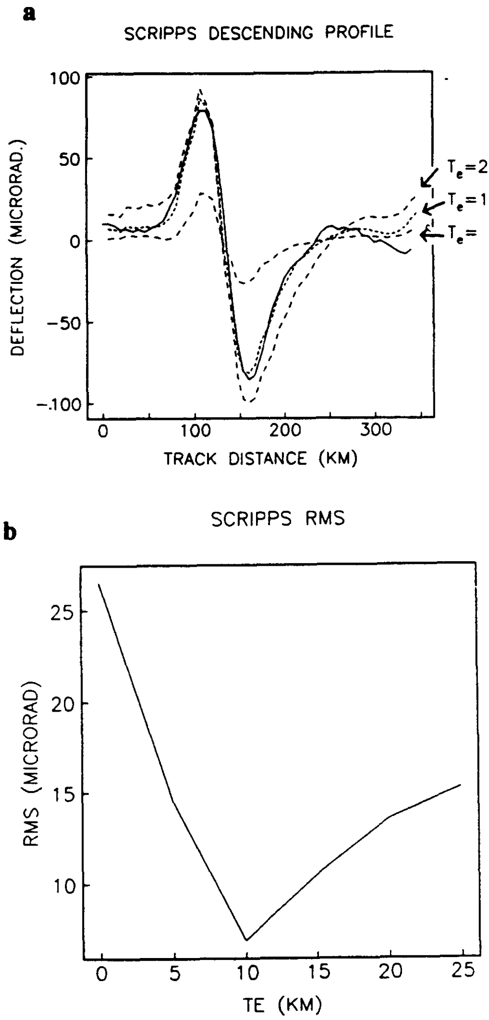

Fig. 5. (*a*) Deflection of the vertical over Scripps seamount. Descending Seasat track is shown as a straight line. Synthetics for T_e = 0, 10, and 25 km are shown as dashed lines. (*b*) RMS misfit between oberved and calculated deflection of the vertical plotted against the elastic plate thickness parameter.

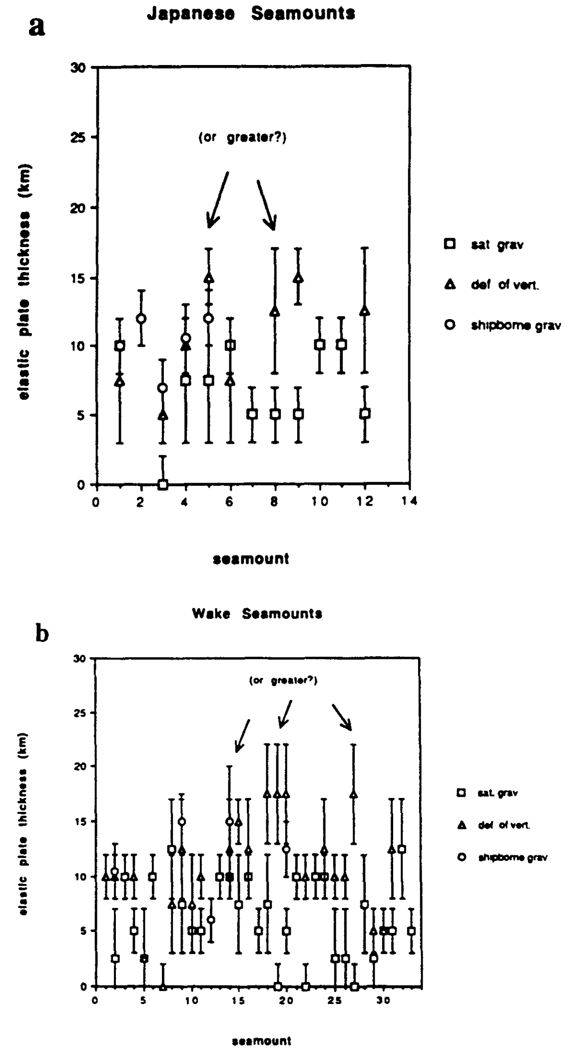

Fig. 6. Elastic plate thicknesses of Darwin Rise guyots obtained from the study of satellite gravity, satellite deflection of the vertical, and shipborne gravity. See Table 2 for locations of seamounts plotted in figures. (*a*) Japanese Seamounts, including those surveyed on *Roundabout* leg 10: 1, Takuyo-Daini and Seiko; 2, Winterer; 3, Stout and Thomas Washington; 4, Isakov; and 5, Makarov. (*b*) Wake Guyots, including those surveyed on *Roundabout* leg 10: 2, Scripps; 9, Lamont; 12, Vibelius; 14, Woods Hole; and 20, Pot. (*c*) Mid-Pacific Mountains, including Darwin (2), surveyed on *Roundabout* leg 10.

comparable to the shallowest depth on a guyot. Volcanoes with nearby neighbors, such as the pair Takuyo-Daini and Seiko or the cluster in the Winterer group containing Winterer, Charlie Johnson, Stout, and Thomas Washington, were modeled using the bathymetry of all adjacent features. A smooth linear interpolation from the seamount flanks to the regional depth was used to fill in grid points surrounding the seamounts in order to produce an array extending 200 km from the center of the load.

For Woods Hole guyot in the Wake group and Darwin Guyot located at the western edge of the Mid-Pacific Group (seamount 2 in Table 2c), SASS maps were not available, but the coverage from *Roundabout* leg 10 was sufficient to model gravity. The SASS bathymetry for Lamont did not include a satellite seamount surveyed on the northern track line. A circular model of this satellite was added to the bathymetry, although the final results using the southern track line were not sensitive to the presence or absense of this feature. The SASS positions of Wilde and Vibelius guyots, which were well-surveyed by *Roundabout* leg 10, were found to be mislocated almost 1° north. Moreover, while the SASS bathymetry for Vibelius was consistent with our shipboard data, for Wilde a large discrepancy existed in regards to its size.

Fig. 6. (Continued)

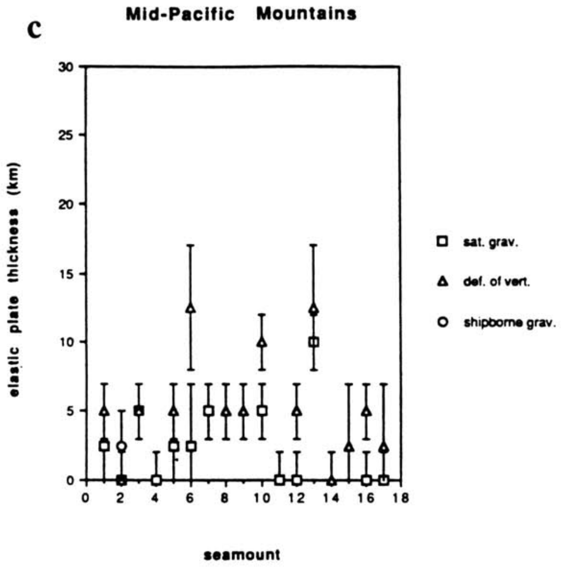

Equations (1) and (2) were again used on this denser grid to produce a grid of gravity. Figure 8 shows one example of a three-dimensional gravity model of Takuyo-Daini and Seiko seamounts, and Figure 9 compares the predicted gravity to the observed along the ship track across Seiko for three different choices of elastic plate thickness. A 5-km-thick plate produces a flexural moat which is too deep, a flexural wavelength which is too short, and a gravity anomaly which is too small over the top of the seamount (Figure 9*a*). A plate as thick as 20 km produces a flexural wavelength and gravity amplitude which are both too large (Figure 9*c*). A 10-km-thick plate clearly provides an excellent fit to the sea surface gravity data.

We quantitatively assessed the fit between synthetic and actual gravity profiles by plotting contours of RMS misfit as a function of T_e and ρ_c. We favor the use of RMS misfit rather than contours of the "objective function" [*Smith et al.*, 1989], for which preferred models have both a low RMS and a low correlation between the residual gravity (observed minus model) and topography. Our T_e results were well-constrained by the RMS criterion, and we were not able to constrain densities confidently using the objective function of Smith et al. Figure 10*a* shows the RMS misfit contours for Seiko. The best fitting T_e in this case changes only slightly over different density values, from an estimated 9 km at 2800 kg/m^3 to 12 km at 2600 kg/m^3. Although we could not select a preferred density based on RMS misfit alone, a visual inspection of the fit of models to the data throughout the Japanese group showed that for densities less than 2700 kg/m^3, the synthetic profile at the best fitting T_e value underestimated the peak gravity anomaly over the seamount. It is unlikely that the bulk of the seamount would have a density any less than this value that best fits the anomaly at the summit since many of the Japanese seamounts are capped by reefs. In the Wake group, where only Vibelius has a reefal cap, we also prefer solutions for higher crustal densities. Therefore, in cases for which there was some trade-off between density and T_e on the misfit plots, we chose the value of T_e which gave the minimum misfit for ρ_c = 2700 to 2800 kg/m^3. This choice is consistent with that of *Calmant and Cazenave* [1987], who used ρ_c = 2800 kg/m^3, allowing us to directly compare our elastic thickness values from the Darwin Rise with theirs from the superswell.

Figure 10 shows the RMS contours for the five guyots we surveyed in the Japanese Seamounts. Values for T_e obtained from shipborne data are included in Figure 6*a*. Note the good agreement with the results from analyzing the satellite data, even at the detail of both studies indicating a lower elastic plate thickness for Thomas Washington and Stout compared to the others in the cluster. The possibility of an elastic plate thickness greater than 15 km for Makarov based on the shape of the misfit curve for deflection-of-the-vertical data is not seen in the results from modeling the sea surface data. We believe that unmodeled high-frequency information in the satellite deflection data is responsible for this discrepancy.

Figure 11 shows RMS contours for five guyots in the Wake Guyots, and Figure 12 shows RMS contours for Darwin Guyot in the Mid-Pacific Mountains. Values for T_e obtained from shipborne

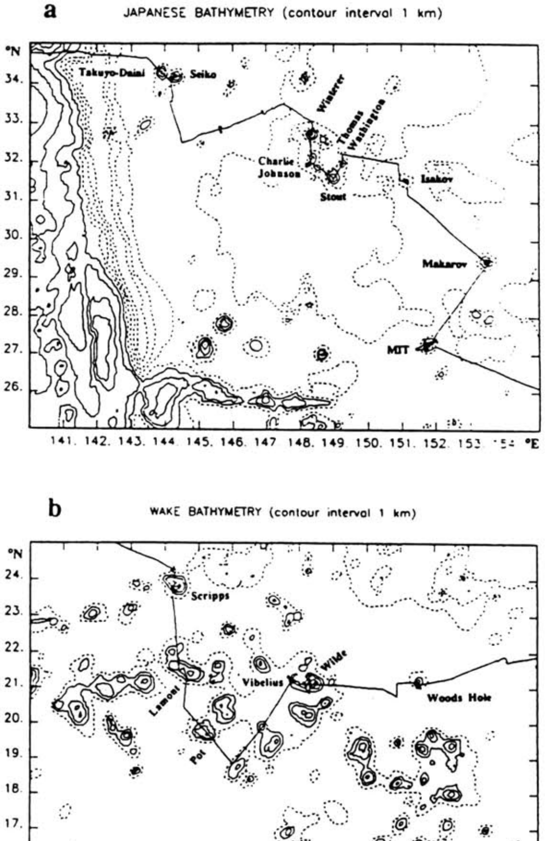

Fig. 7. Track of *Roundabout* Leg 10, with bathymetry as in Figure 2. (*a*) The Japanese Seamounts. (*b*) The Wake Guyots.

TABLE 2*a*. DBDB5 Location of Seamounts in Figure 6*a*

Seamount	Latitude	Longitude
1	34.2°N	143.9°E
2	32.8°N	148.3°E
3	31.7°N	149.0°E
4	31.5°N	151.0°E
5	29.5°N	153.5°E
6	27.8°N	145.8°E
7	27.2°N	145.2°E
8	27.2°N	151.8°E
9	27.0°N	148.7°E
10	26.0°N	144.0°E
11	26.0°N	145.0°E
12	25.8°N	147.0°E

TABLE 2*b*. DBDB5 Location of Seamounts in Figure 6b

Seamount	Latitude	Longitude
1	23.8°N	158.3°E
2	23.8°N	159.5°E
3	23.4°N	162.2°E
4	23.2°N	158.0°E
5	23.1°N	156.9°E
6	22.8°N	155.8°E
7	22.8°N	156.0°E
8	22.7°N	160.9°E
9	21.3°N	159.8°E
10	21.2°N	157.7°E
11	21.2°N	158.3°E
12	21.2°N	162.8°E
13	21.2°N	163.5°E
14	21.2°N	166.5°E
15	20.5°N	160.7°E
16	20.3°N	156.5°E
17	20.2°N	163.2°E
18	19.9°N	161.9°E
19	19.8°N	157.5°E
20	19.7°N	160.2°E
21	19.7°N	166.9°E
22	19.5°N	167.7°E
23	19.3°N	166.7°E
24	19.3°N	167.5°E
25	18.4°N	165.0°E
26	18.3°N	165.9°E
27	18.0°N	167.5°E
28	16.9°N	162.7°E
29	16.6°N	165.2°E
30	16.5°N	167.0°E
31	16.0°N	163.1°E
32	15.8°N	155.3°E
33	15.6°N	160.4°E

TABLE 2*c*. DBDB5 Location of Seamounts in Figure 6c

Seamount	Latitude	Longitude
1	22.6°N	176.3°E
2	22.1°N	171.6°E
3	21.9°N	175.1°E
4	21.4°N	176.3°E
5	21.2°N	173.8°E
6	21.2°N	174.2°E
7	21.2°N	178.0°E
8	21.0°N	178.5°E
9	20.2°N	174.1°E
10	20.1°N	172.0°E
11	19.0°N	173.2°E
12	18.4°N	180.3°E
13	18.2°N	171.2°E
14	17.9°N	178.2°E
15	17.9°N	178.6°E
16	17.3°N	174.0°E
17	17.1°N	182.8°E

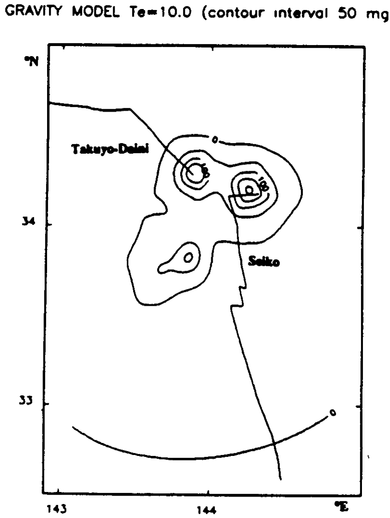

Fig. 8. Gravity model over Takuyo-Daini and Seiko seamounts, $T_e = 10$ km, $\rho_c = 2800$ kg/m^3. Ship track is shown for reference.

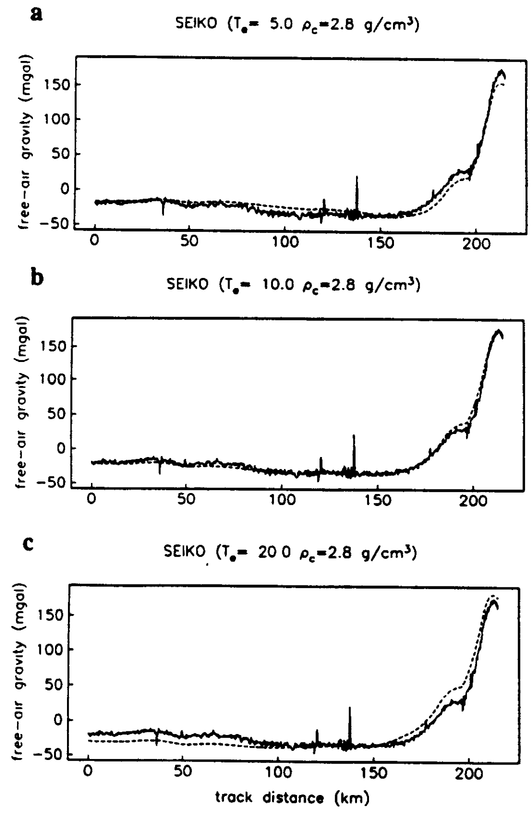

Fig. 9. Profiles of observed gravity (straight line) and synthetics (dashed line) over Seiko seamount, $\rho_c = 2800$ kg/m^3. (*a*) $T_e = 5$ km. (*b*) $T_e = 10$ km. (*c*) $T_e = 20$ km.

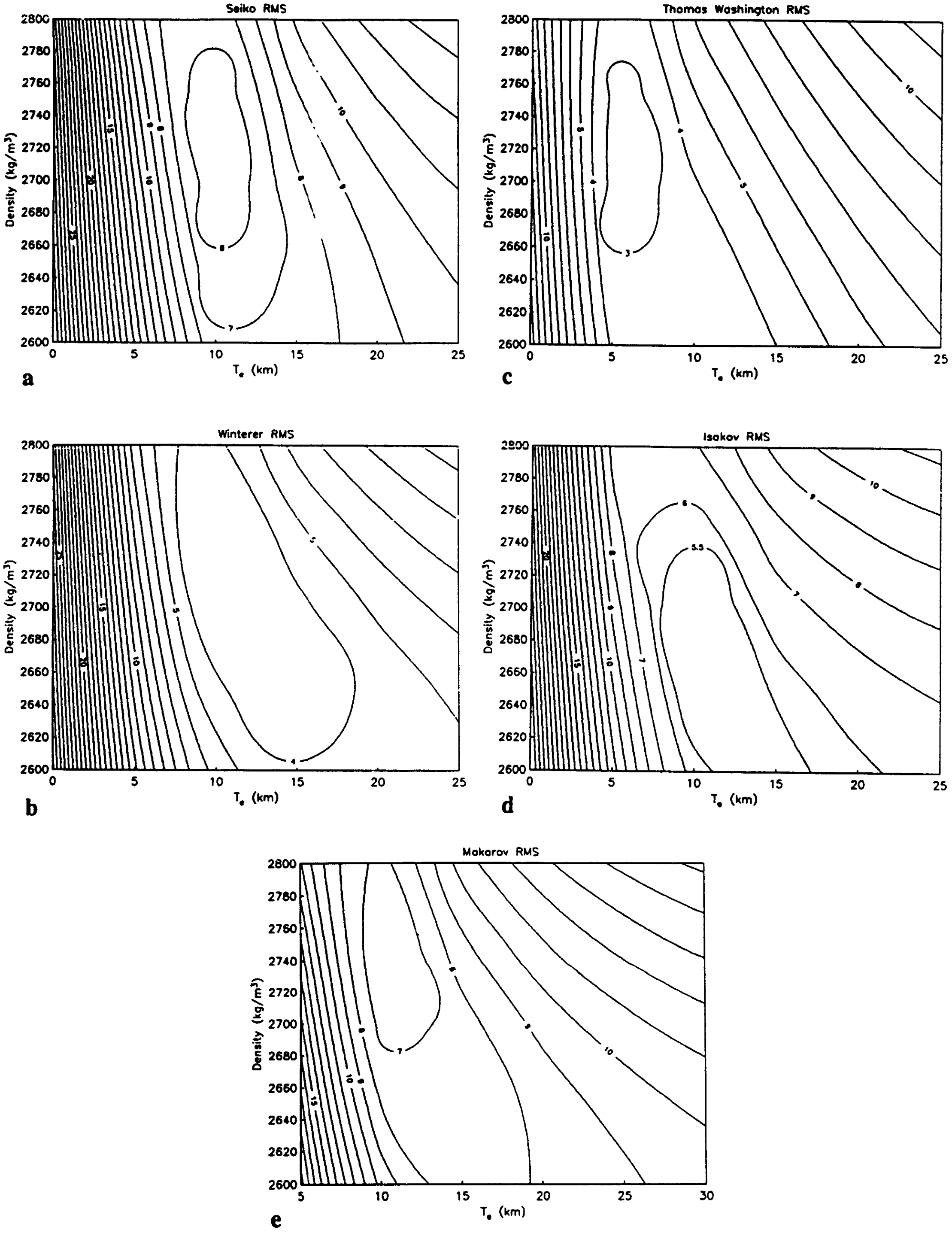

Fig. 10. Contour maps of RMS misfit between real and sythetic gravity lines gridded against the parameters of elastic plate thickness and density for five seamounts in the Japanese group. (*a*) Seiko. (*b*) Winterer. (*c*) Thomas Washington. (*d*) Isakov. (*e*) Makarov.

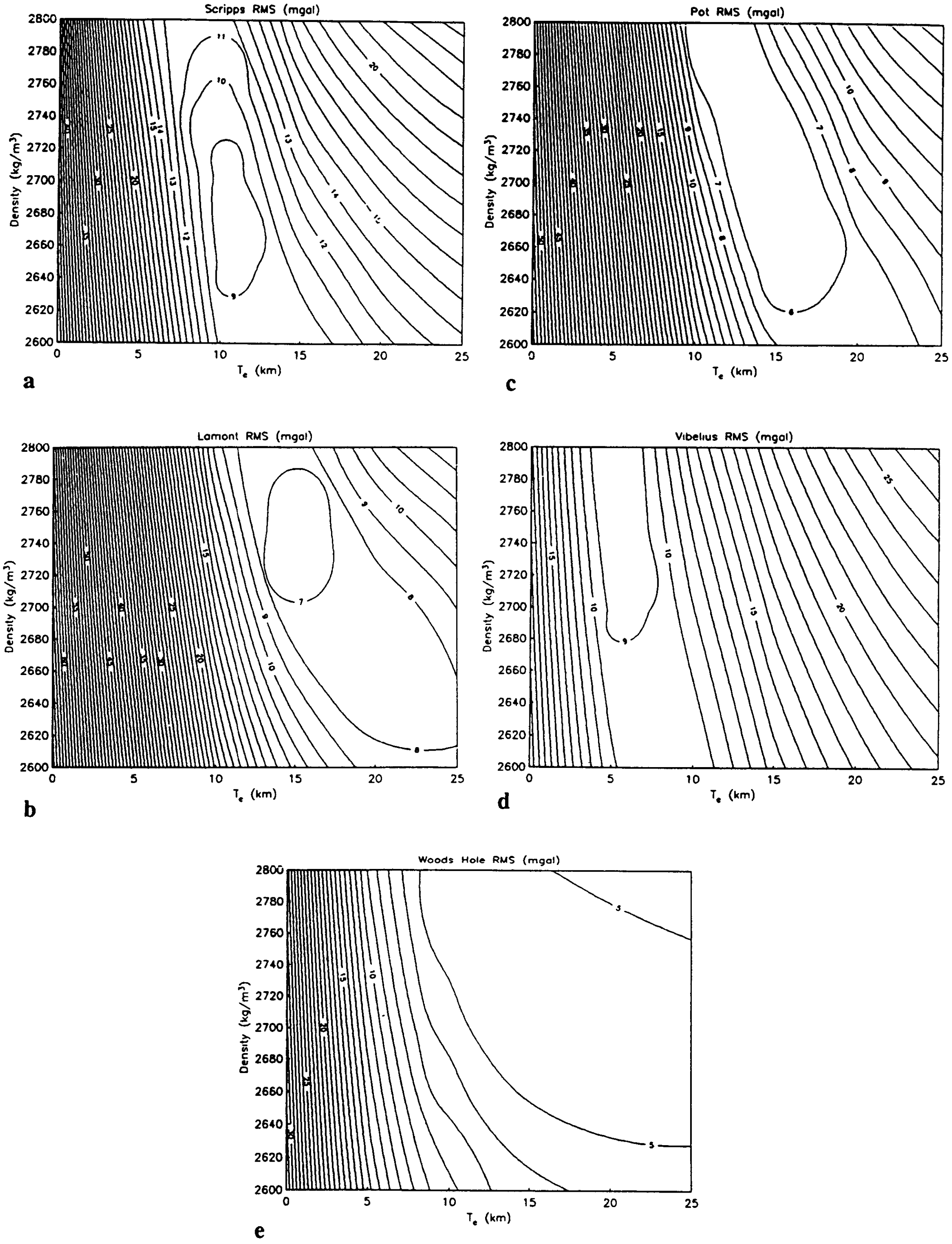

Fig. 11. Contour maps of RMS misfit between real and sythetic gravity lines gridded against the parameters of elastic plate thickness and density for five seamounts in the Wake group. (*a*) Scripps. (*b*) Lamont. (*c*) Pot. (*d*) Vibelius. (*e*) Woods Hole.

data (Figures 6*b* and 6*c*) again showing good agreement with the satellite results. The T_e values for Scripps, Pot, and Lamont are all constrained between 10 and 15 km for higher crustal densities; the values for Vibelius and Darwin are lower, at 5 and 0 km, respectively; the value for Woods Hole is constrained only to be greater than 10 km.

In general, given the high-quality of the shipborne gravity data and of the SASS bathymetry, results from shipborne gravity provide the best estimate of T_e. Values of deflection give the next best estimate, provided that the seamount is well-located and that the bathymetry is of good quality. Satellite gravity results underestimate elastic plate thicknesses over seamounts.

In order to constrain whether the Japanese and Wake seamounts formed on young lithosphere, we estimate the age of the lithosphere from the magnetic lineations of *Nakanishi et al.* [1989], and the age of the volcanoes is based on ^{40}Ar/^{39}Ar dating [*Ozima et al.*, 1977] and fossil minimum ages from reefal material [*Matthews et al.*, 1974]. Volcanic and reefal material collected from guyots during *Roundabout* leg 10 are also being analyzed to obtain radiometric and paleontological dates. Preliminary results for the Japanese guyots give radiometric dates of 103 and 108 Ma for Isakov and Winterer. In the Wake group, dates of 91 and 82 to 96 Ma have been obtained for Wilde and Lamont (R. Duncan, personal communication, 1990). Paleontological dates for the reef-capped guyots indicate that these reefs drowned at approximately 98 Ma [*R. Van Waasbergen et al.*, 1990]. In the case of Darwin guyot, magnetics indicate that this seamount was formed in M-series, before 118 Ma (W. Sager, personal communication, 1989).

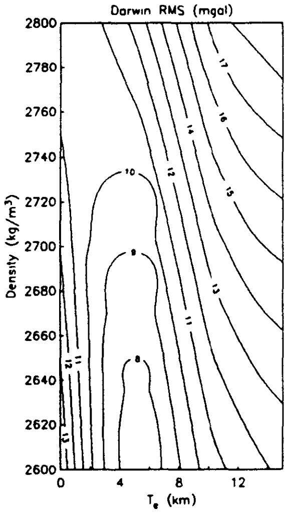

Fig. 12. Contour map of RMS misfit between real and sythetic gravity lines gridded against the parameters of elastic plate thickness and density for Darwin seamount in the Mid-Pacific group.

Based on these ages, all of the constrained *Te* values are less than expected for normal oceanic lithosphere, and fall in the superswell region on Figure 1. The age of the lithosphere at the time of loading for most of the Japanese Seamounts is 40 to 60 m.y., in some cases just marginally large enough to distinguish truly the superswell range of T_e values from those of normal lithosphere elsewhere. The age of the lithosphere at the time of loading is larger, being 50 to 80 m.y., for most of the Wake Seamounts, which erupted later than the Japanese group on lithosphere that formed during the Jurassic Quiet Zone (160-169 Ma). The results from modeling the sea surface gravity data we collected in the Wakes also confirm the low-T_e values seen in the satellite data, providing strong evidence for the existence of weak lithosphere on the Darwin Rise when the seamount groups formed.

CONCLUSIONS

Based on modeling Seasat gravity and deflection of the vertical over seamounts of the Darwin Rise, we find that the Mid-Pacific Mountains formed on the weakest plate, consistent with formation of these volcanoes in a near-ridge environment, as proposed by *Winterer and Metzler* [1984]. The T_e values for the Japanese and Wake region show more scatter, but nowhere are values definitely greater than 15 km. Despite the generally good agreement between T_e values derived from the interpolated gravity maps and the direct modeling of deflection of the vertical along satellite passes, errors in the dbdb5 data set may lead to incorrect choices of elastic plate thickness. Therefore, we used shipborne gravity to obtain more precise estimates of T_e for five seamounts in the Japanese group, five in the Wake group, and one in the Mid-Pacific Mountains. The preferred T_e values show reasonable agreement with satellite values and confirm that the lithosphere was anomalously weak at the time of volcanism, supporting the hypothesis that the seamounts formed in a superswell-type environment.

Acknowledgments This research was supported by NSF grant 8717826-OCE. We thank Peter Shaw and Paul Filmer for their help in the beginning phase of this study. We are indebted to Bill Haxby and David Sandwell for suggestions that improved the manuscript.

REFERENCES

Calmant, S., and A. Cazenave, Anomalous elastic thickness of the oceanic lithosphere in the south-central Pacific, *Nature, 328*, 236-238, 1987.

Cazenave, A., B. Lago, K. Dominh, and K. Lambeck, On the response of the ocean lithosphere to sea-mount loads from Geos 3 satellite radar altimeter observations, *Geophys. J. R. Astron. Soc., 63*, 233-252, 1980.

Freedman, A. P., and B. Parsons, Seasat-derived gravity over the Musicians seamounts, *J. Geophys. Res., 91*, 8325-8340, 1986.

Goetze, C., and B. Evans, Stress and temperature in the bending lithosphere as constrained by experimental rock mechanics, *Geophys. J. R. Astron. Soc., 59*, 463-478, 1979.

Hart, S. R., A large-scale isotope anomaly in the southern hemisphere mantle, *Nature, 309*, 753-757, 1984.

Haxby, W. F., G. D. Karner, J. L. Lebrecque, and J. K. Weissel, Digital images of combined oceanic and continental data sets and their use in tectonic studies, *Eos Trans. AGU, 64*, 995-1004, 1983.

Kirby, S. H., Tectonic stresses in the lithosphere: Constraints provided by experimental deformation of rocks, *J. Geophys. Res., 85*, 6353-6363, 1980.

Matthews, J. L., B. C. Heezen, R. Catalano, A. Coogan, M. Tharp, J. Natland, and M. Rawson, Cretaceous drowning of reefs on Mid-Pacific and Japanese guyots, *Science, 184*, 462-464, 1974.

McNutt, M. K., and K. M. Fischer, The south Pacific superswell, in *Seamounts, Islands, and Atolls*, edited by B. Keating, P. Fryer, R. Batiza, and G. W. Boehlert, *Geophys. Monogr. Ser.*, vol. 43, AGU, Washington, D.C., 1987.

McNutt, M., and H. W. Menard, Lithospheric flexure and uplifted atolls, *J. Geophys. Res.*, *83*, 1206-1212, 1978.

McNutt, M.K., E.L. Winterer, W. Sager, J. Natland, and G. Ito, The Darwin rise: A Cretaceous superswell?, *Geophys. Res. Lett.*, *17*, 111-114, 1990.

Menard, H. W., *Marine Geology of the Pacific*, 271 pp., McGraw-Hill, New York, 1964.

Menard, H. W., Darwin reprise, *J. Geophys. Res.*, *89*, 9960-9968, 1984.

Nakanishi, M., K. Tamaki, and K. Kobayashi, Mesozoic magnetic anomaly lineations and seafloor spreading history of the northwestern Pacific, *J. Geophys. Res.*, *94*, 15,437-15,462, 1989.

Natland, J. H., and E. Wright, Magmatic lineages and mantle sources of Cretaceous seamounts of the central Pacific, *Eos Trans. AGU*, *65*, 1075-1076, 1984.

Ozima, M., M. Honda, and K. Saito, ^{40}Ar-^{39}Ar ages of guyots in the western Pacific and discussion of their evolution, *Geophys. J. R. Astron. Soc.*, *51*, 475-485, 1977.

Parker, R. L., The rapid calculation of potential anomalies, *Geophys. J. R. Astron. Soc.*, *31*, 447-455, 1973.

Parsons, B., and J. G. Sclater, An analysis of the variation of ocean floor bathymetry and heat flow with age, *J. Geophys. Res.*, *82*, 803-827, 1977.

Sandwell, D. T., Along-track deflection of the vertical from Seasat: GEBCO overlays, *NOAA Tech. Memo, NOS NGS-40*, 1984.

Smith, W. H. F., H. Staudigel, A. B. Watts, and M. S. Pringle, The Magellan seamounts: Early Cretaceous record of the south Pacific isotopic and thermal anomaly, *J. Geophys. Res.*, *94*, 10,501-10,523, 1989.

Smoot, N. C., The Marcus-Wake seamounts and guyots as paleo-fracture indicators and their relation to the Dutton ridge, *Mar. Geol.*, *88*, 117-131, 1989.

Staudigel, H., K.-H. Park, M. Pringle, W. H. F. Smith, and A. Zindler, The longevity of the south Pacific isotopic and thermal anomaly, *Earth Planet. Sci. Lett.*, in press, 1990.

Van Waasbergen, R., W. Sliter, I. Premoli-Silva, R. Duncan, J. Natland, E. Winterer, Radiometric and paleontological age constraints on the birth and death of NW Pacific early Cretaceous atolls, *Eos Trans. AGU*, *71*, 1661, 1990.

Vogt, P. R., and N. C. Smoot, The Geisha guyots: Multibeam bathymetry and morphometric interpretation, *J. Geophys. Res.*, *89*, 11,085-11,107, 1984.

Walcott, R. I., Flexure of the lithosphere at Hawaii, *Tectonophysics*, *9*, 435-446, 1970.

Watts, A. B., and J. R. Cochran, Gravity anomalies and flexure of the lithosphere along the Hawaiian-Emperor seamount chain, *Geophys. J. R. Astron. Soc.*, *38*, 119-141, 1974.

Watts, A. B., and N. M. Ribe, On geoid heights and flexure of the lithosphere at seamounts, *J. Geophys. Res.*, *89*, 11,152-11,170, 1984.

Watts, A. B., J. H. Bodine, and N. R. Ribe, Observations of flexure and the geological evolution of the Pacific ocean basin, *Nature*, *283*, 532-537, 1980.

Winterer, E. L., and C. V. Metzler, Origin and subsidence of guyots in Mid-Pacific Mountains, *J. Geophys. Res.*, *89*, 9969-9979, 1984.

M.K. McNutt and C. J. Wolfe, Department of Earth, Atmospheric, and Planetary Sciences, Massachusetts Institute of Technology, Cambridge, MA 02139.

(Received March 29, 1990;
revised August 16, 1990;
accepted August 16, 1990.)

CHAPTER 2

THE MARQUESAS ARCHIPELAGIC APRON: SEISMIC STRATIGRAPHY AND IMPLICATIONS FOR VOLCANO GROWTH, MASS WASTING, AND CRUSTAL UNDERPLATING

ABSTRACT

Multichannel seismic lines, sonobuoy and gravity data across the Marquesas Islands are used to study volcano growth, island mass-wasting, and crustal underplating at island chains with overfilled moats. The Marquesas bathymetry reflects the changing thickness of the sedimentary infill rather than the basement topography. The moat contains two major regions of differing seismic stratigraphy: (1) the moat edges, where a unit of continuous layered reflectors is present containing minor lenses of chaotic diffractors and (2) the central moat, where the deep moat basins are overfilled by an acoustically opaque unit of discontinuous reflectors of up to 2 km thickness, in places capped by a ponded unit. Plate-flexure models require broad underplating of the crust by low density (crustal?) material at the Marquesas Islands to explain the depth to volcanic basement and gravity observations. The seismic velocities and seismic stratigraphy, as well as the general structure of the islands and surrounding seafloor, indicate the apron is mostly debris from island mass wasting. Reflectors of the outermost moat generally onlap the flexural arch in the lower section and offlap and overfill it in the upper section. In the central moat, reflectors change shape from concave up in the lower section to convex in the upper section. Three-dimensional diffusion models of sedimentation, which incorporate a time-dependent seafloor deflection from progressive island loading and vary sediment influx as islands are formed and mass waste, suggest that three main factors make the moat stratigraphy at the Marquesas different from Hawaii: (1) the Marquesas moat is overfilled, while the Hawaiian moat is underfilled, (2) sediment diffusivities are lower at the Marquesas, and (3) the Marquesas islands are separated by deep sedimentary basins, in contrast to Hawaii, where islands are separated by a shallow ridge. The lower sediment diffusivity at the Marquesas may reflect a larger proportion of "blocky", massive material in the central Marquesas moat or alternatively a change in the dominant process of sediment transport. While there is similar sediment supply for a given along-moat distance at both the Marquesas and Hawaii, the underfilled moat at Hawaii is apparently a consequence of

greater moat volumes due to the larger size of the Hawaiian volcanoes, and possibly variations in underplating, that load the plate. The difference in sediment/edifice ratios is likely related to the larger eruption rates at Hawaii and different styles of volcano construction between Hawaii and the Marquesas.

INTRODUCTION

The Marquesas Islands of French Polynesia (Figure 1) form a 100 km wide by 400 km long linear island chain where hotspot volcanism has been relatively short-lived, from about 6 Ma at Eaio to 1 Ma at Fatu Hiva [e.g., *Duncan and McDougall*, 1974; *Brousse et al.*, 1990; *Desonie et al.*, 1993]. No flexural depression is evident in the bathymetry, but instead there is a classic archipelagic apron [*Menard*, 1956] covering the moat and preexisting seafloor. The underlying flexure from island loads is apparent in the gravity data and can be modeled with an elastic plate of about thickness (T_e) 17 km [*Filmer et al.*, 1993], much less than the T_e of about 30 km observed at the Hawaiian islands, where a moat and arch are observed [*Watts,* 1978; *Wessel*, 1993]. This study uses seismic stratigraphy and quantitative flexural and sedimentation models to learn more about the processes that form the Marquesas apron and make it different from the underfilled moat at Hawaii.

ten Brink and Watts [1985] model the seismic stratigraphy on a line across the Hawaiian chain using a two-dimensional loading geometry and assuming that each sediment unit fills the moat depression to an even level. The pattern of onlap of the arch in the lower section and offlap in the upper section can be generated by prolonged (> 1 m.y.) viscoelastic relaxation of the lithosphere. However, a more realistic model using 3-D loading geometry and considering the progressive loading of an elastic plate by new islands can create a similar pattern of across-moat stratigraphy without requiring viscoelastic relaxation [*Watts and ten Brink*, 1989]. The study of several across-moat and along-moat profiles of single channel seismic reflection data indicates that Hawaiian moat stratigraphy is influenced by the dual effects of lithospheric flexure from progressive island loading and sedimentation from large-scale mass wasting [*Rees et al.*, 1993]. This result is consistent with GLORIA images revealing submarine landslide deposits from slumps or debris avalanches throughout the Hawaiian moat [*Moore et al.*, 1989]. Such landslide deposits segment the moat into a series of sub-basins and control lateral transport of sediment along the moat [*Moore et al.*, 1989; *Rees et al.*, 1993]. Previously collected single-channel seismics and 3.5 kHz data at the Marquesas apron also indicate a large component of volcanic debris [*Filmer et al.*, 1994], yet this data is of low signal-to-noise and limited penetration.

Island construction and erosion at the Marquesas is distinctive. The volcanoes exhibit a succession of edifice building stages: generally an outer volcano is formed and followed by caldera collapse, then an inner volcano is formed within the caldera and similarly followed by caldera collapse [c.f., *Chubb*, 1930; *Brousse et al.*, 1978; *Brousse et al.*, 1990]. Unlike Hawaiian volcanoes, the intensity of successive magmatic phases does not diminish with time [*Brousse et al.*, 1990]. Catastrophic mass wasting occurred at several islands following construction (Eiao, Hatutu, Nuku Hiva, Ua Huka, Hiva Oa, Fatu Hiva, Tahuata, and Motagne--note the crescent shape of most of these islands in Figure 1), in each case resulting in the disappearance of up to half of the subaerial structure, leaving a crescent-shaped caldera and a well-developed amphitheater that borders the sea [c.f. *Chubb*, 1930; *Brousse et al.*, 1978].

In this paper multichannel seismic lines, sonobuoy and gravity data across the Marquesas Islands are used to characterize the seismic stratigraphy of an archipelagic apron, compare the depth to the volcanic basement with plate flexure models, and understand how apron stratigraphy is influenced by the dual effects of sediment influx and subsidence from progressive island loading of an elastic plate. We find that plate-flexure models provide evidence for crustal underplating beneath the Marquesas and use models of diffusive sedimentation and flexure from progressive island loading to help explain why the sedimentation history of the flexural moats at the Marquesas and Hawaii are so different.

DATA ACQUISITION AND PROCESSING

The R/V *Maurice Ewing* cruise EW 91-03 collected cross-moat profiles of multichannel seismic (MCS) reflection data at three inter-island regions (Figure 1). The MCS streamer had 148 channels with 25 m spacing and data were recorded at a 4 milliseconds sampling interval. Twenty airguns were deployed with a total source volume of 8385 in^3, and shots were fired at a 20 s interval. Individual traces were binned at 25 m, gathered, and stacked at Lamont-Doherty Earth Observatory. Digitized line drawings shown in Figure 2 were made from bandpassed common depth point (CDP) data (6-60 Hz), corrected for spherical divergence and redisplayed at large scales.

Sixteen sonobuoys were deployed across line 1162, which give velocity information on the sedimentary section and constrain depth to volcanic basement. Solutions from forward modelling are shown in Figure 3. The flexure of the oceanic lithosphere from island loading is apparent in the changing depth to volcanic basement and depth to Moho, although Moho reflections were only observed away from the central island region. Outside the moat, a unit of thin, low velocity (~2.5 km/s) sediment is present. Within the moat, sediments thicken and velocities increase to $\geq$ 4.0 km/s, as indicated by both refraction data (see Figure 4) and independent semblance analysis of MCS data. Such high seismic velocities have been reported for the moat infill at Hawaii [*ten Brink and Watts*, 1985; *Rees et al.*, 1993] and the Marquesas [*Filmer et al.*, 1994], and are consistent with volcanic material derived from island mass wasting. There is about 2-3 km of this high-velocity sedimentary material within the Marquesas central island moat (Figures 3 and 5).

The digitized time sections in Figure 2 are converted to depth sections (Figure 5) for more complete study of seismic stratigraphy, to constrain the depth to volcanic basement for flexural modeling and to compare the results of diffusion modeling with moat stratigraphy. For line 1162 sonobuoy velocities are used and for lines 1153 and 1155 we adopt a generalized velocity model, based on velocities along line 1162, consisting of 0.2 s of 2.5 km/s material overlying a unit of 4.0 km/s material.

STRATIGRAPHY OF THE MARQUESAS MOAT

We define three regions of different stratigraphy: the abyssal hill area, the moat edges, and the central moat (Figure 2). As shown below, the seismic stratigraphy indicates that the Marquesas moat is overfilled with sediment primarily derived from island mass wasting. The high seismic velocities of moat sediments (Figure 3) and evidence from island structure for catastrophic mass wasting [c.f., *Chubb*, 1930; *Brousse et al.*, 1978; *Brousse et al.*, 1990] are consistent with this conclusion.

Outside the moat, a thin (~0.2 s), well-bedded sedimentary unit is present that partially fills the lows between the abyssal hills (Figures 2 and 6). The low sediment velocities and thicknesses of this unit are consistent with pelagic sediment that has accumulated over time on the underlying basement. Diffractive volcanic basement is apparent beneath this thin unit (Figure 6), but gradually disappears near the moat edges as sediments thicken.

At the moat edges, the flexed volcanic basement is completely buried by a well-defined section of continuous reflectors 0.2-1.0 s thick, containing occasional lenses of diffractive material (Figure 7). This unit resembles the landslide unit observed by *Rees et al.* [1993] at the outer portion of the Hawaiian moat. The chaotic zones are characterized by a high frequency of diffractions that are not clearly associated with complex stratal geometries or stratal discontinuities. *Rees et al.* [1993] suggest that incoherent diffractions result from large (~100 m) basaltic blocks embedded in a matrix of poorly sorted volcanic debris, whereas the continuous reflectors are likely finer-grained and better-sorted turbidites that form the distal facies of these landslide deposits. Across-moat transport of sediment is evident at the western side of line 1155, where material traveling outwards from the central moat region is dammed by a local high (Figure 7).

In the central moat, proximal to the islands, there is a unit with seismic characteristics (hummocky reflectors, chaotic diffractors, discontinuous reflectors, and acoustic opaqueness) indicating that it contains a large component of poorly sorted material from island mass wasting. In this region, the moat is overfilled, with seafloor bathymetry indicating the changing thickness of the sedimentary section rather than the position of the flexed basement beneath (Figure 5), and contains a thick ($\geq$1 s) unit of discontinuous reflectors associated with high ($\geq$4.0 m/s) seismic velocities. This unit is more acoustically opaque than the oceanic crust beneath, and is capped by a ponded section of more continuous reflectors, sometimes containing lenses of chaotic diffractors. Although no well-defined basement reflector is present, we interpret the base of the reflective unit to mark volcanic basement, consistent with sonobuoy velocity models along line 1162.

At regions of steep volcanic topography, there is evidence of slumping in the uppermost section (lines 1153 and 1162). Reflectors having hummocky topography, a characteristic feature of the seafloor at landslides [e.g., *Prior*, 1984; *Lipman et al.*, 1988; *Moore et al.*, 1989], can be traced on the upper sections. On line 1162, for example, a hummocky reflector near 4.8 s (Figure 2 and Figure 8) marks the boundary between a ponded unit of continuous reflectors above and a unit of discontinuous reflectors below. Migration collapses diffractions throughout the section and reveals only a slightly more continuous pattern of reflectors (Figure 8b). Note that diffractions at the basal layer, near 6.0 s and CDP 16300, are bowties from synclines. On lines 1153 and 1155, the deep reflectors are more discontinuous and difficult to trace laterally than on line 1162 (Figure 9). There are landslide ridges along line 1162 and line 1153 (Figures 2 and 5), reminiscent of the debris ridges produced by island mass wasting at the Hawaiian moat [*Moore et al.*, 1989].

While sediment fill at the moat edges resembles the landslide unit observed at the Hawaiian moat, no equivalent to the Marquesas central moat unit has been observed at Hawaii. The character of the MCS data indicates a higher proportion of poorly sorted and blocky landslide material within the Marquesas central moat than at the moat edges. Chaotic diffractors can be identified in the ponded unit and in the topmost portion of the unit of discontinuous reflectors, but they cannot be identified at greater depths where the section is opaque and entirely "chaotic". A similar pattern has been noted to occur at a continental margin, where subbottom profiles of debris flow deposits show no coherent internal reflectors, although zones of high-amplitude returns are present [*Prior et al.*, 1984]. The discontinuous nature of deep reflectors at the Marquesas may result from deposition of finer-grained sediments in an area where seafloor topography changes rapidly as multiple landslide events occur, creating local basins that channel sediment transport. Remolding of fine-grained turbidite or ponded sequences by submarine landslides may also be important. Some remolding of seafloor sediments and incorporation into a debris flow was suggested by *Prior et al.* [1984] to occur at a continental margin area.

The stratigraphic pattern at the Marquesas is also distinct from that observed at Hawaii [*ten Brink and Watts,* 1985; *Watts and ten Brink*, 1989; *Rees et al.*, 1993]. On line 1162, in the center of the island chain (Figure 5), moat edge reflectors onlap the arch in the lower section and offlap and overfill the moat in the upper section. Reflectors at the moat edges along line 1153 and the eastern side of 1155 also suggest this pattern of onlap and offlap, although reflectors are laterally discontinuous and difficult to interpret (Figure 5). In the central moat, reflectors change shape from concave up in the lower section to convex in the upper section.

LITHOSPHERIC FLEXURE: EVIDENCE FOR UNDERPLATING

Seismic studies at the Marquesas [*Caress et al.*, 1992] and Hawaii [*Watts et al.*, 1985] indicate that deep crustal underplating of high-velocity crustal material, or alternatively low-velocity mantle, occurs beneath the center of these island chains. We find that basement deflection and gravity data at the Marquesas also provide evidence for broad underplating of low-density (relative to mantle) material.

Flexural models using a simple elastic plate model with a thickness of about 17 km can successfully fit gravity data across the Marquesas [*Filmer et al.*, 1993], but consistently overestimate the deflection of volcanic basement (Figure 5). This misfit occurs both near the moat edges, where the thinly-sedimented diffractive basement is well-constrained, and in the thickly-sedimented central moat regions, where basement is not as clearly defined and may be overlain by a volcanic carapace. The misfit is large and cannot be accounted for by reasonable variations in crustal density or elastic plate thickness. While the top loading model in Figure 5 is that which fits the gravity (T_e=17 km), no top loading model is capable of fitting the seismic reflectors. The larger elastic plate thickness required to match the maximum basemennt deflection produces a moat that is too wide for the observations and gravity anomalies far in excess of anything seen. Separate calculations were made using seafloor bathymetry and using reduced bathymetry corrected for swell topography (refer to *Filmer et al.* [1994] for further information), since incorrectly modeling swell topography as surface loads, rather than as a response to subsurface thermal loads, will overpredict deflection. This effect has been shown to be significant at Hawaii [*Wessel,* 1993]. Because swell amplitudes at the Marquesas are small (about 500 m peak to peak), deflections obtained from raw and reduced bathymetry are similar, and we only show models made with raw bathymetry. There is a region of anomalously deep seafloor in the southwest (Figure 1), unrelated to island loading and causing the seafloor to slope along lines 1162 and 1153 (see Figures 2 and 5 and note that on line 1162 a scarp marks the transition to deep seafloor). Top-loading models for these two lines had a plane removed prior to the flexure calculations, which was later added back to the deflection.

We follow a method based on *Forsyth* [1985] to explore the effect of loading from below by underplating of low-density (relative to the mantle) material beneath the Marquesas (Figure 10). We assume that surface and subsurface loads are anti-correlated, such that high volcanic edifices are underlain by thick underplated crust. In the Fourier domain, the expression for relief of the Moho, $W_T(\mathbf{k})$, and topography, $H_T(\mathbf{k})$, from the applied load $(\rho_c-\rho_w)(H_T(\mathbf{k})-W_T(\mathbf{k}))$ on top on the plate is:

$$W_T(\mathbf{k})=\frac{-(\rho_c-\rho_w)H_T(\mathbf{k})}{(\rho_m-\rho_c)\xi} \tag{1}$$

where

$$\xi=1+\frac{Dk^4}{(\rho_m-\rho_c)g} \tag{2}$$

and

$$D=\frac{ET_e^3}{12(1-\nu^2)} \tag{3}$$

D is the flexural rigidity of the plate, calculated using an elastic plate thickness (T_e) of 17 km and a Young's modulus (E) of 8×10^{10} N/m, ν is Poisson's ratio, taken as 0.25, g is the gravitational acceleration, $\mathbf{k}$ is the two-dimensional wavenumber, $k=2\pi/\lambda=|\mathbf{k}|$, ρ_c is the average crustal density and also the density of the infilling moat material (2650 kg/m^3), ρ_m is mantle density (3300 kg/m^3), and ρ_w is water density (1000 kg/m^3).

Loading on the Moho by an applied underplating load $-(\rho_m-\rho_u)(W_B(\mathbf{k})-H_B(\mathbf{k}))$, where ρ_u is the density of the underplating material, results in a final relief at the Moho, $W_B(\mathbf{k})$, and elevation at the surface, $H_B(\mathbf{k})$, such that:

$$W_B(\mathbf{k})=\frac{-(\rho_u-\rho_w)H_B(\mathbf{k})\phi}{(\rho_m-\rho_u)} \tag{4}$$

where

$$\phi=1+\frac{Dk^4}{(\rho_u-\rho_w)g} \tag{5}$$

If the ratio of the weight of the applied bottom load to the weight of the applied top load is *f* and loads from below and above are 180° out of phase, then the bathymetry, $H(\mathbf{k})$, can be separated into $H_T(\mathbf{k})$ and $H_B(\mathbf{k})$, and one can calculate $W_T(\mathbf{k})$ and $W_B(\mathbf{k})$. At an average level of seafloor bathymetry, z_t, basement deflection is $(H_B(\mathbf{k})+W_T(\mathbf{k}))$. At the average Moho level, z_m, the crustal/underplating interface is $W_T(\mathbf{k})$, and underplating/Moho interface is $(W_B(\mathbf{k})+W_T(\mathbf{k}))$. The gravity anomaly is calculated by *Parker's* [1973] method using five terms. The gravity anomaly arises from (1) bathymetry, $H(\mathbf{k})$, with density anomaly $(\rho_c-\rho_w)$ at z_t, and (2) crustal topography, $W_T(\mathbf{k})$ at depth z_m, with density anomaly $(\rho_m-\rho_c)$, and (3) underplating material at depth z_m, having bottom interface $(H_B(\mathbf{k})+W_T(\mathbf{k}))$ and top interface $W_T(\mathbf{k})$, with density contrast $(\rho_m-\rho_u)$.

We find that a single f ratio at all wavelengths cannot simultaneously model both basement deflection and gravity data. We relax this assumption and allow the underplating body to be smoother than the bathymetry because this is needed to fit both sets of data. Gravity profiles (Figure 11) and basement deflection (Figures 5 and 12a) are well predicted using an *f* value of about 0.25 for wavelengths > 300 km and an *f* of zero for wavelengths < 300 km ($f=0$ reduces to the standard flexural equations (1) and (2)). *Wessel* [1993] constrained infill density and T_e at Hawaii by a parameter search minimizing the root-mean-square (rms) difference between predicted and observed plate deflection on an across moat line. Because of the range of free parameters in this study (underplating geometry as well as T_e and ρ_c), we perform only a limited search of different underplating models, using fixed T_e and ρ_c, that visually fit gravity and seismic data. Since there is a trade-off between underplating density and underplating thickness, MCS and gravity data can be fit either with underplating by up to 8 km of high-density 3100 kg/m^3 material (Figure 12b) or up to 2 km of average crustal material (2650 kg/m^3). Our model also contains negative underplating, equivalent to about 500 m of crustal thinning, in the anomalous region of deep seafloor to southwest, but we do not suggest that such thinning is necessarily real.

MCS data and flexural models imply broad crustal underplating beneath the Marquesas Islands (Figure 12b) so that basement deflections (Figure 12a) are less than the prediction of simple top-loading models. Although we cannot uniquely resolve the density structure, our model of underplating by high density crustal material is consistent with the high seismic velocities observed beneath the Marquesas and Hawaii, applying laboratory-derived velocity-density relations for oceanic rocks [*Christensen and Salisbury*, 1975]. The predicted thickness of such material beneath line 1162 is consistent in amplitude and position with preliminary results of an OBS experiment along this same track [*Caress et al.*, 1992], but it is of broader extent. The effects of underplating on plate deflection have not been adequately explored at Hawaii, although there the underplating hypothesis has been controversial [*Lindwall*, 1988]. *Watts and ten Brink* [1989], using 2-D models, find observed basement deflection can be predicted by either a 40-km plate with surface loading or a 25-km plate with both surface and subsurface loads. *Wessel* [1993], however, has shown that basement deflection can also be fit by a 25-km plate with surface loading once raw bathymetry has been corrected for the significant effects of swell loading from below. Further work using 3-D models that account for swell loads and possible underplating geometries could help to evaluate the influence of underplating at Hawaii.

MODELS OF MOAT SEDIMENTATION AT MARQUESAS AND HAWAII

The stratigraphy at the Marquesas and Hawaiian moats can be described using flexural models to account for progressive island loading and simple diffusive models of sediment transport, where the slope of topography and location of sediment supply are important factors. The diffusion theory of erosion and sediment transport was first proposed by *Culling* [1960], and has since been applied at various tectonic settings [e.g., *Kenyon and Turcotte*, 1985; *Moretti and Turcotte*, 1985; *Flemings and Jordan*, 1989; *Webb and Jordan*, 1993]. *Kenyon and Turcotte* [1985] show that the diffusion equation is a good approximation of bulk-sediment movements (at low slopes), such as creep and landsliding, in subaqueous environments.

If the seafloor bathymetry is a combination of basement height, $b(\mathbf{x},t)$, and sediment thickness, $s(\mathbf{x},t)$, then the 3-dimensional diffusion equation can be written as:

$$\frac{\partial s}{\partial t} = \kappa \nabla^2 (b+s) + F(\mathbf{x},t) \tag{6}$$

where κ is the diffusivity governing lateral transport and the sedimentation rate, $F(\mathbf{x},t)$, is the sediment source term at the two-dimensional position **x** and time t. This result follows from assuming that lateral sediment flux, **fl**, is proportional to slope:

$$\mathbf{fl} = -\kappa \nabla (b+s) \tag{7}$$

and applying the continuity equation:

$$\frac{\partial s}{\partial t} = -\nabla \cdot \mathbf{fl} + F(\mathbf{x},t) \tag{8}$$

We use an explicit method, based on the work of *Webb and Jordan* [1993], to solve (6) numerically on an nCUBE massively parallel computer. For each calculation, the time interval, Δt, is chosen such that $\kappa \Delta t/(\Delta x)^2=0.2$ to ensure stability. Sediment thickness, $s(\mathbf{x},t)$, is constrained to be greater than or equal to zero to prevent basement erosion. We allowed seafloor height to change according to the change in basement deflection as progressive island loading flexes an elastic lithosphere (see previous section). The flexure calculation includes the sediment effect in the bouyancy term and does not account for variations in the sediment fill. Because the volcanoes are the largest loads on the plate, variations in overfilling versus underfilling are second order in the deflection. The position of the sediment sources, $F(\mathbf{x},t)$, was changed over time as islands are formed and mass waste. Synthetic sediment units are defined from the thickness of sediments deposited within a constant time interval (0.75 m.y.) when no flexure is ongoing. Immediately prior to a change in deflection, the previously diffusing sediment unit is fixed and subsequently not allowed to change thickness. The actual deflection of the seafloor will be more gradual than these simple models, and in addition the moat will widen and deepen as it is filled by sediment.

The loading geometries taken to model sediment stratigraphy over a period of 6 m.y. at the Marquesas and Hawaii are given in Figure 13. These geometries were chosen because the Marquesas bathymetry is 3-dimensional, with islands being separated by deep basins, while the bathymetry at Hawaii is more 2-dimensional, with islands separated by shallow ridges. A Marquesas-type model is created by placing a circular load of 50 km radius and 4.5 km height onto a 20-km elastic plate every 1.5 m.y.. Loads are centered 160 km apart, deflections are calculated assuming the moat is filled to the level of the surrounding, flat seafloor, and load density is reduced to 2300 kg/m^3 to simulate the effect of underplating and produce slopes similar to those in Figure 5. The effect of island mass-wasting is included by placing sediment sources, $F(\mathbf{x},t)$, within a 10-km thick ring around the base of a circular load. Grid spacing is 8 km. A Hawaiian-type model is created by changing the spacing to 80 km, loading the plate every 0.75 m.y., and using a normal density, to approximate slopes shown by *Watts and ten Brink* [1989]. In both cases, sedimentation rates around each load are high only for a period of 1.5 m.y. after emplacement; the Hawaiian-type model contains an additional 0.75 m.y. of low sediment flux, creating a topmost ponded unit. We put a similar volume of sediment in Hawaiian and Marquesas models (the sedimentation rate at the Marquesas edifaces is set to be slightly higher).

The Marquesas-type stratigraphy in Figure 14 (κ=1.0x10^{10} m^2/m.y.) bears similarity to the seismic stratigraphy at the northeastern section of line 1162 (Figure 5): onlap in the lower section, with concave up units in the central basin, then offlap and overfill in the upper section, with central units convex in the central basin. The development of this pattern occurs as follows. Sediment from a newly formed island diffuses into a thinly sedimented moat (the basal unit is from sediment transported along-moat prior to emplacement of nearby islands), at each time interval creating a higher central mound of sediment that extends greater distances from the source. After 1.5 m.y., another island load flexes the seafloor, changing the shape of central moat reflectors from convex to concave up and creating new space for sediment, which causes offlap in the sediment unit following this event. Sediments then continue to overfill the moat and extend outward. Because the Hawaiian-type model in Figure 14 uses a high diffusivity (κ=2.5x10^{11} m^2/m.y.), it resembles the synthetic stratigraphy of *Watts and ten Brink* [1989], which was created using the assumption that each sediment unit fills the moat up to an even level. Such a model is in agreement with across-moat stratigraphy at Hawaii [*Rees et al.*, 1993]. The horizontal limit of sediment infilling at Hawaii is controlled by the sloping moat edges and flexural arch, while at the Marquesas sediments mound in the central moat and the lateral extent of the apron is limited because sediment diffusivities are low. Higher diffusivites at the Marquesas would cause central moat sediments to be thinner and sediments would be transported out to a broader lateral extent. Lower diffusivities at Hawaii would cause sediments to mound near the edges of volcanic edifices.

These models suggest that three main factors cause seismic stratigraphy at the Marquesas to differ from that at Hawaii: (1) the Marquesas moat is overfilled, while the Hawaiian moat is underfilled, (2) sediment diffusivities are lower at the Marquesas, and (3) the Marquesas bathymetry is 3-dimensional, with islands being separated by deep basins, in contrast to the more 2-dimensional bathymetry at Hawaii, where islands are separated by a shallow ridge. Viscoelastic relaxation of the lithosphere is not required to model the complex stratigraphy at these two island chains.

In the along-moat direction, diffusion models show sediment units tilted in the direction of load migration, although these predictions of along-moat stratigraphy may not be as relevant. *Rees et al.* [1993] find that along-moat stratigraphy at Hawaii does not follow the prediction of *Watts and ten Brink* [1989] (and of our diffusion models), and suggest this discrepancy arises because mass-wasting is episodic and along-moat transport is affected by landslide deposits that segment the moat into a series of sub-basins. Since changes in slope from progressive island loading are greatest in the along-moat direction, previously-deposited material (which sediment models fix to the seafloor) may also be deformed in the direction of load migration, smoothing out the along-moat pattern of stratigraphy.

DISCUSSION

Plate flexure, island geometries, and sediment influx from island mass wasting are important influences on moat stratigraphy, but why is the moat underfilled at Hawaii and overfilled at the Marquesas? Below we examine sediment/edifice ratios, which imply that the relationships between volcano growth, mass wasting, and moat infill are not the same at these two island chains.

Grids of seafloor bathymetry (Figure 1) and the depth of deflected volcanic basement (Figure 12a) are used to infer the volume of material filling Marquesas moat over an apron area consistent with the seismic data of EW91-03 and moat limits of *Filmer et al.* [1994] Taking features shallower than 2.5 km depth to be volcanic edifices the moat contains 240,000 km^3 sediment. The volume of volcanoes calculated from a base of 4 km depth is 50,000 km^3; the total volume of volcanoes above the base of the deflected basement is 90,000 km^3. At Hawaii, our estimates are less precise. *Rees et al.* [1993] estimate over 90,000 km^3 of sediment in the northeastern portion of the moat between Hawaii and Kauai, which suggests there is about 200,000 km^3 moat sediment in a region similar in along-moat length to the length of the Marquesas. Using dbdb5 bathymetry, we find that the volume of material above a base of 4 km depth (presumed to be volcanic edifice) is 230,000 km^3. Since the deflected basement reaches depths of 8 km [e.g., *Watts et al.*, 1985], the total volume of volcanoes could be as much as twice this amount. These estimates neglect sediment deposited between islands. For example, a basin in the volcanic ridge at Molokai channel contains up to 4 km thickness of sediment [*ten Brink and Brocher*, 1987].

According to these rough calculations there is about an equal amount of sediment in the moat between Hawaii and Kauai as in the Marquesas, but that the ratio of sediment volume to total island volcanics above the deflected basement could be as small as 1 to 2 at Hawaii, whereas it is greater than 2 to 1 at the Marquesas. Different moat volumes for same amount of sediment explains the underfilled moat at Hawaii and overfilled moat at the Marquesas. For the same given volume of infilling sediment, there is greater moat volume at Hawaii than at the Marquesas, which is caused by greater edifice loads and also possibly differences in underplating between the two island chains.

The difference in the elastic plate thickness at the Marquesas (T_e about 17 km) and Hawaii (T_e 25 to 30 km) is not an important influence on moat volumes. Isostasy requires that the integrated plate flexure is equal to the sum of loads above the plate, weighted inversely by the density contrast between displaced and infilling material (this relation applies to flexure induced by loading from below as well). For a given volcanic load, the total volume of the flexural basin, which is filled with both sediment and the volcano root, is thus similar regardless of T_e. However, the space available for sediment fill increases for stiffer plates, since deflections decrease beneath the volcanic load, reducing the proportionate volume of the root. The effect should be minor for the elastic plate thicknesses and size of volcanoes observed at the Marquesas and Hawaii (Figure 15a). The moat volume will more directly reflect the loads on the plate (Figure 15b).

The large ratio of sediment volume to that of the volcanoes at the Marquesas has previously been observed [*Menard*, 1956; *Filmer et al.*, 1994], although former estimates were not well constrained. Because the apron volume is greater than the volume of volcanoes, *Menard* [1956] suggested that much of the Marquesas moat is filled by submarine fissure flows rather than from erosion of the islands. While submarine flows may contribute to moat filling, the MCS data and flexural models (Figure 5) indicate that this contribution is minor and most of the apron is sediment from island mass wasting. Thus active Marquesas volcanoes must frequently build up and mass waste, producing about twice their volume in debris.

One analogue for this process may come from recent study of the eruption history at Mount Augustine, a calk-alkaline volcano in the eastern Aleutian arc of Alaska [*Bége̒t and Kienle*, 1992]. The summit has repeatedly collapsed and regenerated at least 11 times over the past 2,000 years. Dome growth since the last major debris avalanche in 1883 has buried the amphitheater crater and created an oversteepened dome. Although the

Marquesas volcanoes are tholeiitic to alkaline and eruption rates are 10-100 times larger, continued collapse and build up of summits is not unreasonable. Present-day subaerial structures prove that caldera collapse and catastrophic mass-wasting were important in the mid-to-late stages of volcanic activity [c.f., *Chubb*, 1930; *Brousse et al.*, 1978; *Brousse et al.*, 1990]. Slope failures may have occurred at earlier stages as well, with volcanism burying the evidence. *Moore et al.* [1989], using similar reasoning, argue that while some of the largest Hawaiian landslides occur near the end of shield building, mass-wasting probably occurs throughout the shield-building stage. At Loihi, the youngest volcano with a summit 1 km below sea level, more than half of the surface area has already been modified by landsliding.

Our estimates of sediment/edifice ratios imply that island formation at the Marquesas is different than at Hawaii. Most island chains exhibit an archipelagic apron rather than an underfilled moat and arch [*Menard*, 1956]; the low proportion of mass-wasting at Hawaii appears anomalous. This low proportion is likely related to the larger eruption rates and different style of volcano construction. As pointed out by *Walker* [1973], lava flow length depends on effusive rate, with high effusion rates having lower slopes. This argument predicts steeper volcano slopes, which are more prone to mass waste, at the Marquesas than at Hawaii. The more 2-dimensional nature of the Hawaiian ridge also implies that slopes are lower between islands than across the chain. During construction, many volcanoes were buttressed by earlier-formed edifices [*Fiske and Jackson*, 1972].

Well-developed rift zones are found at the Hawaiian Islands but are not apparent at the major Marquesas islands and are rarely found at other islands (rift zones are, however, found at many seamounts [*Vogt and Smoot*, 1984]). Rift zones at Hawaii facilitate the growth of broad volcanoes: magma from the summit moves laterally through rift zones and intrusion into rift zones may account for a significant fraction of the total volume of Hawaiian volcanoes [c.f., *Fiske and Jackson*, 1972; *Dietrich*, 1988]. Rift zones form along the tensional zones at the head of landslides, but also magma injection into rift zones induces landsliding [*Moore et al.*, 1989]. Slip on faults, possibly deep faults at the preexisting seafloor/edifice boundary, could permit the flanks of Hawaiian volcanoes to spread and accommodate growth by injection of magma into rifts [e.g., *Fiske and Jackson*, 1972; *Swanson et al.*, 1976; *Dietrich*, 1988]. This mechanism of volcano growth may be more efficient in terms of the proportion of mass-wasting. At the Marquesas, repeated buildup and mass wasting of oversteepened slopes around local volcanic centers could occur because rift zones, which allow lateral magma transport and construction of a broad volcano, are absent.

While much of the sediment in the Marquesas and Hawaiian moats is derived from island mass wasting, our models suggest that diffusivities differ by an order of magnitude. The lower diffusivity at the Marquesas may reflect the larger proportion of "blocky", massive material in the central Marquesas moat: the unit of discontinuous reflectors seen in the central Marquesas moat has not been documented at Hawaii. The primary modes of slope failure may be influential as well. At Hawaii, there are two types: slumps, which are broad and steep, and result from slow, creep-like movement; and debris avalanches, which are narrow, far-reaching landslides showing well-developed amphitheaters in their upper parts and representing a single episode of rapid movement [e.g., *Moore et al.*, 1989]. The apparent difference in diffusivities may reflect a change in the dominant processes of sediment transport rather than in sediment properties. Side-scan sonor data suggest fast-moving debris avalanches at the Hawaiian Islands travel up the flank of the flexural arch [*Moore et al.*, 1989] and the landslide unit observed by *Rees et al.* [1993] also extends upslope onto the arch, which may explain the high-diffusivity required to model Hawaiian stratigraphy (since diffusion transports material downslope, it is, however, not the best proxy for this process). In constrast, at the Marquesas sediments mound up, perhaps because slumping rather than debris avalanches are more common and the flow more closely approximates diffusion-like creep. The high diffusivities required to successfully predict seismic stratigraphy at these two island chains are of the same magnitude as diffusivities found by *Kenyon and Turcotte* [1985] (ranging from 2.4×10^{10} to 5.6×10^{11} m^2/m.y.) in three prograding deltas, where subaqueous sediment transport also occurs by creep and landsliding.

It would be interesting in the future to examine how the processes that influence moat stratigraphy at the Marquesas and Hawaii, such as crustal underplating, the interplay between volcano growth and mass-wasting, and sediment diffusion, operate at other oceanic islands. *Rees et al.* [1993] argue that large-scale mass wasting is likely important in the history of many oceanic volcanoes. At the island of Réunion, for example, Seabeam data has been used to confirm previous suggestions of landsliding at the Grand Brûlé trough on the east flank of Piton de la Fournaise [*Lénat et al.*, 1989]. Like the Marquesas Islands, Piton de la Fournaise shows a series of concentric half-calderas that open towards the sea. The Grand Brûlé slide extends outward from the break in the summit caldera.

CONCLUSION

The seismic velocities and seismic stratigraphy, as well as the general structure of the islands and surrounding seafloor, indicate that the Marquesas apron is overfilled with debris from island mass wasting. The apron contains two major regions of differing stratigraphy: (1) at the moat edges, where a unit of continuous layered reflectors is present containing minor lenses of chaotic diffractors and (2) at the deep moat basins, where there is an acoustically opaque unit of discontinuous reflectors of up to 2 km thickness, in places capped by a ponded unit. Reflectors of the outermost moat generally onlap the flexural arch in the lower section and offlap and overfill it in the upper section. In the central moat, reflectors change shape from concave up in the lower section to convex in the upper section.

Plate-flexure models require broad, low-density (relative to mantle) underplating beneath the Marquesas Islands to explain the depth to volcanic basement, such that basement deflections are everywhere less than the prediction of simple top-loading models. Although we cannot uniquely resolve the density structure, underplating by high-density crustal material (3100 kg/m^3) is consistent with high seismic velocities of material observed beneath the Marquesas and at Hawaii. The maximum thickness of such material predicted by our models is consistent with preliminary seismic results at the Marquesas.

Three-dimensional time-dependent diffusion models of sedimentation suggest that three main factors make stratigraphy at the Marquesas differ from Hawaii: (1) the Marquesas moat is overfilled, while the Hawaiian moat is underfilled, (2) sediment diffusivities may be lower at the Marquesas, and (3) the Marquesas islands are separated by deep sedimentary basins, in contrast to at Hawaii, where islands are separated by a shallow ridge. Simple diffusion and flexure models (uniform T_e) can produce complex stratigraphies without requiring viscoelastic relaxation of the lithosphere. The lower diffusivity at the Marquesas may reflect the larger proportion of "blocky", massive material in the central Marquesas moat or alternatively a change in the dominant process of sediment transport.

While there is similar sediment supply at both the Marquesas and Hawaii, the underfilled moat at Hawaii is apparently a consequence of greater moat volumes due to the greater edifice volumes, and possibly differences in crustal underplating, that load the plate. The variation in elastic plate thickness between the two chains is not an important influence on moat volumes. The difference in sediment/edifice ratios is likely related to the larger eruption rates at Hawaii and different styles of volcano construction between Hawaii and the Marquesas. The greater sediment/edifice ratio at the Marquesas is probably typical of island chains having an archipelagic apron. Therefore, estimates of hotspot volcanism based soley on the size of volcanoes will severely underestimate the amount of erupted material.

Acknowledgements

We thank Peter Buhl for help with MCS processing at Lamont and David Caress for help with sonobuoy data and for providing the preliminary Marquesas OBS results in advance. Jim Dolan gave computer and seismic processing support at Woods Hole. Helen Webb and Tom Jordan provided preprints and a prototype of their diffusion code. The diffusion models were run on an nCUBE2 parallel computer at the ERL/nCUBE Geophysical Center for Parallel Processing at the Earth Resources Laboratory at MIT. We thank ERL for making computer time available and Ted Charrett and Joe Matarese for their instruction. We thank the USGS at Woods Hole for allowing use of their digitizing facilities. We acknowledge Javier Escartin for drawing Figure 10. Paul Wessel provided a constructive review. This research was supported by NSF 8817764-OCE to M. McNutt at MIT and NSF-9296016-OCE to R. Detrick at WHOI.

REFERENCES

Béget, J.E., and J. Kienle, Cyclic formation of debris avalanches at Mount St. Augustine volcano, *Nature, 356*, 701-704, 1992.

Brousse, R., J.-P. Chevalier, M. Denizot, and B. Salvat, Étude géomorphologique des iles Marquises, *Cahiers du Pacifique, 21*, 9-74, 1978.

Brousse, R., H.G. Barsczus, H. Bellon, J.-M. Cantagrel, C. Diraison, H. Guillou, and C. Leotot, Les Marquises (Polynésie française): volcanologie, géochronologie, discussion d'une modèle de point cahd, *Bull. Soc. géol. France, 6*, 933-949, 1990.

Caress, D.W., J.C. Mutter, M.K. McNutt, and R.S. Detrick, An OBS seismic refraction experiment across the Marquesas Islands: the deep crustal structure of a hotspot trace (abstract), in *AGU 1992 Fall Meeting, EOS Trans. AGU, 73, Suppl.*, 489-490, 1992.

Christensen, N.I., and M.H. Salisbury, Structure and constitution of the lower oceanic crust, *Rev. Geophys. Space Phys., 13*, 57-86, 1975.

Chubb, The geology of the Marquesas islands, *B.P. Bishop Museum Bull., 68*, 1-71, 1930.

Culling, W.E.H., Analytical theory of erosion, *J. Geol., 68*, 336-344, 1960.

Desonie, D.L., R.A. Duncan, and J.H. Natland, Temporal and geochemical variability of volcanic products of the Marquesas hotspot, *J. Geophys. Res., 98*, 17,649-17,665, 1993.

Dietrich, J.H., Growth and persistence of Hawaiian volcanic rift zones, *J. Geophys. Res., 93*, 4258-4270, 1988.

Duncan, R.A., and I. McDougall, Migration of volcanism with time in the Marquesas Islands, *Earth Planet. Sci. Lett., 21*, 414-420, 1974.

Filmer, P.E. M.K. McNutt, and C.J. Wolfe, Elastic thickness of the lithosphere in the Marquesas and Society islands, *J. Geophys. Res., 98*, 19,565-19,5577, 1993.

Filmer, P.E. M.K. McNutt, H.F.Webb, and D.J. Dixon, Volcanism and archipelagic aprons: a comparison of the Marquesan and Hawaiian Islands, *Marine Geophys. Res.*, in press, 1994.

Fiske, R.S., and E.D. Jackson, Orientation and growth of Hawaiian volcanic rifts: the effect of regional structure and gravitational stresses, *Proc. R. Soc. Lond. A, 329*, 299-326, 1972.

Flemings, P.B., and T.E. Jordan, A synthetic stratigraphic model of foreland basin development, *J. Geophys. Res., 94*, 3851-3866, 1989.

Forsyth, D.W. Subsurface loading and estimates of the flexural rigidity of continental lithosphere, *J. Geophys. Res., 90*, 12,623-12,632, 1985.

Kenyon, P.M., and D.L. Turcotte, Morphology of a delta prograding by bulk sediment transport, *Geolog. Soc. Am. Bull., 96*, 1457-1465, 1985.

Lénat, J.-F., Vincent, P., and Bachelery, P., The off-shore continuation of an active basaltic volcano: Piton de la Fournaise (Reunion Island, Indian Ocean), *J. Volcanol. Geotherm. Res., 36*, 1-36, 1989.

Lindwall, D.A., A two-dimensional seismic investigation of crustal structure under the Hawaiian Islands near Oahu and Kauai, *J. Geophys. Res., 93*, 12,107-12,122, 1988.

Lipman, P.W., W.R. Normark, J.G. Moore, J.B. Wilson, and C.E. Gutmacher, The giant submarine Alika debris slide, Mauna Loa, Hawaii, *J. Geophys. Res., 93*, 4279-4299, 1988.

Menard, H.W., Archipelagic aprons, *Bull. Amer. Assoc. Petrol. Geol., 40*, 2195-2210, 1956.

Moore, J.G., D.A. Clague, R.T. Holcomb, P.W. Lipman, W.R. Normark, and M.E. Torresan, Prodigious submarine landslides on the Hawaiian Ridge, *J. Geophys. Res., 94*, 17,465-17,484, 1989.

Moretti, I., and D.L. Turcotte, A model for erosion, sedimentation, and flexure with application to New Caledonia, *J. Geodyn. 3*, 155-168, 1985.

Parker, R.L., The rapid calculation of potential anomalies, *Geophys. J.R. Astr. Soc., 31*, 447-455, 1973.

Prior, D.B., B.D. Bornhold, and M.W. Johns, Depositional characteristics of a submarine debris flow, *J. Geology, 92*, 707-727, 1984.

Rees, B.A., R.S. Detrick, and B.J. Coakley, Seismic stratigraphy of the Hawaiian flexural moat, *Geol. Soc. of Amer. Bull., 105*, 189-205, 1993.

Swanson, D.A., W.A. Duffield, and R.S. Fiske, Displacement of the south flank of Kilauea Volcano: the result of forceful intrusion of magma into the rift zones, *U.S. Geol. Surv. Prof. Pap., 963*, 39 pp., 1976.

ten Brink, U.S., and A.B. Watts, Seismic stratigraphy of the flexural moat flanking the Hawaiian Islands, *Nature, 317*, 421-424, 1985.

ten Brink, U.S., and T.M. Brocher, Multichannel seismic evidence for a subcrustal intrusive complex under Oahu and a model for Hawaiian volcanism, J. Geophys. Res., 92, 13,687-13,707, 1987.

Vogt, P.R., and N.C. Smoot, The Geisha Guyots: multibeam bathymetry and morphometric interpretation, *J. Geophys. Res., 89*, 11,085-11,107, 1984.

Walker, G.P.L., Lengths of lava flows, *Philos. Trans. R. Soc. London Ser. A., 274*, 107-118, 1973.

Watts, A.B., An analysis of isostasy in the World's oceans 1. Hawaiian-Emperor seamount chain, *J. Geophys. Res., 83*, 5989-6004, 1978.

Watts, A.B., U.S. ten Brink, P. Buhl, and T.M. Brocher, A multichannel seismic study of lithospheric flexure across the Hawaiian-Emporer seamount chain, *Nature, 315*, 105-111, 1985.

Watts, A.B., and U.S. ten Brink, Crustal structure, flexure, and subsidence history of the Hawaiian Islands, *J. Geophys. Res., 94*, 10,473-10,500, 1989.

Webb, H.F., and T.H. Jordan, Quantifying the distribution and transport of pelagic sediments on young abyssal hills, *Geophys. Res. Lett., 20*, 2203-2206, 1993.

Wessel, P., A re-examination of the flexural deformation beneath the Hawaiian Islands, *J. Geophys. Res., 98*, 12,177-12,190, 1993.

FIGURE CAPTIONS

Figure 1. Bathymetry at the Marquesas Islands; 500 m contour interval, Mercator projection. Locations of MCS lines 1153, 1162, and 1155 are shown. Subaerial regions shaded black and islands are identified by name. The crescent shapes of individual islands is the result of catastrophic mass wasting, which leaves a crescent-shaped caldera and a well-developed amphitheater that borders the sea. Bathymetry data is from French bathymetric charts and selected DBDB5 data, and was gridded and merged with profiles from *EW9103*. See *Filmer et al.* [1993a] for further information.

Figure 2 . Line drawings of seismic stratigraphy in time section. Sonobuoy locations along line 1162 given in italics. Horizontal bars show locations of Figures 6 through 9. The moat contains two major regions of different stratigraphy: (1) at the moat edges, where a unit of continuous layered reflectors is present (2) at the central moat, where there is a unit of discontinuous reflectors. At the edge of regions of steep volcanic topography, there is evidence of slumping in the uppermost section (lines 1153 and 1162). Reflector having hummocky topography, a characteristic feature of the seafloor at landslides, is noted on line 1162. Landslide ridges are present along line 1162 and line 1153. Across-moat transport of sediment is evident at the western side of line 1155, where material traveling outwards from the central moat region has dammed at a local high. Outside the moat, there is a thin, well-bedded sedimentary unit that partially fills the lows between the abyssal hills.

Figure 3. Sonobuoy velocities across line 1162. For reference, dashed line shows the predicted basement deflection plotted in Figure 5. Dotted vertical lines show locations of sonobuoys. The flexure of the oceanic lithosphere from island loading is apparent in the changing depth to volcanic basement and depth to Moho, although Moho reflections were only observed away from the central island region. Outside the moat, a unit of thin, low velocity (~2.5 km/s) sediment is present. Within the moat, sediments thicken and velocities increase to $\geq$ 4.0 km/s, as indicated by both refraction data (see Figure 4) and independent semblance analysis of MCS data.

Figure 4. Data for sonobuoy 22, in the central moat region of line 1162. Thick black lines show travel times calculated from the velocity depth solution in Figure 3.

Figure 5. Line drawings of seismic stratigraphy in depth section. Sloping arrows show the pattern of onlap and offlap. Vertical arrows point to the change in central moat reflectors from concave up to convex on Line 1162. On line 1162, in the center of the

Marquesas island chain, reflectors onlap the arch in the lower section and offlap and overfill the moat in the upper section. The reflectors along line 1153 and the eastern side of 1155 also suggest this pattern of onlap and offlap, although reflectors are laterally discontinuous and difficult to interpret The central moat is overfilled, with seafloor bathymetry indicating the changing thickness of the sedimentary section rather than the position of the flexed basement beneath. Dotted line is basement deflection for top-loading model, solid line is deflection for crustal underplating model, both using uncorrected bathymetry. Basement deflection is consistently overpredicted by the top-loading model, but is well predicted by a model including bottom-loading from crustal underplating. See text for further details.

Figure 6. The transition from moat sediments to abyssal hill sediments on line 1162. (a) MCS data. (b) Line drawing. Diffractive basement is evident near 6 s.

Figure 7. (a) Seismic section from line 1155. (b) Line drawing.

Figure 8. (a) MCS section along line 1162, in the Marquesas Islands moat. A hummocky reflector near 4.8 s marks the boundary between a ponded unit of continuous reflectors above and a unit of discontinuous reflectors below. Diffractions at the basal layer, near 6.0 s and CDP 16300, are bowties from synclines. (b) Migrated section, using the sonobuoy 23 velocity model. Migration collapses diffractions throughout the section and revels only a slightly more continuous pattern of reflectors. (c) Line drawing. Vertical arrows point to change in reflectors from concave up to convex (see also Figure 5).

Figure 9. Interisland sediments at line 1155. (a) MCS data. (b) Line drawing. The deep reflectors are more discontinuous and difficult to trace laterally than on line 1162. This sediment unit is acoustically opaque and entirely "chaotic".

Figure 10. Sketch of the double loading scenario. Volcano depresses the plate, while underplating material buoys it up. T_e is the elastic plate thickness; ρ_c, ρ_m, ρ_u, and ρ_w are the densities of crust and sediment infill, mantle, underplating material, and water, respectively.

Figure 11. Observed gravity anomaly (solid line) and calculated gravity anomaly (dashed line) from flexural model including crustal underplating by 3100 kg/m^3 material.

Figure 12. (a) Basement deflection at the Marquesas from flexural model including crustal underplating by 3100 kg/m^3 material; 500-m contour interval, Mercator projection. (b) Underplating thickness from flexural model including crustal underplating by 3100 kg/m^3 material; 1000-m contour interval, Mercator projection.

Figure 13. Loading geometries for sediment diffusion models. A Marquesas-type model is created by placing a circular load of 50 km radius and 4.5 km height on a 20-km

elastic plate every 1.5 m.y.. Loads are centered 160 km apart, deflections are calculated assuming the moat is filled to the level of the surrounding, flat seafloor, and load density is reduced to 2300 kg/m^3 to simulate the effect of underplating. The effect of island mass-wasting is included by placing sediment sources, $F(\mathbf{x},t)$, within a 10-km thick ring around the base of a circular load. A Hawaiian-type model is created by changing the spacing to 80 km, loading the plate every 0.75 m.y., and using a normal crustal density. Sediment fluxes around each load are high only for a period of about 1.5 m.y. after emplacement.

Figure 14. (a) Across-moat stratigraphy from a Marquesas-type model, taken near the center of the chain. Sloping arrows point to the pattern of onlap and offlap. Vertical arrows point to the change in central moat reflectors from concave up to concave down. (b) Across-moat stratigraphy from a Hawaiian-type model, taken near the center of the chain.

Figure 15. (a) Volume of volcano root, sediment, and total fill (sediment + root) within a flexural basin induced by a cylindrical island load (50 km radius, 4.5 km height) for varying elastic plate thickness. (b) Volume of volcano root, sediment, and total fill within a flexural basin induced by a cylindrical island loads of varying volume. The cylinder radius ranges from 10 to 50 km and height is fixed (4.5 km).

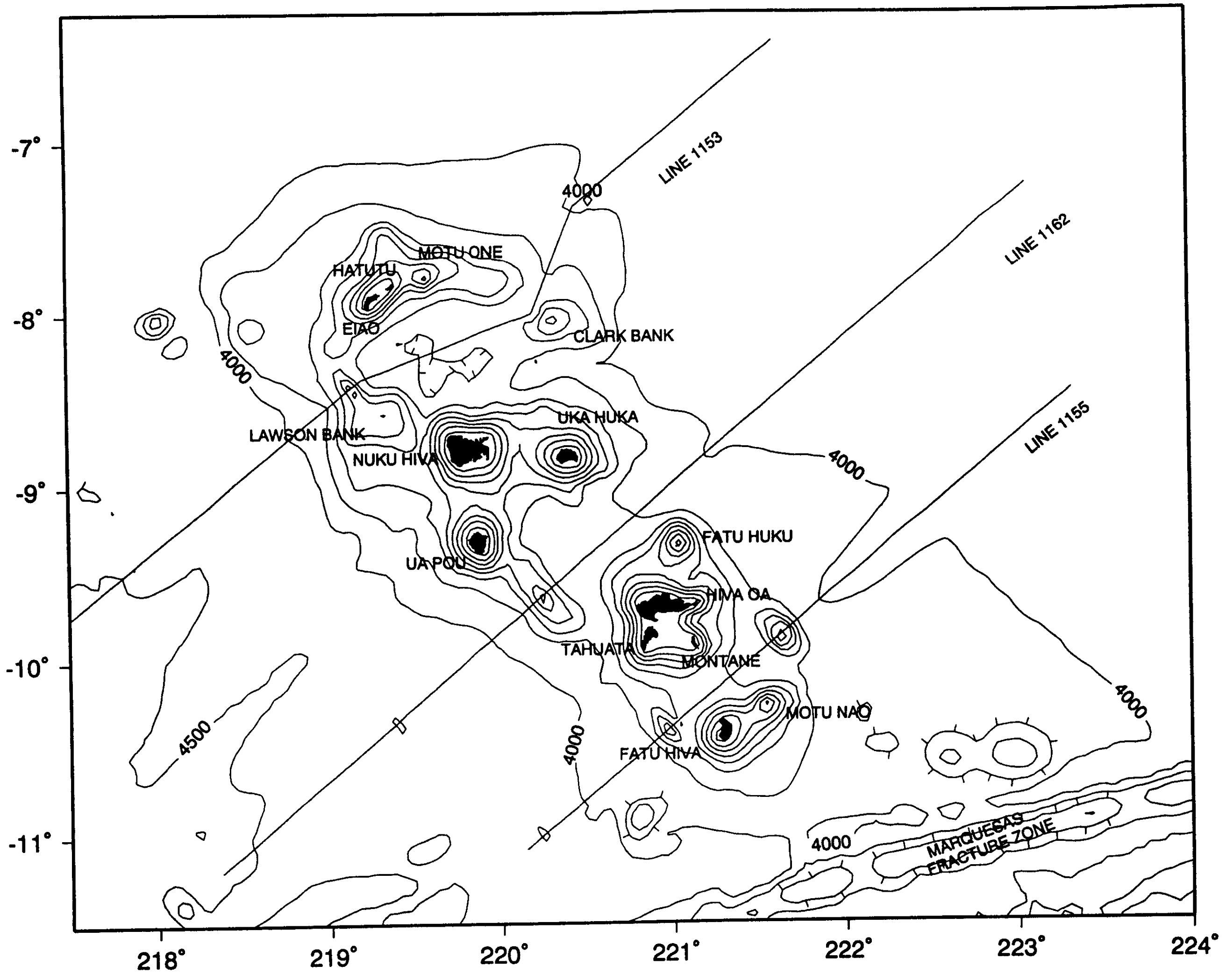

-7°
-8°
-9°
-10°
-11°
218°
219°
220°
221°
222°
223°
224°
LINE 1153
LINE 1162
LINE 1155
4000
4500
MOTU ONE
HATUTU
EIAO
CLARK BANK
UKA HUKA
LAWSON BANK
NUKU HIVA
UA POU
FATU HUKU
HIVA OA
TAHUATA
MONTANE
MOTU NAO
FATU HIVA
MARQUESAS FRACTURE ZONE

Figure 1

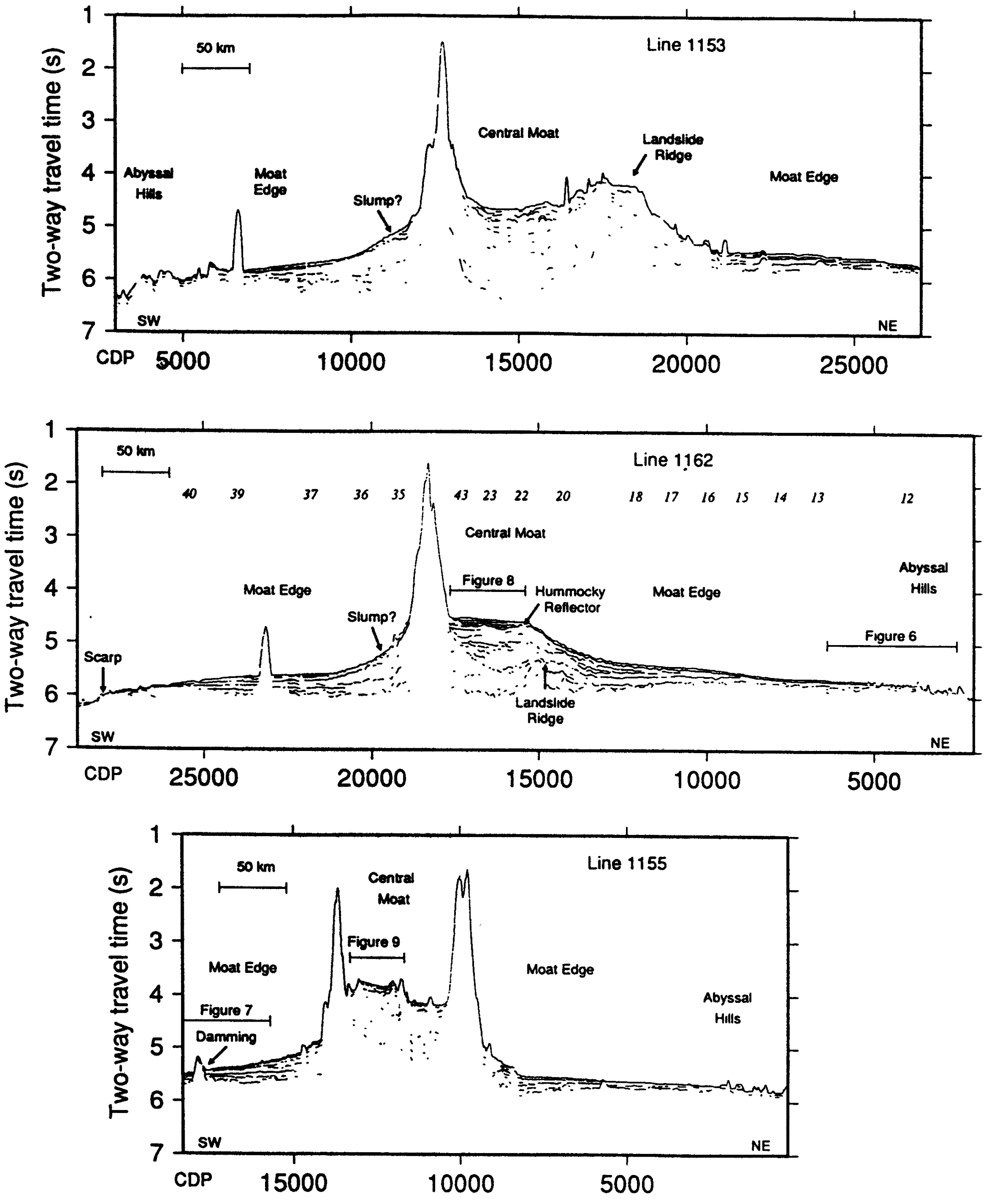
Line 1153
50 km
Two-way travel time (s)
1
2
3
4
5
6
7
Abyssal Hills
Moat Edge
Slump?
Central Moat
Landslide Ridge
Moat Edge
SW
NE
CDP
5000
10000
15000
20000
25000
Line 1162
50 km
40
39
37
36
35
43
23
22
20
18
17
16
15
14
13
12
Central Moat
Moat Edge
Slump?
Figure 8
Hummocky Reflector
Moat Edge
Abyssal Hills
Figure 6
Scarp
Landslide Ridge
SW
NE
CDP
25000
20000
15000
10000
5000
Line 1155
50 km
Central Moat
Figure 9
Moat Edge
Moat Edge
Abyssal Hills
Figure 7
Damming
SW
NE
CDP
15000
10000
5000

Figure 2

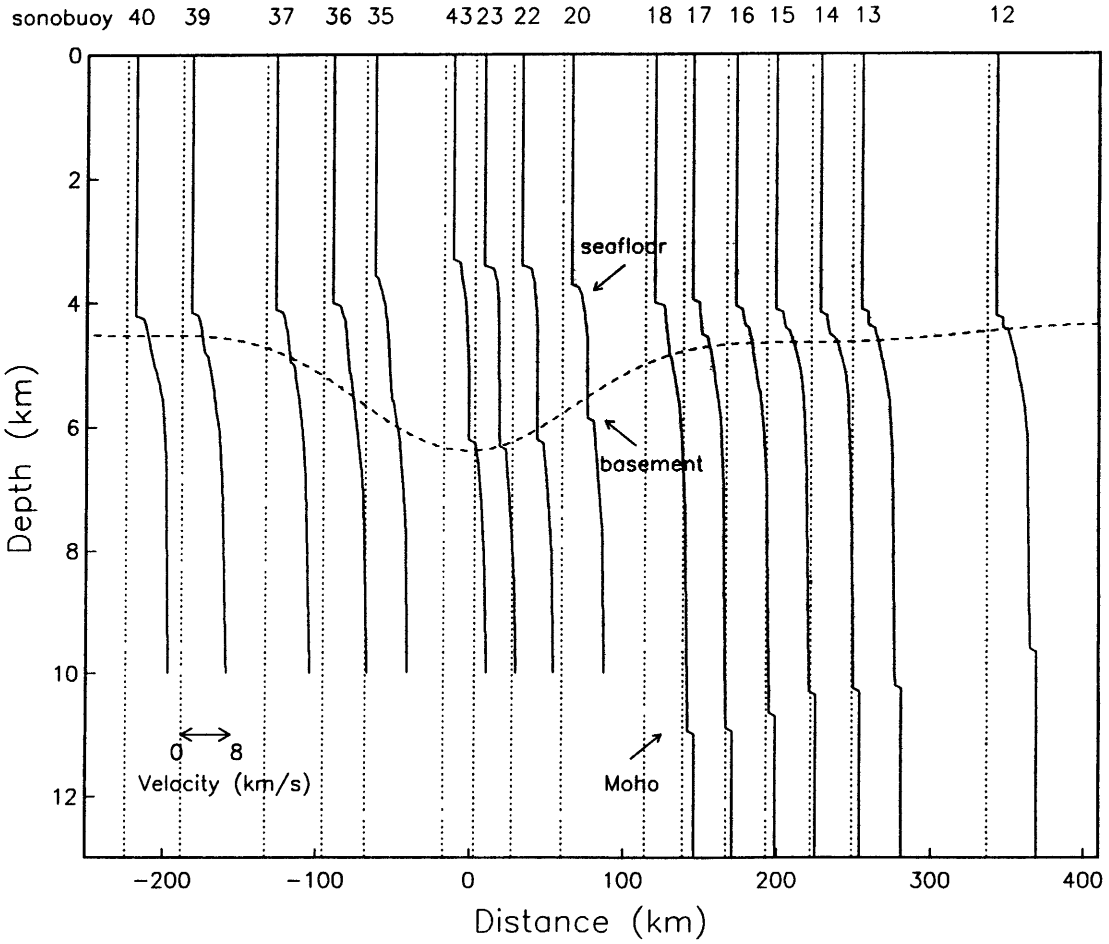
sonobuoy
40
39
37
36
35
43
23
22
20
18
17
16
15
14
13
12
0
2
4
6
8
10
12
Depth (km)
seafloor
basement
Moho
0
8
Velocity (km/s)
−200
−100
0
100
200
300
400
Distance (km)

Figure 3

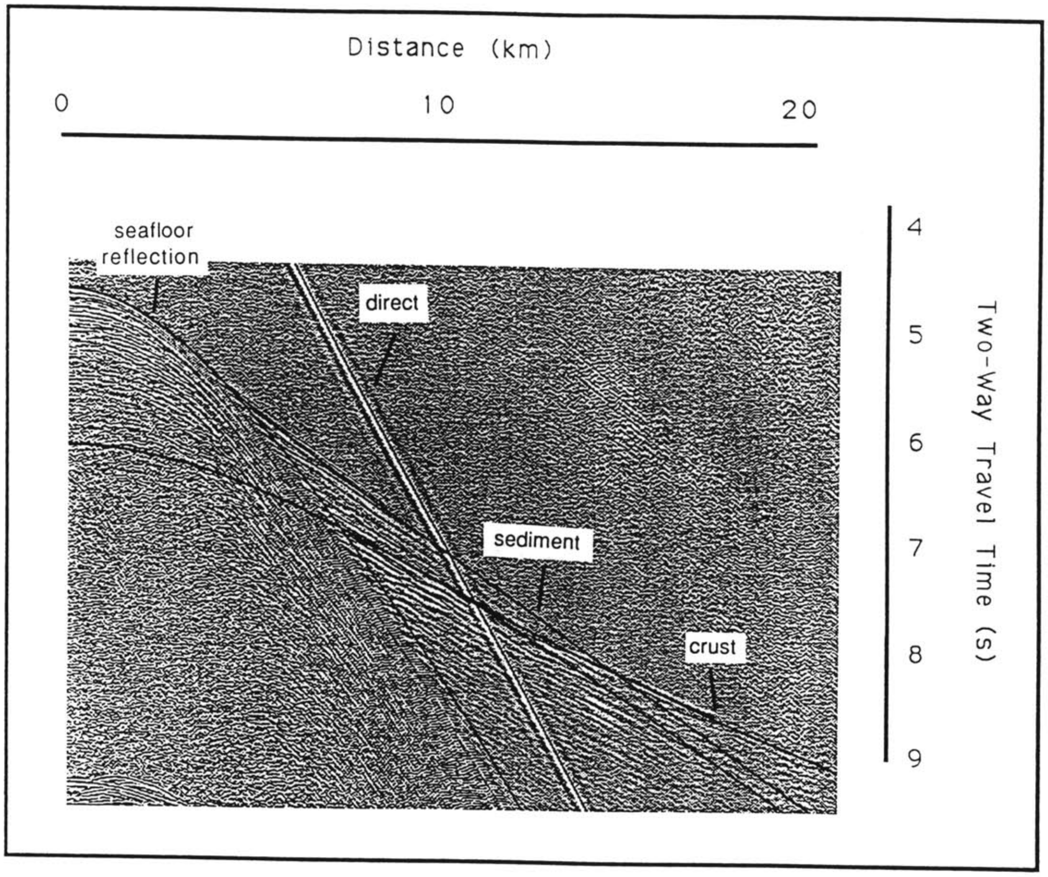
Distance (km)
0
10
20
seafloor reflection
direct
sediment
crust
4
5
6
7
8
9
Two-Way Travel Time (s)

Figure 4

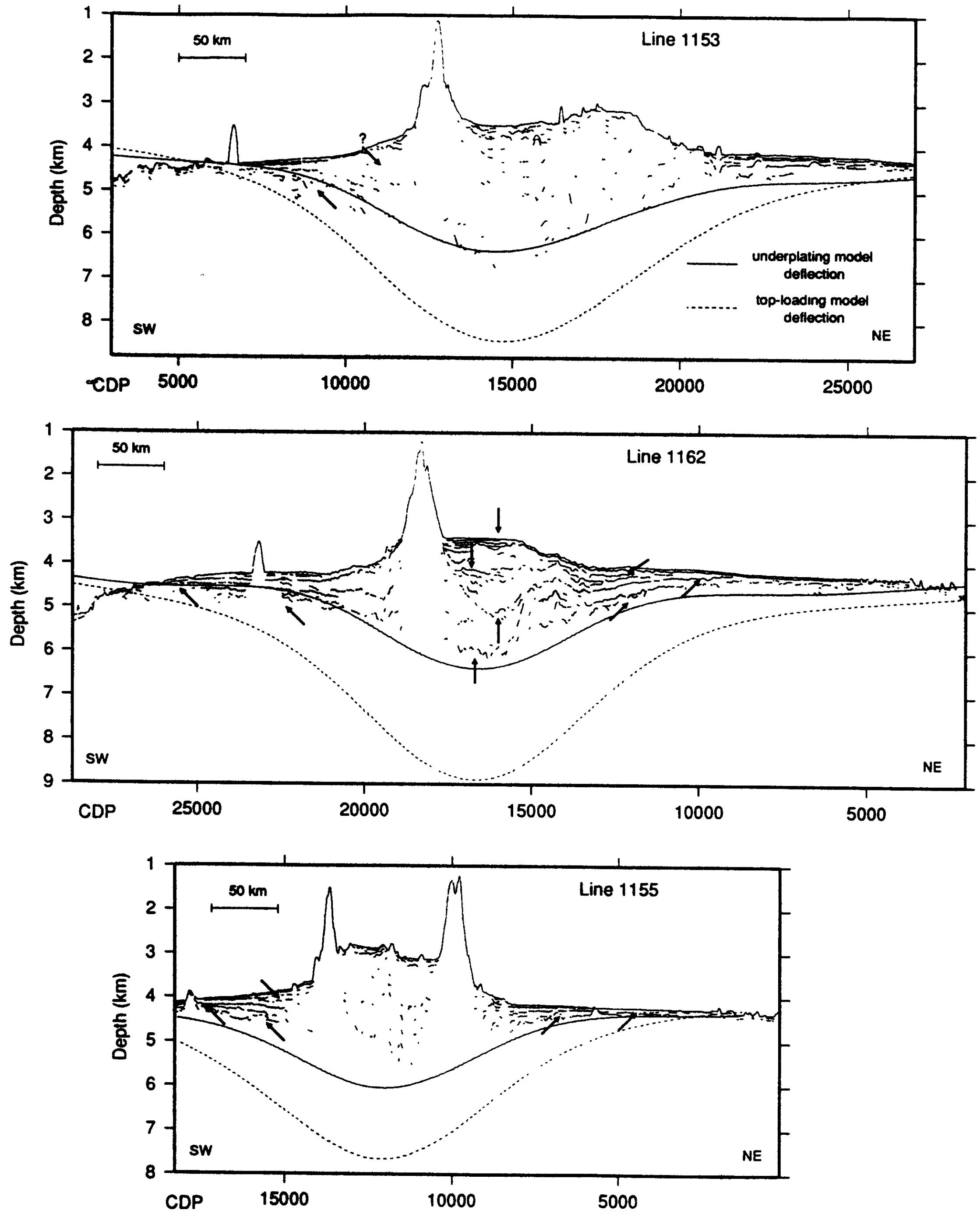
Line 1153
50 km
Depth (km)
1
2
3
4
5
6
7
8
?
underplating model deflection
top-loading model deflection
SW
NE
CDP
5000
10000
15000
20000
25000
Line 1162
50 km
Depth (km)
1
2
3
4
5
6
7
8
9
SW
NE
CDP
25000
20000
15000
10000
5000
Line 1155
50 km
Depth (km)
1
2
3
4
5
6
7
8
SW
NE
CDP
15000
10000
5000

Figure 5

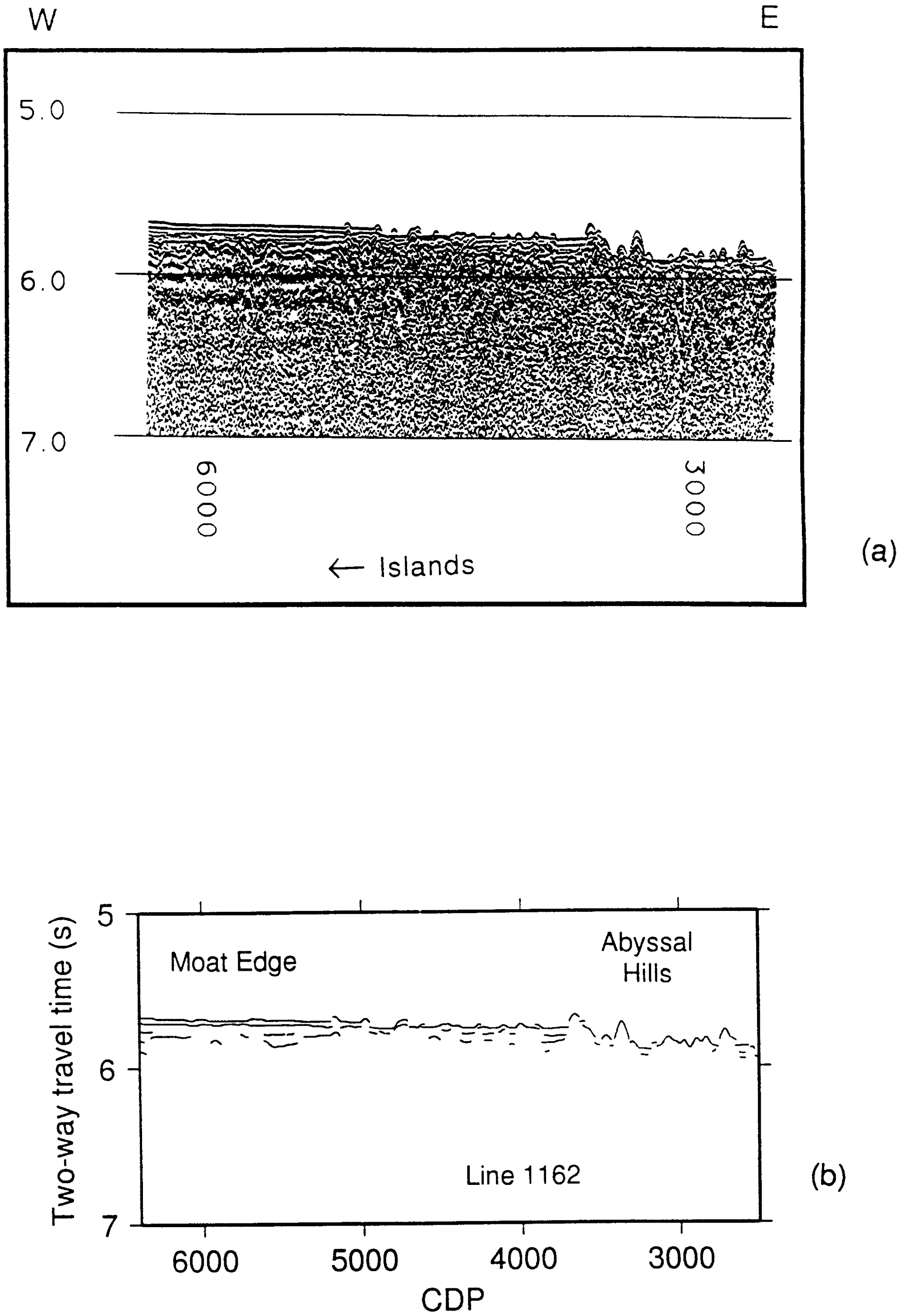
W
E
5.0
6.0
7.0
6000
3000
← Islands
(a)
Two-way travel time (s)
5
6
7
Moat Edge
Abyssal Hills
Line 1162
(b)
6000
5000
4000
3000
CDP

Figure 6

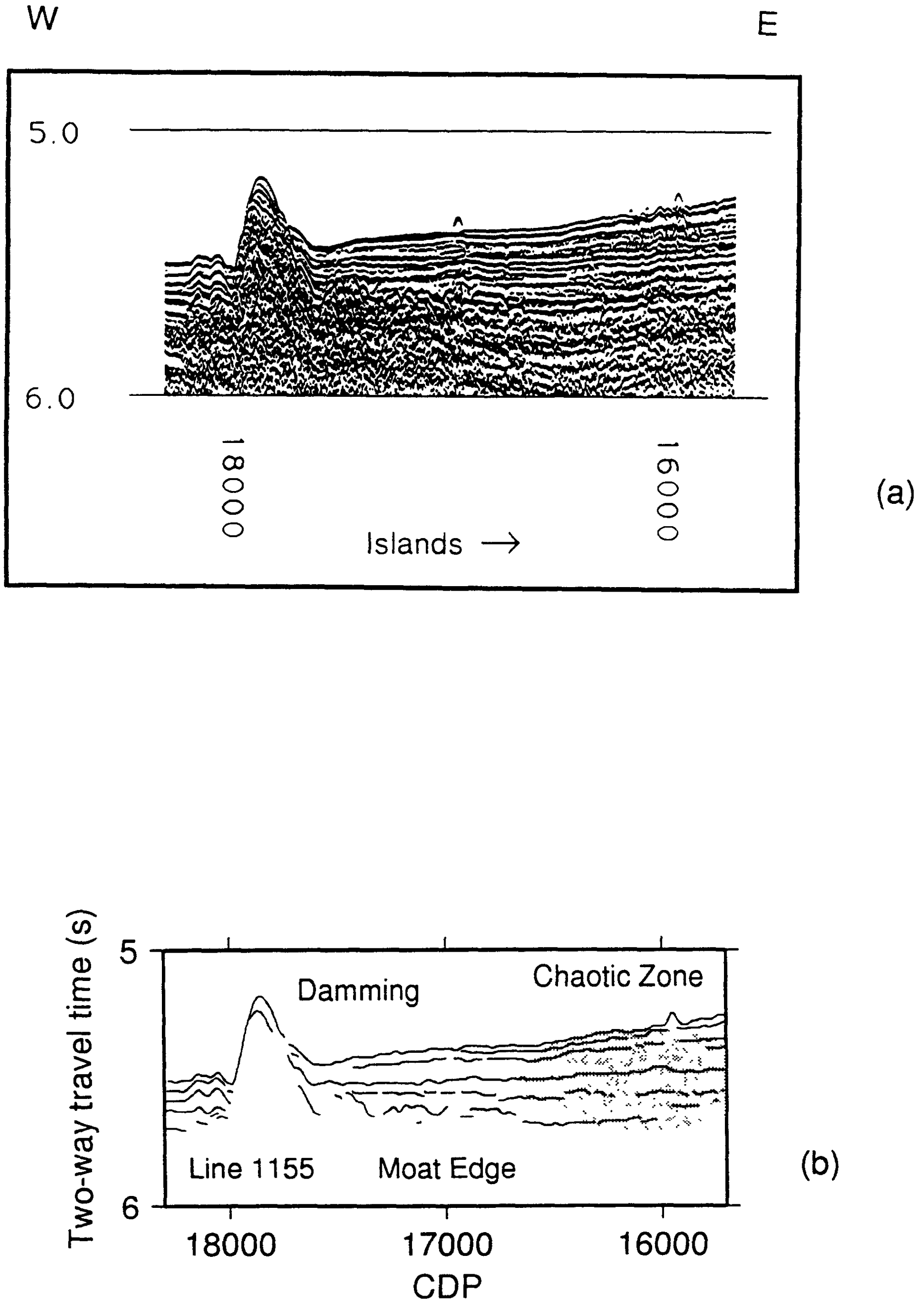
W
E
5.0
6.0
18000
16000
Islands →
(a)
Two-way travel time (s)
5
6
Damming
Chaotic Zone
Line 1155
Moat Edge
18000
17000
16000
CDP
(b)

Figure 7

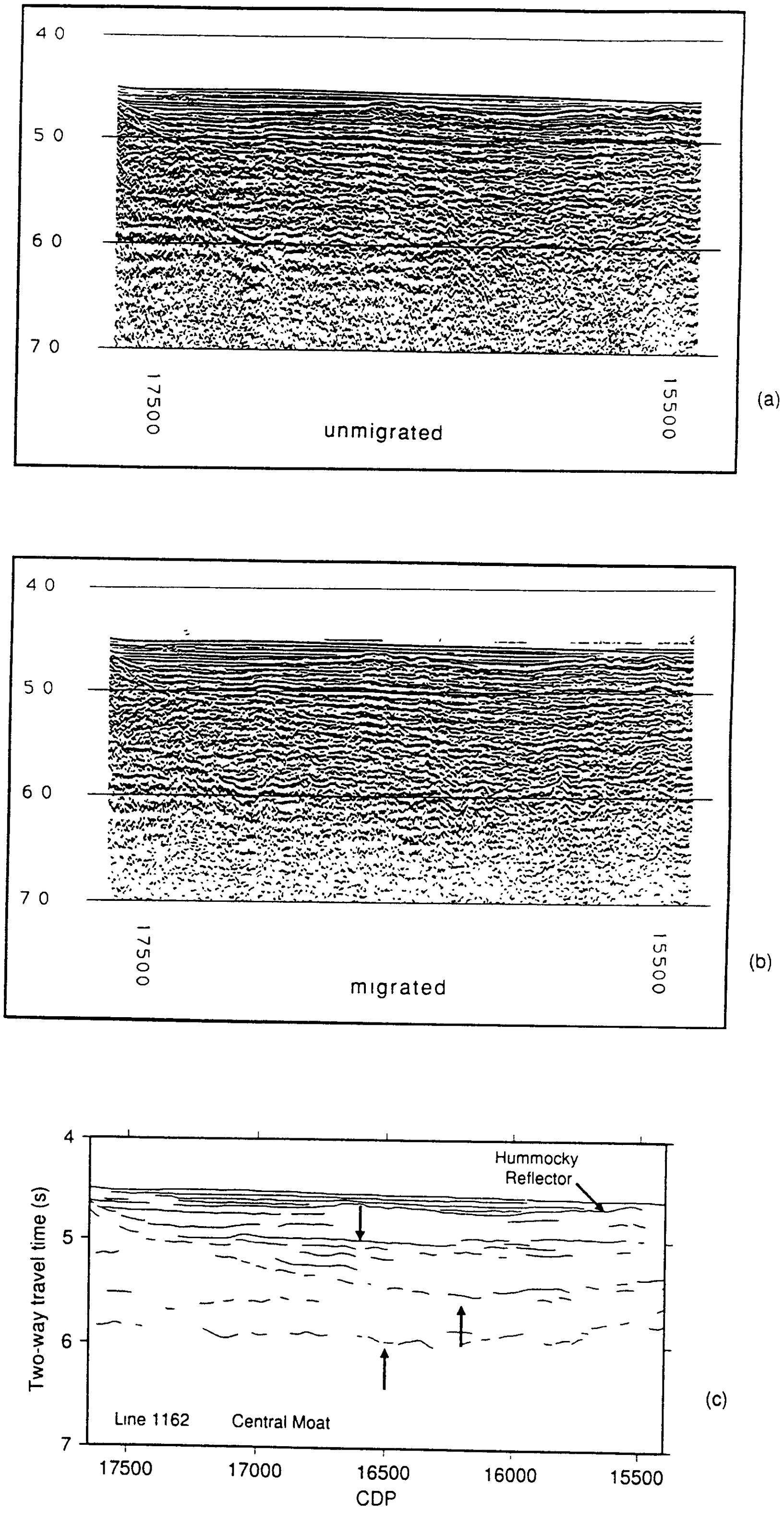
4 0
5 0
6 0
7 0
17500
15500
unmigrated
(a)
4 0
5 0
6 0
7 0
17500
15500
migrated
(b)
4
5
6
7
Two-way travel time (s)
Hummocky
Reflector
Line 1162
Central Moat
17500
17000
16500
16000
15500
CDP
(c)

Figure 8

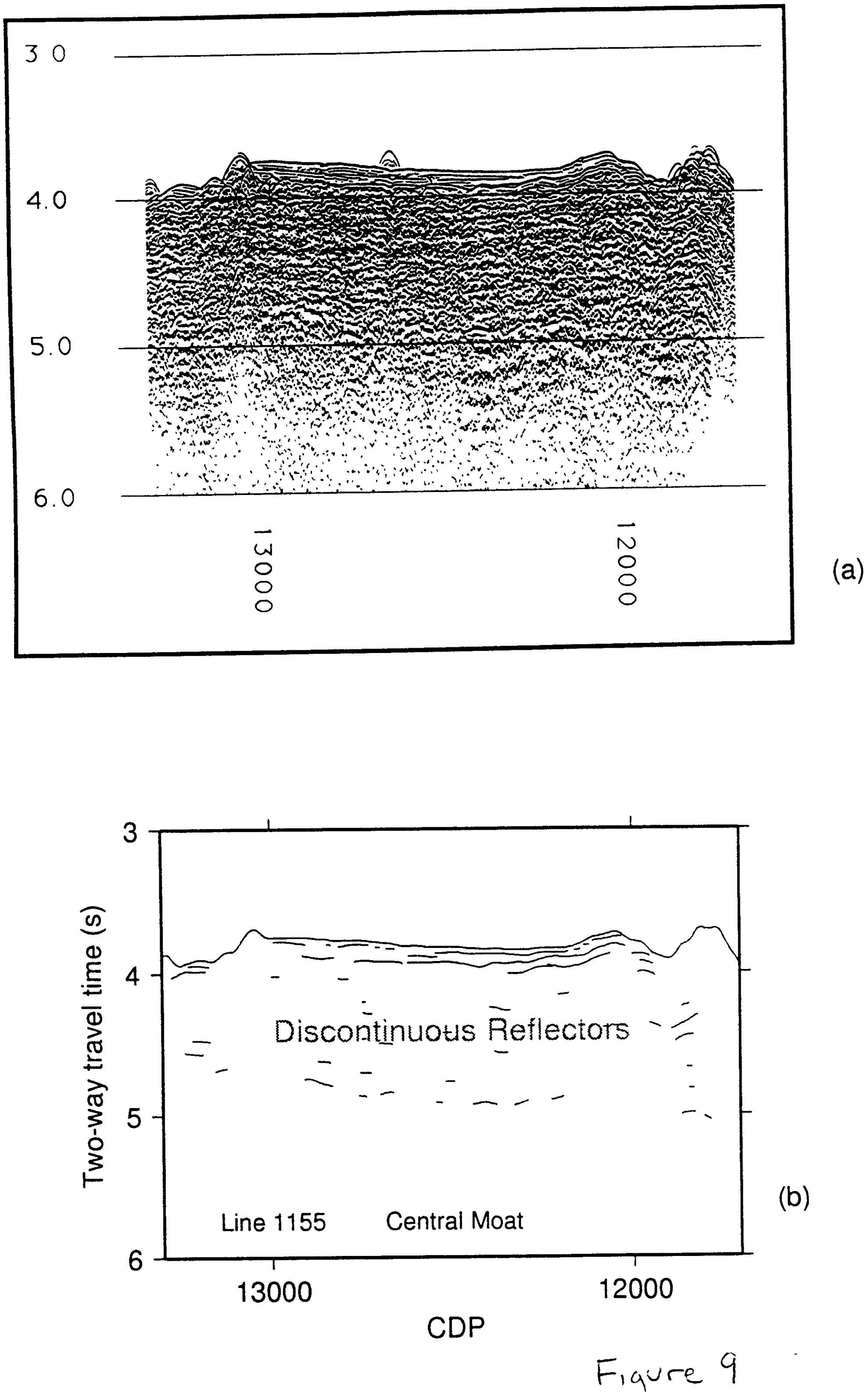
3 0
4.0
5.0
6.0
13000
12000
(a)
3
4
5
6
Two-way travel time (s)
Discontinuous Reflectors
Line 1155
Central Moat
13000
12000
CDP
(b)

Figure 9

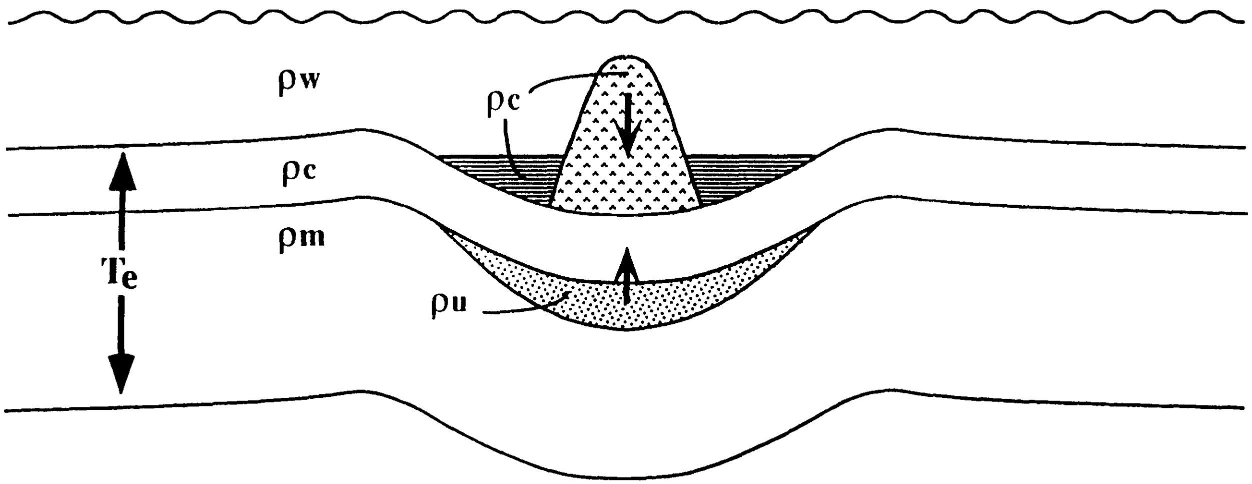

Figure 10

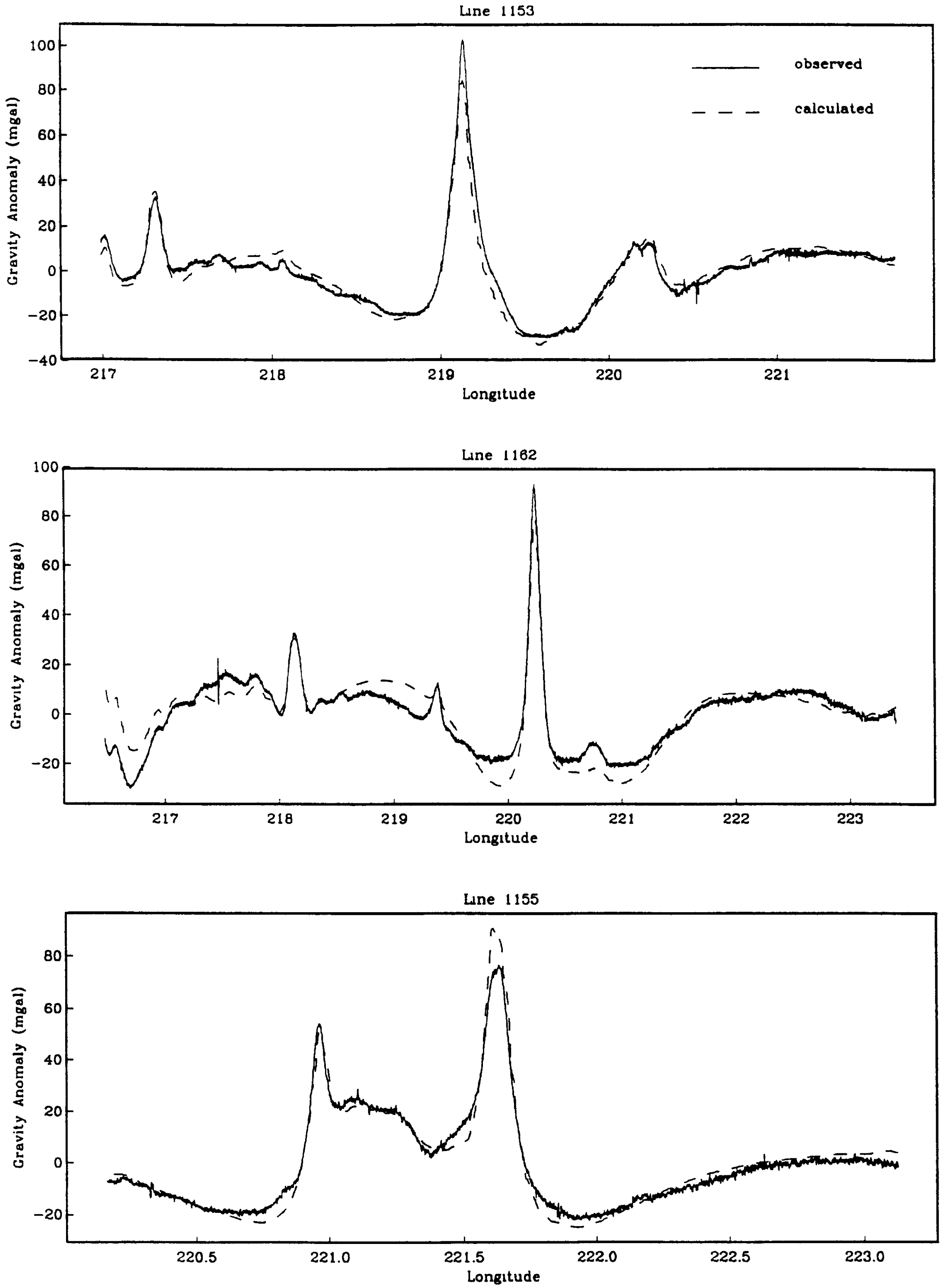
Line 1153
observed
calculated
Gravity Anomaly (mgal)
100
80
60
40
20
0
-20
-40
217
218
219
220
221
Longitude
Line 1162
Gravity Anomaly (mgal)
100
80
60
40
20
0
-20
217
218
219
220
221
222
223
Longitude
Line 1155
Gravity Anomaly (mgal)
80
60
40
20
0
-20
220.5
221.0
221.5
222.0
222.5
223.0
Longitude

Figure 11

Model Basement Depth

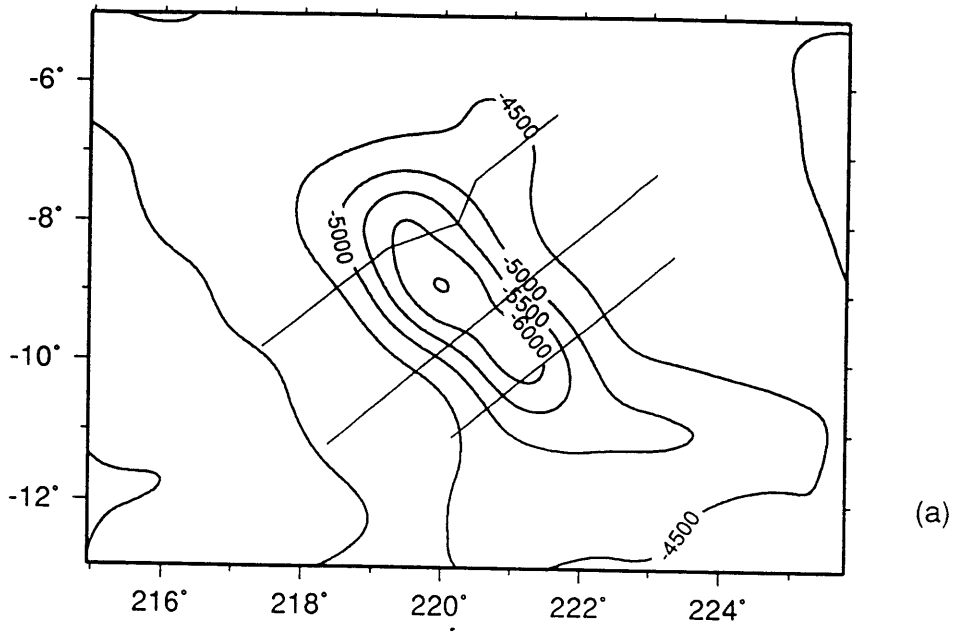

Underplating Thickness (3100 kg/m^3 Material)

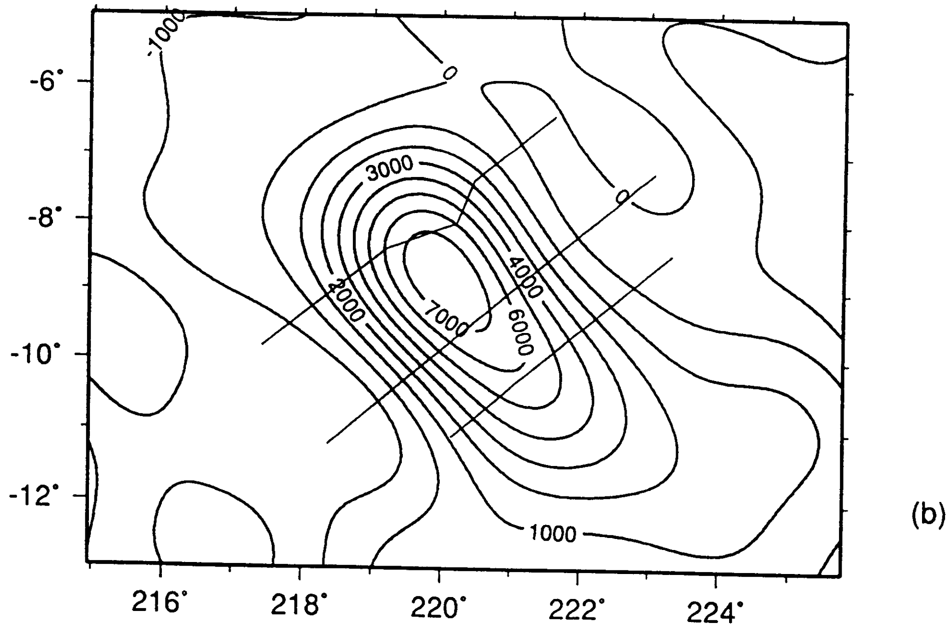

Figure 12

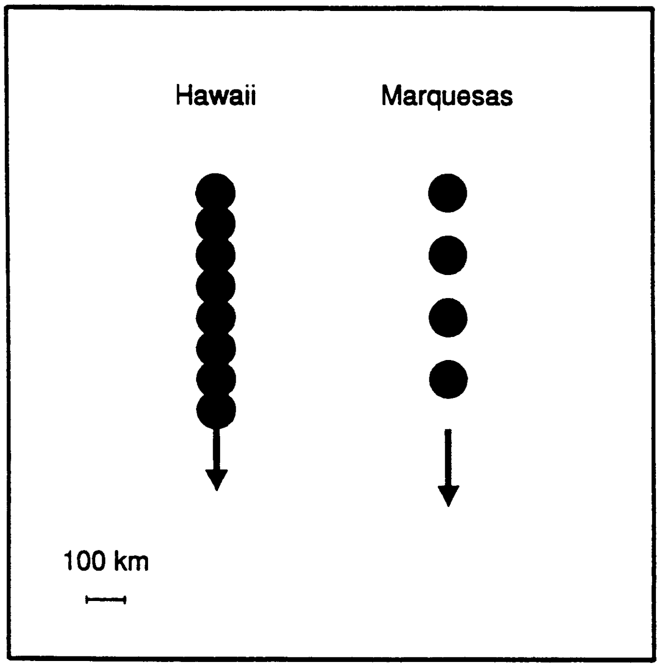

Figure 13

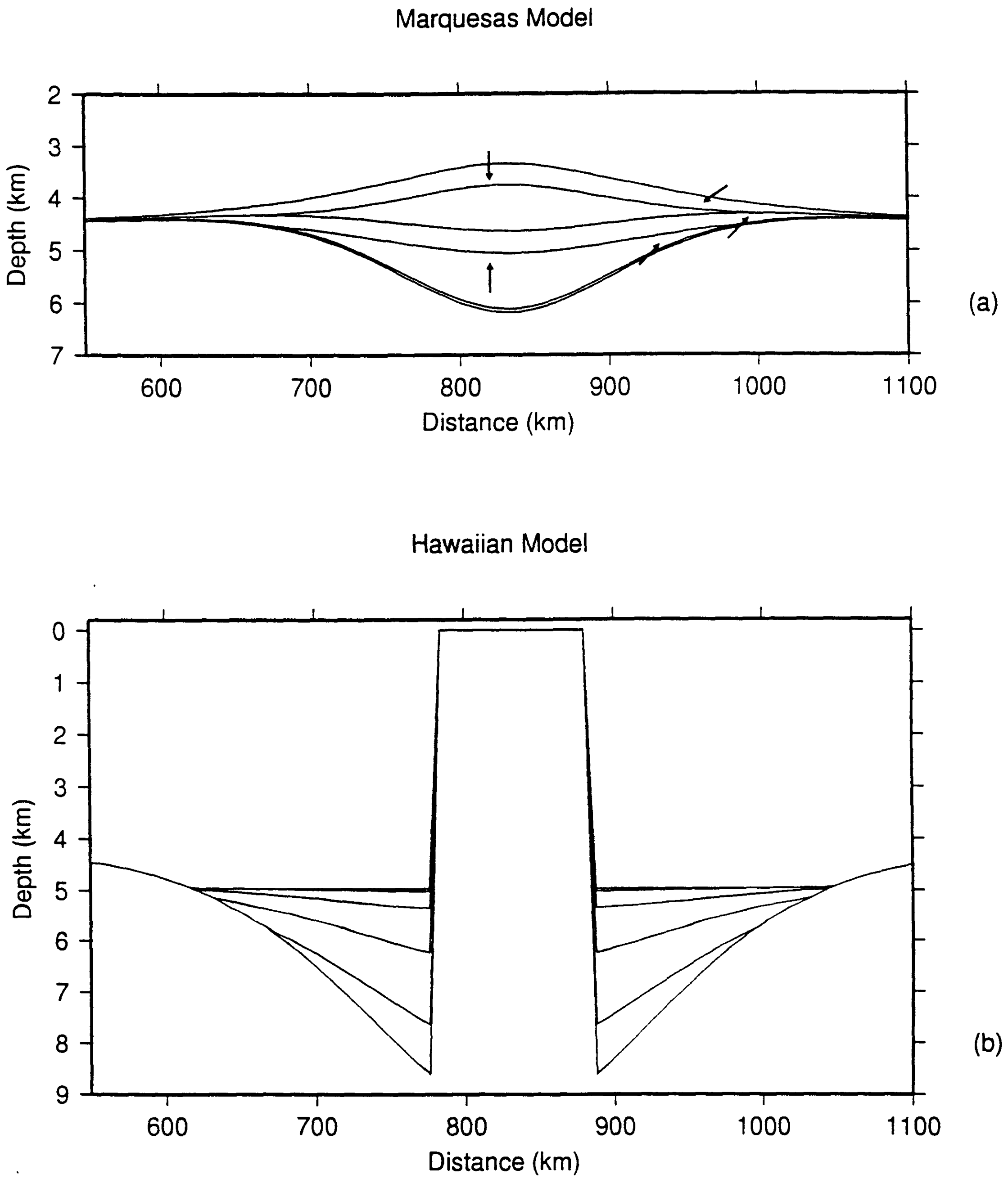
Marquesas Model

Hawaiian Model

Figure 14

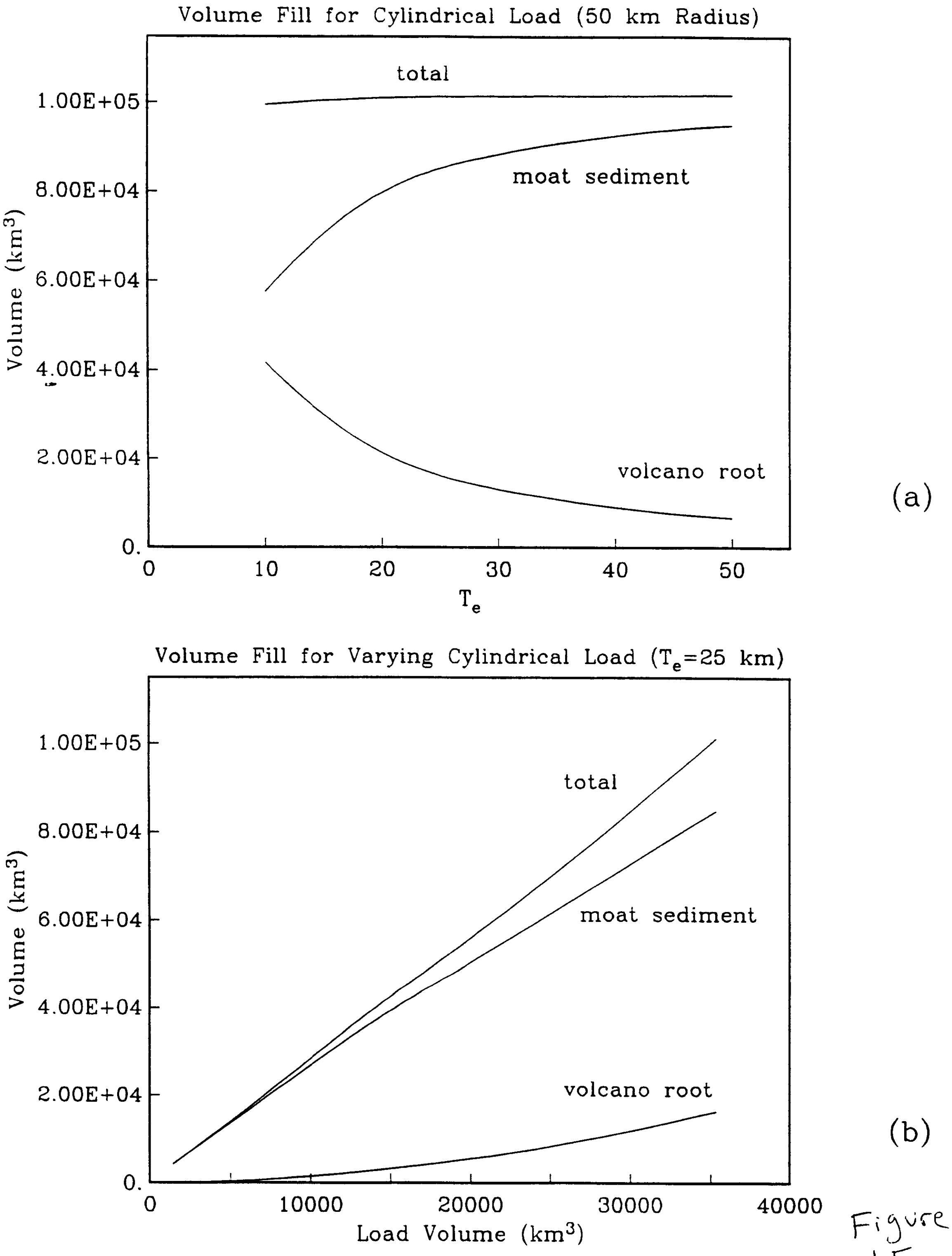
Volume Fill for Cylindrical Load (50 km Radius)
Volume (km^3)
1.00E+05
8.00E+04
6.00E+04
4.00E+04
2.00E+04
0.
total
moat sediment
volcano root
0
10
20
30
40
50
T_e
(a)
Volume Fill for Varying Cylindrical Load (T_e=25 km)
Volume (km^3)
1.00E+05
8.00E+04
6.00E+04
4.00E+04
2.00E+04
0.
total
moat sediment
volcano root
0
10000
20000
30000
40000
Load Volume (km^3)
(b)

Figure 15

CHAPTER 3

OCEANIC TRANSFORM EARTHQUAKES WITH UNUSUAL MECHANISMS OR LOCATIONS: RELATION TO FAULT GEOMETRY AND STATE OF STRESS IN THE ADJACENT LITHOSPHERE

JOURNAL OF GEOPHYSICAL RESEARCH, VOL. 98, NO. B9, PAGES 16,187–16,211, SEPTEMBER 10, 1993

Oceanic Transform Earthquakes With Unusual Mechanisms or Locations: Relation to Fault Geometry and State of Stress in the Adjacent Lithosphere

CECILY J. WOLFE, ERIC A. BERGMAN,[1] AND SEAN C. SOLOMON[2]

Department of Earth, Atmospheric, and Planetary Sciences, Massachusetts Institute of Technology, Cambridge

On oceanic transforms, most earthquakes are expected to occur on the principal transform displacement zone (PTDZ) and to have strike-slip mechanisms consistent with transform-parallel motion. We conducted a search for transform earthquakes departing from this pattern on the basis of source mechanisms and locations taken from the Harvard centroid moment tensor catalogue and the bulletin of the International Seismological Centre, respectively. Events with unusual mechanisms occur on several transforms. We have determined the source mechanisms and centroid depths of 10 such earthquakes on the St. Paul's, Marathon, Owen, Heezen, Tharp, Menard, and Rivera transforms from inversions of long-period body waveforms. Relative locations of earthquakes along these transforms have been determined with a multiple-event relocation technique. Much of the anomalous earthquake activity on oceanic transforms is associated with complexities in the geometry of the PTDZ or the presence of large structural features that may influence slip on the fault. Reverse-faulting earthquakes occur at a compressional bend in the Owen transform in the area of Mount Error and at the St. Paul's transform near St. Peter's and St. Paul's Rocks. A normal-faulting earthquake on the Heezen transform is located at the edge of a pull-apart basin marking an extensional offset of the fault. Normal-faulting earthquakes along the Tharp, Menard, and Rivera transforms may also be related to extensional offsets. Some events with unusual mechanisms occur outside of the transform fault zone, however, and do not appear to be related to fault zone geometry. For instance, earthquakes with mechanisms indicating reverse-faulting on ridge-parallel fault planes are located near the ridge-transform intersections of the St. Paul's and the Marathon transforms. Possible additional contributors to the occurrence of anomalous earthquakes include recent changes in plate motion, differential lithospheric cooling, and the development of a zone of weakness along the fault zone, but we do not find strong evidence to confirm the influence of these processes.

INTRODUCTION

Since *Sykes's* [1967] study of earthquakes on mid-ocean ridges confirmed the transform fault hypothesis [*Wilson*, 1965], the mechanisms of most earthquakes along oceanic transforms have been generally well-explained by a simple model. Such earthquakes are expected to have strike-slip mechanisms consistent with transform motion, to have vertical or nearly vertical fault planes, and to occur on the principal transform displacement zone (PTDZ). A corollary of this standard model, from the classical theory of faulting [*Anderson*, 1951], is that the direction of the most compressive principal stress σ_1 is horizontal and makes an angle of about 30° (on the basis of laboratory-derived coefficients of friction [*Byerlee*, 1978]) to the strike of the fault. Two current lines of research, however, suggest that this model bears closer scrutiny. First, studies of earthquake characteristics and fault mechanics along oceanic [*Prothero and Reid*, 1982; *Tréhu and Solomon*, 1983; *Bergman and Solomon*, 1988] and continental transforms [e.g., *Segall and Pollard*, 1980; *King and Nabelek*, 1985; *Sibson*, 1985, 1986; *Nabelek et al.*, 1987; *Barka and Kadinsky-Cade*, 1988; *Saucier et al.*, 1992] have shown that bends or offsets in the fault can strongly affect the state of stress and pattern of earthquake faulting near such features. Second, there is increasing evidence that at least some oceanic and continental transforms act as weak zones relative to the adjacent lithosphere and that the stress state near the fault departs from classical theory [*Zoback et al.*, 1987; *Mount and Suppe*, 1987; *Wilcock et al.*, 1990]. In this paper, we present new information from a study of oceanic transform earthquakes with unusual mechanisms or locations confirming that a vertical strike-slip fault along the PTDZ is not always an adequate model for transform geometry and slip.

Recent studies of individual oceanic transforms with high-resolution bathymetric mapping, side-scan sonar imaging, and observations from submersibles have revealed complex fault geometries and structures within the transform domain [*Fox and Gallo*, 1984, 1986]. Extensional or compressional jogs (bends or offsets) in the PTDZ have been documented along several transforms [e.g., *Macdonald et al.*, 1979, 1986; *Lonsdale*, 1986; *Gallo et al.*, 1986; *Fornari et al.*, 1989]. Microearthquake experiments conducted with ocean bottom seismometers have indicated patterns of seismicity and fault plane solutions consistent with the presence of extensional relay zones along the Rivera [*Prothero and Reid*, 1982] and Orozco [*Tréhu and Solomon*, 1983] transforms. Large earthquakes occurring near compressional fault jogs on the Kane and Vema transforms in the Atlantic have been shown to consist of primary strike-slip events and secondary events with reverse faulting mechanisms [*Bergman and Solomon*, 1988]. *Engeln et al.* [1986] also noted eight Atlantic transform earthquakes with apparently shallowly dipping fault planes or a dip-slip component of displacement, but independent body waveform inversions have shown that two of these events are normal-faulting earthquakes occurring on the nearby ridge segment and one is a strike-slip earthquake on a steeply dipping plane with a smaller reverse-faulting precursor [*Huang et al.*, 1986; *Bergman and Solomon*, 1988].

---

[1] Now at U.S. Geological Survey, National Earthquake Information Center, Golden, Colorado.

[2] Now at Department of Terrestrial Magnetism, Carnegie Institution of Washington, D.C.

Copyright 1993 by the American Geophysical Union

Paper numer 93JB00887.
0148-0227/93/93JB-00887$05.00

Studies of continental strike-slip faults have illustrated the importance of fault geometry on the pattern of faulting. Jogs in strike-slip faults are known to produce uplift or subsidence along the fault, depending of whether the sense of the jog is compressional or extensional [*Sylvester*, 1988; *Bilham and King*, 1989; *Anderson*, 1990]. Earthquake rupture can be stopped by both compressional and extensional jogs [*Segall and Pollard*, 1980; *King and Nabelek*, 1985; *Sibson*, 1985, 1986]. Numerical models of strike-slip faults that are offset or contain bends show that such geometry can considerably alter the state of stress [*Segall and Pollard*, 1980; *Saucier et al.*, 1992]. For instance, the thrust faulting component to the mechanism of the Loma Prieta earthquake has been attributed to the event's location at a local bend in the San Andreas fault in the Santa Cruz Mountains [*McNally et al.*, 1989]. In the North China Basin [*Nabelek et al.*, 1987] and along strike-slip faults in Turkey [*Barka and Kadinsky-Cade*, 1988] earthquake mechanisms and locations in conjunction with geologic information indicate normal faulting at extensional jogs and reverse faulting at compressional jogs.

The orientation of stresses in central California, as inferred from borehole breakout data, off-fault focal mechanisms, and the trends of active reverse faults and thrust-related anticlines along the fault system, indicate that σ_1 is nearly perpendicular to the San Andreas fault within only a few kilometers of the fault zone [*Zoback et al.*, 1987; *Mount and Suppe*, 1987; *Jones*, 1988]. Such an orientation differs from that of the stress field farther (~100 km) from the fault. The lack of a heat flow anomaly across the San Andreas fault requires that shear stresses acting on the fault plane be low, less than about 20 MPa [*Brune et al.*, 1969; *Lachenbruch and Sass*, 1980]. These results, and a small predicted component of convergence between the Pacific and North American plates, have led to the suggestion that plate motion along the San Andreas is decoupled by a weak fault zone into a low-stress, strike-slip component along the fault and a high-stress, compressional component off the fault [*Zoback et al.*, 1987; *Mount and Suppe*, 1987].

The orthogonality of ridge-transform plate boundaries suggests that oceanic transforms are also comparatively weak. A perpendicular ridge-transform-ridge configuration minimizes the energy dissipated along the plate boundary if the transform is a zone of weakness, i.e., if stresses resisting plate separation along the ridge axis are larger than the shear stresses along the transform [*Lachenbruch and Thompson*, 1972; *Froidevaux*, 1973; *Stein*, 1978]. Curvature of the ridge axis neovolcanic zone toward the transform fault as the ridge-transform intersection is approached is also consistent with ridge axis stresses being several times larger than shear stresses on the transform [*Phipps Morgan and Parmentier*, 1984]. Fracture zone bathymetry and magnetic anomalies indicate that oceanic transforms are zones of weakness that adjust to changes in plate motion and can be deformed by compression or extension [*Menard and Atwater*, 1968]. In a microearthquake experiment along the active transform portion of the Kane Fracture Zone, *Wilcock et al.* [1990] observed that while the PTDZ was inactive during the experiment, seismic activity near the base of the southern transform valley wall was characterized by normal faulting, with the axis of least compressive stress σ_3 oriented perpendicular to the transform. Such a stress state is consistent with the hypothesis that the transform acts as a zone of weakness.

To investigate further the nature of shear stress and deformation in the vicinity of oceanic transform faults, we have conducted a global search of large (body wave magnitude $m_b \geq 4.5$) earthquakes on and near oceanic transforms for those events with unusual source mechanisms and locations. From an initial examination of the Harvard catalogue of centroid moment tensor (CMT) solutions [*Dziewonski et al.*, 1981], we identified transform earthquakes with mechanisms differing from the expected model of strike-slip motion on a vertical fault. We limit the present study to seven transforms on which we found anomalous earthquakes suitable for further study using an inversion of long-period body waveforms [*Nabelek*, 1984]. To provide better constraints on the pattern of seismicity and its relation to fault geometry, we relocated earthquakes along these transforms with a multiple-event relocation technique [*Jordan and Sverdrup*, 1981]. We consider the implications of these results for the standard fault model for transform slip, for the importance of geometrical irregularities in the fault trace, and for the state of stress near and along transforms.

A SEARCH FOR EVENTS WITH ANOMALOUS MECHANISMS

The search of the Harvard CMT catalogue for 1977-1989 for oceanic transform events with mechanisms differing significantly from the prediction of the standard model was conducted as follows. Earthquake epicenters from the catalogue of the International Seismological Centre (ISC) for 1964-1989 served to define the geometry of the ridge-transform system. Transforms are identified by the trend of ISC epicenters and strike-slip mechanisms with the expected sense of motion. For large-offset transforms, on which there is a significant amount of earthquake activity, this means of identification is adequate. Figure 1 shows a sample map of earthquake epicenters and CMT mechanisms along the active portion of the Eltanin Fracture Zone, made up of three transforms

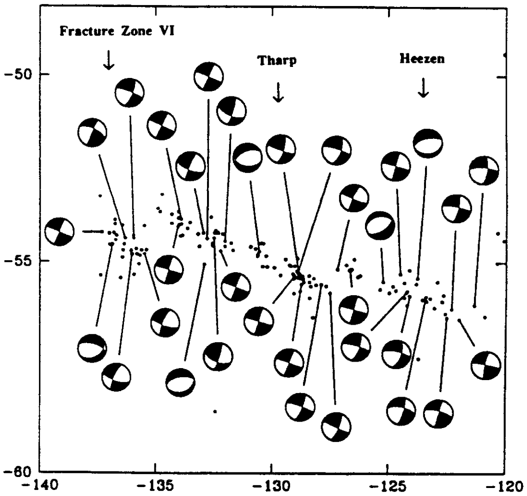

Fig 1. Earthquake epicenters (International Seismological Centre (ISC)) and centroid moment tensor (CMT) mechanisms for earthquakes along the Eltanin fault system on the Pacific-Antarctic plate boundary. Epicenters are depicted by dots; mechanisms are equal-area projections of the lower focal hemisphere, with compressional quadrants shaded. The Eltanin system is made up of the Heezen and Tharp transforms and a transform identified as Fracture Zone VI by *Molnar et al.* [1975].

along the Pacific-Antarctic plate boundary; several anomalous normal-faulting mechanisms are evident in this region. We excluded from this study areas where the ridge approaches a trench or a continent (e.g., the Gulf of California and the Gulf of Aden). There is possible bias in the search procedure in that earthquakes that displayed normal-faulting mechanisms and occurred near the ridge-transform intersection with one or both nodal planes oriented parallel to the ridge axis were assumed to be related to the spreading process.

We identified 15 large-offset oceanic transform faults where earthquakes with anomalous mechanisms occurred during the 13-year study interval (we include the Udintsev transform in this list, where an anomalous strike-slip earthquake occurred in 1990). The mechanisms vary from reverse, to normal, to strike-slip with the wrong sense of slip for transform motion. Only 10 of these earthquakes (occurring on seven transforms) are well-enough recorded to permit body waveform inversion. Table 1 lists the source parameters derived for these earthquakes. The CMT source parameters of other anomalous transform earthquakes are listed in Table 2. Figure 2 shows the location of the seven transforms that we have investigated in detail.

WAVEFORM INVERSION

In CMT analysis [*Dziewonski et al.*, 1981; *Dziewonski and Woodhouse*, 1983], long-period digital waveforms are inverted for the six independent components of the moment tensor, as well as centroid origin time and location. The inversion includes all seismic phases that arrive at a station prior to the arrival of Rayleigh or Love waves (for earthquakes having scalar moment M_0 greater than about 1×10^{25} dyn cm long-period mantle waves are included). Data are filtered to exclude periods less than 45 s and do not constrain shallow centroid depths. In addition, for shallow earthquakes the components of the moment tensor corresponding to a vertical dip-slip or horizontal thrust mechanism are the least well resolved.

We have refined the mechanisms and centroid depths of the anomalous transform earthquakes using an inversion of long-period teleseismic *P* and *SH* waveforms [*Nabelek*, 1984] from stations of the World-Wide Standardized Seismograph Network (WWSSN). Because long-period WWSSN instruments have peak responses at 15-s period, this inversion can usually constrain the centroid depth and the vertical dip-slip or horizontal strike-slip component of shallow earthquakes [*Nabelek*, 1984]. (However, CMT solutions are more sensitive to data at longer periods and better describe the seismic moment.) For 13 earthquakes, there is a good azimuthal distribution of stations with clear *P* and *S* arrivals on WWSSN analogue records. WWSSN records were digitized and corrected for differences in magnification and epicentral distance as described by *Bergman et al.* [1984]. Global Digital Seismic Network (GDSN) *S* wave data were included when necessary to improve *SH* coverage. In a few cases, additional *P*

TABLE 1 Epicentral Data and Source Parameters From Body Waveform Inversion

Date	Origin Time,[a] UT	Latitude,[a] °N	Longitude,[a] °E	m_b[a]	M_S[a]	M_0[b]	Mechanism[c]	Depth,[d] km	STF,[e] s
Carlsberg Ridge: Owen Transform									
Sept. 29, 1983	1803:59.8	10.45	56.91	5.7	5.0	2.0×10^{24}	214/89/298	11	4
Sept. 7, 1986	1626:56.5	10.31	56.81	6.2	6.1	3.7×10^{25}	238/36/095	4	8
Mid-Atlantic Ridge: St. Paul's Transform									
Oct. 11, 1973	0207:51.8	0.52	-29.47	5.9		6.2×10^{25}	264/82/183	12	11
Oct. 14, 1982	1729:24.7	0.99	-29.07	5.1	5.2	9.0×10^{24}	86/66/172	11	5
Oct. 12, 1985	2220:42.8	0.87	-29.90	5.4	5.9	4.2×10^{25}	76/72/174	10	17
Sept. 20, 1986	0131:14.2	0.88	-29.25	5.4	4.8	1.8×10^{24}	227/53/050	14	3
Apr. 4, 1988	0425:36.7	0.97	-30.27	5.8	5.4	2.7×10^{24}	189/52/107	8	3
Dec. 23, 1988	2149:09.1	0.77	-29.41	5.7	5.5	6.0×10^{24}	228/56/072	9	4
Mid-Atlantic Ridge: Marathon Transform									
Sept. 22, 1985	1823:12.9	12.52	-44.31	5.6	5.5	4.2×10^{24}	140/54/051	4	4
Pacific-Antarctic Ridge: Heezen Transform									
Feb. 17, 1978	0140:03.1	-55.71	-125.24	5.7	5.2	2.4×10^{24}	241/16/309	11	3
Pacific-Antarctic Ridge: Tharp Transform									
May 27, 1989	0301:24.7	-55.24	-133.14	5.5	5.7	1.5×10^{25}	275/59/287	12	7
East Pacific Rise: Menard Transform									
May 15, 1987	1349:14.6	-49.91	-115.3	5.5	4.7	1.9×10^{24}	50/37/247	9	2
East Pacific Rise: Rivera Transform									
Sept. 21, 1977	1315:58.2	19.97	-109.26	5.5		4.9×10^{24}	353/35/291	4	6

[a] Epicentral data, m_b, and M_S are from the International Seismological Centre

[b] Seismic moment in units of dyne centimeters.

[c] Strike/dip/slip, in degrees, using the convention of *Aki and Richards* [1980]

[d] Depth of centroid below the seafloor

[e] Duration of the source time function (STF)

wave coverage was gained by using broad-band seismograms constructed by combining long-period and short-period GDSN data in the frequency domain [*Harvey and Choy*, 1982]. For such a construction we used a procedure similar to that of *Ekström* [1989]; short-period data were resampled at 0.2 s and broad-band data were filtered with a three-pole band-pass Butterworth filter with corner frequencies at 0.015 and 1.0 Hz.

The source parameters in the inversion are centroid depth, double-couple mechanism, seismic moment, and the source time function (STF). The number of elements in the STF, taken as a series of overlapping triangles, is assigned prior to inversion and represents an additional parameter to be tested. In some cases the event is parameterized as two point sources or as a unilateral, horizontally propagating rupture along the strike of one of the nodal planes. For the latter situation a rupture velocity of 3.5 km/s is assumed. Values for the attenuation parameter t^* [*Futterman*, 1962] are taken to be 1.0 s for long-period P waves and 4.0 s for long-period S waves.

The assumed source velocity structure has an effect on the inversion results, in that takeoff angles of the rays and delay times of depth phases depend on the source structure. For slow slipping transforms, we adopted the velocity structure used by *Bergman and Solomon* [1988], which was based on the refraction studies of *Bowen and White* [1986] and *Louden et al.* [1986] of the Vema transform (Table 3). For fast slipping transforms, data on the velocity structure are limited: a study at the Orozco transform [*Tréhu and Purdy*, 1984] found anomalous velocity structure associated with relict ridge features and normal oceanic crust to the south of the transform. A model for normal oceanic crust (Table 3) was used for the source region along fast slipping transforms.

Body wave modeling has proven useful in determining the centroid depths of earthquakes in a number of tectonic settings, but the uncertainty in depths determined with this method is often difficult to establish. Discussions of the errors in determining centroid depths are given by *Nabelek* [1984], *Huang et al.* [1986], *Stein and Wiens* [1986], *Goff et al.* [1987], and *Bergman and Solomon* [1988]. Factors such as signal-to-noise (S/N) ratio, station distribution, mechanism, and depth of faulting can all influence the magnitude of uncertainties.

For all events, we conducted a series of inversions with the

TABLE 2. Epicentral Data and Centroid Moment Tensor Source Parameters of Additional Unusual Transform Earthquakes

Date	Origin Time,[a] UT	Latitude,[a] °N	Longitude,[a] °E	M_0[b]	Mechanism[c]	Source
			East Pacific Rise. Gofar Fracture Zone			
Oct 8, 1980	2019.47.0	-4.87	-106.15	4.55×10^{24}	280/72/197	*Dziewonski et al.* [1988*a*]
			Pacific-Antarctic Ridge. Heezen Transform			
Aug. 16, 1984	1530:59.8	-55.40	-123.75	1.57×10^{24}	257/63/268	*Dziewonski et al.* [1985]
			Pacific-Antarctic Ridge Tharp Transform			
Oct 10, 1982	1744:45.2	-54.73	-130.54	6.18×10^{23}	246/54/250	*Dziewonski et al.* [1988*c*]
			Pacific-Antarctic Ridge. Fracture Zone VI			
Sept. 17, 1982	1108:31.7	-54.55	-136.86	6.65×10^{23}	287/61/298	*Dziewonski et al.* [1983*a*]
			Pacific-Antarctic Ridge: Udintsev Transform			
Nov. 1, 1990	0156:44.6	-56.00	-143.19	8.04×10^{23}	264/90/180	*Dziewonski et al.* [1991]
			Pacific-Antarctic Ridge: Unnamed Transform			
May 28, 1977	1510:13.6	-65.04	175.71	4.16×10^{24}	153/46/129	*Dziewonski et al.* [1987*a*]
			Southeast Indian Ridge: Unnamed Transform			
June 20, 1983	2241:57.3	-42.82	83.57	4.97×10^{23}	247/49/134	*Dziewonski et al.* [1983*b*]
			Southeast Indian Ridge: Unnamed Transform			
May 5, 1988	2335:34.7	-49.82	115.38	4.03×10^{24}	112/69/130	*Dziewonski et al.* [1989*b*]
			Southwest Indian Ridge: Discovery II Transform			
Aug. 17, 1977	1041:40.3	-40.95	42.70	8.00×10^{23}	145/58/070	*Dziewonski et al.* [1987*a*]
			Carlsberg Ridge: Owen Transform			
Sept 29, 1986	0710:37.7	10.58	57.05	7.47×10^{23}	242/72/167	*Dziewonski et al.* [1987*b*]
			Juan de Fuca Ridge: Blanco Transform			
Oct. 17, 1987	0812:21.4	43.30	-126.65	1.52×10^{24}	28/90/078	*Dziewonski et al.* [1989*a*]
Jan. 11, 1989	1223:33.1	44.60	-129.69	4.52×10^{23}	140/48/262	*Dziewonski et al.* [1990*a*]
			Mid-Atlantic Ridge: St Paul's Transform			
Dec. 30, 1989	2016:02.2	1.00	-30.15	6.85×10^{23}	304/90/000	*Dziewonski et al.* [1990*c*]

[a] Epicentral data, m_b, and M_S are from the International Seismological Centre, expect that data for the earthquake of November 1, 1990, are from the National Earthquake Information Center's Preliminary Determination of Epicenters.

[b] Seismic moment in units of dyne centimeters.

[c] Strike/dip/slip, in degrees, using the convention of *Aki and Richards* [1980]

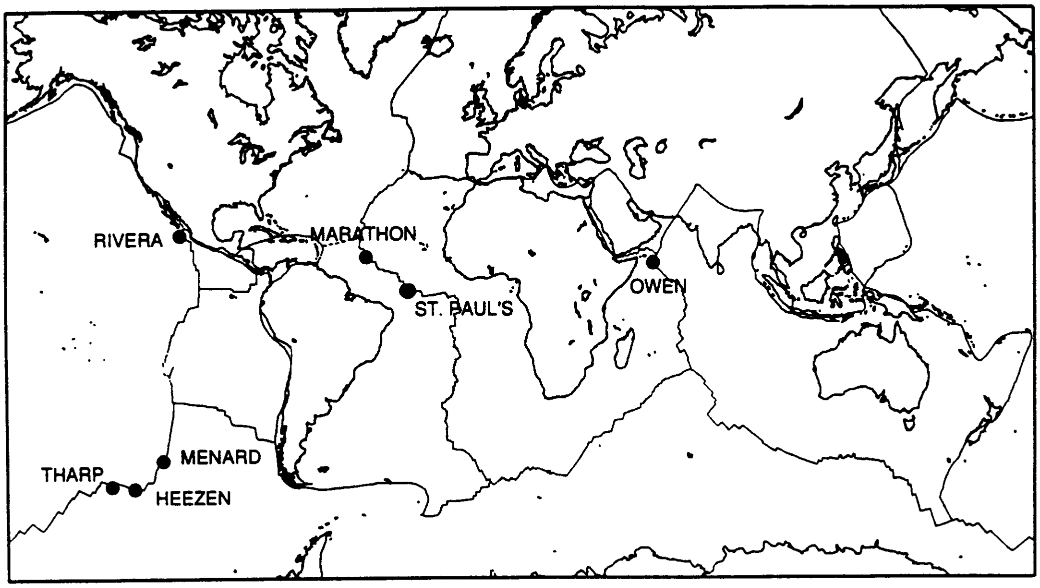

Fig. 2. Location of the seven transforms considered in this study. Locations of the earthquakes along these transforms with anomalous mechanisms and for which we have performed body waveform inversion are shown as solid circles. Also shown are plate boundaries and continents in Mercator projection.

depth fixed at values spanning a wide range; at each depth we solved for the remaining source parameters. The alignment between observed and synthetic seismograms and the length of the STF are both critical elements in this process. Seismograms are checked for proper alignment during each inversion, and STF lengths are chosen so that the final element tends toward zero amplitude. Our estimates of centroid depths are based on the interval over which the residual variance, given by the weighted mean squared difference between the observed and synthetic waveforms divided by the data variance (weighted mean squared observed waveforms), is minimized [*Huang et al.*, 1986]. While *Huang et al.* [1986] developed formal estimates of depth resolution using a statistical approach, *Bergman and Solomon* [1988] suggest that the range in centroid depth over which the residual variance varies by no more than a small percentage of the data variance also allows a simple yet conservative estimate of the uncertainty in centroid depth. The presence of distinguishable depth phases provides another important constraint on centroid depths. However, apparent depth phases can be generated either by surface reflections from a simple source or by a source at a shallower depth with a complex STF. Within a range of minimum residual variance, we prefer solutions for which the STF is single-peaked and matches depth phases.

The results of the waveform inversions are given in Table 1. The inversions for individual events are discussed in the appendix.

EARTHQUAKE RELOCATIONS

We applied a multiple-event relocation technique [*Jordan and Sverdrup*, 1981] to study the pattern of seismicity in the vicinity of unusual transform events. The advantage of a multiple-event relocation is its ability to reduce the effect of path-correlated noise on the relative locations of earthquakes within a small region. In the hypocentroidal decomposition method of *Jordan and Sverdrup* [1981], an inversion for the relative locations between events (the cluster vectors) is performed first, and then the global position of the average location of events within a cluster (the hypocentroid) is determined. This technique has advantages over other methods for multiple-event location in that it does not require fixing a master event and it makes full use of all available data.

This method is well suited for studying the relative locations of oceanic events with teleseismic data [*Jordan and Sverdrup*, 1981; *Bergman and Solomon*, 1990; *Wiens and Petroy*, 1990]. As with the single earthquake location problem, the epicentroid can be biased by errors in the theoretical travel times and uneven station distribution. *Bergman and Solomon* [1990] found by comparison with epicenters from a local ocean bottom seismograph network

TABLE 3. Seismic Velocity Models Assumed for Source Regions

Layer	Thickness, km	V_P, km/s	V_S, km/s	ρ, g/cm^3
		Fast Slipping Transforms		
1	variable	1.5	0.0	1.0
2	6.0	6.4	3.7	2.8
3	half-space	8.1	4.6	3.4
		Slow Slipping Transforms		
1	variable	1.5	0.0	1.0
2	2.2	4.3	2.5	2.5
3	2.6	5.9	3.4	2.6
4	half-space	8.1	4.6	3.4

V_P and V_S are the *P* wave and *S* wave velocity, respectively; ρ is the density.

that the teleseismic epicentroid of a cluster of events on the northern Mid-Atlantic Ridge may be biased systematically to the north by as much as 15 km because of the concentration of stations in North America and Europe. The relative pattern of multiple-event locations tends to be less affected by such systematic error, although station distribution for individual events still affects the axis orientation and aspect ratio of confidence ellipses, and errors may be significant for earthquakes with few arrivals in a single quadrant.

The ISC catalogue for January 1964 to March 1989 was searched for earthquakes near each of the transforms of interest. We excluded events that could not be reliably located, for example events with fewer than seven arrival times or events with data in less than three azimuth quadrants. Details of the data selection and inversion procedures, including the travel time calculation, ellipticity correction, and weighting of the data, were generally as described by *Bergman and Solomon* [1990]. The stations in the inversion were constrained to be within epicentral distances of 20° to 98°. Focal depths were fixed at 10 km below sea level. The relocation procedure drops data with residuals greater than 10 s in the first iteration and then uses 3 s as a maximum residual. The relocation procedure is repeated so that data with large relative errors can be flagged and omitted in the next inversion for relative location, although all such data are included in the final hypocentroidal inversion.

Examples of the relative positions of relocated earthquakes, including 95% confidence ellipses, at the Heezen and St. Paul's transforms are shown in Figure 3. The absolute positions of all relocated earthquakes are plotted in Figures 4-10.

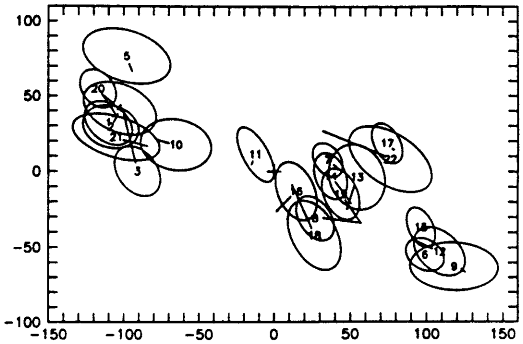

Fig. 3*a*. Relative locations of earthquakes (1964 to March 1989) on a central portion of the Heezen transform. For each earthquake the relative location is indicated by the event number, the 95% confidence ellipse for the cluster vector is shown, and the change in relative position from the starting (ISC) location is indicated by a line. The position of the average location of events within a cluster (the hypocentroid) is indicated by a cross The distance scales are in kilometers north and east of the hypocentroid. Events are numbered in chronological order

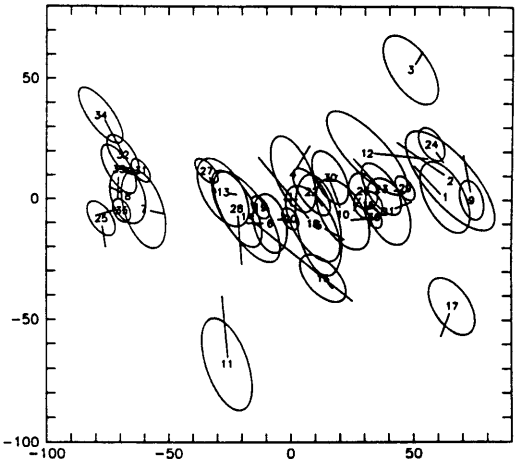

Fig. 3*b*. Relative locations of earthquakes on the western portion of the St Paul's transform (ISC locations west of 29°W).

TRANSFORM FAULTS WITH UNUSUAL EARTHQUAKE MECHANISMS AND LOCATIONS

The anomalous transform mechanisms analyzed in this study occurred on seven oceanic transform faults along both slow and fast spreading ridges (Figure 2). In this section we present a synthesis of earthquake mechanisms and relocated epicenters on these oceanic transforms and of the relation of the earthquake characteristics to the geometry and structure of the transform fault zone.

Owen Transform

The Owen transform offsets the Carlsberg Ridge and the Sheba Ridge by 300 km. The present plate configuration was established at 10 Ma, when magnetic anomalies indicate that spreading in the Gulf of Aden commenced [*Laughton et al.*, 1970; *Cochran*, 1981]. The boundary of a magnetic quiet zone, marking the limit of recent spreading on the Sheba Ridge, is presently located about 150 km from the ridge [*Cochran*, 1981], only halfway along the transform. *Stein and Cochran* [1985] argue on the basis of basement depths and heat flow measurements that the Error Ridge complex and the Sharbithat Ridge complex, which border the magnetic quiet zone, were formed by rifting of old oceanic lithosphere during the early stages of opening of the Gulf of Aden. Changes in the trend of the inactive limbs of the fracture zone are also observed near its intersection with Error Ridge [*Matthews*, 1966; *Cochran*, 1981] and Sharbithat Ridge [*Whitmarsh*, 1979].

Three earthquakes with unusual mechanisms have occurred on the southwestern portion of the transform fault zone in the vicinity of Error Ridge (Figure 4): the thrust-faulting event of July 7, 1986, the vertical dip-slip (or low-angle strike-slip) event of July 29, 1983, and the September 29, 1986, event having a strike-slip mechanism with an unusual fault orientation. In relocating earthquakes using the multiple-event technique, the assumption that *P* waves have traveled similar paths begins to break down at interevent distances larger than perhaps 200-300 km. We therefore divided the large area around the southwestern ridge-transform intersection into three regions, and we relocated subsets of earthquakes on the ridge, at the ridge-transform intersection, and on the central portion of the transform. The September 29, 1986, earthquake is one of a series of aftershocks northwest of the large ($M_0 = 2 \times 10^{25}$ dyn cm) strike-slip main event of September 17, 1986. Three earthquakes occurred after the July 7, 1986, earthquake, two on the transform, one on the ridge. Body waveform inversions for the July 29, 1983, and July 7, 1986, earthquakes are given in the appendix (Figures A1 and A2).

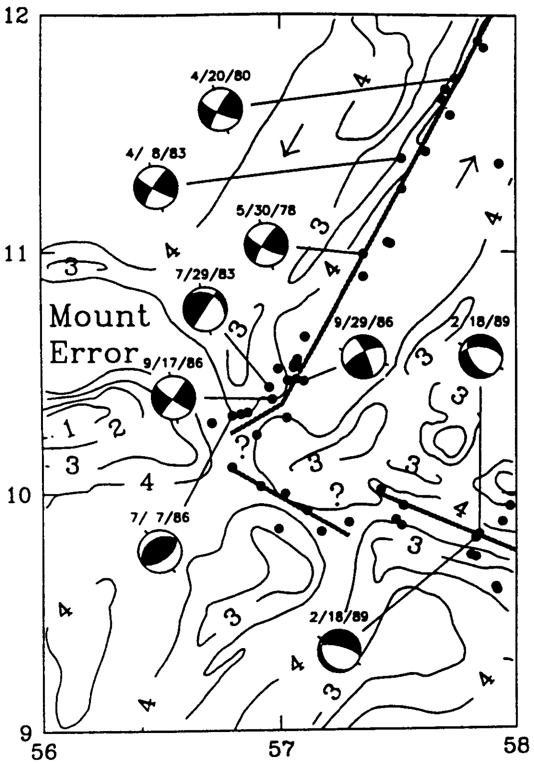

Fig. 4. Earthquake locations and mechanisms along the southwestern portion of the Owen transform. Bathymetry is adapted from *Cochran* [1988]; 1-km contour interval. Mount Error is at about 10.3°N, 56.2°E and reaches depths of < 1 km. The southeastern portion of Error Ridge includes both Mount Error and the elongate high at about 11°N, 56.2°E. Suggested plate boundary geometry is shown as a stippled line; question marks show portions of the boundary where the geometry is poorly constrained. The northeastern transform boundary is taken as a small circle about the African-Indian Euler vector, and arrows denote relative plate motion directions [*DeMets et al.*, 1990]. Epicenters (solid circles) are of relocated events from January 1964 to March 1989. The mechanisms of the earthquakes of July 29, 1983, and July 7, 1986, are from this study. All other mechanisms are from the Harvard CMT catalogue. Tic marks denote the azimuth of the maximum compressive horizontal stress, under the assumption that the *P* axis and *T* axis correspond to the axes of maximum and minimum principal stress, respectively. This assumption may not always be valid [*McKenzie*, 1969].

In the vicinity of the ridge-transform intersection, the earthquake epicenters and the bathymetry indicate an apparent compressional jog (Figure 4), although the transform in this area may be made up of several faults accommodating slip. To the northeast of the jog, the slip vectors of the strike-slip mechanisms and the epicenters follow a linear trend defining the transform fault zone. The July 29, 1983, and September 17, 1986, earthquakes, located near the northeastern end of the jog, both have one nodal plane on which horizontal slip would be in the expected direction of transform motion. The mechanism of the September 29, 1986, aftershock, however, is incompatible with expected transform motion. The orientations of both nodal planes of the July 7, 1986, reverse-faulting earthquake are rotated clockwise from the transform-parallel direction, a sense that is consistent with slip occurring at a compressional jog. The orientation of the maximum horizontal compressive stress indicated by the anomalous mechanism of the earthquake of July 29, 1983, is similar to that for most strike-slip events along the transform. The orientation of σ_1 for the September 29, 1986, earthquake indicates transform-perpendicular compression.

St. Paul's Transform

The three large equatorial transforms, the St. Paul's, the Romanche, and the Chain, offset the Mid-Atlantic Ridge by about 630, 940, and 300 km, respectively. In the central and eastern portion of the St. Paul's transform there are at least three volcanically active extensional relay zones [*Schilling et al.*, 1987]. A notable feature of this transform is the presence of St. Peter's and St. Paul's Rocks (hereafter referred to as just St. Paul's Rocks), a small group of nonvolcanic islets. While previous studies place the islets along a transverse ridge on the northern boundary of the transform, a revised bathymetric map indicates that the transform divides this feature (Figure 5). Studies have shown that St. Paul's Rocks consist mostly of mylonitized peridotite and hornblendite and are likely an upper mantle-derived intrusion [e.g., *Melson et al.*, 1972]. Recent volcanism is postulated to have occurred north of St. Paul's Rocks, where an alkali basalt associated with Quaternary sediments and carrying mylonitized ultramafic xenoliths was dredged [*Sinton*, 1979].

Several earthquakes with unusual mechanisms and locations are found in the area around St. Paul's Rocks (Figure 5). Because the study area is large, we have relocated events in three smaller subsets, with one group containing the area of the ridge north of the transform intersection and two groups covering the western part of the transform. As can be seen directly in the elongation of the confidence ellipses (Figure 3*b*), the distribution of stations for these events gives poorest epicentral resolution in the northwest to southeast direction. Events with anomalous locations (on October 11, 1973, November 14, 1982, and October 12, 1985) or CMT mechanisms (on September 20, 1986, April 20, 1988, and December 23, 1988) were selected for further study using waveform inversion. Data are not yet available for the earthquake of December 30, 1989, but this event had a small moment (7×10^{23} dyn cm) and likely cannot be analyzed by body waveform inversion with WWSSN data.

The orientation of the greatest horizontal compressive stress indicated by the mechanisms of the two reverse-faulting earthquakes of September 20, 1986, and December 23, 1988, are similar, although rotated to more nearly perpendicular to the transform than the directions given by the strike-slip events. We postulate that these earthquakes may be associated with a small compressional jog in the vicinity of St. Paul's Rocks and that the presence of anomalous structure has an influence on fault motion. Further information is needed on the fault geometry and transform structure near St. Paul's Rocks before this conjecture can be evaluated. The April 20, 1988, reverse-faulting earthquake shows a fault plane striking parallel to the ridge, and the direction of maximum horizontal compressive stress is transform-parallel (σ_2 is perpendicular to the transform); this event was followed by a series of aftershocks (events 32, 33, 34, and 35 in Figure 3*b*). The mechanism of the unusual strike-slip event of December 30, 1989, is consistent with a maximum horizontal compressional stress that is transform parallel in this region (and σ_3 perpendicular to the transform).

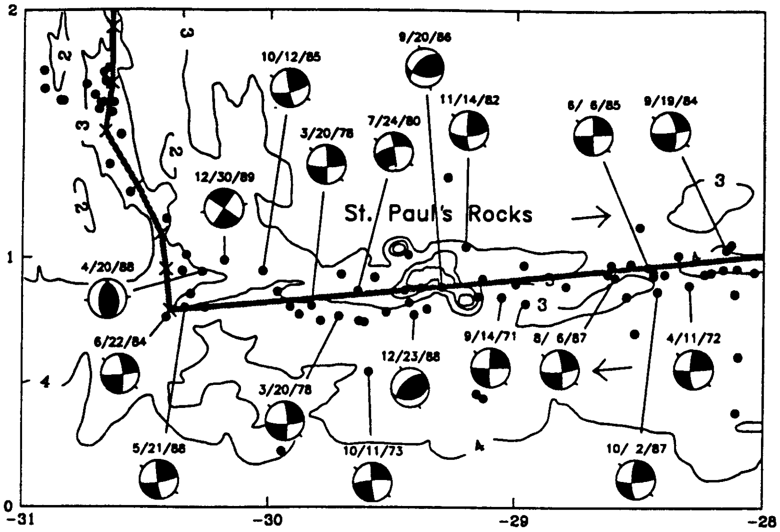

Fig. 5. Earthquake locations and mechanisms along the western portion of the St. Paul's transform. Bathymetric contours are from the General Bathymetric Chart of the Oceans (GEBCO) Digital Atlas, as supplied by the British Oceanographic Data Centre, Bidston, England, March 1992; 1-km contour interval, Mercator projection. The location of the December 30, 1989, event is from the ISC. Mechanisms of earthquakes on October 11, 1973; November 14, 1982; October 12, 1985; September 20, 1986; April 20, 1988; and December 23, 1988, are from this study. Mechanisms of the events on September 14, 1971, and April 11, 1972, are from *Engeln et al.* [1986]. Mechanisms of other events are taken from the Harvard CMT catalogue Crosses show the location of the Mid-Atlantic Ridge and its intersection with the St. Paul's transform, as given by J.-G. Schilling (Lamont-Doherty Earth Observatory, unpublished cruise report, 1987). The transform boundary is taken as a small circle about the South American-African Euler vector [*DeMets et al.*, 1990]. See Figure 4 for further details

Seismic activity outside of the transform fault zone (Figure 5) between longitudes 29° and 30°W could be the result of the anomalous stresses in the vicinity of St. Paul's Rocks. The anomalous locations of the larger events, however, are more likely the result of travel time errors. For instance, the off-transform location of the October 11, 1973, earthquake (event 16 in Figure 3*b*) is strongly influenced by data from only two stations in the southern hemisphere; the event has a complicated source time function, which introduces large picking errors. The October 12, 1985, earthquake (event 27 in Figure 3*b*) has a long source time function; picking errors could again be large. The November 14, 1982, earthquake (event 24 in Figure 3*b*), with a simple STF, provides stronger evidence for deformation occurring outside the transform fault zone, slightly to the north of St. Paul's Rocks.

Marathon Transform

Between the Fifteen Twenty Fracture Zone and the Vema Fracture Zone, the Mid-Atlantic Ridge is offset by two smaller transforms, the Mercurius, which offsets the ridge by 45 km at 12°10'N, and the Marathon, which offsets the ridge by 80 km at 12°40'N [*Collette et al.*, 1979, 1980, 1984]. An anomalous reverse-faulting earthquake occurred on September 22, 1985, near the Marathon transform (Figure 6).

The ridge segments to the immediate north and south of the transform do not display recent seismic activity. Activity on the transform has been limited to the ridge-transform intersections, an area along the central portion of the transform, and a sequence of events to the southeast of the transform valley (Figure 6). The anomalous thrust earthquake of September 22, 1985, was the first in a series of five events that occurred over a 4-day period on the southern transverse ridge. The period of the water reverberations in the *P* waveforms is consistent with a shallow water depth of 2-3 km.

Heezen and Tharp Transforms

The Heezen and Tharp transforms are two large-offset transforms on the fast spreading Pacific-Antarctic plate boundary, which is called the East Pacific Rise to the north and the Pacific-Antarctic Ridge to the south of these fracture zones. The Heezen and Tharp transforms are closely spaced (100 km), offset the ridge by 350 and 650 km, respectively, and collectively constitute most of the transform portions of the Eltanin Fracture Zone (Figure 1). The seismic history of the Eltanin system has been investigated by *Stewart and Okal* [1983], who suggested that seismic slip from 1920 to 1981 was about one tenth that predicted by plate motion models. They attributed the deficit to a lack of larger earthquakes, since there have been few earthquakes with $M_S > 6$ and none with $M_S > 7$.

Earthquakes with extensional mechanisms occur along both the Heezen and the Tharp transforms. Figure 7*a* shows relocated events along a central portion of the Heezen transform. A normal-faulting earthquake occurred on the transform on February 17, 1978 (event 11 in Figure 3*a*), and another occurred in a trough north of the transform on August 16, 1984 (event 17 in Figure 3*a*). Figure 8 shows relocated events along a central portion of the Tharp transform. A normal-faulting earthquake occurred on the transform on October 10, 1982. The May 27, 1989, normal-faulting earthquake is considered an intraplate event.

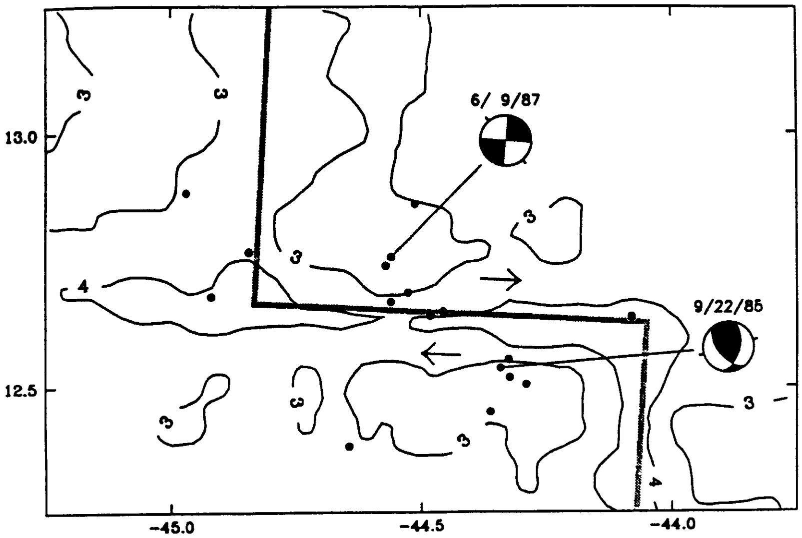

Fig. 6. Earthquake locations and mechanisms along the Marathon transform. Bathymetry is from *Collette et al* [1984]; 1-km contour interval, Mercator projection. The mechanism of the September 22, 1985, earthquake is from this study The June 9, 1987, mechanism is from the Harvard CMT catalogue. The transform boundary is taken as a small circle about the South American-African Euler vector [*DeMets et al.*, 1990]. See Figure 4 for further details

The earthquakes of February 17, 1978, and May 27, 1989, were suitable for body waveform inversion (Figures A11 and A12) The August 16, 1984, earthquake on the Heezen transform and the October 10, 1982, earthquake on the Tharp display dilatational first motions on many short-period seismograms, consistent with the normal-faulting mechanisms indicated by CMT analysis.

A multibeam survey of a portion of the Heezen transform [*Lonsdale*, 1986] helps to identify the tectonic framework of the extensional events. Between 125°W and 126°W, there are three extensional offsets of the fault trace, with two of the offsets forming deep pull-apart basins [*Lonsdale*, 1986] (Figure 7*b*). The February 17, 1978, earthquake was located near the easternmost offset. The August 16, 1984, event occurred off the Heezen transform; a recent multibeam and side-scan sonar imaging survey of this area shows a transform-parallel trough that extends from the ridge (P. Lonsdale, personal communication, 1991).

The area of the Tharp transform near the epicenter of the October 10, 1982, normal-faulting earthquake has not been mapped with multibeam bathymetry. Because the pattern of earthquake seismicity is similar to that along the Heezen, however, we suggest that an extensional offset may be present along the Tharp transform in the vicinity of the epicenter.

Menard Transform

The Menard transform, north of the Eltanin system, is a large-offset transform on the fast spreading Pacific-Antarctic plate boundary. Bathymetric and geophysical data for this transform are given by *Molnar et al.* [1975]. A normal-faulting earthquake occurred along this transform on May 15, 1987 (Figure 9).

An apparent gap in seismicity about 50 km long occurs to the west of the anomalous event. Waveform inversion for the May 15, 1987, earthquake is given in Figure A13. The direction of maximum horizontal compressive stress of the normal-faulting earthquake is similar to that of the strike-slip earthquakes.

Multibeam data from a recent survey indicate that a small extensional offset may be present at 116°W, where two parallel troughs, offset of by 1-2 km, overlap (P. Lonsdale, personal communication, 1991) The bathymetry within the Menard transform does not indicate the presence of a large extensional offset similar to that along the Heezen transform.

Rivera Transform

The current plate configuration at the Rivera transform was established around 3.5 Ma, when spreading ceased on the Mathematician Ridge and transferred to the Pacific-Cocos Rise [*Klitgord and Mammerickx*, 1982]. An abrupt change in orientation and tectonic character occurs midway along the transform near longitude 107.5°W. West of this area, seismicity is more diffuse, bathymetry exhibits greater relief, and the fracture zone consists of several subparallel valleys, although it is not known how slip is being accommodated among them [*Ness and Lyle*, 1991]. Teleseismically recorded earthquakes are generally smaller and more frequent in the western area, and there is a greater tendency for swarms to occur [*Prothero and Reid*, 1982]. *DeMets and Stein* [1990] find that the azimuths of the transform strike and earthquake slip vectors west of 108.3°W are systematically rotated by several degrees clockwise relative to the azimuths predicted by the Pacific-Rivera Euler vector. An extensional offset of the transform has been identified at 108°W on the basis of bathymetry and an en echelon pattern of microearthquakes [*Prothero and Reid*, 1982]. *Prothero and Reid* [1982] found a second en echelon offset of microearthquakes west of 109°W, possibly indicating another extensional relay.

Figure 10 shows relocated earthquakes ($m_b \geq 4.5$) and mechanisms along a portion of the western Rivera transform. The

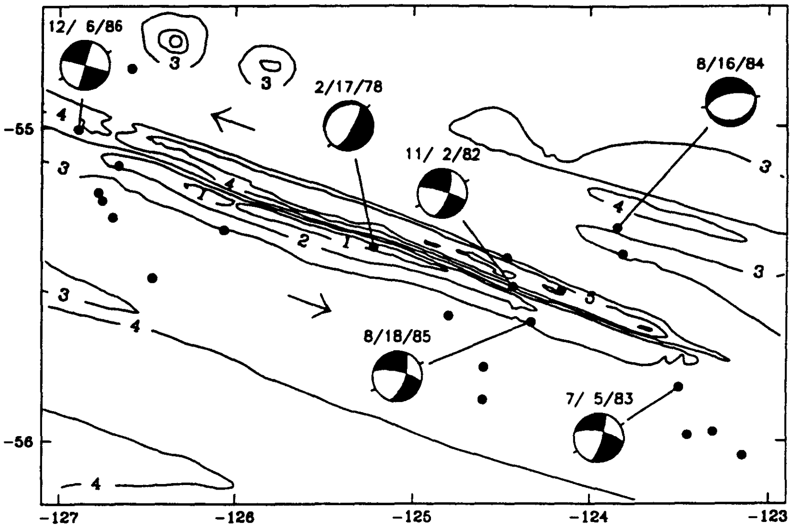

Fig. 7*a*. Earthquake locations and mechanisms along the central portion of the Heezen transform. Bathymetry is adapted from *Lonsdale* [1986]; 1-km contour interval. The mechanism of the earthquake of February 17, 1978, is from this study All other mechanisms are from the Harvard CMT catalogue. See Figure 4 for further details

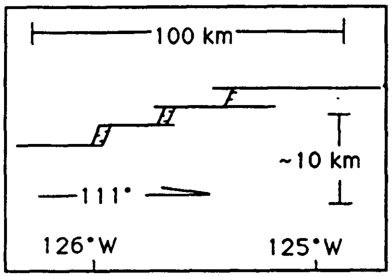

Fig. 7*b*. Geologic sketch map of the Heezen transform, adapted from *Lonsdale* [1986], oblique projection.

location uncertainty in the northeast-southwest direction is large because of a lack of arrivals to the southwest (epicentral confidence ellipses derived from multiple-event relocation are elongated in this direction). While most earthquake epicenters and mechanisms are consistent with the expected transform motion, to the west of 109°W some earthquake epicenters appear to lie north of the transform. This pattern occurs near the area where *Prothero and Reid* [1982] report an en echelon pattern of microearthquake epicenters.

Several earthquakes with anomalous mechanisms are located west of 109°W. The normal-faulting earthquake of September 21, 1977, occurred in the seismically active inner corner of the rise-transform intersection. In addition, three earthquakes with predominantly strike-slip mechanisms but with the strike directions of the probable fault planes rotated clockwise from the expected transform direction occurred on May 8, 1983. These earthquakes are a part of a sequence of about 15 events that span a 3-day period. The May 9, 1983, earthquake having a strike-slip mechanism with an anomalous fault dip is the largest event in this sequence ($M_0 = 4.2 \times 10^{25}$ dyn cm). The earthquake of February 17, 1984, is located to the east of a short offset of the rise axis, a region where deformation may be more complex than simple strike-slip motion [*Lonsdale*, 1991] The mechanism of this earthquake also shows a strike direction of the probable fault plane that is rotated clockwise from the expected direction of transform slip. Current bathymetric information does not permit a clear association of the unusual pattern of epicenters and mechanisms with morphologic features and physical processes.

CENTROID DEPTHS

Centroid depths of strike-slip earthquakes along the St. Paul's transform and the two reverse-faulting earthquakes near St. Paul's Rocks may be compared with results for other large earthquakes [*Engeln et al.*, 1986; *Bergman and Solomon*, 1988] and for microearthquakes [*Francis et al.*, 1978; *Wilcock et al.*, 1990] on slow slipping transforms. In contrast, centroid depths are not well resolved on the Heezen and Menard transforms because of the poor *P* wave S/N and the sparse sampling of waveforms. The age offset of the Owen transform is not fully developed, because oceanic crust generated by spreading on the Sheba ridge to the north extends only halfway along the transform, so the depth of seismic faulting cannot be simply related to thermal models.

From body waveform modeling, *Engeln et al.* [1986] reported centroid depths along Atlantic transforms from 2 to 7 km below the seafloor and suggested that earthquake faulting is limited by the 600°C isotherm. *Bergman and Solomon* [1988] disputed this result and on the basis of a more thorough waveform inversion procedure found that centroid depths on such transforms are generally 7-10 km, consistent with a nominal limiting isotherm of 900° ± 100°C. The centroid depths of 10-14 km that we determine for earthquakes along the St. Paul's transform are in agreement with the conclusions of *Bergman and Solomon* [1988]. To estimate the value of the isotherm limiting earthquake faulting, we follow the

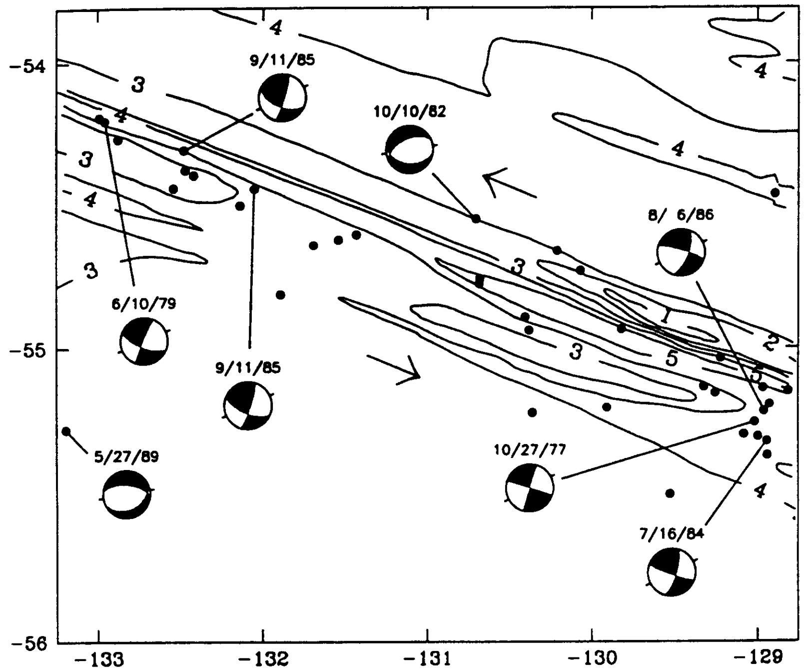

Fig. 8. Earthquake locations and mechanisms along a portion of the Tharp transform Bathymetry is adapted from *Lonsdale* [1986]; 1-km contour interval The mechanism of the May 27, 1989, earthquake is from this study Other earthquake mechanisms are from the Harvard CMT catalogue. The epicenter of the May 27, 1989, earthquake is taken from the ISC catalogue. See Figure 4 for further details.

method of *Bergman and Solomon* [1988]: we average the isotherms in adjoining lithospheric plates, in which temperatures are calculated from a standard plate-cooling model [*Parsons and Sclater*, 1977], and we calculate the depth extent of faulting using the method of *Ebel et al.* [1978], which relates the radius of a circular fault to the duration of the souce time function (further details are described by *Bergman and Solomon* [1988]). The depth extent of faulting is assumed to be twice the centroid depth for the two strike-slip earthquakes of October 11, 1973, and October 12, 1985, which have a caculated fault radius greater than the centroid depth.

The presence of volcanically active relay zones within the transform and the lack of magnetic anomaly information on age offset complicate specification of a thermal model. For a constant half-spreading rate of 16 mm/yr [*DeMets et al.*, 1990] and a fault offset of 630 km, the depth of faulting is limited by a temperature of 750° ± 100°C (Figure 11*a*). If the fault offset is shortened to 300 km by postulating that volcanically active relay zones have thermal structures similar to fully developed ridge segments, the limiting isotherm may be as high as 1000°C (Figure 11*b*). However, since our thermal model neglects three-dimensional convective and conductive heat transfer across the transform, the thermal structure resulting from a short ridge segment within the long St. Paul's transform fault will differ from the two-dimensional approximation [e.g., *Phipps Morgan and Forsyth*, 1988]. When three-dimensional effects are considered, it is likely that the thermal effect of a short ridge will not be as extreme as predicted in Figure 11*b*.

The depths of microearthquakes are typically somewhat shallower than the inferred maximum depths of faulting of large earthquakes. From a microearthquake experiment at the eastern intersection of the St. Paul's transform and the Mid-Atlantic Ridge, *Francis et al.* [1978] found that earthquakes occurred in two depth intervals: shallow shocks at 0-1 km depth occurred mostly as small swarms on the ridge axis, while events clustered near 7 km depth occurred on the active transform. *Wilcock et al.* [1990] reported microearthquake focal depths along the Kane transform of 3-6 km near the ridge-transform intersection and 5-9 km in the transform fault zone distant from the intersection.

DISCUSSION

The mechanisms of transform earthquakes provide important information about mechanical processes occurring along the transform. In this section we evaluate the possible processes contributing to the occurrence of such events by comparing the characteristics of anomalous earthquakes to be expected from each process against our observations.

Importance of Fault Geometry and Structure

Bends or offsets in strike-slip faults are capable of generating anomalous stresses in the adjoining blocks, producing uplift or subsidence, and influencing the pattern of faulting [e.g., *Segall and Pollard*, 1980; *King and Nabelek*, 1985; *Sibson*, 1985, 1986; *Nabelek et al.*, 1987; *Barka and Kadinsky-Cade*, 1988; *Bilham and King*, 1989; *McNally et al.*, 1989; *Anderson*, 1990; *Saucier et al.*,

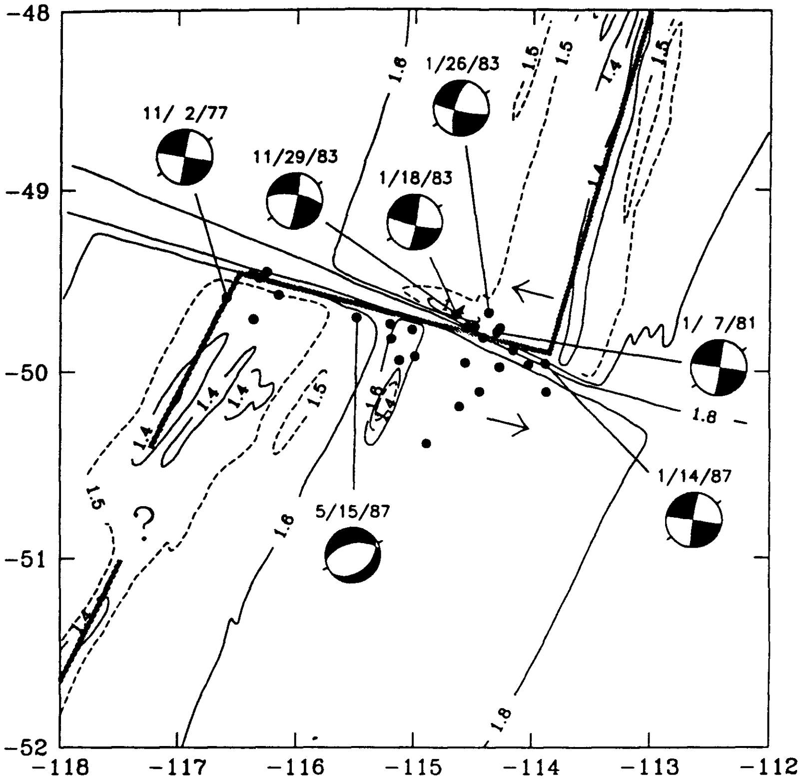

Fig 9. Earthquake locations and mechanisms along the Menard transform Bathymetry is adapted from *Mammerickx et al.* [1975], contours are in thousands of fathoms, with a 100-fathom contour interval and the 1500-fathom contour dashed. The mechanism of the May 15, 1987, earthquake is from this study. Other earthquake mechanisms are from the Harvard CMT catalogue. The transform boundary is taken as a small circle about the Pacific-Antarctic Euler vector [*DeMets et al.*, 1990]. See Figure 4 for further details.

1992]. Previous studies [*Prothero and Reid*, 1982; *Tréhu and Solomon*, 1983; *Bergman and Solomon*, 1988] have shown that anomalous patterns of seismicity can also occur at bends or offsets in oceanic transforms. The observations of this study provide additional evidence that the presence of complex fault geometry and structure can influence the pattern of earthquake locations and mechanisms along oceanic transforms. Such irregularities in fault geometry can be expected to arise from a variety of processes influencing the temporal evolution of the PTDZ (e.g., changes in plate motion, diapiric rise of altered blocks of lower crustal or upper mantle material, volcanic construction, fault-normal compression or extension, variability in crustal accretion at adjoining ridge segments, or small deviations of transform strike from the ideal small circle).

At the western ridge-transform intersection of the Owen transform, as noted above, bathymetry, earthquake epicenters, and the presence of earthquakes with anomalous mechanisms indicate the existence of a compressional fault jog (Figure 4). The interaction of the active transform with Error Ridge, anomalous structure inherited from the opening of the Gulf of Aden, may account for the complex fault geometry.

At the St. Paul's transform, the reverse-faulting earthquakes occurring near St. Paul's Rocks (Figure 5) may be associated with a compressive fault jog, similar to the case at the Owen transform. Elemental and isotopic chemistry, mineralogy, and geothermometry of islet samples suggest that St. Paul's Rocks may be a relict of subcontinental mantle, left behind in the opening of the Atlantic and subsequently emplaced as surface blocks [*Bonatti*, 1990]. While complexities in fault geometry may be responsible for the present deformation near St. Paul's Rocks, it is less likely that fault geometry was the principal cause for the original emplacement of this feature. Rapid ascent from depths greater than about 30 km and emplacement in the solid state are suggested by the presence of mantle-equilibrated primary assemblages in the form of augen within a variably recrystallized mylonite matrix [*Melson et al.*, 1972]. Uplifted blocks have been found on the walls of many transforms; petrologic investigations suggest that these blocks are made up of gabbro or peridotite that originated in the lower crust or upper mantle [e.g., *Bonatti*, 1978; *Bonatti and Hamlyn*, 1978].

Along the Pacific-Antarctic plate boundary, the normal-faulting earthquakes occurring on the Heezen, Tharp, and Menard transforms appear to be associated with extensional jogs in the trace of the PTDZ. At the Heezen transform, a normal-faulting earthquake occurred on the border of an extensional offset (Figure 7*a*), possibly reflecting a normal fault at the edge of a pull-apart basin. Normal-faulting earthquakes on the Tharp (Figure 8) and

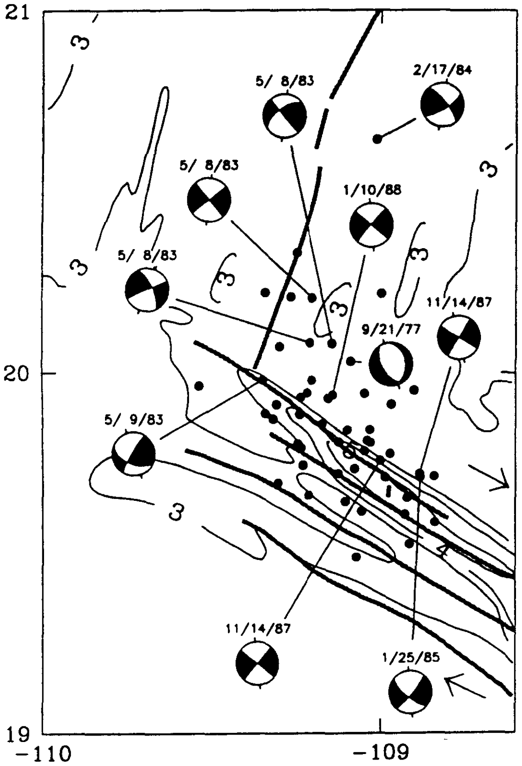

Fig 10. Earthquake locations and mechanisms along the western Rivera transform. Bathymetry is adapted from *Dauphin and Ness* [1991]; 1-km contour interval. Plate boundary is taken from *Ness and Lyle* [1991], who identify possible fault lineations on the basis of bathymetry and seismicity. Arrows denote relative plate motion directions [*DeMets and Stein*, 1991]. See Figure 4 for further details.

the Menard (Figure 9) transforms may also be associated with extensional offsets.

At the western ridge-transform intersection of the Rivera transform, a normal-faulting earthquake and several strike-slip events with anomalously striking fault planes have occurred (Figure 10). Earthquake epicenters appear offset to the northeast of the expected transform location, although the constraint on locations in the direction perpendicular to the transform is weak. An extensional offset of the Rivera transform may occur west of 109°W. Alternatively, the earthquakes with anomalous mechanisms may reflect internal deformation of the Rivera plate.

Fox and Gallo [1984] argue that higher strain rates and the juxtaposition of thinner lithosphere will allow relay zones to develop more easily along transforms at fast spreading ridges. In accord with this hypothesis, extensional relay zones have been mapped along a number of other transforms along the East Pacific Rise, including the Tamayo [*Macdonald et al.*, 1979], the Orozco [*Tréhu and Solomon*, 1983; *Madsen et al.*, 1986], the Clipperton [*Gallo et al.*, 1986], and the Siqueiros [*Fornari et al.*, 1989] transforms, and the Quebrada, Discovery, Gofar, Wilkes, and Garrett transforms on the Pacific-Nazca spreading center [*Lonsdale*, 1989]. (A recent compilation of transforms known to have extensional relay zones is given by *Fornari et al.* [1989].) The CMT catalogue does not include events with normal-faulting mechanisms along these transforms. An anomalous strike-slip earthquake, having a sense of slip opposite to that expected for transform motion, occurred along the right-stepping Gofar transform (Table 2), but this earthquake is probably associated with one of two small left-stepping offsets south of the Gofar [*Lonsdale*, 1989].

The lack of teleseismically observable normal-faulting earthquakes along most of the fastest slipping transforms may be because many of these extensional relay zones occur as intratransform spreading centers. At fast spreading rates, such relays would not be expected to display significant seismicity at teleseismic distances. Crustal thinning and magmatic activity (either intrusive or extrusive) within the extending region of the transform could yield anomalously high temperatures, at most a thin seismogenic layer, and thus a paucity of observable activity. The presence of amphibolite-facies metamorphic rocks collected in the vicinity of the pull-apart at 125.7°W on the Heezen transform provides indirect evidence for limited magmatic intrusion associated with crustal thinning [*Lonsdale*, 1986].

Extensional offsets may also have an influence on the rate of release of seismic moment along fast slipping transforms. The maximum moment of transform earthquakes appears to decrease and the moment rate deficit increases with increasing spreading rate [*Burr and Solomon*, 1978; *Kawasaki et al.*, 1985]. The presence of fault offsets could inhibit rupture of long fault segments and limit the maximum moments of earthquakes, although it is not clear how fault offsets would affect the total moment release. The thermal and compositional effects of offsets could also be important.

Influence of Changes in Spreading Direction

Changes in plate motion may lead to the occurrence of earthquakes with anomalous mechanisms by altering fault geometry and by introducing a component of compression or extension along the fault. For instance, along the Pacific-Nazca plate boundary, a recent small clockwise rotation is inferred to have created intratransform spreading centers within large-offset, right-stepping transforms [*Lonsdale*, 1989]. Others have suggested that recent plate motion changes have occurred along the Rivera, Eltanin, and St. Paul's transforms [*Lonsdale*, 1986; *DeMets and Stein*, 1990; *J.-G. Schilling*, unpublished cruise report, 1987]. We examine whether these changes appear to have been a significant influence in the occurrence of earthquakes with anomalous mechanisms and locations.

The Pacific-Rivera magnetic lineations show that the rise crest has progressively rotated 5-15° in a clockwise direction in the last 5 m.y. [*DeMets and Stein*, 1990], putting the left-stepping Rivera transform in compression. This change in spreading direction is compatible with the apparent rotation of stresses toward transform-perpendicular compression inferred from the anomalous strike-slip earthquakes near the ridge-transform intersection. Such a change would tend to destroy extensional relay zones along the left-stepping transform, although at least one such relay zone has been suggested on the basis of seismicity and bathymetry.

Recent plate motion changes at the Eltanin may explain the occurrence of several earthquakes with normal-faulting mechanisms. Magnetic anomalies north of the Heezen transform show a 10° clockwise rotation of spreading in the past 4 m.y., which would put the right-stepping transform in extension in the

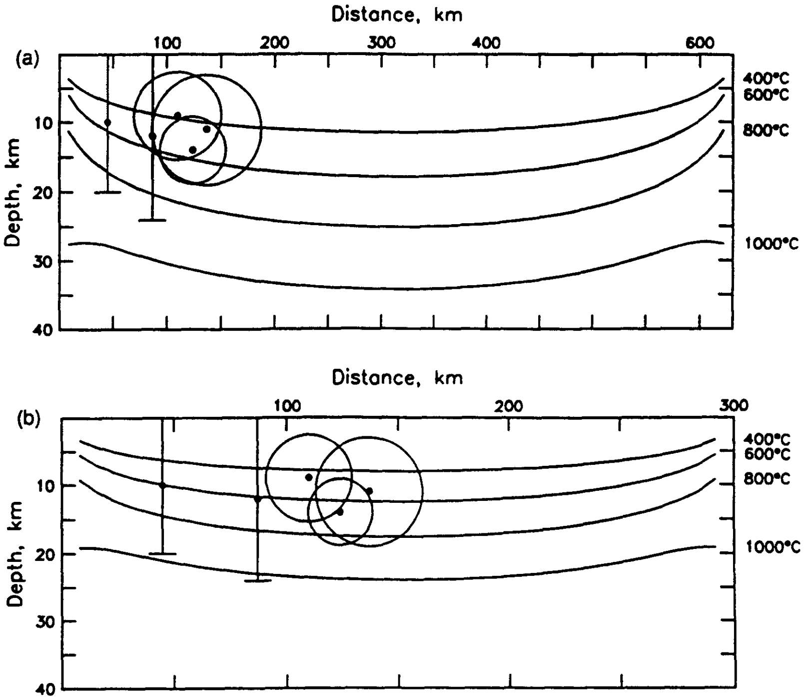

Figure 11. Centroid depths of earthquakes along the St. Paul's transform (*a*) Thermal model derived for an offset of 630 km and an age difference of 39 Ma (*b*) Thermal model derived for an offset of 300 km and an age difference of 19 Ma. Circles denote the areal extent of faulting for a circular fault model Vertical bars denote a depth extent of faulting that is twice the centroid depth. See text for further details

more recent past and would favor the development of extensional offsets [*Lonsdale*, 1986], similar to the situation along the Pacific-Nazca plate boundary.

The normal-faulting mechanisms along the Eltanin fault system and at the Menard transform may also reflect regional stresses caused by plate motion changes. Minor internal plate deformation in the past 20 m.y. near this region of the Pacific-Antarctic plate boundary has been suggested to explain the possible mismatch of fracture zones from plate reconstructions [*Stock et al.*, 1991]. Analysis of bathymetric and magnetic data [*Molnar et al.*, 1975; *Lonsdale*, 1986] and of geoid data [*Mayes et al.*, 1990] demonstrates the evolution of spreading direction in the past: the spacing between the Heezen and Tharp fracture zones decreased by 100 km due to changes in the spreading direction along the Pacific-Antarctic spreading center about 20-35 m.y. ago. The destruction of small, left-offsetting fracture zones and the creation of many small, right-offsetting fracture zones occurred during this counterclockwise change in plate motion [*Molnar et al.*, 1975], consistent with the view that transforms, particularly along fast spreading rises, are zones of weakness that can adjust readily during plate motion changes [*Menard and Atwater*, 1968]. Regional deformation may explain the occurrence of normal-faulting earthquakes with similar orientation both along the transforms and in intraplate settings, such as south of the Tharp transform.

A survey of the Mid-Atlantic Ridge north of the St. Paul's transform [*Schilling et al.*, 1987; *J.-G. Schilling*, unpublished cruise report, 1987] revealed that the morphologic grain changed orientation from about N340-350°E to 0° over the past 0.2 My and that the ridge has propagated northward from the transform, perhaps in response to a clockwise change in spreading direction and rotation of the fracture zone, as proposed by *Bonatti and Crane* [1982] for the Vema transform. The change in ridge orientation may explain the ridge-perpendicular compressive stresses indicated by earthquakes with unusual mechanisms near the western ridge-transform intersection. *J.-G. Schilling* (unpublished cruise report, 1987) has suggested that this clockwise change in orientation may have led to the development of extensional relay zones in the transform.

In summary, there is some indication that changes in plate motion are responsible for the occurrence of anomalous earthquake activity along some oceanic transforms, but further evidence is required to support this hypothesis.

Thermal Stresses

Thermal stresses generated by the differential cooling of oceanic lithosphere have been suggested as a primary cause of oceanic intraplate earthquakes on the basis of the pattern of earthquake source characteristics with depth and seafloor age [*Bratt et al.*, 1985; *Parmentier and Haxby*, 1986]. Two-dimensional models of thermal stresses predict large, ridge-parallel extensional stresses near the ridge-transform intersection [*Sandwell*, 1986; *Haxby and Parmentier*, 1988]. It has also been proposed that fracture zones form in response to such ridge-parallel extension [*Collette*, 1974; *Turcotte*, 1974]. The presence of earthquakes with mechanisms indicating that the least compressive horizontal stress is ridge-parallel in the vicinity of the ridge-transform intersections of the St. Paul's and Marathon transforms is thus consistent with a controlling influence by thermal stresses. A quantitative analysis comparing a larger set of earthquake data with appropriate three-dimensional models of thermal stress near oceanic transforms is necessary to provide a rigorous test of this hypothesis.

Evidence for a Weak Fault

As noted earlier, some oceanic and continental transforms appear to act as zones of weakness, with low shear stresses on the fault and a horizontal principal stress oriented in a nearly fault-normal direction in the lithosphere adjacent to the fault [*Zoback et al.*, 1987; *Mount and Suppe*, 1987; *Wilcock et al.*, 1990]. In this section, we consider whether transform earthquakes with anomalous mechanisms provide additional evidence for the presence of a weak fault zone.

On the St. Paul's and Marathon transforms, shallow reverse-faulting events with ridge-parallel fault strikes occur near the ridge-transform intersections. A strike-slip event with an unusual orientation occurred near the site of the reverse-faulting event at the St. Paul's transform. The mechanisms of these earthquakes indicate transform-perpendicular extension near the ridge-transform intersection. Near St. Paul's Rocks, on the other hand, the reverse-faulting focal mechanisms imply that the horizontal stresses are rotated toward transform-perpendicular compression. Differences in fault geometry and structure may account for this difference in the ordering of principal stresses. In the area of the compressive fault jog at the Owen transform, an anomalous strike-slip earthquake indicating transform-perpendicular compression occurred as an aftershock to an earthquake with mechanism compatible with transform-parallel motion. At the Eltanin transform, several normal-faulting earthquakes show an orientation of stresses similar to that of a normal-faulting intraplate earthquake that occurred 100 km south of the Tharp transform (Figure 1) and thus are more likely a response to a regional stress field. Earthquakes with anomalous strike-slip mechanisms near the Rivera transform indicate a stress field tending toward transform-perpendicular compression.

We see no strong evidence in these data to support the view that oceanic transforms are generally weaker than the surrounding lithosphere on the basis of a systematic perturbation to the regional stress field. Neither do the observations invalidate this hypothesis, however. The mechanisms of the large anomalous earthquakes in this study appear to be dominated by factors other than a systematically reduced strength on the transform. We note that no anomalous large earthquakes were found on the Kane transform, where the microearthquake experiment of *Wilcock et al.* [1990] found several events within the transform valley indicative of extension perpendicular to the transform.

CONCLUSIONS

A number of large earthquakes with mechanisms or locations inconsistent with simple models have occurred near large-offset oceanic transform faults. Much of the anomalous earthquake activity can be associated with complex fault geometry or large structural features that apparently influence slip on the fault. Compressional fault jogs associated with anomalous structures are likely responsible for earthquakes with unusual mechanisms on the Owen and St. Paul's transforms. A normal-faulting earthquake on the Heezen transform occurs at the edge of an extensional offset, and other normal-faulting earthquakes on transforms along the East-Pacific Rise may likewise be associated with extensional offsets.

Several other factors may contribute to the occurrence of such earthquakes, but we do not find strong evidence to support their influence. Recent changes in plate motion, suggested to have occurred at the Eltanin, Rivera, and St. Paul's transforms, could contribute to the presence of anomalous earthquakes by influencing fault geometry or the state of stress along the fault. Thermal stresses near ridge-transform intersections may lead to earthquakes having reverse-faulting mechanisms characterized by a ridge-parallel least compressive stress; events with such mechanisms are seen near the ridge-transform intersections of the St. Paul's and Marathon transforms. While some earthquakes show evidence for a nearly transform-perpendicular orientation of one of the principal horizontal stresses, consistent with a weak fault zone, our results do not resolve whether oceanic transforms are generally weaker than surrounding lithosphere.

APPENDIX: EARTHQUAKE SOURCE MECHANISMS FROM BODY WAVEFORM INVERSION

In this appendix we present the details of long-period *P* and *SH* waveform inversion for the 13 transform earthquakes listed in Table 1. The orientation (strike/dip/slip) of each double-couple mechanism is presented according to the convention of *Aki and Richards* [1980]. Centroid depths are given relative to the seafloor.

July 29, 1983, Owen Transform (Figure A1)

Waveform inversion for this event indicates a mechanism of 214/89/298, similar to the CMT solution of 37/71/44 [*Dziewonski et al.*, 1984], and consistent with either predominantly dip-slip motion on a nearly vertical fault oriented approximately parallel to the transform or primarily right-lateral strike-slip motion on a northeasterly dipping low-angle fault. Vertical short-period records at KEV and CHG were examined to confirm the polarity of the first pulses. The *SH* wave data for this event provide strong constraints on the unusual mechanism. The minimum residual occurs for centroid depths between 6 and 16 km.

July 7, 1986, Owen Transform (Figure A2)

The earthquake of July 7, 1986, on the Owen transform is the largest event ($M_0 = 3.7\times10^{25}$ dyn cm) in the catalogue of anomalous transform events. There is good coverage of the focal sphere, and the waveforms are best fit by a reverse-faulting solution (238/36/095) at a centroid depth of 4 km. This source mechanism is similar to the CMT solution of 242/42/098 [*Dziewonski et al.*, 1987*b*]. Solutions constrained to be shallower or deeper than 4 km have jagged source time functions and higher rms residual variances. *P* wave reverberations indicate a water depth of 4 km.

October 11, 1973, St. Paul's Transform (Figure A3)

On October 11, 1973, the ISC reported two events separated by approximately 10 s. The earlier, smaller event falls on the map trend of transform activity while the later, larger event occurred off-trend (Figure 4 and events 15 and 16 in Figure 3*b*). The unusual

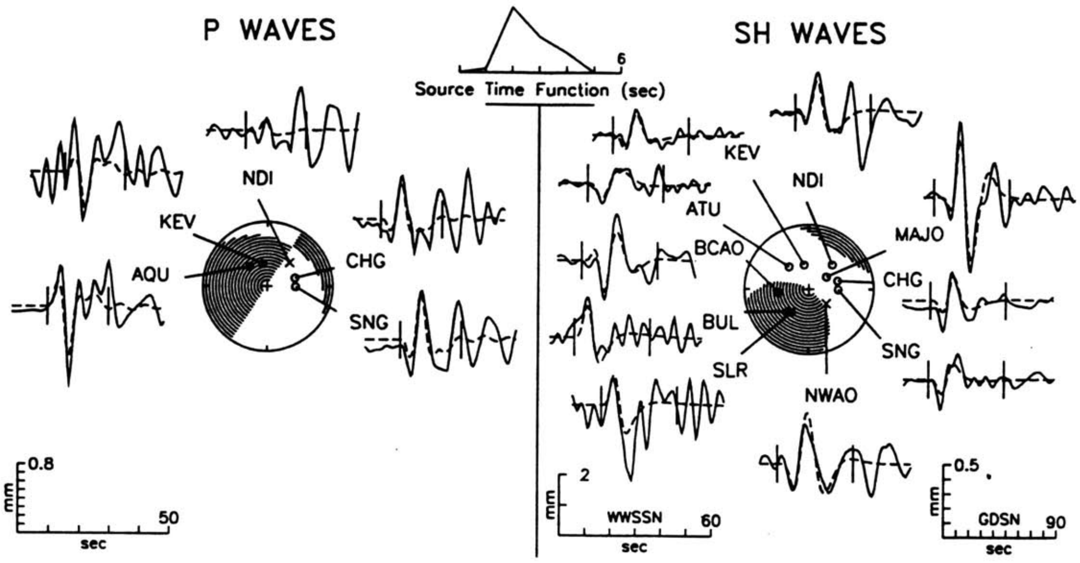

Fig. A1. Observed (solid curve) long-period *P* and *SH* waveforms from the earthquake of July 29, 1983, compared with synthetic waveforms (dashed curves) generated from the best fitting point source model found from body waveform inversion. Waveforms from GDSN stations (MAJO, NWAO, and BCAO) are plotted at the scale shown in the lower right. *P* and *SH* radiation patterns are shown on the lower focal hemisphere (equal-area projection). For *SH* waves, compression corresponds to positive motion as defined by *Aki and Richards* [1980]. All amplitudes are normalized to an epicentral distance of 40° and a WWSSN instrument magnification of 1500; the amplitude scales correspond to the waveforms that would be observed on an original seismogram from such an instrument. The two vertical lines show the portion of each time series used in the inversion. Open circles denote dilatational first motions, solid circles denote compressional first motions, and crosses denote emergent arrivals.

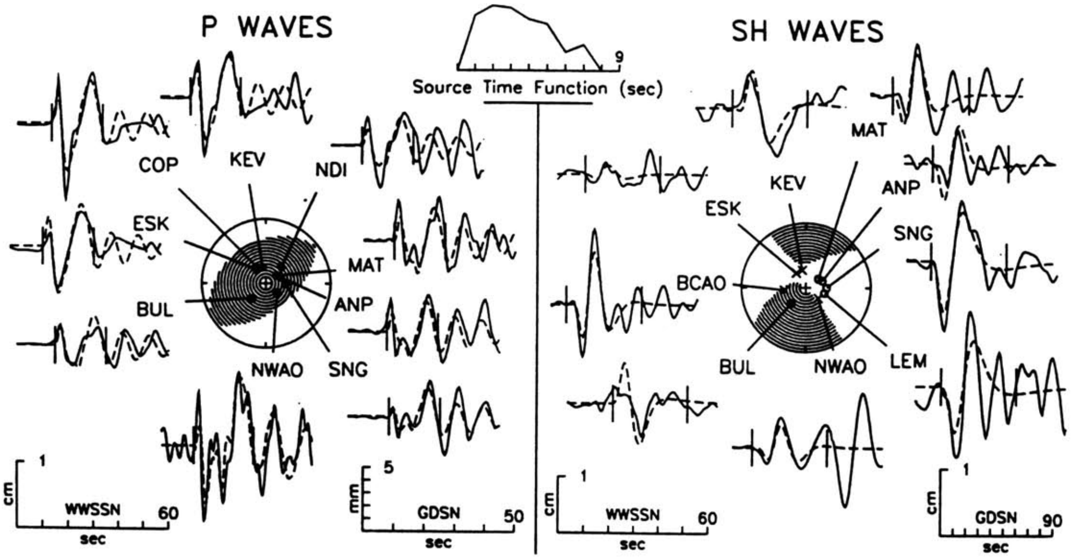

Fig. A2. Observed *P* and *SH* waveforms from the earthquake of July 7, 1986, compared with synthetic waveforms generated from the best fitting point source model found from body waveform inversion. See Figure A1 for further details.

character of these locations made body waveform analysis of these events desirable. For the smaller event, we could not resolve a mechanism, and we fixed the parameters to those of a conventional strike-slip event. For the larger event, we parameterized the STF as a horizontal rupture along the nodal plane striking at 264°. Minimization of the rms residual indicates a centroid depth in the range 9-15 km, consistent with apparent depth phases in *P* waves at ESK, IST, and JER.

November 14, 1982, St. Paul's Transform (Figure A4)

Our analysis shows that this earthquake involved almost purely strike-slip faulting, although the probable fault plane appears to depart from the vertical. This event is well fit by a simple STF at 9-13 km centroid depth. Our solution of 86/66/172 is in good agreement with the CMT solution of 85/90/180 [*Dziewonski et al.*, 1983*a*].

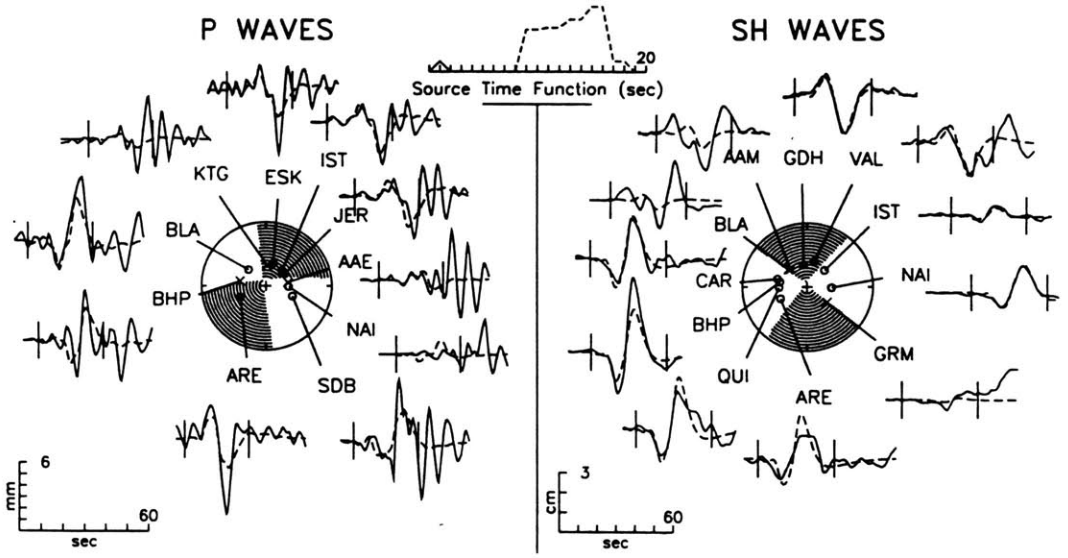

Fig. A3. Observed *P* and *SH* waves from the earthquake of October 11, 1973, compared with synthetic waveforms generated for a source model with two point sources. The parameters of the first, smaller, event were fixed in the inversion; the source parameters of the second event are found from body waveform inversion. The radiation pattern of the larger subevent is shown. See Figure A1 for further details.

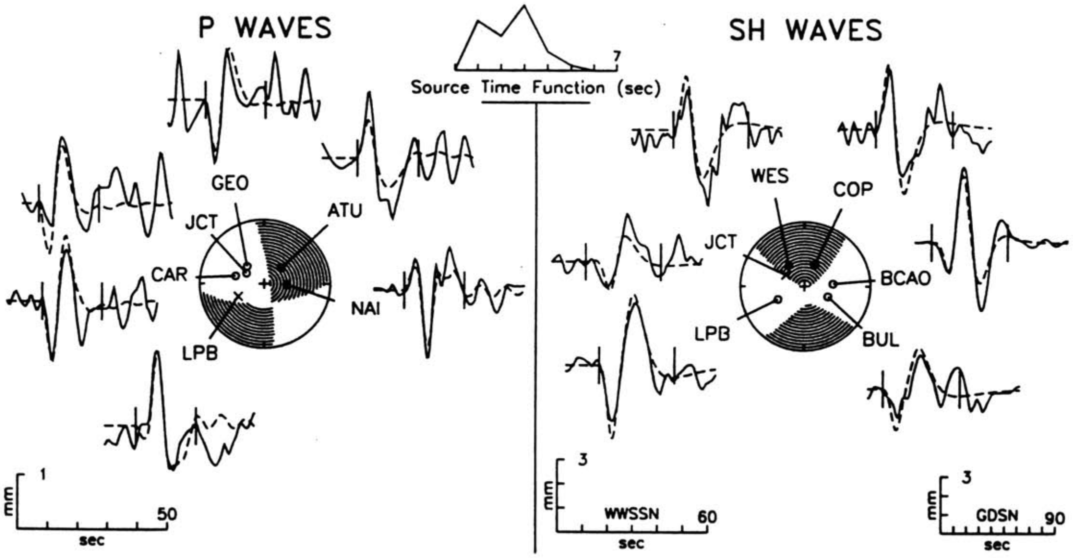

Fig. A4. Observed *P* and *SH* waveforms from the earthquake of November 14, 1982, compared with synthetic waveforms generated from the best fitting point source model found from body waveform inversion. See Figure A1 for further details.

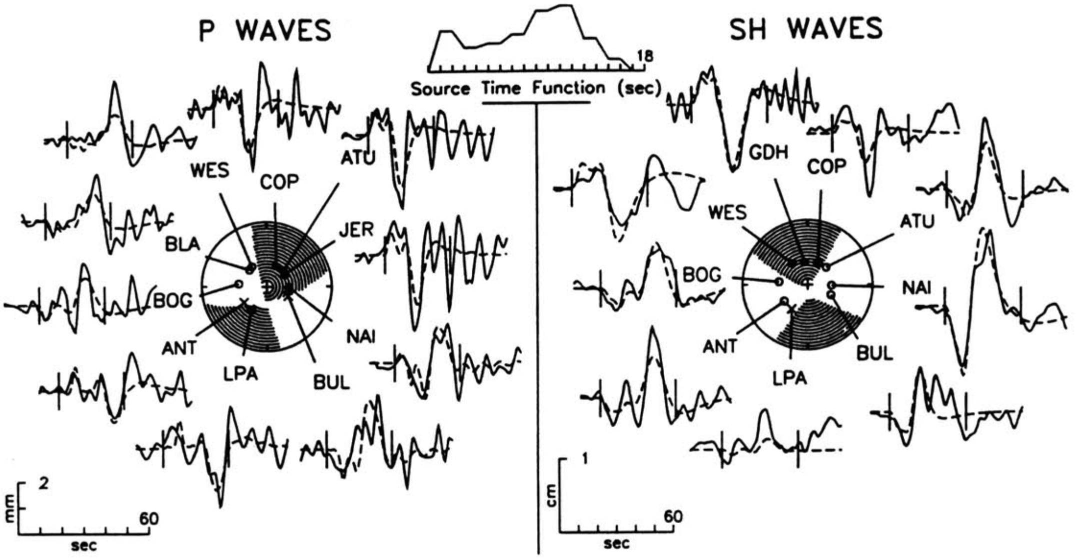

Fig. A5. Observed *P* and *SH* waveforms from the earthquake of October 12, 1985, compared with synthetic waveforms generated from the best fitting point source model found from body waveform inversion. See Figure A1 for further details.

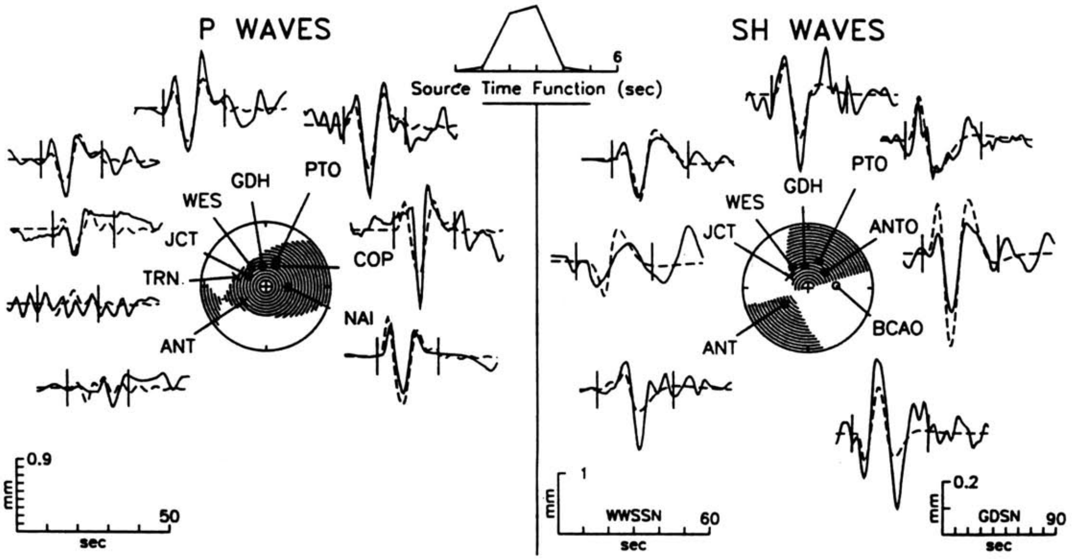

Fig. A6. Observed *P* and *SH* waveforms from the earthquake of September 20, 1986, compared with synthetic waveforms generated from the best fitting point source model found from body waveform inversion. ANTO is a GDSN station. See Figure A1 for further details.

October 12, 1985, St. Paul's Transform (Figure A5)

For this earthquake we parameterized the STF as a horizontal rupture along the nodal plane striking at 76°. Analysis of waveform data indicates a predominantly strike-slip mechanism. The minimum residual occurs at 7-13 km centroid depth. The STF length of 17 s is unusually long for an event of moment 4×10^{25} dyn cm, and the relatively high level of low-frequency excitation indicated by free oscillation amplitudes indicates that this is a slow earthquake (T.H. Jordan, personal communication, 1991). Our mechanism solution of 76/72/174 is in good agreement with the CMT solution of 83/75/179 [*Dziewonski et al.* 1986*b*].

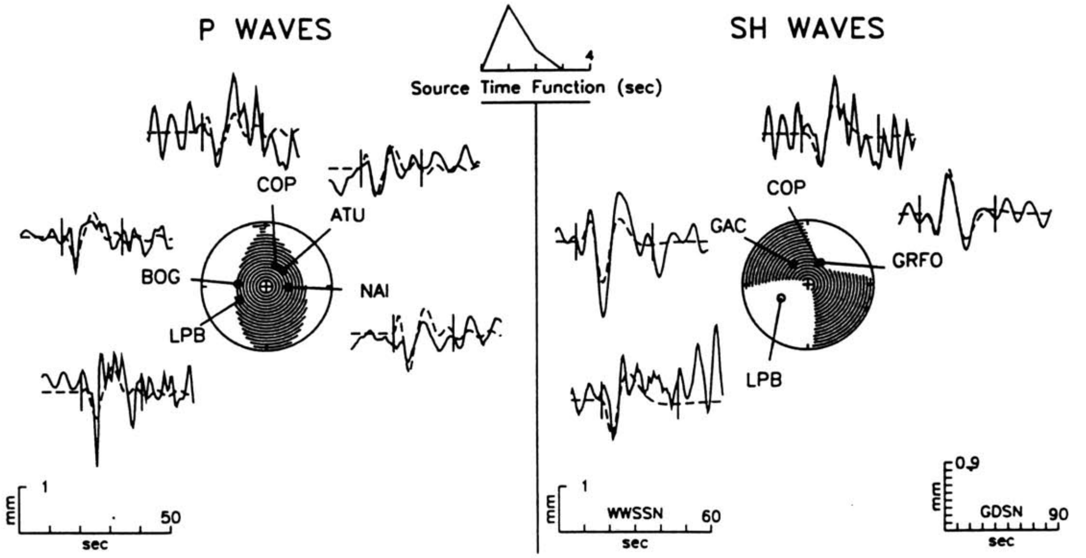

Fig. A7. Observed *P* and *SH* waveforms from the earthquake of April 20, 1988, compared with synthetic waveforms generated from the best fitting point source model found from body waveform inversion. GRFO is a GDSN station. See Figure A1 for further details.

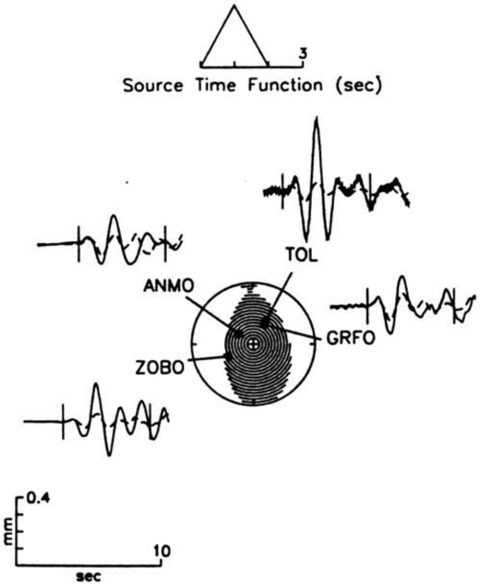

Fig. A8. Observed short-period *P* waveforms from the earthquake of April 20, 1988, compared with synthetic waveforms generated from the mechanism found from long-period body waveform inversion. All data are from GDSN stations. See Figure A1 for further details.

September 20, 1986, St. Paul's Transform (Figure A6)

Although this earthquake is located along the trend of principal seismic activity, a thrust mechanism (246/60/090) is reported in the Harvard CMT catalogue [*Dziewonski et al.*, 1987*b*]. Despite the small moment of this event, we were able to obtain good *P* and *SH* coverage of the focal sphere. The mechanism (227/53/50) obtained from body waveform inversion contains a small strike-slip component; this strike-slip motion is in the expected direction for transform slip if the southward dipping nodal plane is the fault plane. The overall fit as described by the rms residual displays a distinct minimum over the centroid depth range 12-16 km.

April 20, 1988, St. Paul's Transform (Figures A7 and A8)

Our reverse-faulting solution of 189/52/107 differs somewhat from the CMT solution of 196/78/108 [*Dziewonski et al*, 1989*b*], which has a steeper dip. The discrepancy may be attributed to the poor signal-to-noise ratio for this small event. The identification of the first pulse is ambiguous in the long-period *P* wave data (Figure A7), but compressional first motions, consistent with a thrust mechanism, are confirmed in the vertical short-period waveforms (Figure A8). For the short-period *P* wave synthetics, a value of 0.6 s is taken for t^*, and the mechanism is that from long-period waveform inversion. A centroid depth of 8 km is required by long-period data and also provides a good fit to the short-period data. Water reverberations indicate a seafloor depth of about 2.5 km.

December 23, 1988, St. Paul's Transform (Figure A9)

The Harvard CMT catalogue lists a reverse-faulting mechanism of 245/57/094 for this earthquake [*Dziewonski et al.*, 1989*c*]. Inversion of body waveforms from WWSSN records indicates a mechanism of 228/56/072, a similarly reverse-faulting solution but with different strike and slip angles from the CMT solution. Our preferred centroid depth is in the range of 7-11 km, on the basis of both the residual variance and the observed fit to the waveforms. The small first *SH* arrivals at WES and BLA provide constraints on the strike of the source mechanism.

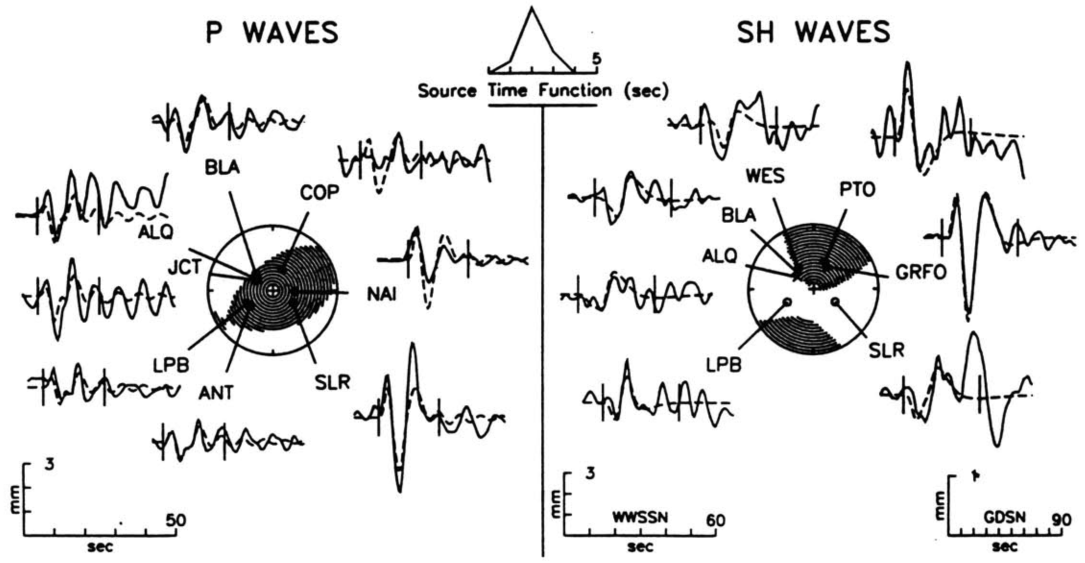

Fig. A9. Observed *P* and *SH* waveforms from the earthquake of December 23, 1988, compared with synthetic waveforms generated from the best fitting point source model found from body waveform inversion. See Figure A1 for further details.

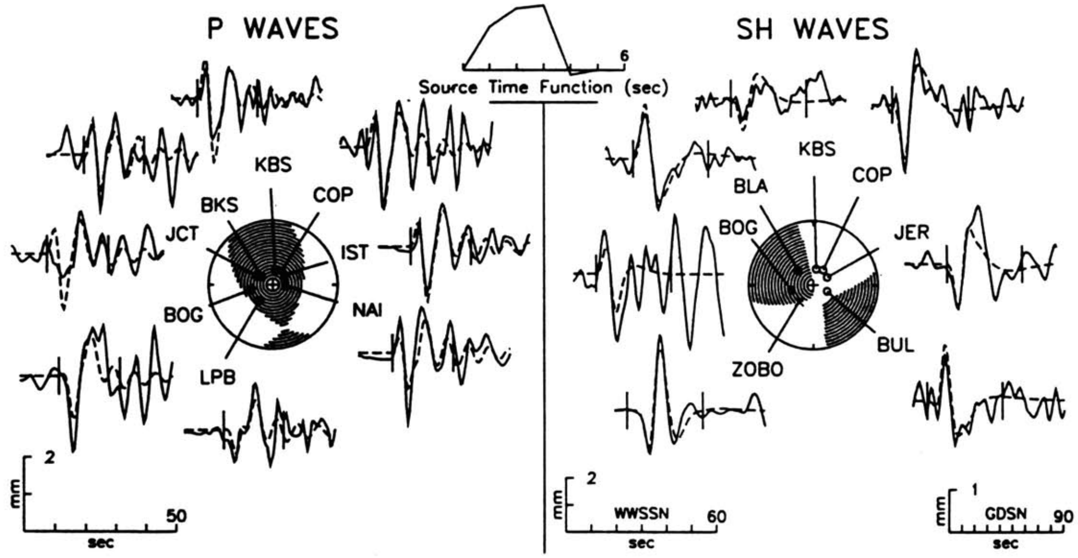

Fig. A10. Observed *P* and *SH* waveforms from the earthquake of September 22, 1985, compared with synthetic waveforms generated from the best fitting point source model found from body waveform inversion. ZOBO is a GDSN station. See Figure A1 for further details.

September 9, 1985, Marathon Transform (Figure A10)

Our mechanism solution for this event is 140/54/051, corresponding to primarily reverse faulting on a fault oblique or orthogonal to the transform. The CMT reverse-faulting solution is 196/31/111 [*Dziewonski et al,* 1986*a*]. The polarity was found to be reversed on ZOBO (*SH*). This is a well-fit shallow event, with a centroid depth of 3-5 km, as required by a minimization of the rms residual.

February 17, 1978, Heezen Transform (Figure A11)

Although coverage is sparse and the signal-to-noise ratio is low, the combination of both *P* and *S* waveforms suggests a mechanism

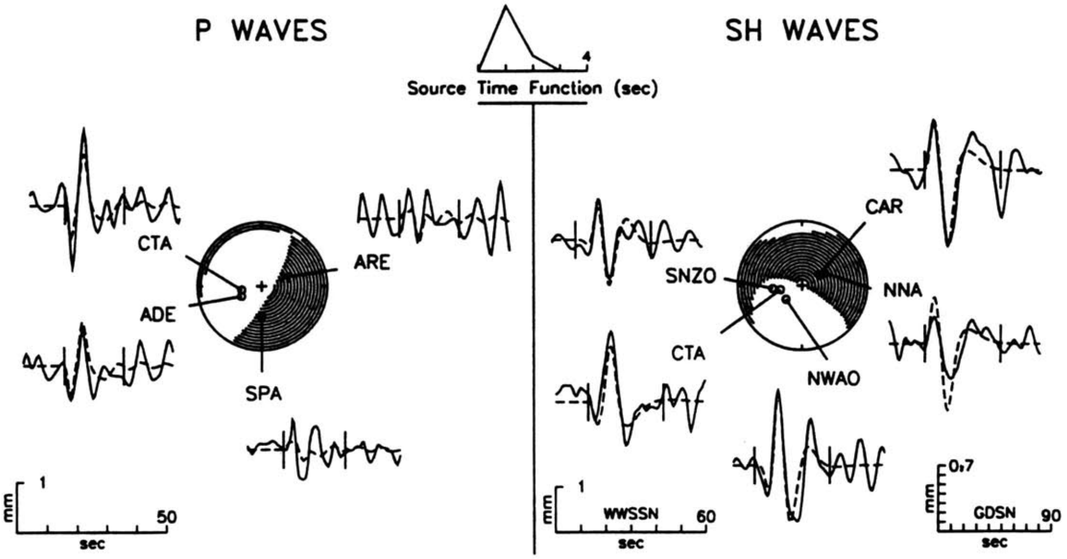

Fig. A11. Observed *P* and *SH* waveforms from the earthquake of February 17, 1978, compared with synthetic waveforms generated from the best fitting point source model found from body waveform inversion. SNZO is a GDSN station. See Figure A1 for further details.

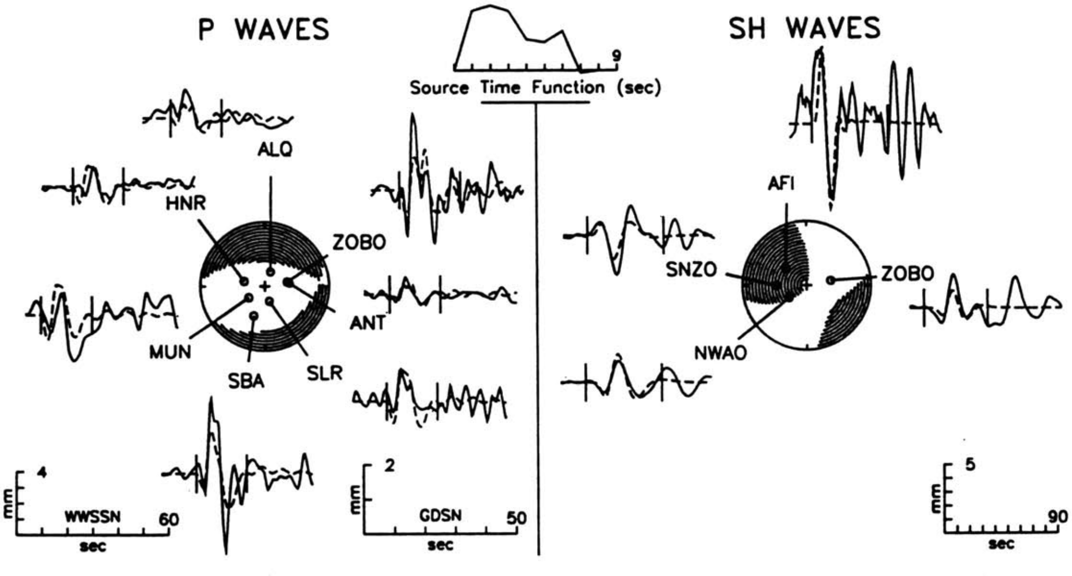

Fig. A12. Observed *P* and *SH* waveforms from the earthquake of May 27, 1989, compared with synthetic waveforms generated from the best fitting point source model found from body waveform inversion. AFI is a GDSN station. See Figure A1 for further details.

of 241/16/301, which has a smaller dip and a larger strike-slip component than the CMT mechanism of 256/34/287 [*Dziewonski et al.*, 1987*c*]. The best fitting centroid depth ranges from 8 to 14 km, but *P* wave coverage is poor. The predicted polarity of *P* wave first motions is in agreement with short-period records.

May 27, 1989, Tharp Transform (Figure A12)

Our normal-faulting solution of 275/59/287 is similar to the CMT mechanism of 258/57/277 [*Dziewonski et al.*, 1990*b*]. Examination of short-period records shows that this event has a

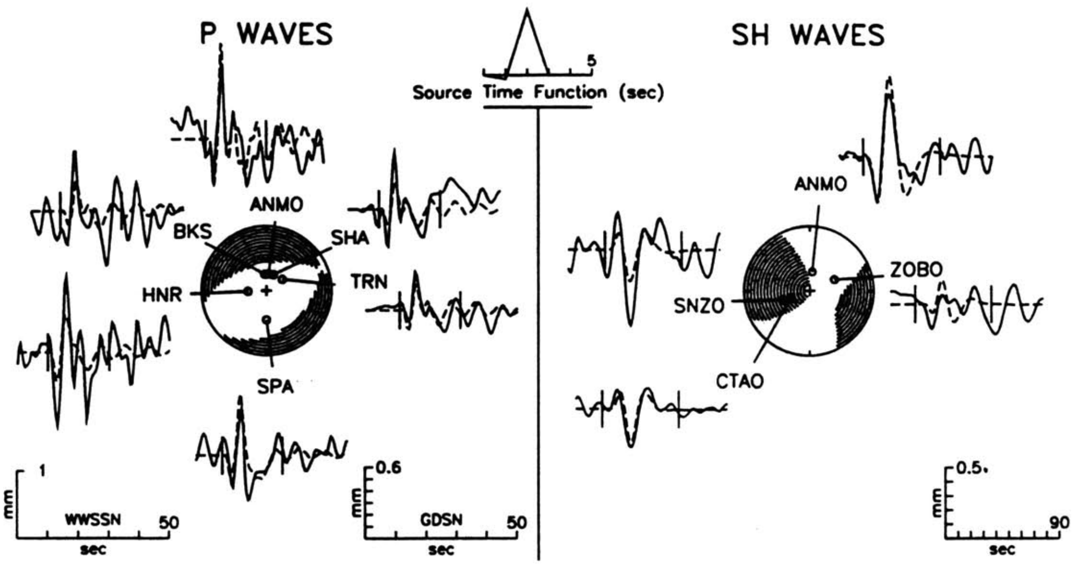

Fig. A13. Observed *P* and *SH* waveforms from the earthquake of May 15, 1987, compared with synthetic waveforms generated from the best fitting point source model found from body waveform inversion. CTAO and ANMO are GDSN stations. See Figure A1 for further details.

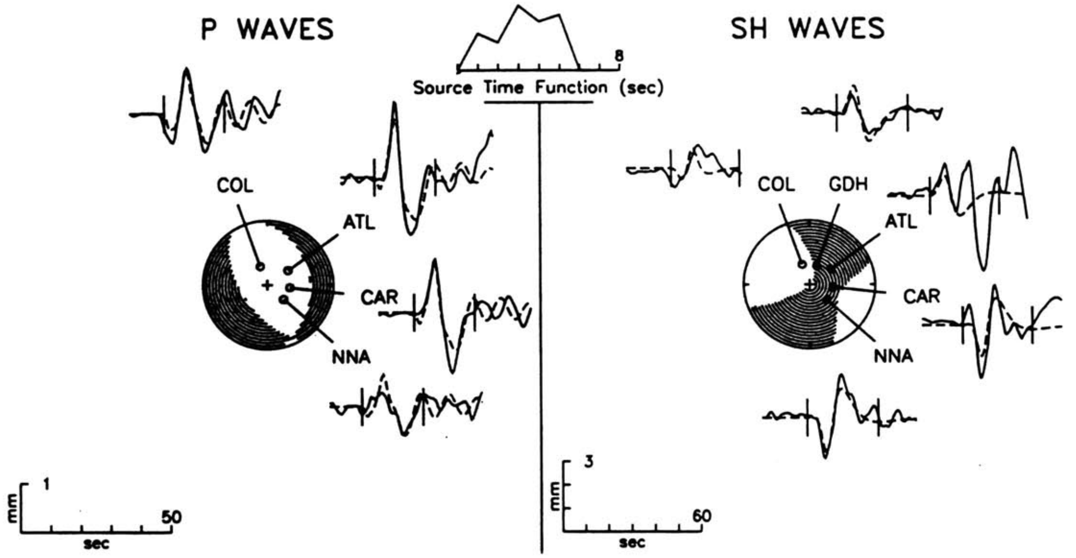

Fig. A14. Observed *P* and *SH* waveforms from the earthquake of September 21, 1977, compared with synthetic waveforms generated from the best fitting point source model found from body waveform inversion. See Figure A1 for further details.

precursor that is not evident in the long-period records, although there are high noise levels on long-period records prior to the onset of the *P* wave of the main event. Our best fitting centroid depth is approximately 10 km, but the *P* wave signal-to-noise ratio is poor.

May 15, 1987, Menard Transform (Figure A13)

We find a normal-faulting mechanism of 50/37/247, in agreement with the CMT solution of 53/37/260 [*Dziewonski et al.*, 1988*b*]. The dilatational first motions are confirmed by examination of short-period vertical records. Centroid depth is within the range 7-11 km, but the *P* wave signal-to-noise ratio is low.

September 21, 1977, Rivera Transform (Figure A14)

We find a normal-faulting mechanism of 353/35/291. The CMT mechanism is 346/72/254 [*Dziewonski et al.*, 1987*a*]. The preferred centroid depth is 4 km, but the *P* wave signal-to-noise ratio is low.

Acknowledgements. We thank Jim Cochran, Peter Hunter, Peter Lonsdale, and Jean-Guy Schilling for providing survey data for individual transforms. We also thank Geoff Abers, Göran Ekström, Tom Jordan, and Bob Woodward for helpful information and Marcia McNutt for contributing support for this project. Jian Lin, Aristeo Pelayo, and Anne Tréhu provided constructive reviews. This research was supported by the National Science Foundation under grant EAR-9004750 and the National Aeronautics and Space Administration under grants NAG5-1921 and NAG5-2206.

REFERENCES

Aki, K., and P. G. Richards, *Quantitative Seismology: Theory and Methods*, vol 1, p. 114, W.H. Freeman, New York, 1980.

Anderson, E M , *The Dynamics of Faulting and Dyke Formation With Applications to Britain*, 2nd ed., 206 pp , Oliver and Boyd, Edinburgh, 1951

Anderson, R. S., Evolution of the northern Santa Cruz Mountains by advection of crust past a San Andreas fault bend, *Science*, *249*, 397-401, 1990.

Barka, A. A , and K Kadinsky-Cade, Strike-slip fault geometry in Turkey and its influence on earthquake activity, *Tectonics*, *7*, 663-684, 1988.

Bergman, E. A., and S. C. Solomon, Transform fault earthquakes in the North Atlantic: Source mechanisms and depth of faulting, *J. Geophys. Res*, *93*, 9027-9057, 1988.

Bergman, E. A., and S C. Solomon, Earthquake swarms on the Mid-Atlantic Ridge Products of magmatism or extensional tectonics?, *J. Geophys. Res.*, *95*, 4943-4965, 1990.

Bergman, E A , J.L Nabelek, and S. C. Solomon, An extensive region of off-ridge normal-faulting earthquakes in the southern Indian Ocean, *J. Geophys Res.*, 89, 2425-2443, 1984

Bilham, R , and G. King, The morphology of strike-slip faults: Examples from the San Andreas fault, California, *J. Geophys. Res.*, *94*, 10,204-10,216, 1989

Bonatti, E., Vertical tectonism in oceanic fracture zones, *Earth Planet. Sci Lett.*, *37*, 369-379, 1978

Bonatti, E., Subcontinental mantle exposed in the Atlantic Ocean on St Peter-Paul islets, *Nature*, *345*, 800-802, 1990.

Bonatti, E , and K. Crane, Oscillatory spreading explanation of anomalously old uplifted crust near oceanic transforms, *Nature*, *300*, 343-345, 1982

Bonatti, E , and P. R. Hamlyn, Mantle uplifted block in the western Indian Ocean, *Science*, *201*, 249-251, 1978.

Bowen, A. N., and R. S. White, Deep-tow seismic profiles from the Vema transform and ridge-transform intersection, *J. Geol. Soc. London*, *143*, 807-817, 1986.

Bratt, S. R., E. A. Bergman, and S.C. Solomon, Thermoelastic stress: How important as a cause of earthquakes in young oceanic lithosphere?, *J. Geophys. Res.*, *90*, 10,249-10,260, 1985

Brune, J. N , T. L Henyey, and R. F. Roy, Heat flow, stress, and rate of slip along the San Andreas fault, California, *J. Geophys. Res.*, *74*, 3821-3827, 1969.

Burr, N. C., and S. C. Solomon, The relationship of source parameters of oceanic transform earthquakes to plate velocity and transform length, *J. Geophys. Res.*, *83*, 1193-1205, 1978.

Byerlee, J., Friction of rocks, *Pure Appl. Geophys.*, *116*, 615-626, 1978.

Cochran, J. R., The Gulf of Aden: Structure and evolution of a young ocean basin and continental margin, *J. Geophys. Res.*, *86*, 263-287, 1981.

Cochran, J. R., Somali Basin, Chain Ridge, and origin of the northern Somali Basin gravity and geoid low, *J. Geophys. Res.*, *93*, 11,985-12,008, 1988.

Collette, B. J., Thermal contraction joints in a spreading seafloor as origin of fracture zones, *Nature*, *251*, 299-300, 1974.

Collette, B. J., A. P. Slootweg, and W. Twigt, Mid-Atlantic Ridge crest topography between 12° and 15° N, *Earth Planet. Sci. Lett.*, *42*, 103-108, 1979.

Collette, B. J., J. Verhoef, and A. F. J. de Mulder, Gravity and a model of the median valley, *J. Geophys.*, *47*, 91-98, 1980.

Collette, B. J., A. P. Slootweg, J. Verhoef, and W. R. Roest, Geophysical investigations of the floor of the Atlantic Ocean between 10° and 38°N (Kroonvlag-project), *Proc. K. Ned. Akad. Wet., Ser. B*, *87*, 1-76, 1984.

Dauphin, J. P., and G. E. Ness, Bathymetry of the gulf and peninsular province of the Californias, *AAPG Mem.*, *47*, 21-23, 1991.

DeMets, C., and S. Stein, Present-day kinematics of the Rivera plate and implications for tectonics in southwestern Mexico, *J. Geophys. Res.*, *95*, 21,931-21,948, 1990.

DeMets, C., R. G. Gordon, D. F. Argus, and S. Stein, Current plate motions, *Geophys. J. Int.*, *101*, 425-478, 1990.

Dziewonski, A. M., and J. H. Woodhouse, An experiment in systematic study of global seismicity: Centroid-moment tensor solutions for 201 moderate and large earthquakes in 1981, *J. Geophys. Res.*, *88*, 3247-3271, 1983.

Dziewonski, A. M., T. A. Chou, and J. H. Woodhouse, Determination of earthquake source parameters from waveform data for studies of global and regional seismicity, *J. Geophys. Res.*, *86*, 2825-2852, 1981.

Dziewonski, A. M., A. Friedman, D. Giardini, and J. H. Woodhouse, Global seismicity of 1982: Centroid-moment tensor solutions for 308 earthquakes, *Phys. Earth Planet. Inter.*, *33*, 76-90, 1983*a*.

Dziewonski, A. M., J. E. Franzen, and J. H. Woodhouse, Centroid-moment tensor solutions for April-June 1983, *Phys. Earth Planet. Inter.*, *33*, 243-249, 1983*b*.

Dziewonski, A. M., J. E. Franzen, and J. H. Woodhouse, Centroid-moment tensor solutions for July-September 1984, *Phys. Earth Planet Inter.*, *34*, 1-8, 1984.

Dziewonski, A. M., J. E. Franzen, and J. H. Woodhouse, Centroid-moment tensor solutions for October-December 1984, *Phys. Earth Planet. Inter.*, *39*, 147-156, 1985

Dziewonski, A. M., J. E. Franzen, and J. H. Woodhouse, Centroid-moment tensor solutions for July-September 1985, *Phys. Earth Planet Inter.*, *42*, 205-214, 1986*a*.

Dziewonski, A. M., J. E. Franzen, and J. H. Woodhouse, Centroid-moment tensor solutions for October-December 1985, *Phys. Earth Planet. Inter.*, *43*, 185-195, 1986*b*.

Dziewonski, A. M., G. Ekström, J. E. Franzen, and J H Woodhouse, Global seismicity of 1977: Centroid-moment tensor solutions for 471 earthquakes, *Phys. Earth Planet Inter.*, *45*, 11-36, 1987*a*

Dziewonski, A. M., G Ekström, J E Franzen, and J H. Woodhouse, Centroid-moment tensor solutions for July-September 1986, *Phys. Earth Planet. Inter.*, *46*, 305-315, 1987*b*

Dziewonski, A. M., G. Ekström, J. E Franzen, and J. H. Woodhouse, Global seismicity of 1978: Centroid-moment tensor solutions for 512 earthquakes, *Phys. Earth Planet Inter.*, *46*, 316-342, 1987*c*.

Dziewonski, A. M., G. Ekström, J. E. Franzen, and J. H. Woodhouse, Global seismicity of 1980: Centroid-moment tensor solutions for 515 earthquakes, *Phys. Earth Planet. Inter.*, *50*, 127-154, 1988*a*.

Dziewonski, A. M., G. Ekström, J H. Woodhouse, and G. Zwart, Centroid-moment tensor solutions for April-June 1987, *Phys. Earth Planet. Inter.*, *50*, 215-225, 1988*b*

Dziewonski, A. M., G. Ekström, J. E. Franzen, and J. H. Woodhouse, Global seismicity of 1982 and 1983: Additional centroid-moment tensor solutions for 553 earthquakes, *Phys. Earth Planet. Inter.*, *53*, 17-45, 1988*c*

Dziewonski, A. M., G. Ekström, J. H. Woodhouse, and G. Zwart, Centroid-moment tensor solutions for October-December 1987, *Phys. Earth Planet. Inter.*, *54*, 10-21, 1989*a*

Dziewonski, A M., G. Ekstrom, J. H. Woodhouse, and G. Zwart, Centroid-moment tensor solutions for April-June 1988, *Phys. Earth Planet. Inter.*, *54*, 199-209, 1989*b*

Dziewonski, A. M., G. Ekström, J. H Woodhouse, and G. Zwart, Centroid-moment tensor solutions for October-December 1988, *Phys. Earth Planet. Inter.*, *57*, 179-191, 1989*c*.

Dziewonski, A. M., G. Ekström, J. H. Woodhouse, and G. Zwart, Centroid-moment tensor solutions for January-March 1989, *Phys. Earth Planet. Inter.*, *59*, 233-242, 1990*a*.

Dziewonski, A. M., G. Ekström, J. H. Woodhouse, and G. Zwart, Centroid-moment tensor solutions for April-June 1989, *Phys. Earth Planet. Inter.*, *60*, 243-253, 1990*b*

Dziewonski, A. M., G. Ekström, J. H. Woodhouse, and G. Zwart, Centroid-moment tensor solutions for October-December 1989, *Phys. Earth Planet. Inter.*, *62*, 194-207, 1990*c*.

Dziewonski, A. M., G. Ekström, J. H. Woodhouse, and G. Zwart, Centroid-moment tensor solutions for October-December 1990, *Phys. Earth Planet. Inter.*, *68*, 201-204, 1991.

Ebel, J. E., L. J. Burdick, and G. S. Stewart, The source mechanism of the

August 7, 1966 El Golfo earthquake, *Bull. Seismol. Soc. Am.*, *68*, 1281-1292, 1978.

Ekström, G., A very broad band inversion method for the recovery of earthquake source parameters, *Tectonophysics*, *166*, 73-100, 1989.

Engeln, J. F., D. A. Wiens, and S. Stein, Mechanisms and depths of Atlantic transform earthquakes, *J. Geophys. Res.*, *91*, 548-577, 1986.

Fornari, D. J., D. G. Gallo, M. H. Edwards, J. A. Madsen, M. R. Perfit, and A. N. Shor, Structure and topography of the Siqueiros transform fault system: Evidence for the development of intra-transform spreading centers, *Mar. Geophys. Res.*, *11*, 263-300, 1989.

Fox, P. J., and D. G. Gallo, A tectonic model for ridge-transform-ridge plate boundaries: Implications for the structure of oceanic lithosphere, *Tectonophysics*, *104*, 205-242, 1984.

Fox, P. J., and D. G. Gallo, The geology of North Atlantic transform plate boundaries and their aseismic extensions, in *The Geology of North America*, vol. M, *The Western North Atlantic Region*, edited by P. R. Vogt and B. E Tuckolke, pp. 157-172, Geological Society of America, Boulder, Colo., 1986.

Francis, T. J. G., I. T. Porter, and R. C. Lilwall, Microearthquakes near the eastern end of St. Paul's Fracture Zone, *Geophys. J. R. Astron. Soc.*, *53*, 201-217, 1978.

Froidevaux, C., Energy dissipation and geometric structure at spreading plate boundaries, *Earth Planet. Sci. Lett.*, *20*, 419-424, 1973.

Futterman, W. I., Dispersive body waves, *J. Geophys. Res.*, *67*, 5279 -5291, 1962.

Gallo, D., P. J. Fox, and K. C. Macdonald, A Sea Beam investigation of the Clipperton transform fault: The morphotectonic expression of a fast-slipping transform boundary, *J. Geophys. Res.*, *91*, 3455-3467, 1986.

Goff, J. A., E A. Bergman, and S. C. Solomon, Earthquake source mechanisms and transform fault tectonics in the Gulf of California, *J. Geophys. Res.*, *92*, 10,485-10,510, 1987

Harvey, D., and G. L. Choy, Broad-band deconvolution of GDSN data, *Geophys. J. R. Astron. Soc.*, *69*, 659-668, 1982.

Haxby, W. F., and E. M. Parmentier, Thermal contraction and the state of stress in the oceanic lithosphere, *J. Geophys. Res.*, *93*, 6419-6429, 1988.

Huang, P. Y., S C. Solomon, E. A. Bergman, and J. L. Nabelek, Focal depths and mechanisms of Mid-Atlantic Ridge earthquakes from body waveform inversion, *J. Geophys. Res.*, *91*, 579-598, 1986

Jones, L., Focal mechanisms and the state of stress on the San Andreas fault in southern California, *J. Geophys. Res.*, *93*, 8869–8891, 1988.

Jordan, T. H., and K. A. Sverdrup, Teleseismic location techniques and their applications to earthquake clusters in the south-central Pacific, *Bull Seismol. Soc. Am.*, *71*, 1105-1130, 1981.

Kawasaki, I., Y. Kawahara, I. Takata, and N. Kosugi, Mode of seismic moment release at transform faults, *Tectonophysics*, *118*, 313-327, 1985.

King, G., and J. Nabelek, Role of fault bends in the initiation and termination of earthquake rupture, *Science*, *228*, 984-987, 1985.

Klitgord, K., and J. Mammerickx, Northern East Pacific Rise: Magnetic anomaly and bathymetric framework, *J. Geophys. Res.*, *87*, 6725-6750, 1982.

Lachenbruch, A. H., and J. H. Sass, Heat flow and energetics of the San Andreas fault zone, *J. Geophys. Res.*, *85*, 6185-6222, 1980.

Lachenbruch, A. H., and G. A. Thompson, Oceanic ridges and transform faults: Their intersection angles and resistance to plate motion, *Earth Planet. Sci. Lett.*, *15*, 116-122, 1972.

Laughton, A. S., R. B. Whitmarsh, and M. T. Jones, The evolution of the Gulf of Aden, *Philos. Trans. R. Soc. London, Ser. A.*, *267*, 227-266, 1970.

Lonsdale, P., Tectonic and magmatic ridges in the Eltanin fault system, south Pacific, *Mar. Geophys. Res.*, *8*, 203-242, 1986.

Lonsdale, P., Segmentation of the Pacific-Nazca spreading center, 1° N-20° S, *J. Geophys. Res.*, *94*, 12,197-12,225, 1989.

Lonsdale, P., Structural patterns of the Pacific floor offshore of peninsular California, *AAPG Mem.*, *47*, 87-125, 1991.

Louden, K. E., R. S. White, C. G. Potts, and D. W. Forsyth, Structure and seismotectonics of the Vema Fracture Zone, Atlantic Ocean, *J. Geol. Soc. London*, *143*, 795-805, 1986.

Macdonald, K. C., K. Kastens, S. Miller, and F. N. Spiess, Deep-tow studies of the Tamayo transform fault, *Mar. Geophys. Res.*, *4*, 37-70, 1979.

Macdonald, K. C., D. A. Castillo, S. P. Miller, P. Fox, K.A. Kastens, and E. Bonatti, Deep-tow studies of the Vema Fracture Zone, 1: Tectonics of a major slow slipping transform fault and its intersection with the Mid-Atlantic Ridge, *J. Geophys. Res.*, *91*, 3334-3354, 1986.

Madsen, J. A., P. J. Fox, and K. C. Macdonald, Morphotectonic fabric of the Orozco transform fault: Results from a Sea Beam investigation, *J. Geophys. Res.*, *91*, 3439-3454, 1986.

Mammerickx, J., S. M. Smith, I. L. Taylor, and T. E. Chase, Topography of the South Pacific, map, Scripps Inst. Oceanogr., Univ. of Calif., San Diego, La Jolla, 1975.

Matthews, D. H., The Owen Fracture Zone and the northern end of the Carlsberg Ridge, *Philos. Trans. R. Soc. London, Ser. A*, *259*, 172-197, 1966.

Mayes, C. L., L. A. Lawver, and D. T. Sandwell, Tectonic history and new isochron chart of the South Pacific, *J. Geophys. Res.*, *95*, 8543-8568, 1990.

McKenzie, D. P., The relation between fault plane solutions for earthquakes and the directions of the principal stresses, *Bull. Seismol. Soc. Am.*, *59*, 591-601, 1969.

McNally, K. C., T. Lay, M. Protti-Quesada, G. Valensise, D. Orange, and R. S. Anderson, Santa Cruz Mountains (Loma Prieta) earthquake, *Eos Trans. AGU*, *70*, 1463, 1467, 1989.

Melson, W. G., S. R. Hart, and G. Thompson, St. Paul's rocks, equatorial Atlantic: Petrogenesis, radiometric ages and implications on sea-floor spreading, *Mem. Geol. Soc. Am.*, *132*, 241-272, 1972.

Menard, H. W., and T. Atwater, Changes in direction of sea floor spreading, *Nature*, *219*, 463-467, 1968.

Molnar, P., T. Atwater, J. Mammerickx, and S. M. Smith, Magnetic anomalies, bathymetry and the tectonic evolution of the South Pacific since the late Cretaceous, *Geophys. J. R. Astron. Soc.*, 40, 383-420, 1975.

Mount, V. S., and J. Suppe, State of stress near the San Andreas fault: Implications for wrench tectonics, *Geology*, *15*, 1143-1146, 1987.

Nabelek, J. L., Determination of earthquake source parameters from inversion of body waves, Ph.D. thesis, 346 pp., Mass. Inst. of Technol., Cambridge, 1984.

Nabelek, J., W.-P. Chen, and H. Ye, The Tangshan earthquake sequence and its implications for the evolution of the North China Basin, *J. Geophys. Res.*, *92*, 12,615-12,628, 1987.

Ness, G. E., and M. W. Lyle, A seismo-tectonic map of the gulf and peninsular province of the Californias, *AAPG Mem.*, *47*, 71-77, 1991.

Parmentier, E. M., and W F. Haxby, Thermal stresses in the oceanic lithosphere: Evidence from geoid anomalies at fracture zones, *J. Geophys Res.*, *91*, 7193-7204, 1986.

Parsons, B., and J. G. Sclater, An ananlysis of the variation of ocean floor bathymetry and heat flow with age, *J. Geophys. Res.*, *82*, 803-827, 1977.

Phipps Morgan, J., and D. W. Forsyth, Three-dimensional flow and temperature perturbations due to a transform offset: Effects on oceanic crustal and upper mantle structure, *J. Geophys. Res.*, *93*, 2955-2966, 1988.

Phipps Morgan, J., and E. M. Parmentier, Lithospheric stress near a ridge-transform intersection, *Geophys. Res. Lett.*, *11*, 113-116, 1984.

Prothero, W. A., and I. D. Reid, Microearthquakes on the East Pacific Rise at 21° N and the Rivera Fracture Zone, *J. Geophys. Res.*, *87*, 8509-8518, 1982.

Sandwell, D. T., Thermal stress and the spacings of transform faults, *J. Geophys. Res.*, *91*, 6405-6417, 1986.

Saucier, F. J., E. D. Humphreys, and R. J. Weldon, Stress near geometrically complex strike-slip faults: Application to the San Andreas fault at Cajon Pass, southern California, *J. Geophys. Res.*, *97*, 5081-5094, 1992.

Schilling, J.-G., B. McCully, and H. Bougault, Mid-Atlantic Ridge volcanism in the equatorial region (3°S-5°N) (abstract), *Eos Trans. AGU*, *68*, 1508, 1987.

Segall, P., and D. D. Pollard, Mechanics of discontinuous faults, *J. Geophys. Res.*, *85*, 4337-4350, 1980.

Sibson, R. H., Stopping of earthquake ruptures at dilational fault jogs, *Nature*, *316*, 248-251, 1985.

Sibson, R. H., Rupture interaction with fault jogs, in *Earthquake Source Mechanics, Geophys. Monogr. Ser.*, vol. 37, edited by S. Das, J. Boatwright, and C. H. Scholz, pp. 157-167, AGU, Washington, D. C., 1986

Sinton, J. M., Ultramafic inclusions and high-pressure xenocrysts in submarine basanitoid, equatorial Mid-Atlantic Ridge, *Contrib. Mineral. Petrol*, *70*, 49-57, 1979.

Stein, C. A., and J. R. Cochran, The transition between Sheba Ridge and Owen Basin: Rifting of old oceanic lithosphere, *Geophys. J. R. Astron. Soc., 81*, 47-74, 1985.

Stein, S., A model for the relation between spreading rate and oblique spreading, *Earth Planet. Sci. Lett., 39*, 313-318, 1978.

Stein, S., and D. A. Wiens, Depth determination for shallow teleseismic earthquakes: Methods and results, *Rev. Geophys., 24*, 806-832, 1986.

Stewart, L. M., and E. A. Okal, Seismicity and aseismic slip along the Eltanin Fracture Zone, *J. Geophys. Res., 88*, 10,495-10,507, 1983.

Stock, J. M., K. M. Marks, and F. R. Schult, Mismatch of fracture zones across the Pacific-Antarctic Ridge (abstract), *Eos Trans. AGU, 72 (44)*, Fall Meeting, suppl., 444, 1991.

Sykes, L. R., Mechanism of earthquakes and nature of faulting on the mid-oceanic ridges, *J. Geophys. Res., 72*, 2131-2153, 1967.

Sylvester, A. G., Strike-slip faults, *Geol. Soc. Am. Bull., 100*, 1666-1703, 1988.

Tréhu, A. M., and G. M Purdy, Crustal structure in the Orozco transform zone, *J. Geophys. Res., 89*, 1834-1842, 1984.

Tréhu, A. M., and S. C. Solomon, Earthquakes in the Orozco transform zone: Seismicity, source mechanisms, and tectonics, *J. Geophys. Res., 88*, 8203-8255, 1983.

Turcotte, D. L., Are transform faults thermal contraction cracks?, *J. Geophys. Res., 79*, 2573-2577, 1974.

Whitmarsh, R. B., The Owen Basin off the southeast margin of Arabia, *Geophys. J R. Astron Soc., 58*, 441-470, 1979.

Wiens, D. A., and D. E. Petroy, The largest recorded earthquake swarm: Intraplate faulting near the Southwest Indian Ridge, *J. Geophys. Res., 95*, 4735-4750, 1990.

Wilcock, W. S. D., G. M. Purdy, and S. C. Solomon, Microearthquake evidence for extension across the Kane transform fault, *J. Geophys. Res., 95*, 15,439-15,462, 1990.

Wilson, J. T., A new class of faults and their bearing on continental drift, *Nature, 207*, 343-347, 1965.

Zoback, M. D., et al., New evidence on the state of stress of the San Andreas fault system, *Science, 238*, 1105-1111, 1987.

E. A. Bergman, U.S. Geological Survey, P.O. Box 25046, Mail Stop 967, Denver Federal Center, Denver, CO 80225.

S. C. Solomon, Department of Terrestrial Magnetism, Carnegie Institution of Washington, 5241 Broad Branch Road, N. W., Washington, DC 20015.

C. J. Wolfe, Department of Earth, Atmospheric, and Planetary Sciences, Room 54-822, Massachusetts Institute of Technology, Cambridge, MA 02139.

(Received March 27, 1992;
revised March 23, 1993;
accepted April 1, 1993.)

CHAPTER 4

MICROEARTHQUAKES AND CRUSTAL VELOCITY STRUCTURE AT 29°N ON THE MID-ATLANTIC RIDGE: THE ARCHITECTURE OF A SLOW-SPREADING SEGMENT

ABSTRACT

We report the results of a 41-day microearthquake experiment conducted along the southern half of a segment at 29°N on the Mid-Atlantic Ridge. Hypocenters were determined for 235 microearthquakes, with 106 of these resolving focal depths. Microearthquakes clustered in three separate along-axis regions: (1) the southern distal end near 28°55'N, (2) the central along-axis topographic high near 29°11'N, slightly north of the Broken Spur hydrothermal vent field, and (3) a region midway between, beneath an along-axis volcano near 29°02'N. The greatest number of microearthquakes were recorded in a diffuse zone off-axis at the inside corner on a non-transform offset, which is likely an area of complex deformation. At the segment end near 28°55'N, fault-plane solutions indicate high-angle normal faulting consistent with lithospheric stretching. Two-dimensional (2-D) and three-dimensional (3-D) delay time tomography has been applied to travel times from shots along an axial refraction line; inversion solutions indicate that the velocity structure in the lower crust is heterogeneous, with higher velocities and thin crust occurring near the segment end, and lower velocities and a thickened layer 3 occurring towards the central bathymetric high. The thickness of the lower crust at the segment end is asymmetric across axis, with lesser thickness beneath the inside corner. The microearthquake characteristics show complexities not explained by a spreading cell model. Along axis, well-resolved focal depths determined with a 3-D velocity model range from 3 to 6 km beneath the seafloor and do not shallow from the segment end to the segment center. The significant seismicity at the segment center is likely associated with volcanic and hydrothermal processes at the axial volcanic ridge (the largest microearthquake is located 4 km beneath Broken Spur). Microearthquakes with anomalous focal mechanisms beneath an along-axis volcano may be the result of stresses related to magma migration or cooling. The microearthquakes in this study have rupture lengths on the order of only 100 m and therefore are sensitive to small-scale variations in the influence of recent magmatism and hydrothermal circulation. The characteristics of large ($m_b > 4.5$) earthquakes on the MAR, in contrast, may behave more nearly in accordance with a spreading cell model because of larger rupture lengths, on the order of 10 km, that sample structure on the segment scale.

INTRODUCTION

Accretion at mid-ocean ridges is a three-dimensional, temporally varying process that reflects the balance between magmatism and tectonism. Mid-ocean ridges are divided into distinct segments separated by axial discontinuities; current models suggest that this segmentation is the result of focused magmatic centers, spaced one per segment, along axis [e.g., *Francheteau and Ballard*, 1983; *Whitehead et al.*, 1984; *Schouten et al.*, 1985; *Macdonald et al.*, 1988; *Sempere et al.*, 1990; *Lin et al.*, 1990]. According to these spreading-cell models, the along-axis bathymetric highs at segment centers are the locus of hot ascending melt, whereas the deep distal ends of segments are cooler areas of lesser melt supply. The implied thermal structure predicts a systematic variation in the mechanical strength of the lithosphere and depth of faulting [*Harper*, 1985; *Sempere et al.*, 1990; *Shaw*, 1992; *Shaw and Lin*, 1993]. At cooler distal ends of segments where the mechanical lithosphere is relatively strong, according to this model, extension is dominant and faulting extends to greater depths due to the greater thickness of the brittle layer, while faulting is shallower and magmatism more predominant at the hot, weak segment centers.

Temporal variation in melt supply is suggested by the considerable morphological diversity among ridge segments on the Mid-Atlantic Ridge (MAR) [*Sempere et al.*, 1990]. Differences among the mantle Bouguer anomaly (MBA) bull's eye lows typically found at segment centers [*Kuo and Forsyth*, 1988; *Lin et al.*, 1990; *Morris and Detrick*, 1990; *Blackman and Forsyth*, 1991; *Detrick et al.*, 1994] also imply episodicity, since MBA lows within segments most likely reflect greater crustal thickness from increased melt supply [*Tolstoy et al.*, 1993]. However, little is known in detail about the emplacement of magma and cooling of the crust, although recent models have shown that the interplay between these processes can have an important influence on ridge-axis morphology and crustal structure [e.g., *Henstock et al.*, 1993; *Neumann and Forsyth*, 1993; *Phipps Morgan and Chen*, 1993].

Earthquake studies provide direct information on the depth distribution, mechanism, and moment release of seismic faulting at mid-ocean ridges, and are thus important to the understanding of the active tectonics of ridge segments and for constraining the mechanical structure of the lithosphere, which is primarily dependent on temperature and rheology. Previously, only two well-constrained microearthquake experiments on the MAR have been conducted, one at an along-axis deep at 23°N [*Toomey et al.*, 1985, 1988] on a segment with no MBA low [*Morris and Detrick*, 1990] and one at an along-axis high near the TAG hydrothermal field at 26°N [*Kong et al.*, 1992], where an MBA low is observed (J. Lin, personal communication, 1994). The results of these two experiments are supportive of the spreading cell model. The survey at 23°N reported microearthquake mechanisms and locations consistent with brittle extension of relatively cool lithosphere at a segment end. At 26°N, median valley microearthquakes at the along-axis high at the segment center occurred at shallower depths (many less than 4 km) than at the along axis deep at the segment end (focal depths of 4 to 8 km). Also a low-velocity zone beneath the along-axis high may indicate a site of recent magmatic injection.

In the fall of 1992, experiments were conducted along segments at 29°N and 35°N on the Mid-Atlantic Ridge to investigate further the relationship of earthquake and seismic structural characteristics to spreading processes. In the following sections, we describe the microearthquake characteristics and crustal velocity structure along the segment at 29°N. Tomographic images of crustal *P* wave velocity demonstrate that the lower crust is thin at the segment end and thickens towards the segment center, in a manner consistent with a spreading-cell model and similar to the along-axis velocity structure reported by *Tolstoy et al.* [1993] for a segment on the southern MAR. The microearthquake locations and mechanisms, however, are not consistent with this simple model; we argue that they instead reflect spatial and temporal variations in magmatic injection, hydrothermal activity, or thermal stresses.

THE MID-ATLANTIC RIDGE AT 29°N

The microearthquake experiment was carried out at the central and southern portion of a segment at 29°10'N on the Mid-Atlantic Ridge (MAR) (Figures 1 and 2). This 60-km long ridge segment has been previously studied by means of multibeam bathymetry [*Sempere et al.*, 1990; *Shaw*, 1992; *Sempere et al.*, 1993], gravity and magnetics [*Lin et al.*, 1990; *Escartin and Lin*, 1993], and deep-towed side-scan sonar [e.g., *Smith and Cann*, 1993].

Bathymetry and gravity data at 29°N are consistent with enhanced magmatism at the segment center. The segment has an hourglass shape (Figure 1), with a narrow, shallow median valley at the central area near 29°10'N and a wide, deep median valley at the northern and southern terminations. An axial volcanic ridge (AVR) extends from the southern deep to the central bathymetric high, terminating where it intersects the western median valley wall. A large mantle Bouguer anomaly (MBA) low occurs in the center of the segment, consistent with about a 3 km increase in crustal thickness relative to the segment ends [*Lin et al.*, 1990]. There is a characteristic pattern of seafloor faults at this and other segments with well-developed MBA lows: closely spaced small-throw faults occur at the segment center, while at the ends more widely spaced, larger-throw faults predominate [*Shaw*, 1992; *Shaw and Lin*, 1993]. This pattern suggests that localized extension at large-throw faults contributes to crustal thinning at segment ends, while at the more magmatic segment center the thinner lithosphere does not allow the sustained growth of large-throw faults [*Shaw and Lin*, 1993]. At the inside corners the MBA is more positive, and the crust probably thinner, than that at the outside corners, as is typical for segments on the MAR [*Escartin and Lin*, 1993]. Note that no large, teleseismically-recorded earthquakes occurred at the segment center during the period January 1964 to June 1993, but a few have occurred near the southern terminus during that interval (Figure 1).

Some four months following our survey, Broken Spur hydrothermal vent field was discovered at the segment center (29° 10.15'N) on the crest of the axial volcanic ridge [*Elderfield et al.*, 1993; *Murton et al.*, 1993]. The lateral extent of the vent field is as yet uncertain.

To the south, at 28°50'N, is a shorter (~20 km long) segment that has a wide, deep median valley and no large mantle Bouguer anomaly. Several large teleseismically-recorded earthquakes ($m_b > 4.5$) have occurred at the western edge and northern boundary of this presumably less magmatic segment (Figure 1).

THE SEISMIC EXPERIMENT

The seafloor seismic network consisted of 15 Office of Naval Research (ONR) Ocean Bottom Seismometer (OBS) instruments [*Jacobson et al.*, 1991] and had an along-axis aperture of 35 km (Figure 2). The network was deployed in August 1992 and recorded data over 41 days. The OBSs operated 4 channels (hydrophone, and a vertical and two horizontal seismometers) and recorded digitally in event-detect mode, triggering off the hydrophone the first 25 days and off the vertical seismometer channel the last 16 days. Data acquisition software contained a "lockout," which permitted no more than 35 triggers to be recorded within a four-hour period to prevent the filling up of the data disks by spurious triggers and to ensure that the recorded events would be distributed throughout the experiment.

A substantial quantity of data was recorded, although not all OBSs were completely functional [Unpublished R/V Ewing Cruise Report, EW9210, 1992]. Nine instruments recorded data throughout most of the experiment. Three instruments returned partial data: OBS 60 recorded one day of earthquake data; and OBSs 53 and 55 primarily provided shot data from the first 3 days of recording. (OBS 55 failed to lift off from the ocean bottom following release of its anchor because the anchor was wedged by volcanic rock. The instrument was dislodged from the seafloor during an ALVIN dive six months later.) No useful data were recorded on three other OBSs. In addition, several seismometers did not function because the sensor was tilted more than ~15°. For these OBSs useful hydrophone data were still recorded, but were of variable quality. Examples of good seismometer and hydrophone data are shown in Figure 3. *S* wave records were primarily restricted to OBSs 59, 63, 56, 54, and 61. The rough median valley topography resulted in seismometer coupling problems, which were most severe at OBS 61, but clear *P* and *S* arrivals could often be picked (Figure 3).

Earthquake activity at the ridge segment was high (~200 events per day). Fully operational instruments continually reached the 35-trigger "lockout" limit, with small earthquakes (moments less than 10^{17} to 10^{18} dyn cm) constituting the majority of events. Triggers were also caused by microseisms, electronic noise, and earthquake codas. A smaller subset of earthquakes, about 20 per day during hydrophone event-detect and 35 per day during vertical-seismometer event-detect, were large enough to trigger simultaneously four or more OBSs (Figure 4), of which 10 to 20% yielded sufficient *P* and *S* wave first arrival times to be locatable. The majority of these earthquakes were recorded during hydrophone event-detect, since during vertical event-detect the instrument "lockout" was saturated by *S* wave triggers of small, unlocatable earthquakes.

Twenty-six 6-lb. ranging shots were detonated, and an axial refraction line was shot with forty 60-lb. charges at 1-km spacing (Figure 2). Travel times of water-wave arrivals from the explosive shots, picked from the hydrophone or vertical seismometer, were used to relocate 11 instruments by the method of *Creager and Dorman* [1982], as adapted for microearthquake networks by *Toomey et al.* [1985]. Initial positions from the Global Positioning System (GPS) were used for shots and OBSs, and initial OBS depths at drop locations were from the Sea Beam bathymetry of *Purdy et al.* [1990]. The water velocity profile was taken from *Crouch and Osborne* [1981]. A total of 340 observations (206 travel times, 41 GPS shot positions and shot origin times, and 11 instrument depths) were used to estimate 156 parameters (11 instrument positions and depths, 41 horizontal shot positions and origin times). The relocation was performed, and Sea Beam depths for the relocated OBS positions were then taken as input for another relocation. The final average change for OBS positions from the initial estimate was 150 m, for shot positions 100 m, and for shot origin time about 2 ms. Resulting solutions for OBS depths were each within 25 m of Seabeam depths. The root-mean-square (rms) travel time residual after relocation was about 8 ms. Given the relocated OBS positions, most remaining shots were individually relocated from water-wave data.

HYPOCENTRAL LOCATION

Microearthquakes recorded on 4 or more OBSs were located using HYPOINVERSE [*Klein*, 1978], an algorithm for solving the nonlinear problem for earthquake hypocenter and origin time by linear approximation and iteration until convergence. Using singular value decomposition, the algorithm calculates the generalized inverse of the travel time partial derivative matrix with respect to solution parameters (latitude, longitude, origin time, and depth). The method allows calculation of the covariance matrix, used to derive error estimates for the linearized problem. Picks are weighted according to the quality of observations. Step-length damping stabilizes the iterative process, and an eigenvalue cutoff is specified to prevent solution changes in poorly constrained directions. A homogeneous velocity model and initial hypocenters are assumed.

Arrival Time Data

Instrument clocks were corrected assuming linear drift rates, ranging from 0.5 ms to 3 ms per day. No drift rate correction was made for OBS 55. *P* and *S* wave arrival times were assigned errors of 10, 20, 40, and 80 ms, and corresponding weights in the location procedure of 1, 0.75, 0.5, and 0.25, respectively. The first onset of most *P* waves could be read to within about 20 ms; errors in *S* wave arrivals read off the horizontal channels were estimated to be higher, 40 to 80 ms. *S* wave data were further downweighted by a factor of 0.75 to account for the higher uncertainty of *S* wave picks due to poor coupling of seismometers (Figure 3). Arrivals with large residuals (0.5 s) were not used.

The OBSs were initially referenced to a common datum of 3220 m below sea level by calculating station delays under the assumption of a uniform crustal velocity of 6.5 km/s. Final station delays were determined iteratively from 23 well-located events by reducing the mean travel time residual to zero at each instrument. This method takes into account crustal heterogeneities beneath receivers as well as errors in instrument depth. Epicenters obtained with the final station delays were shifted by 1 km on average and reduced the total rms residual by 20% compared with solutions using initial station delays. The relocated instrument positions and station delays are given in Table 1.

Location Parameters

We adopt a layered, one-dimensional (1-D) *P* wave velocity structure based on the model *Purdy and Detrick* [1986] obtained from a refraction study of the MAR at 23°N (Figure 5). This velocity model has been used in previous microearthquake studies [*Toomey et al.*, 1985, 1988; *Kong et al.*, 1992] and therefore facilitates comparison of results. Examination of travel times and waveforms from the along-axis refraction line, however, indicates significant lateral heterogeneity in crustal structure, as has also been found at the MAR at 26°N [*Kong et al.*, 1992]. An assigned V_p/V_s ratio of 1.8 is used to convert *P* wave velocities to *S* wave velocities. V_p/V_s ratios of 1.80 to 1.83 (Figure 6) are estimated applying the method of *Francis* [1976] to three OBS pairs (the distribution of data for other OBS pairs was significantly poorer).

The starting solution was a trial epicenter located at the nearest station, with an initial origin time 2 s prior to the earliest arrival time and an initial depth of 5 km beneath datum. For events with poor depth control, such as events located more than about one focal depth away from the nearest recording station [*Lilwall and Francis*, 1978; *Duschenes et al.*, 1983], focal depths were fixed at 5 km.

Formal errors are calculated with a user-specified HYPOINVERSE "picking error," which is the square root of the arrival time data variance and reflects uncertainties in arrival time picks, instrument locations, clock drifts, and the assigned velocity model. An a priori "picking error" of 50 ms was used. Following *Wilcock and Toomey* [1991], the a posteriori values were calculated as 50 ms for all earthquakes, and as 40 ms for earthquakes with resolved focal depth.

HYPOINVERSE Solutions

Hypocenters were determined for 235 earthquakes; for 122 events focal depths can be resolved (Figure 7 and Table 2). The 95% confidence intervals in Table 2 are calculated by multiplying the HYPOINVERSE 1-σ vertical error by 1.96 (for a system with one degree of freedom) and the 1-σ horizontal error by 2.45 (for a system with two degrees of freedom). The locations of 173 earthquakes were constrained by at least one *S* wave arrival; of these 106 have resolvable focal depths. Previous studies [*Duschenes et al.*, 1983; *Wilcock and Toomey*, 1991] have shown that the inclusion of *S* wave information significantly improves hypocentral resolution and also reduces the effects of nonlinearities on the estimated errors.

To evaluate the influence of the assumed 1-D velocity structure, we also located all events using the velocity model derived for the Mid-Atlantic Ridge at 37°N by *Fowler* [1976]. This model has a thinner crust and lower upper mantle velocities than the *Purdy and Detrick* [1986] model (Figure 5). For 60% of the events, the hypocentral changes are less than the 95% confidence limits. Almost all events with hypocentral changes greater than this amount occur outside the network. For well-recorded events within or close to the network, the choice of 1-D velocity model does not have a significant affect on hypocenter locations. Furthermore, we have made a close examination of the distribution of earthquake epicenters and focal depths determined with *Fowler's* [1976] velocity model, and find that the conclusions stated in the following section remain valid. Later, we will reevaluate the resolution of hypocentral parameters using an improved three-dimensional velocity model.

EARTHQUAKE CHARACTERISTICS

Hypocenters

The seismic activity recorded over the 41-day experiment period is shown in Figures 7-10. Figures 11 and 12 display the depth distribution of microearthquakes. Events clustered into three separate along-axis regions: (1) the southern deep near 28°55'N, (2) the central high near 29°11'N, at the Broken Spur hydrothermal vent field and slightly to the north, and (3) a region midway between these two near 29°02'N. Significant off-axis activity also occurred at the southern end of the segment at the inside corner of a non-transform offset. Earthquake depths ranged between 3 and 8 km beneath the seafloor. We do not find a shoaling of focal depths progressing along-axis from the southern deep toward the central high (Figure 11), as observed at 26°N [*Kong et al.*, 1992]. To confirm this result, we also examine the depth distribution of a high quality subset of hypocenters located with data from 5 or more OBSs (Figures 13 and 14). While in each area the depth extent of seismic faulting is confined to a more limited, and shallower, region, the conclusion that focal depths do not shoal toward the central high also holds for this more restricted data set (Figure 13).

The southern deep near 28°55'N. 32 events occurred beneath the inner floor near 28°55'N (Figure 8). The majority of the seismicity extended over a limited area 10-km across axis by 5 km along axis near the southern termination of the AVR. Focal depths of all events range from 4 to 7 km below datum. Events were located both beneath the AVR and the two basins on either side (Figure 8).

The along-axis high near 29°10'. Significant seismic activity (55 events) occurred at the segment center. Most events were restricted to a narrow (~2 km across axis) and long (~6 km along axis) band of activity to the north of the network, near the region where the axial valley ridge intersects the western valley wall (Figure 9). The hypocenters lie beneath the eastern edge of the AVR and near Broken Spur hydrothermal vent field. The largest event during the experiment occurred almost directly beneath Broken Spur (Table 2). The focal depths are mostly 3 to 7 km.

The inner floor at 29°02'. During the experiment period, no activity was recorded between the southern deep and the along-axis high (Figure 7), except for a very small subset of 13 microearthquakes near 29°02' located beneath a volcano on the axial valley ridge (Figure 8). All but one occurred during a 24-hour period and with epicenters confined to a 1 by 1 km area. Most focal depths are 6 to 8 km below datum. On individual instruments, the waveforms of several earthquakes are well correlated, indicating a similar mechanism and location.

The inside corner region. The largest number of microearthquakes (95) were located off axis in a diffuse zone of activity, about 15 km by 15 km in area, at the southwestern inside corner (Figures 7 and 10). The bathymetry in this region is also complex: a ridge-parallel basin partially separates the high inside corner from the median valley floor. Relative to the seafloor, focal depths off-axis are similar to focal depths beneath the southern deep (Figure 12).

The segment at 28°50'N. 32 events were located in this southern segment, none with focal depth resolved (Figure 7).

Focal Mechanisms

First motion data were used to constrain focal mechanisms, presumed to be double-couples. The polarities on OBS records were determined from the water wave arrivals of the closest shots. The azimuths and takeoff-angles were from HYPOINVERSE solutions. Plots of first motion data on an equal area projection of the lower focal hemisphere were initially made for all events with resolved focal depth. Well-recorded events were then sorted into groups with similar focal mechanisms and locations. Polarities were reevaluated by checking the seismograms of these events. Because much of the earthquake activity is distributed outside the network and the OBS stations are widely spaced, we obtained a well-constrained focal mechanism only for events in the southern deep. At this locale, a composite solution shows normal faulting on planes having strikes slightly rotated (~20°) from the axis-parallel direction (Figures 15a and 16), as identified by the large scale trend of the median valley walls. Limited information is available for earthquake mechanisms at 29°02'. Polarities can be satisfied by two types of mechanisms. One mechanism involves predominantly reverse faulting along axis-parallel planes (Figure 15b). The second mechanism involves either normal faulting on a ridge-perpendicular plane or left-lateral strike-slip faulting on a low-angle, ridge-parallel plane (Figure 15c). No reliable information is available for mechanisms at the segment center. Polarities for two microearthquakes located at the northern edge of the network are shown in Figure 15d and 15e. The small number of data and limited coverage are not sufficient to determine a mechanism.

Seismic Moments and Source Dimensions

Using the theory of *Brune* [1970], the moments (M_0) of located microearthquakes were estimated from the low-frequency displacement spectra of *P* and *S* waves, calculated by means of standard procedures [*Tréhu and Solomon*, 1983; *Toomey et al.*, 1988]. Because most earthquake mechanisms are poorly constrained, the earthquake moments in Table 2 are an average of values calculated on several OBSs. Moments range from 10^{17} to 10^{20} dyn cm (Table 2). The largest earthquake ($M_o=1x10^{20}$ dyn cm) occurred in the segment center directly beneath Broken Spur hydrothermal vent field. Since the summed moment release is dominated by larger earthquakes, over the experiment interval the segment center was the area of greatest seismic moment release (the total moment release by region was as follows: $3.7x10^{20}$ dyn cm, bathymetric high; $2.2x10^{20}$, inside corner; $1.8x10^{20}$, 28°50'N segment; $1.5x10^{20}$, southern deep; $9x10^{18}$, 29°02'). Corner frequencies ranged from 9 to 25 Hz, indicating fault radii of 50 to 100 m. The distribution of events by seismic moment is often plotted as the cumulative number N of earthquakes greater than M_o versus M_o. A B value is the slope of a line $\log_{10}N(M_o)=A-B\log_{10}(M_o)$ that best fits the data. The B value of all events is 0.82±0.05 (Figure 17).

SHOT TOMOGRAPHY

Inversions for P Wave Velocity Structure

We have performed a series of two-dimensional (2-D) and three-dimensional (3-D) tomographic inversions using *P* wave first arrivals from 43 well-located shots (Figure 18). A new tomographic method [*Toomey et al.,* 1994] was used, which employs an accurate three-dimensional ray tracer [*Moser*, 1991] and incorporates smoothing constraints to stabilize the inversion (see Appendix). The initial velocity model consists of a three-dimensional grid of finely spaced nodes (250 m in horizontal and vertical directions) that conforms to bathymetry by shearing nodes in the vertical direction. The inversion solves for perturbations to a more coarsely-spaced model. Horizontal and vertical smoothing parameters, λ_h and λ_v, determine the weighting of smoothness constraints. Decay parameters (τ_x, τ_y, τ_z) are assigned to fix the length scales of smoothing, where the coordinates x, y, and z denote across axis (positive east), along axis (positive north), and down.. The tomographic inversion weights individual travel times by an estimated error.

P wave arrival times are assigned errors of 10, 20, 40, and 80 ms, depending on the clarity of the first arrival; the first onset of most *P* waves could be generally be read to within about 20 ms. Not all shots were recorded on individual OBSs, because instruments were saturated with triggers from shot and earthquake events and continually reached the 35-trigger "lockout" limit. Because the spacing of OBS receivers is irregular and all shots were on axis, the ray coverage varies substantially throughout the model. For all inversions we therefore examine the spatially-averaged derivative weight sum (DWS) [c.f. *Toomey et al.*, 1994], which provides a measure of the ray density in the perturbational velocity model and indicates where the velocity solution is well constrained. Within the network, the crustal structure on axis is well sampled, but ray coverage decreases farther off axis.

Two-dimensional inversions for along-axis velocity structure were conducted using 6 instruments (OBSs 58, 59, 57, 56, 55, and 54) located near the center of the axial valley (Figure 18). Two instruments in the southeastern axial valley, OBSs 63 and 53, were not included, because travel times at these instruments were early compared with those at OBSs 57 and 59 at similar positions along-axis, indicating that structure varies off-axis to the southeast. This interpretation is consistent with results of subsequent 3-D solutions.

A 2-D solution using the *Toomey et al.* [1994] method is shown in Figure 19a. The inversion solves for perturbations at nodes spaced 3 km along axis (τ_y=3.1 km and λ_h=100) and 1 km in the vertical direction (τ_z=1.1 and λ_v=100). The initial rms misfit is 97 ms for a *Purdy and Detrick* [1986] starting velocity model, and the final rms misfit is 56 ms (66% variance reduction). The DWS is plotted in Figure 19b. Shallow structure (<5 km) is constrained between -10 and 25 km along axis (Figure 19b); deeper structure (5 to 7 km) is resolved only between -5 to 20 km.

For comparison, the velocity structure derived using the *Thurber* [1981, 1983] tomographic method, which uses an approximate 3-D ray tracer and no inversion constraints, is shown in Figure 20. Velocity nodes are at 200, -10, 0, 10, 20, and 200 km in the horizontal direction, and -50, 0, 1, 3, 5, and 50 km in the vertical. Node spacing is chosen to obtain generally good resolution values (~0.7), defined by the diagonal elements of the resolution matrix [*Wiggins*, 1972]; velocities between nodes are derived by linear interpolation. The initial rms misfit is 100 ms for a starting velocity model derived from a 1-D inversion, and the final rms is 65 ms. As with the 2-D inversions with the method of *Toomey et al.* [1994], higher velocities are indicated for the lower crust toward the segment end.

The results of a 3-D inversion, conducted using arrival times from all 11 instruments, are shown in Figure 21. The method of *Toomey et al.* [1994] was used, because the technique of *Thurber* [1981, 1983] cannot accurately model the steep bathymetric relief. The parameters are similar to the 2-D inversion, but also include nodes spaced at 2 km across axis (τ_x=2.1 km). The initial rms misfit is 115 ms, and the final rms misfit is 32 ms (92% variance reduction). The lower crustal structure is now asymmetric across axis, with higher velocities toward the inside corner (x=1 km) than toward the outside corner (x=-1 km). A volume of anomalously high velocities in the lower crust occurs to the east (x=3 and 5 km) near the point 15 km along axis, explaining the generally fast travel times recorded at OBSs 53 and 63. Plots of the derivative weight sum (Figure 21b) show that there is little resolution of structure off axis at x=-7,-5, and 7 km. Velocities appropriate to mantle material (8 km/s) are well-resolved only near x=-1 and -3 km, y=0 km.

Resolution of the 3-D Model

Following *Toomey et al.* [1994], we evaluate model resolution by reconstructing a known pattern of anomalies using the initial ray set in the tomographic inversion. Figure 21c shows that we image three areas of major perturbations: (1) high-velocity perturbations at the segment end (y=-10 to 0 km), (2) low-velocity perturbations toward the segment center (y=10 to 20 km, z > 6 km), and (3) high-velocity perturbations to the east (x=3 to 7 km). In this section, we evaluate model resolution in these areas by conducting inversions for synthetic models. In all cases, anomalies are taken as a horizontal cylander of rectangular cross section (extending infinitely in either the x or y direction) with velocity of 7 km/s imbedded within an otherwise homogeneous 6 km/s medium, and the inversion solves for the perturbations to a homogeneous 6 km/s starting model.

(1) Resolution of high-velocity perturbations at the segment end. Figure 22a shows the 2-D synthetic model, containing a 1 km/s velocity perturbation toward the segment end. The results of a 3-D inversion using ray paths from the actual experiment are shown in Figure 22b. The magnitude of the anomaly is underestimated, and the shape of the anomaly is considerably smoothed. The anomaly is best resolved at x=-1 to 1 km, with resolution decreasing farther off-axis. Note that the reconstructed anomaly is symmetric about the axis. This result indicates that the asymmetry in Figure 21c, with higher velocities occurring at the inside corner region, is required by the travel-time data and is not an artifact of the uneven distribution of ray paths.

(2) Resolution of low-velocity perturbations towards the segment center. Figure 23a shows the 2-D synthetic model, containing a 1 km/s velocity perturbation at 6 to 8 km depth toward the segment center. The results of a 3-D inversion are shown in Figure 23b. The magnitude of the anomaly is underestimated, and the shape is considerably smoothed. The anomaly is poorly resolved at x=-5 and -7 km. This result indicates that while tomography (Figure 21c) can detect an increase in crustal thickness toward the segment center, the shape and magnitude of the anomaly will not be well resolved.

(3) *Resolution of high-velocity perturbations to the east.* At 23°N, *Purdy and Detrick* [1986] and *Toomey et al.* [1988] find that *P* wave velocities in the lower crust are diminished on axis and increase with age off-axis, perhaps due to gradual sealing of cracks and pores by hydrothermal alteration. Figure 24a shows a 2-D input model in which velocities are low on axis and increase off axis, designed to test whether the high-velocity perturbations to the east (Figure 21c) could be the result of such aging. Although the input model (Figure 24a) is symmetric about the axis, the reconstructed pattern (Figure 24b) is

asymmetric because of the larger number of ray paths that sample structure to the east (see also contours of the derivative weight sum in Figure 21b). Similarly, while the input structure does not vary along axis, tomography images high velocity anomalies only where ray coverage is more complete (y=0 to 20 km). Comparison with the perturbations in Figure 21c thus suggests that the high-velocity perturbations to the east of the axis could be the result of ray paths sampling more mature crust. Figure 24b also shows that a region of much less pronounced anomalies is predicted to the west of the axis. Such a region is not imaged in our models (Figure 21c), however, indicating either that the maturing of the crust is not symmetric across axis or that the imaged structure to the east is caused by other processes.

These results demonstrate that a thinner crust beneath the segment end and asymmetry between the inside and outside corner regions can be resolved by the experiment, but that the magnitude and shape of the anomalies will not be well defined. The finer scale features in the tomographic images should thus be interpreted with caution.

EFFECT OF HETEROGENEOUS VELOCITY STRUCTURE ON HYPOCENTERS

The microearthquake hypocenters discussed above were obtained by the use of HYPOINVERSE and the assumption of a 1-D velocity model. However, tomographic inversions indicate that there is considerable 3-D structure, especially in the lower crust. To evaluate the influence of crustal heterogeneity, we locate microearthquakes in an improved 3-D velocity model. It is particularly important to assess whether the along-axis pattern of focal depths is robust with respect to the velocity model.

We locate a subset of 73 median valley microearthquakes in the velocity model of Figure 19 using the grid search method described by *Wilcock and Toomey* [1991]. This method conveniently couples with the tomography, since for every iteration of the inversion, the *Moser* [1991] raytracer produces travel times from each OBS to the positions of all velocity nodes. A grid search of rms travel time residual has the additional benefit of avoiding problems of local minima and nonlinearities associated with generalized inverse methods. S wave travel times were calculated using a V_p/V_s ratio of 1.8. Weights were applied to arrival times in the same manner as described above.

The epicenters and focal depths obtained with the 3-D model are not significantly different from the HYPOINVERSE solutions, so our conclusions remain valid (Figures 25 and 26). Near the center of the segment, events are shifted somewhat to the west relative to 1-D solutions; the large microearthquake originally located beneath Broken Spur hydrothermal vent field does not move appreciably (the microearthquake is still within a few hundred meters from the location given by *Elderfield et al.* [1993]). At the segment deep, several earthquakes beneath the axial valley ridge are shifted to the eastern basin, but the distribution at the western basin remains the same. Focal depths derived with the heterogeneous velocity model move upward, but still do not shoal toward the along-axis high (Figure 26a). Focal depths of a high quality subset of hypocenters located using 5 or more OBSs are all between 3 and 6 km beneath the seafloor (Figure 26b).

To evaluate errors in focal depth, we examined the variation of minimum rms residual over a range of focal depths held to fixed values. The 95% confidence region is calculated from equation (7) of *Wilcock and Toomey* [1991], using the standard deviation of 40 ms determined from those HYPOINVERSE solutions with focal depth resolved. Most events show a sharp minimum, indicating a solution with a well-constrained depth (Figure 27). However, some events display greater errors. The small subset of microearthquakes that locate at depths of 1 km or less have focal depth poorly constrained and may be much deeper (Figures 28a and 28b). The 95% confidence intervals for the three deepest earthquakes at 29°02'N are large (Figure 28c). We also find increased depth errors for many events located with only 4 OBSs (at least one *S* but only four *P* wave arrivals) (Figure 28d), which is the case for many of the deepest earthquakes ($\geq$ 6 km depth with the grid search relocation).

DISCUSSION

The microearthquake characteristics of the MAR at 29°N indicate the present-day location, mechanism, fault dimensions, and depth distribution of seismogenic brittle faulting. Tomographic images of *P* wave velocity describe the spatial variability of the crustal accretion process. Here, we review our results and discuss implications for the spreading cell model.

Deformation of the Inside Corner Region

It is generally assumed that faulting occurs predominantly on axis along the median valley walls. However, the largest number of microearthquakes in our experiment were located in a diffuse zone off axis at the southern inside corner high (Figure 7), a morphologically complex area that is probably undergoing intense deformation. The several teleseismic earthquakes located at the northern boundary of the short segment at 28°50'N may also be the result of faulting at the inside corner of a non-transform offset.

Off-axis faulting may be a major process at inside corners of segment and transform boundaries [see also *Rowlett*, 1981]. A microearthquake experiment at 35°N also found a high level of seismicity at the inside corner of a non-transform offset [*Barclay et al.*, 1993].

Diffuse microearthquake activity has been found to occur at inside corners of the St. Paul's, Vema, Oceanographer, and Rivera transforms [*Francis et al.*, 1978; *Rowlett*, 1981; *Prothero and Reid*, 1982; *Rowlett and Forsyth*, 1984]. In addition, large transform earthquakes with anomalous mechanisms (reverse-faulting, normal-faulting, and strike-slip faulting on planes oblique to the transform) reported by *Wolfe et al.* [1993] near ridge-transform intersections at the Marathon, St. Paul's, and Rivera may result from inside corner faulting. Gravity and magnetic data have been interpreted as indicating greater crustal thinning at inside corners than at outside corners [*Escartin and Lin*, 1993]. High levels of seismicity demonstrate that some crustal deformation occurs at inside corners after the lithosphere has moved outside the median valley. Off-axis tectonism could contribute to the complex bathymetry, magnetic, and gravity anomalies generally found at inside corners.

Variation in Crustal Structure

At the MAR, the pattern of mantle Bouguer anomalies suggests that crust is thinner than average at segment discontinuities and is thicker near segment centers [e.g., *Lin et al.*, 1990]. Tomographic images in this study support such a conclusion and demonstrate further that most of the variation occurs in the lower crust. Although the position of Moho is relatively unconstrained, our models are consistent with higher velocities and a thin lower crust occurring near the southern deep, and lower velocities and a thicker layer 3 occurring near the central bathymetric high.

In Figure 29, we compare the 3-D velocity solution with the crustal thickness variations calculated by *Lin et al.* [1990] from gravity data. For comparison, Figure 30 shows profiles of the residual gravity anomaly, equal to the MBA corrected for the effects of lithospheric cooling [*Lin et al.*, 1990]. Both methods imply a similar variation in crustal thickness towards the segment end (x=-3, -1, and 1; y=-10 to 10). There is also good agreement in the cross-axis variations, with crust being thinner towards the inside corner. Tests of resolution (Figures 22 and 23), however, show that the magnitude and shape of velocity anomalies may not be well-defined, and plots of derivative weight sum indicate that the velocity model does not resolve deep structure (> 5 km) towards the segment center (y > 20 km).

The anomalous region of high-velocity lower crust imaged in the eastern valley midway between the segment center and the segment end (x=3 and 5 km; y=10 to 20 km) is not associated with particularly thin crust (Figures 29 and 30). At the MAR at 23°N, *Purdy and Detrick* [1986] and *Toomey et al.* [1988] find that P wave velocities in the lower crust are lower than normal on axis and progressively increase with age off-axis. They attribute this phenomenon to the gradual sealing of cracks and pores by hydrothermal alteration. At

29°N, the off-axis region of high velocities may simply result from rays sampling slightly older, more mature crust, as compared to the axial model of *Purdy and Detrick* [1986]. As shown in our previous tests of resolution the apparent along-axis variation could be an artifact of the incomplete ray coverage (Figure 24).

At the southern MAR, *Tolstoy et al.* [1993] also find that MBA variations along axis correspond to a thinner or thicker lower crustal layer. Their experiment recorded both *P* and *PmP* arrivals, important for constraining Moho, at 3 OBSs (spaced ~20 km apart along-axis) from a 109-km refraction line along the median valley. While their experiment produced a more complete along-axis image of Moho variation, the crustal velocity structure they observed is coarser than that obtained in this study because of the large instrument spacing. Furthermore, their 2-D model does not resolve asymmetry at inside and outside corners.

Fault Geometry

Source mechanisms have been obtained in two areas: the western basin of the southern deep and beneath the along-axis volcano near 29°02'N (Figure 16). Normal-faulting at the southern deep takes place on steeply dipping (~45°), nearly axis-parallel planes, as is typically observed for both microearthquakes [e.g., *Toomey et al.*, 1985, 1988] and large earthquakes [e.g., *Huang and Solomon*, 1988] on the MAR, and is consistent with the expected ridge-perpendicular extension. The observed ~20° rotation of fault planes from the large-scale trend of the median valley may be controlled by small-scale structure of local faults bounding the basin.

The composite solutions for microearthquakes beneath the along-axis volcano near 29°02'N cannot occur by this process (Figure 16), and more likely result from thermal stresses induced by differential cooling or stresses associated with magma movement. On land, seismicity associated with magma movement is associated with such phenomena as inflation or deflation events, harmonic tremor, and eruptions [e.g., *Klein*, 1987; *Einarsson*, 1979]. We do not have sufficient information to verify such associations with our data set. There are two possible fault-plane solutions: one indicating reverse faulting along axis-parallel planes (Figure 15b), the other consistent with either normal faulting on an axis-perpendicular plane or left-lateral strike-slip faulting on a low-angle, axis-parallel plane (Figure 15c). Events with reverse slip on faults oriented along-axis were found beneath a ridge axis volcano at 26°N by *Kong et al.* [1992] and were attributed to thermal stresses induced by cooling of a recent intrusion now identifiable as a mid-crustal low-velocity volume. Large ($m_b \geq 5$) reverse-faulting earthquakes on planes nearly parallel to the plate boundary have also been reported at Bárdabunga volcano in central Iceland by *Einarsson* [1991], who suggests that these earthquakes occur in response to pressure variations in an underlying magma chamber. No large low-velocity volume was resolved at 29°02'N (Figure 21). However, reverse-faulting on axis-parallel planes may commonly occur at axial volcanoes of the MAR.

Hydrothermal Circulation

The epicenters of a series of microearthquakes cluster at Broken Spur Hydrothermal Vent Field and to the north (Figure 9). The largest microearthquake recorded during the experiment (about a magnitude 2) is located 4 km beneath Broken Spur. It is plausible that the high level of seismicity around Broken Spur hydrothermal field is caused by stresses associated with fluid flow, hydrofracturing, or differential cooling of the crust. Seismic faulting could also influence seawater circulation: hydrologic changes are observed to follow many large earthquakes on continents, perhaps in response to increased permeability as a result of ground shaking [e.g., *Rojstaczer and Wolf,* 1992] or coseismic strain release and a consequent change in crustal porosity [e.g., *Muir-Wood and King*, 1993].

A hydrothermal system requires a zone of permeability to allow seawater transport (e.g., faults, fissures, interpillow spaces, and dike joints) and a heat source to drive circulation. Little is known about the depth extent of hydrothermal flow, the geometry of fluid pathways, or the efficiency of hydrothermal cooling, although the measured seafloor heat flow at mid-ocean ridges is obviously diminished by convective seawater circulation [*Lister*, 1972].

While the maximum depth of seismic faulting and the depth to probable magmatic heat sources shoal with spreading rate [*Huang and Solomon*, 1988; *Purdy et al.,* 1992], the chemistry of water samples from hydrothermal systems at fast and slow-spreading ridges are remarkably similar and do not indicate different pressures and temperatures of circulation [*Campbell et al.*, 1988]. The application of quartz geobarometry to MAR hydrothermal solutions from the Snake Pit hydrothermal field at 23°N yields a maximum depth of circulation only 500 m below the seafloor [*Von Damm et al.*, 1991], but these results depend on the validity of several assumptions (for example, that solutions have not precipitated quartz) [*Von Damm et al.*, 1985].

However, there is evidence from ophiolites and gabbroic samples from the ocean that seawater penetrates into the lower crust. From $\delta^{18}O$ patterns in dikes and gabbros at the Samail ophiolite (likely from a fast-spreading ridge [*Nicolas et al.*, 1988]), *Gregory and Taylor* [1982] concluded there were two decoupled hydrothermal systems: a shallow system in the dikes above the magma chamber and a deeper (> 5 km) one in the gabbros with lower ratios of water to rock and higher temperatures (> 400°C). Mineralogical and petrological data at Samail suggest that the entire crust has been affected by hydrothermal metamorphism, localized along veins and shear zones in the plutonics [*Nehlig and Juteau*, 1988]. Metamorphic assemblages of gabbroic rocks from slow-spreading ridges indicate that interaction with seawater can initiate at temperatures of up to 700°C during ductile deformation [e.g., *Mével and Cannat*, 1991; *Vanko and Stakes*, 1991; *Gillis et al.*, 1993], although hydration of samples may be associated with tectonic unroofing at segment discontinuities rather than in situ at depth. *Mével and Cannat* [1991] propose that ductile shear zones associated with extension of a hot lower crust create permeable zones that allow seawater penetration at high temperatures and accelerate cooling.

Microearthquakes are another source of information about hydrothermal circulation. No microearthquakes were detected within about 2 km of the TAG vent field by *Kong et al.* [1991]. On the basis of microearthquake and tomographic results for the along-axis high at 26°N, *Kong et al.* [1991] proposed a model whereby permeable fault planes associated with normal-faulting microearthquakes at the eastern valley wall provide pathways for water transport down to the top of a recently intruded heat source. In contrast, at Broken Spur some hypocenters occur in close vicinity to the vent site, perhaps in response to penetrative circulation that has helped to cool the crust. The lack of fault-plane solutions leaves the mechanism of this seismicity open to speculation. While both TAG and Broken Spur are situated at along-axis highs, TAG is located close to the fault scarps of the eastern valley wall, about 2 km from the zone of axial volcanism [*Rona et al.*, 1986]. Broken Spur, in contrast, sits on the crest of the axial volcanic ridge, and is thus more similar in setting to the Snake Pit hydrothermal vent field. The seismicity we observe could thus also be associated with volcanic processes.

Focal Depths

Current knowledge of the controls on earthquake faulting within the crust and uppermost mantle provides a context for interpreting observations along the MAR. Earthquakes occur where frictional sliding on faults is unstable [*Brace and Byerlee*, 1966]. The part of the lithosphere that can nucleate earthquakes is bounded by lower and upper stability transitions [*Scholz*, 1990; *Cowie et al.*, 1993]. The maximum depth of faulting is temperature dependent and located at approximately the brittle-ductile transition [e.g., *Chen and Molnar*, 1983; *Tse and Rice*, 1986]. A minimum depth of faulting usually arises from the stabilizing effect of low normal stresses at shallow depths [*Scholz*, 1988]. While earthquakes cannot nucleate at depths outside the bounded region of instability, large earthquakes can rupture to greater and shallower depths [*Tse and Rice*, 1986]. For mid-ocean ridge microearthquakes the maximum depth of faulting will be directly related to temperature and rheology, whereas the minimum depth generally reflects pressure.

On mid-ocean ridges, centroid depths of large teleseismic earthquakes range from about 1 to 6 km below the seafloor, and the maximum centroid depth decreases with spreading rate [*Huang and Solomon*, 1988] due to generally higher temperatures and thus a shallower brittle-ductile transition. Three previously conducted microearthquake experiments on the MAR [*Toomey et al.*, 1985, 1988; *Murray et al.*, 1984; *Kong et al.*, 1992] imply a systematic intrasegment variation in focal depths. At the along-axis deep at 23°N, a segment without a well-developed MBA, microearthquakes were located between 4 and 8 km depth [*Toomey et al.*, 1985, 1988]. A shallower range of 3 to 5 km depth was reported at an along-axis high near 35.3°N [*Murray et al.*, 1984], where there is an MBA low [*Detrick et al.*, 1993]. At the segment at 26°N, which also has a developed MBA low, *Kong et al.* [1992] found that median valley microearthquakes clustered at shallower depths (2 to 6 km) at the along-axis high at the segment center than at the along-axis deep at the segment end (4 to 8 km).

In contrast, at 29°N well-constrained focal depths range from 3 to 6 km and do not shoal from the segment end to the segment center. This result is at variance with the simple spreading cell model, since the segment center should have enhanced mantle upwelling, and therefore a thinner seismogenic layer, due to both higher temperatures and a greater thickness of crustal material (MBA data suggest a 3 km increase), which deforms by ductile flow at lower temperatures (400°-550°C) than mantle material (800°C). The observed focal depths contradict both the model predictions of *Neumann and Forsyth* [1993], which imply that crustal thickness variations are associated with major changes in the depth extent of seismicity, and the pattern of faults observed in the bathymetry, which suggest a thinner lithosphere at segment centers than at segment ends [*Shaw and Lin*, 1993].

We propose that microearthquakes reflect the effects of local, time-dependent processes, such as hydrothermal and magmatic injection, and are not necessarily an indication of the long-term mechanical behavior predicted by steady-state models [*Neumann and Forsyth*, 1993] or the pattern of faults [*Shaw*, 1992; *Shaw and Lin*, 1993]. The supply of magma to the slow-spreading MAR is neither 2-D nor steady state. No evidence has yet been found of a magma chamber at slow-spreading ridges, although low-velocity regions interpreted as still-hot intrusions have been detected [e.g., *Fowler and Keen*, 1979; *Purdy and Detrick*, 1986; *Kong et al.*, 1992]. Extrusive magmatism occurs primarily along axial volcanic ridges generally composed of small, discrete volcanoes. These observations have led to models whereby the lower crust is made up of many small plutonic bodies that feed volcanism at higher levels [*Nisbet and Fowler*, 1978; *Smith and Cann*, 1992]. Small, episodically-emplaced intrusions and deep hydrothermal circulation could create a thermal structure that is heterogeneous in both time and space, allowing sections of the lower crust near the segment center to cool and nucleate microearthquakes.

Architecture of the 29°N Spreading Cell

To first order, the segment at 29°N fits well into the spreading cell model. Bathymetry, the pattern of faults, and gravity data support a model of focused magmatism, and the tomographic images of this study add further evidence, indicating the lower crust is thinner at the segment end and toward the inside corner. However, microearthquake characteristics show complexities related to the temporal and spatial variability of volcanism and hydrothermal circulation, and do not follow the simple spreading cell model.

There are two different classes of earthquakes: tectonic and volcanic (associated with magma movement). In Iceland and Hawaii, volcanic earthquakes have generally smaller maximum magnitudes than tectonic earthquakes [*Einarsson*, 1979; 1991; *Klein*, 1982; *Klein*, 1987]. At the MAR, *Lin and Bergman* [1990] observe that the locations of large, teleseismically observed earthquakes ($m_b > 4.5$) at 29°N and other segments between the Kane and Atlantis transforms behave in accordance with a spreading cell model, with most occurring along large-relief half-grabens at segment ends rather than at segment centers. Such large earthquakes are probably all tectonic [*Bergman and Solomon*, 1990]. These earthquakes have rupture lengths on the order of 10 km and are thus sensitive to structure on the scale of a simple spreading cell. This study demonstrates that small earthquakes may be important for exploring volcanic processes on the MAR. The microearthquakes have rupture lengths on the order of 100 m and therefore can sample smaller scale variability in magmatic processes, such as is predicted in the models of *Nisbet and Fowler* [1978] and *Smith and Cann* [1993].

CONCLUSIONS

During the 41-day experiment, microearthquake activity at 29°N was high, with individual OBSs recording up to 200 events per day. Hypocenters were determined for 235 microearthquakes recorded on 4 or more OBSs; for 106 of these events focal depth was resolved. Focal depths of all events ranged from 3 to 8 km beneath the seafloor, while those for events recorded on 5 or more instruments and located using a 3-D velocity model ranged from 3 to 6 km. Seismic moments and fault radii of microearthquakes were 10^{17} to 10^{20} dyn cm and 50 to 100 m, respectively.

The important microearthquake and seismic structural characteristics from our study at 29°N are identified as follows:

1. Microearthquakes clustered into three separate along-axis regions: (1) the southern deep at the segment end, (2) the central high, slightly north of the Broken Spur hydrothermal vent field, and (3) beneath an axial volcano near 29°02'N.

2. There is not a simple shoaling of focal depths progressing along-axis from the southern deep toward the central high, in contrast to the situation at 26°N.

3. At the segment deep, fault-plane solutions indicate high-angle normal faulting consistent with lithospheric stretching. Fault-plane solutions beneath the axial volcano at 29°02'N, however, are inconsistent with this process.

4. The largest microearthquake recorded (10^{20} dyn cm) occurred directly beneath Broken Spur hydrothermal vent field.

5. The greatest number of microearthquakes were recorded in a diffuse zone off axis at the inside corner of a non-transform offset, which is likely an area of complex, active deformation. Off-axis faulting may be a major process at inside corners of segment and transform boundaries.

6. Two-dimensional and three-dimensional tomographic inversions indicate that the velocity structure in the lower crust is heterogeneous, with thinner lower crust occurring near the southern deep, and thicker lower crust occurring toward the central bathymetric high. The 3-D velocity structure also indicates that the lower crust is thinner toward the inside corner region. These results are consistent with crustal thickness variations inferred from gravity data.

Bathymetry, faulting style, gravity, and velocity structure at 29°N are supportive of a spreading cell model. However, microearthquake characteristics do not follow this model. The significant level of seismicity at the segment center and microearthquakes with anomalous focal mechanisms are likely associated with volcanic and hydrothermal processes; focal depths along axis indicate that episodic magmatism and deep hydrothermal circulation influence thermal structure. Microearthquakes may thus be useful for exploring volcanic processes on the MAR; in contrast, large earthquakes are probably mostly tectonic. *Nisbet and Fowler* [1978] and *Smith and Cann* [1993] propose that of small-scale magmatic processes are important at slow-spreading ridges, whereas spreading cell models account only for the large, segment-scale variation. The microearthquakes in this study have rupture lengths on the order of only 100 m and therefore can result from variability at these smaller scales. The characteristics of large ($m_b > 4.5$) earthquakes on the MAR may behave in better accord with the spreading cell model because their large rupture lengths (on the order of 10 km) can sample structure on the segment scale.

APPENDIX: TOMOGRAPHIC METHOD

In this Appendix, we provide an overview of the tomographic method described by *Toomey et al.* [1994]. The travel time along a path P though a slowness model $u(\mathbf{r})$ is:

$$t = \int_P u(\mathbf{r})ds \qquad (1)$$

where $\mathbf{r}$ is the position vector and ds is the incremental path length. For our models, $u(\mathbf{r})$ is defined at nodes spaced 250 m apart in the horizontal and vertical directions and sheared vertically to conform with bathymetry. An accurate three-dimensional ray tracer [*Moser*, 1991] is used to calculate the minimum time paths between shot sources and OBS receivers. The slowness field is related to a prior model by:

$$u(\mathbf{r}) = u_0(\mathbf{r}) + \delta u(\mathbf{r}) \qquad (2)$$

where $\delta u(\mathbf{r})$ is the perturbational model, defined by linear interpolation between the set of velocity perturbations α_i at immediately adjacent nodes:

$$\delta u(\mathbf{r};\alpha_1, ...,\alpha_m) = \sum_{i=1}^{m} w_i(\mathbf{r})\alpha_i(\mathbf{r}) \qquad (3)$$

where w_i are the weights for linear interpolation. The inverse problem is independent of $u(\mathbf{r})$, so nodes can be spaced in any manner or chosen to be one-, two-, or three-dimensional.

Given a small perturbation to a slowness model:

$$\delta t = t(u+\delta u)-t(u+\delta u) = \int_P \delta u ds \qquad (4)$$

where by Fermat's principal the travel time is stationary with respect to $P(u)$ or $P(u+\delta u)$. The relation between a change in travel time and the perturbational model is:

$$\delta t(\alpha_1,...,\alpha_m) = \sum_{k=1}^{m} \frac{\partial t}{\partial \alpha_k}\alpha_k \qquad (5)$$

Combining Equations (3), (4), and (5) and multiplying by the Kronecker delta δ_{nk} yields:

$$\frac{\partial t}{\partial \alpha_n} = \int_P w_n ds \qquad (6)$$

so using (5) and (6) model perturbations to the α_i can be linearly mapped into travel time delays.

In the inverse problem, we solve for values of α_i subject to penalty and smoothing constraints. The functional minimized is:

$$s^2 = \mathbf{d}^T\mathbf{C}_d^{-1}\mathbf{d} + \lambda_p\mathbf{m}^T\mathbf{C}_p^{-1}\mathbf{m} + \lambda_v\mathbf{m}^T\mathbf{C}_v^{-1}\mathbf{m} + \lambda_h\mathbf{m}^T\mathbf{C}_h^{-1}\mathbf{m} \qquad (7)$$

where $\mathbf{d}$ is a vector of travel time delays, and $\mathbf{m}$ is a vector of model parameters α_i. The terms on the right hand side of (7) are the prediction error, a penalty function applied to the perturbational model, and vertical and horizontal smoothness constraints. $\mathbf{C}_d$ is the data covariance matrix, a diagonal matrix whose elements are the estimated variance for individual shot travel times. $\mathbf{C}_p$, $\mathbf{C}_v$, and $\mathbf{C}_h$, are model covariance matrices. λ_p, λ_h, and λ_v allow weighting of the importance of constraints.

Rather than calculating the inverses of $\mathbf{C}_v$ and $\mathbf{C}_h$, smoothing constraints are applied as additional equations in the inverse problem. The equations are defined by:

$$m_i\, {}_o u_i^{-1} = \frac{\sum_{j=1}^{k} \beta_j\, m_j\, {}_o u_j^{-1}}{\sum_{j=1}^{k} \beta_j}, \; i \neq j \tag{8}$$

where ${}_o u_j$ refers to a value from the prior model $u_o(\mathbf{r})$. The β_j are Gaussian weights:

$$\beta_j = \exp\left\{ \frac{-(x_j-x_i)^2}{\tau_x^2} + \frac{-(y_j-y_i)^2}{\tau_y^2} + \frac{-(z_j-z_i)^2}{\tau_z^2} \right\} \tag{9}$$

and the τ are assigned decay lengths. Only nodes within one decay length of a model parameter are given nonzero weight.

The velocity perturbations are estimated from an iterative solution of the linearized problem. The final perturbational model is the sum of all previous perturbational models $\mathbf{i}_{\mathrm{m}}$. The method uses a jumping strategy [*Shaw and Orcutt*, 1985], so model constraints are operative on perturbations with respect to the starting model. The linearized inverse problem for the i+1th iteration is:

$$\begin{bmatrix} \mathbf{C}_d^{-1/2}\mathbf{G} \\ \lambda_p \mathbf{C}_p^{-1/2} \\ \lambda_v \mathbf{C}_v \\ \lambda_h \mathbf{C}_h \end{bmatrix} \left[\mathbf{m}_{i+1}\right] = \begin{bmatrix} \mathbf{C}_d^{-1/2}\mathbf{d} \\ -\lambda_p \mathbf{C}_p^{-1/2}\mathbf{m}_i \\ -\lambda_v \mathbf{C}_v \mathbf{m}_i \\ -\lambda_h \mathbf{C}_h \mathbf{m}_i \end{bmatrix} \tag{10}$$

where G is the Frechet matrix of partial derivatives from (6). The LSQR method is used to solve (10).

Further details are explained in *Toomey et al.* [1994].

Acknowledgements

The success of the experiment was largely due to the technical expertise of John Bailey, Tim Barash, Dave Dubois, John Hallinan, Ken Peal, and Beecher Wooding. We are also grateful to the captain and the crew of the R/V *Oceanus* and the R/V *Ewing* for their help at sea. John Collins graciously provided software for data handling. We thank Andrew Barclay, John Collins, Jian Lin, Peter Shaw, and Debbie Smith for helpful information. This research was supported by the National Science Foundation under grants OCE-9019717 to MIT, OCE-9019683 to WHOI, and OCE-9018389 to UO.

REFERENCES

Barclay, A., D. R. Toomey, G. M. Purdy, and S. C. Solomon, Fara microearthquake experiments III: Results from the Mid-Atlantic Ridge at 35°N (abstract), *Eos Trans. AGU, 74,* Fall Meeting suppl., p. 601, 1993.

Bergman, E. A., and S. C. Solomon, Earthquake swarms on the Mid-Atlantic Ridge: Products of magmatism or extensional tectonics?, *J. Geophys. Res., 95*, 4943-4965, 1990.

Blackman, D. K., and D. W. Forsyth, Isostatic compensation of tectonic features of the Mid-Atlantic Ridge: 25°-27°30'S, *J. Geophys. Res., 96*, 11,741-11,758, 1991.

Brace, W. F., and J. D. Byerlee, Stick slip as a mechanism for earthquakes, *Science, 153*, 1563-1575, 1967.

Campbell, A. C., M. R. Palmer, G. P. Klinkhammer, T. S. Bowers, J. M. Edmond, J. R. Lawrence, J. F. Casey, G. Thompson, S. Humphris, P. Rona, and J. A. Karson, Chemistry of hot springs on the Mid-Atlantic Ridge, *Nature, 335*, 514-519, 1988.

Chen, W.-P., and P. Molnar, Focal depths of intracontinental and intraplate earthquakes and their implications for the thermal and mechanical properties of the lithosphere, *J. Geophys. Res., 88*, 4183-4214, 1983.

Cowie, P. A., C. H. Scholz, M. Edwards, and A. Malinverno, Fault strain and seismic coupling on mid-ocean ridges, *J. Geophys. Res., 98*, 17,911-17,920, 1993.

Creager, K. C., and L. M. Dorman, Location of instruments on the seafloor by joint adjustment of instrument and ship positions, *J. Geophys. Res., 87*, 8379-8388, 1982.

Crouch, J. H. and K. R. Osborne, Atlantic Ocean/ASEPS sound speed profiles, Colborn-analyzed watermass data base, Technical Report, Ocean Data Systems, Inc., San Diego, CA, 1981.

Detrick, R. S., H. D. Needham, and V. Renard, Gravity anomalies and crustal thickness variations along the Mid-Atlantic Ridge between 33°N and 40°N, *J. Geophys. Res.*, submitted 1994

Duschenes, J., R. C. Lilwall, and T. J. G. Francis, The hypocentral resolution of microearthquake surveys carried out at sea, *Geophys. J. R. Astron. Soc., 72*, 435-451, 1983.

Einarsson, P., Earthquakes and present-day tectonism in Iceland, *Tectonophysics, 189*, 261-279, 1991.

Einarsson, P., Seismicity and earthquake focal mechanisms alonng the Mid-Atlantic plate boundary between Iceland and the Azores, *Tectonophysics, 55*, 127-153, 1979.

Elderfield, H., C. R. German, and M. R. Palmer, Hydrothermal activity on the Mid-Atlantic Ridge at 29°N: Results of RRS Charles Darwin Cruise 77 (BRIDGE Cruise No. 8), *BRIDGE Newsletter, 5,* 7-10, 1993.

Escartin, J., and J. Lin, Gravity constraints on the style of crustal thinning at the Mid-Atlantic Ridge (abstract), *Eos Trans. AGU, 74,* Fall Meeting suppl., pp. 664-665, 1993.

Fowler, C. M. R., Crustal structure of the Mid-Atlantic ridge crest at 37°N, *Geophys. J. R. Astron. Soc., 47*, 459-491, 1976.

Fowler, C. M. R., and C. E. Keen, Oceanic crustal structure - Mid-Atlantic Ridge at 45°N, *Geophys. J. R. Astron. Soc., 56*, 219-226, 1979.

Francheteau, J., and R. D. Ballard, The East Pacific Rise near 21°N, 13°N and 20°S: Inferences for along strike variability of axial processes at mid ocean ridges, *Earth Planet. Sci. Lett., 64*, 93-116, 1983.

Francis, T. J. G., The ratio of compressional to shear velocity and rock porosity on the axis of the Mid-Atlantic Ridge, *J. Geophys. Res., 81*, 4361-4364, 1976.

Francis, T. J. G., I. T. Porter, and R. C. Lilwall, Microearthquakes near the eastern end of St. Paul's Fracture Zone, *Geophys. J. R. Astron. Soc., 53*, 201-217. 1978.Francis, T. J. G., I. T. Porter, and R. C. Lilwall, Microearthquakes near the eastern end of St. Paul's Fracture Zone, *Geophys. J. R. Astron. Soc., 53*, 201-217. 1978.

Gillis, K. M., G. Thompson, and D. S. Kelley, A view of the lower crustal component of hydrothermal systems at the Mid-Atlantic Ridge, *J. Geophys. Res., 98*, 19,597-19,619, 1993.

Gregory, R. T., and H. P. Taylor, Jr., An oxygen isotope profile in a section of Cretaceous oceanic crust, Samail Ophiolite, Oman: Evidence for $\delta^{18}O$ buffering of the oceans by deep (> 5 km) seawater-hydrothermal circulation at mid-ocean ridges, *J. Geophys. Res., 86*, 2737-2755, 1981.

Harper, G. D., Tectonics of slow spreading mid-ocean ridges and consequences of a variable depth to the brittle/ductile transition, *Tectonics, 4*, 395-409, 1985.

Henstock, T. J., A. W. Woods, and R. S. White, The accretion of oceanic crust by episodic sill intrusion, *J. Geophys. Res., 98*, 4143-4161, 1993.

Huang, P. Y., and S. C. Solomon, Centroid depths of mid-ocean ridge earthquakes: Dependence on spreading rate, *J. Geophys. Res., 93*, 13,445-13,477, 1988.

Jacobson, R. S., Dorman, L. M., Purdy, G. M., Schultz, A., and Solomon, S. C., New ocean bottom seismometer facilities available for use, *Eos Trans. AGU, 72*, 506, 515.

Klein, F. W., Hypocenter location program HYPOINVERSE, 1, User's guide to versions 1, 2, 3, 4, *U.S. Geological Surv. Open File Rep., 78-694*, 103 pp., 1978.

Klein, F. W., Earthquakes at Loihi submarine volcano and the Hawaiian hot spot, *J. Geophys. Res., 87*, 7719-7726, 1982.

Klein, F. W., The seismicity of Kilauea's magma system, *U. S. Geol. Surv. Prof. Pap. 1350*, 1019-1186, 1987.

Kong, L. S. L., S. C. Solomon, and G. M. Purdy, Microearthquake characteristics of a mid-ocean ridge along-axis high, *J. Geophys. Res., 97*, 1659-1685, 1992.

Kuo, B.-Y., and D. W. Forsyth, Gravity anomalies of the ridge-transform system in the South Atlantic between 31° and 34.5°S: Upwelling centers and variations in crustal thickness, *Mar. Geophys. Res., 10*, 205-232, 1988.

Lilwall, R. C., and T. J. G. Francis, Hypocentral resolution of small ocean bottom seismic networks, *Geophys. J. R. Astron. Soc., 54*, 721-728, 1978.

Lin, J., and E. A. Bergman, Rift grabens, seismicity, and volcanic segmentation of the Mid-Atlantic Ridge: Kane to Atlantis Fracture Zones (abstract), *Eos Trans. AGU, 71*, 1572, 1990.

Lin, J., G. M. Purdy, H. Schouten, J.-C. Sempere, and C. Zervas, Evidence from gravity data for focused magmatic accretion along the Mid-Atlantic Ridge, *Nature, 344*, 627-632, 1990.

Lister, C. R. B., On the thermal balance of an oceanic ridge, *Geophys. J. R. Astron. Soc., 26*, 515-535, 1972.

Macdonald, K. C., P. J. Fox, L. J. Perram, M. F. Eisen, R. M. Haymon, S. P. Miller, S. M. Carbotte, M.-H. Cormier, and A. N. Shor, A new view of the mid-ocean ridges from the behavior of ridge-axis discontinuities, *Nature, 335*, 217-225, 1988.

Mével, C., and M. Cannat, Lithospheric stretching and hydrothermal processes in oceanic gabbros from slow-spreading ridges, in *Ophiolite Genesis and Evolution of Oceanic Lithosphere*, edited by T. J. Peters, A. Nicolas, and R. G. Colman, pp. 293-312, Kluwer Academic, Hingham, Mass., 1991.

Morris, E., and R. S. Detrick, Three-dimensional analysis of gravity anomalies in the MARK area, Mid-Atlantic Ridge 23°N, *J. Geophys. Res., 96*, 4355-4366, 1990.

Moser, T. J., Shortest path calculation of seismic rays, *Geophysics, 56*, 59-67, 1991.

Muir-Wood, R., and G. C. P. King, Hydrological signatures of earthquake strain, *J. Geophys. Res., 98*, 22,035-22,068, 1993.

Murray, M. H., L. Kong, D. W. Forsyth, S. C. Solomon, and D. M. Hussong, An OBS study of microearthquakes in the median valley on the Mid-Atlantic Ridge near 35°N (abstract), *Eos Trans. AGU, 65*, 1009, 1986.

Murton, B. J., K. Becker, A. Brias, D. Edge, N. Hayward, G. Klinkhammer, N. Millard, I. Mitchell, I. Rouse, M. Rudnicki, K. Sayanagi, and H. Sloan, Results of a systematic approach to searching for hydrothermal activity on the Mid-Atlantic Ridge: The discovery of the "Broken Spur" vent site, *BRIDGE Newsletter, 4,* 3-6, 1993.

Nehlig, P., and T. Juteau, Deep crustal seawater penetration and circulation at ocean ridges: Evidence from the Oman ophiolite, *Mar. Geology, 84*, 209-228, 1988.

Neumann, G. A., and D. W. Forsyth, The paradox of the axial profile: Isostatic compensation along the axis of the Mid-Atlantic Ridge, *J. Geophys. Res., 98*, 17,891-17,910, 1993.

Nicolas, A., I. Reuber, and K. Benn, A new magma chamber model based on structural studies in the Oman ophiolite, *Tectonophysics, 151*, 87-105, 1988.

Nisbet, E. G., and C. M. R. Fowler, The Mid-Atlantic Ridge at 37 and 45°N: Some geophysical and petrological constraints, *Geophys. J. R. Astron. Soc., 54*, 631-660, 1978.

Phipps Morgan, J., and Y. J. Chen, The genesis of oceanic crust: Magma injection, hydrothermal circulation, and crustal flow, *J. Geophys. Res., 98*, 6283-6297, 1993.

Prothero, W. A., and I. D. Reid, Microearthquakes on the East Pacific Rise at 21° N and the Rivera Fracture Zone, *J. Geophys. Res., 87*, 8509-8518, 1982.

Purdy, G. M. and R. S. Detrick, Crustal structure of the Mid-Atlantic Ridge at 23°N from seismic refraction studies, *J. Geophys. Res., 91*, 3739-3762, 1986.

Purdy, G. M., J.-C. Sempere, H. Schouten, D. L. Dubois, and R. Goldsmith, Bathymetry of the Mid-Atlantic Ridge, 24°N-31°N: A map series, *Mar. Geophys. Res., 12*, 247-252, 1990.

Purdy, G. M., L. S. L. Kong, G. C. Christeson, and S. C. Solomon, Relationship between spreading rate and the seismic structure of mid-ocean ridges, *Nature, 355*, 815-817, 1992.

Rojstaczer, S., and S. Wolfe, Permeability changes associated with large earthquakes: An example from Loma Prieta, California, *Geology, 20*, 211-214, 1992.

Rona, P. A., G. Klinkhammer, T. A. Nelsen, J. H. Trefry, and H. Elderfield, Black smokers, massive sulfides and vent biota at the Mid-Atlantic Ridge, *Nature, 321*, 33-37, 1986.

Rowlett, H., Seismicity at intersections of spreading centers and transform faults, *J. Geophys. Res., 86*, 3815-3820, 1981.

Rowlett, H., and D. W. Forsyth, Recent faulting and microearthquakes at the intersection of the Vema Fracture Zone and the Mid-Atlantic Ridge, *J. Geophys. Res., 89*, 6079-6094, 1984.

Scholz, C. H., The critical slip distance for seismic faulting, *Nature, 336*, 761-763, 1988.

Scholz, C. H., *The Mechanics of Earthquakes and Faulting*, Cambridge University Press, New York, 439 pp., 1990.

Schouten, H., K.D. Klitgord, and J. A. Whitehead, Segmentation of mid-ocean ridges, *Nature, 317*, 225-229, 1985.

Sempere, J.-C., G. M. Purdy, H. Schouten, The segmentation of the Mid-Atlantic Ridge between 24°N and 30°40'N, *Nature, 344*, 427-431, 1990.

Sempere, J.-C., J. Lin, H. S. Brown, H. Schouten, and G. M. Purdy, Segmentation and morphotectonic variations along a slow-spreading center: The Mid-Atlantic Ridge (24°00'N-30°40'N), *Mar. Geophys. Res., 15*, 153-200, 1993.

Shaw, P. R., Ridge segmentation, faulting and crustal thickness in the Atlantic Ocean, *Nature, 358*, 490-493, 1992.

Shaw, P. R., and J. Lin, Causes and consequences of variations in faulting style at the Mid-Atlantic Ridge, *J. Geophys. Res., 98*, 21,839-21,851, 1993.

Shaw, P. R., and J. A. Orcutt, Waveform inversion of seismic refraction data and application to young Pacific crust, *Geophys. J. R. Astron. Soc., 82*, 375-414, 1985.

Smith, D. K., and J. R. Cann, Building the crust at the Mid-Atlantic Ridge, *Nature, 365*, 707-715, 1993.

Thurber, C. H., Earth structure and earthquake locations in the Coyote Lake area, central California, Ph. D. thesis, 332 pp., Mass. Inst. of Technol., Cambridge, 1981.

Thurber, C. H. Earthquake locations and three-dimensional crustal structure in the Coyote Lake area, central California, *J. Geophys. Res., 88*, 8226-8236, 1983.

Tolstoy, M., A. J. Harding, and J. A. Orcutt, Crustal thickness on the Mid-Atlantic Ridge: Bull's eye gravity anomalies and focused accretion, *Science, 262*, 726-729, 1993.

Toomey, D. R., S. C. Solomon, G. M. Purdy, and M. H. Murray, Microearthquakes beneath the median valley of the Mid-Atlantic Ridge near 23°N: Hypocenters and focal mechanisms, *J. Geophys. Res., 90*, 5443-5458, 1985.

Toomey, D. R., S. C. Solomon, and G. M. Purdy, Microearthquakes beneath the median valley of the Mid-Atlantic Ridge near 23°N: Tomography and tectonics, *J. Geophys. Res., 93*, 9093-9112, 1988.

Toomey, D. R., S. C. Solomon, and G. M. Purdy, Tomographic imaging of the shallow crustal structure of the East Pacific Rise, *J. Geophys. Res.*, submitted 1994

Tréhu, A. M., and S. C. Solomon, Earthquakes in the Orozco transform zone: Seismicity, source mechanisms, and tectonics, *J. Geophys. Res., 88*, 8203-8225, 1983.

Tse, S., and J. R. Rice, Crustal earthquake instability in relation to the depth variation of frictional slip processes, *J. Geophys. Res., 91*, 9452-9472, 1986.

Vanko, D. A., and D. S. Stakes, Fluids in oceanic layer 3: Evidence from veined rocks, Hole 735B, Southwest Indian Ridge, *Proc. Ocean Drill. Program Sci. Results, 118*, 181-215, 1991.

Von Damm, K. L., J. M. Edmond, B. Grant, C. I. Measures, B. Walden, and R. F. Weiss, Chemistry of submarine hydrothermal solutions at 21°N, East Pacific Rise, *Geochim. Cosmochim. Acta, 49*, 2197-2220, 1985.

Von Damm, K. L., J. L. Bischoff, and R. J. Rosenbauer, Quartz solubility in hydrothermal seawater: An experimental study and equation describing quartz solubility for up to 0.5 M NaCl solutions, *Am. J. Sci., 291*, 977-1007, 1991.

Whitehead, J. A., Jr., H. J. B. Dick, and H. Schouten, A mechanism for magmatic accretion under spreading centers, *Nature, 312*, 146-148, 1984.

Wiggins, R. A., The general linear inverse problem: Implication of surface waves and free oscillations for earth structure, *Rev. Geophys., 10*, 251-285, 1972.

Wilcock, W. S. D., and D. R. Toomey, Estimating hypocentral uncertainties for microearthquake surveys conducted at sea: A comparison of generalized inverse and grid search methods, *Mar. Geophys. Res., 13*, 161-171, 1991.

FIGURE CAPTIONS

Figure 1. Bathymetry at the Mid-Atlantic Ridge at 29°N, 500-m contour interval. Filled circles are epicenters of earthquakes (1964 to March 1989) reported by the International Seismological Centre (ISC). According to the Preliminary Determination of Epicenters (PDE) Catalogue, no large earthquakes occurred in this area between April 1989 and June 1993.

Figure 2. Locations of OBSs (filled triangles with OBS numbers) and explosive shots (filled circles). Bathymetry contoured at 500-m interval.

Figure 3. Some typical seismograms of microearthquakes, as recorded on the vertical (V), horizontal (H1 and H2), or hydrophone (HY) channels. Vertical bars mark arrival times of *P* waves on vertical and hydrophone channels and *S* waves on the horizontals. Each seismogram is scaled to the same maximum amplitude. Upward *P* wave first motions correspond to compressions on the vertical and dilatations on the hydrophone. Seismometer coupling problems are evident for OBS 61, but clear *P* and *S* arrivals could nonetheless often be picked.

Figure 4. Number of events versus number of instruments that simultaneously triggered. Over 1000 events (20 to 35 events per day) were recorded on 4 or more OBSs.

Figure 5. One-dimensional velocity-depth model used for HYPOINVERSE (dashed line), compared with the models of *Purdy and Detrick* [1986] (solid line) and *Fowler* [1976] (dash dot line).

Figure 6. Plots of differential *S* wave arrival times versus differential *P* wave arrival times for earthquakes simultaneously recorded on three OBS pairs. Solid lines are least squares fits and give V_p/V_s ratios of 1.80 to 1.83. Note that microearthquakes located at the segment center plot as negative points, while those from the southern segment terminus are positive.

Figure 7. Locations of all microearthquakes. Small filled circles denote microearthquakes with resolved focal depth; white diamonds show microearthquakes with depth fixed at 5 km below datum. OBSs that recorded microearthquake data are shown as filled triangles. OBS 60, which recorded one day of data and was not relocated, is shown as a white triangle. *P* and *S* wave arrivals from this instrument, deployed in the northern section of the network, were important for locating about a dozen microearthquakes near the segment center. Bathymetry contoured at 500-m interval.

Figure 8. Microearthquakes near the southern deep. Bathymetry contoured at 50-m interval. Arrows mark trend of the axial volcanic ridge (AVR). See Figure 7 for further information.

Figure 9. Microearthquakes at the central along-axis high. Arrows mark trend of axial volcanic ridge (AVR). Star is location of Broken Spur Hydrothermal Vent Field from *Elderfield et al.* [1993]. See Figure 7 for further information.

Figure 10. Location of along-axis and cross-axis profiles (solid lines) plotted in Figures 11 and 12. See Figure 7 for further information.

Figure 11. Distribution of microearthquakes along axis. Only microearthquakes with epicenters within 3 km distance of the along-axis profile in Figure 10 are plotted. Solid circles are microearthquake hypocenters, and error bars are 95% confidence intervals. Bathymetry shown as solid line.

Figure 12. (a) Cross-axis distribution of microearthquakes at the segment center. (b) Cross-axis distribution of microearthquakes at the segment end. Only events with epicenters within 5 km of the profiles in Figure 10 are plotted. See Figure 11 for further information.

Figure 13. Along-axis distribution of a subset of high quality focal depths (from microearthquakes recorded on 5 or more OBSs). See Figure 11 for further information.

Figure 14. Cross-axis distribution of a subset of high quality focal depths (from microearthquakes recorded on 5 or more OBSs). a) Cross-axis distribution of microearthquakes at the segment center. b) Cross-axis distribution of microearthquakes at the segment end. Only events with epicenters within 5 km of the profiles in Figure 10 are plotted. See Figure 11 for further information.

Figure 15. a) Composite first motion data for three events near the western basin at the southern deep. Equal-area projection of lower hemisphere. Solid circles are compressional arrivals, open circles are dilatational. Nodal planes and solution (strike/dip/slip) is shown. b) and c) Composite focal mechanism for three events beneath an axial volcano; two possible solutions are shown. d) and e) First motion data for two events at the segment center. The small number of data and limited coverage are not sufficient to determine a mechanism.

Figure 16. Summary of focal mechanisms of microearthquakes at 29°N. Normal faulting is occurring beneath the western basin of the segment deep. Two types of mechanisms are possible for events beneath the along-axis volcano near 29°2'N.

Figure 17. The number N of earthquakes with moment in excess of M_0. The straight line is the least squares fit to the data with $5x10^{17} \leq M_0 \leq 5x10^{19}$.

Figure 18. Locations of shots and 11 OBSs used for tomographic inversions, as discussed in the text. Dashed line shows the vertical plane for 2-D models obtained with data from only 6 OBSs. Box shows region for 3-D models, with along-axis position y ranging

from -14 to 38 km and cross-axis position x ranging from -7 to 7 km (south and west are negative values; dashed line marks x=0).

Figure 19. Solutions from 2-D inversion using the method of *Toomey et al.* [1994]. a) *P* wave velocity; 0.5 km/s contour interval. b) The spatially-averaged derivative weight sum (DWS) [c.f. *Toomey et al.*, 1994], which provides a meaure of the ray density in the perturbational velocity model. Velocity grid is spaced at 250 m in the horizontal and vertical directions. Inversion solves for perturbations at 3 km intervals along axis and 1 km intervals in the vertical direction.

Figure 20. a) 2-D *P* wave velocity obtained with *Thurber's* [1981, 1983] method, 0.5 km/s contour interval. The positions of 6 OBSs are indicated by x's. Velocity nodes are at 200, -10, 0, 10, 20, and 200 km in the horizontal direction, and at -50, 0, 1, 3, 5, and 50 km depth. Velocity between nodes is obtained by linear interpolation [*Thurber*, 1981]. Higher velocities occur at the segment end.

Figure 21. Solutions from 3-D inversion using the method of *Toomey et al.* [1994]. a) Axis-parallel cross sections of *P* wave velocity; 0.5 km/s contour interval. b) DWS, for the same cross sections. The cross-axis position is given by the x coordinate (Figure 18). c) Model perturbations; 0.1 km/s contour interval.

Figure 22. Resolution test at the segment end. a) Input 2-D model. 7 km/s homogeneous velocity material is imbedded in 6 km/s material. b) Pertubational solution; 0.1 km/s contour interval, using the starting ray set for our 3-D model at 29°N.

Figure 23. Resolution test near the segment center. a) Input 2-D model. 7 km/s homogeneous velocity material is imbedded in 6 km/s material. b) Pertubational solution; 0.1 km/s contour interval.

Figure 24. Resolution test for the crust east of the axis. a) Input 2-D model. 7 km/s homogeneous velocity material is imbedded in 6 km/s material. b) Pertubational solution; 0.1 km/s contour interval.

Figure 25. Epicenters determined from a grid search on a 3-D velocity model (white diamonds) and from HYPOINVERSE with a 1-D velocity model (filled circles). Solid lines connect epicenters for commen events. See Figure 10 for further information.

Figure 26. The along-axis distribution of hypocenters determined from a grid search on a 3-D velocity model (white diamonds) and from HYPOINVERSE with a 1-D velocity model (filled circles). Solid lines connect hypocenters for common events. a) All events within 3 km distance of the along-axis profile in Figure 10. b) All microearthquakes recorded by 5 or more OBSs within 3 km distance of the along-axis profile in Figure 10.

Figure 27. Minimum rms misfit to *P* and *S* arrival times versus focal depth (250 m spacing) derived from the grid search limits on focal depth. The dashed line shows the 95% confidence level. The epicenter at the top of each plot is for the best-fitting hypocenter from the grid search. All events shown here have well-constrained focal depth.

Figure 28. Minimum rms misfit to *P* and *S* arrival times versus focal depth (250 m spacing) derived from the grid search limits on focal depth (see Figure 27 for further information). Very shallow focal depths are poorly constrained. Errors in focal depth are large for some earthquakes with subcrustal hypocenters.

Figure 29. A comparison of our 3-D velocity solution (see Figure 21) with crustal thickness variations calculated by *Lin et al.* [1990] from gravity data (bold line). Higher velocities near the segment end are interpreted as indicating a thinner lower crust. The mean crustal thickness inferred from gravity is arbitrary. Wavelengths shorter than 25 km in the gravity field are filtered out to prevent amplification in the process of downward continuation.

Figure 30. Profiles of residual gravity anomaly data, equal to the MBA corrected for the effects of lithospheric cooling [*Lin et al.*, 1990].

Table 1. Relocated Instrument Positions

Instr	Latitude, N	Longitude, W	Depth, m	Station Delay, s
OBS 51	28° 57.57'	43° 17.81'	2738	0.04
OBS 53	28° 55.49'	43° 10.33'	3255	-0.01
OBS 54	29° 10.14'	43° 11.33'	3205	0.01
OBS 55	29° 05.56'	43° 11.73'	3124	0.02
OBS 56	29° 02.58'	43° 11.10'	3458	-0.04
OBS 57	29° 00.22'	43° 14.34'	3284	-0.05
OBS 58	28° 52.95'	43° 17.02'	3869	-0.13
OBS 59	28° 56.52'	43° 13.73'	3425	0.02
OBS 60	29° 07.60'	43° 09.67'	3275	-0.01
OBS 61	29° 08.45'	43° 06.86'	2659	0.14
OBS 63	28° 58.93'	43° 10.17'	3113	-0.09
OBS 64	29° 07.60'	43° 13.17'	2714	0.02

Table 2. Earthquake Hypocenters

Date	Origin Time	REG	Lat., N	Long., W	ERH, km	DBD, km	ERZ, km	P	S	MAG, deg	DCS, km	RMS, s	M_o, dyn cm
08 22	17:16:01.32	5	29 12.57	43 09.08	2.9	5.6	0.6	4	2	294	03	0.05	0.2E+18
08 23	06:29:46.94	2	28 57.22	43 21.34	3.0	4.3	0.5	5	1	308	06	0.02	0.9E+18
08 23	08:27:06.02	5	29 11.96	43 10.20	2.8	5.0	pdc	4	1	289	04	0.06	0.2E+19
08 23	08:32:14.30	5	29 11.63	43 10.13	1.7	3.6	0.4	10	2	282	03	0.08	0.9E+19
08 23	09:39:38.89	2	28 56.62	43 14.97	0.5	4.5	0.6	10	2	102	02	0.02	0.5E+20
08 24	05:23:10.77	5	29 12.04	43 11.07	4.0	4.9	0.9	4	1	279	04	0.00	0.1E+18
08 24	07:14:05.60	3	28 56.36	43 15.01	1.3	5.5	1.1	5	1	196	02	0.01	0.3E+19
08 24	13:17:58.32	6	29 03.51	43 28.48	2.3	5.0	pdc	4	1	304	21	0.14	0.6E+19
08 24	21:34:10.75	5	29 13.86	43 08.26	1.7	5.0	pdc	4	2	311	09	0.18	0.6E+19
08 25	03:02:18.55	2	28 54.19	43 22.06	4.0	5.0	pdc	4	0	285	09	0.01	0.8E+18
08 25	05:11:08.38	2	28 59.25	43 17.09	0.8	5.2	0.7	8	3	181	03	0.04	0.1E+19
08 25	05:25:16.89	5	29 10.39	43 09.48	2.8	6.3	2.1	4	2	228	03	0.01	0.9E+18
08 25	13:04:59.99	5	29 11.03	43 10.10	2.2	5.0	pdc	3	1	261	03	0.02	0.2E+19
08 25	15:49:43.59	3	28 53.91	43 17.10	2.2	5.0	pdc	4	0	176	02	0.02	0.5E+18
08 25	18:15:12.30	5	29 10.04	43 10.55	1.2	5.0	pdc	3	1	197	01	0.06	0.6E+18
08 26	05:22:49.71	2	28 58.23	43 18.61	2.3	5.9	1.1	5	1	221	02	0.02	0.2E+18
08 26	06:46:09.06	5	29 11.49	43 09.59	3.5	5.0	pdc	4	1	272	04	0.01	0.4E+18
08 26	07:38:40.32	2	28 58.35	43 17.53	1.5	5.7	1.9	4	1	184	02	0.01	0.1E+18
08 26	07:45:53.93	2	28 57.18	43 20.44	2.6	5.0	pdc	4	0	247	04	0.01	0.6E+18
08 26	11:54:56.35	3	28 56.18	43 12.99	1.1	5.1	0.6	5	2	187	01	0.05	0.5E+19
08 26	15:18:46.38	5	29 10.96	43 10.11	2.0	5.0	pdc	4	1	258	03	0.02	0.6E+18
08 26	19:30:39.74	2	28 53.89	43 18.74	1.6	5.0	pdc	5	0	258	03	0.02	0.1E+19
08 26	21:29:56.32	3	28 56.82	43 14.85	0.5	4.5	0.7	7	1	100	02	0.01	0.1E+19
08 26	22:39:14.75	2	28 57.30	43 19.38	0.8	5.1	1.1	6	2	233	03	0.03	0.2E+19
08 26	23:14:16.06	5	29 14.75	43 07.85	1.6	5.0	pdc	8	2	318	10	0.19	0.5E+19
08 27	03:45:11.60	4	29 03.83	43 12.67	0.9	3.4	1.2	6	3	154	03	0.06	0.1E+19
08 27	15:35:38.85	3	28 56.37	43 15.61	2.2	4.6	0.9	5	1	242	04	0.01	0.3E+18
08 27	19:50:23.49	5	29 10.19	43 09.79	1.0	4.1	0.6	7	3	216	03	0.05	0.1E+20
08 27	20:44:37.25	5	29 10.02	43 10.40	1.3	4.1	0.5	9	2	259	02	0.04	0.1E+21
08 27	20:53:22.22	5	29 10.92	43 10.95	1.7	5.0	pdc	4	0	325	02	0.03	0.1E+20
08 28	00:42:41.66	5	29 10.16	43 10.01	5.0	4.0	1.9	4	1	272	02	0.02	0.4E+19
08 28	04:55:11.91	2	28 54.87	43 24.03	1.1	5.0	pdc	5	2	289	12	0.07	0.1E+19
08 28	09:33:47.03	1	28 50.56	43 30.70	9.0	5.0	pdc	5	0	322	23	0.07	0.2E+19
08 28	16:59:22.74	5	29 10.25	43 10.29	2.1	4.1	0.9	7	1	276	02	0.08	0.2E+19
08 28	19:19:45.16	6	29 02.25	43 14.98	4.1	5.0	pdc	4	0	316	04	0.01	0.4E+19
08 28	21:33:41.31	6	29 14.24	43 12.38	8.4	5.0	pdc	4	0	304	14	0.03	0.5E+19
08 29	01:22:42.02	2	28 54.35	43 24.34	7.7	5.0	pdc	5	0	314	12	0.11	0.1E+20
08 29	02:36:11.69	2	28 54.38	43 21.22	1.2	5.0	pdc	7	2	290	07	0.13	0.7E+19
08 29	06:26:42.12	5	29 11.87	43 09.80	0.9	3.7	0.5	5	3	288	08	0.01	0.3E+19
08 29	09:02:31.84	5	29 12.40	43 11.68	3.8	5.0	pdc	3	1	336	04	0.01	0.1E+19
08 29	11:15:40.49	5	29 11.27	43 09.65	1.9	3.5	0.5	6	2	291	07	0.04	0.1E+20
08 29	15:24:27.33	1	28 51.22	43 26.28	2.5	5.0	pdc	5	2	327	15	0.07	0.4E+20
08 29	16:53:43.09	2	28 57.26	43 25.47	1.3	5.0	pdc	5	2	283	12	0.11	0.6E+18
08 29	18:03:37.98	1	28 42.64	43 30.28	3.1	5.0	pdc	5	1	343	29	0.04	0.6E+19
08 29	19:09:47.18	5	29 11.93	43 09.53	3.1	5.2	1.1	4	2	284	04	0.01	0.1E+19
08 29	20:08:24.77	2	28 58.30	43 20.65	1.1	4.3	0.9	6	1	246	05	0.05	0.8E+18
08 29	22:40:03.19	5	29 10.62	43 10.51	2.9	5.0	pdc	4	1	331	20	0.10	0.1E+20
08 29	22:58:05.42	5	29 11.79	43 09.64	2.5	5.0	pdc	3	1	287	08	0.05	0.4E+19
08 30	01:30:41.15	5	29 11.58	43 09.54	1.1	5.9	1.0	4	3	275	04	0.02	0.2E+18

08 30	02:53:57.99	5	29 10.59	43 09.73	1.3	6.6	1.5	4	2	237	03	0.03	0.3E+18
08 30	03:27:20.15	5	29 12.18	43 09.58	2.2	7.8	3.0	4	1	290	05	0.02	0.2E+18
08 30	03:29:33.90	5	29 11.66	43 09.51	3.1	5.0	0.9	4	1	277	04	0.01	0.2E+18
08 30	04:50:25.73	3	28 55.47	43 12.91	1.6	4.4	0.4	7	1	202	02	0.05	0.5E+18
08 30	05:46:35.76	5	29 12.06	43 09.74	2.2	4.8	1.6	3	2	289	04	0.02	0.9E+17
08 30	06:03:18.47	5	29 11.18	43 09.76	1.5	5.7	0.7	4	3	264	03	0.02	0.2E+19
08 30	06:06:09.87	5	29 11.47	43 09.66	0.9	5.2	0.5	5	4	273	04	0.04	0.9E+18
08 30	06:15:19.51	5	29 11.75	43 09.57	2.3	6.2	0.8	4	2	280	04	0.03	0.3E+18
08 30	08:05:43.80	5	29 15.43	43 09.14	8.1	5.0	pdc	4	0	319	10	0.02	0.4E+18
08 30	15:10:22.79	5	29 11.25	43 09.86	2.3	5.9	2.3	4	1	266	03	0.00	0.4E+18
08 30	15:51:55.49	5	29 12.41	43 09.61	1.7	6.3	1.9	4	2	294	05	0.02	0.2E+18
08 30	16:03:49.15	2	28 51.57	43 19.28	7.4	5.0	pdc	6	0	317	04	0.06	0.2E+19
08 30	16:14:48.71	5	29 12.19	43 09.75	1.6	6.1	1.1	4	2	291	05	0.02	0.3E+19
08 30	17:38:39.59	5	29 11.38	43 09.81	1.5	6.8	1.5	4	2	270	03	0.02	0.2E+18
08 30	21:51:59.95	5	29 12.07	43 09.02	1.9	3.1	0.6	4	2	285	05	0.03	0.1E+19
08 30	22:28:04.83	1	28 50.10	43 26.99	1.7	5.0	pdc	6	2	323	17	0.07	0.7E+19
08 31	02:01:15.26	2	28 56.16	43 21.25	3.5	3.5	1.2	5	0	275	06	0.00	0.6E+18
08 31	15:07:29.97	3	28 55.06	43 14.20	1.8	4.8	0.4	7	1	188	03	0.02	0.2E+19
08 31	23:13:47.97	1	28 48.65	43 29.91	1.9	5.0	pdc	4	1	328	22	0.04	0.1E+19
09 01	00:33:46.34	5	29 12.12	43 09.17	2.5	5.0	pdc	4	2	287	05	0.11	0.3E+19
09 01	02:14:52.13	1	28 47.41	43 27.61	2.2	5.0	pdc	7	2	333	20	0.06	0.5E+19
09 01	03:16:15.05	2	28 58.64	43 15.33	1.0	3.4	0.5	7	1	127	03	0.05	0.8E+19
09 01	14:19:37.62	2	28 57.52	43 17.52	1.5	4.8	1.6	4	1	175	01	0.02	0.4E+18
09 01	14:34:54.76	2	28 57.40	43 18.03	1.1	4.1	0.8	8	0	214	00	0.03	0.1E+19
09 01	16:01:31.27	1	28 52.65	43 21.82	5.1	5.0	pdc	7	0	301	08	0.07	0.1E+20
09 01	18:23:39.10	5	29 11.87	43 09.99	2.6	6.8	1.6	4	2	286	04	0.05	0.2E+19
09 02	00:19:29.10	3	28 54.95	43 13.59	2.7	5.7	0.7	3	2	270	03	0.02	0.2E+19
09 02	01:36:21.17	5	29 12.80	43 09.48	1.0	5.0	pdc	7	3	300	06	0.21	0.4E+20
09 02	02:04:43.84	3	28 54.30	43 16.92	0.7	3.2	0.9	5	1	163	03	0.01	0.6E+18
09 02	02:28:00.09	5	29 13.61	43 08.89	1.9	4.0	6.0	4	2	309	08	0.01	0.4E+18
09 02	06:52:10.14	5	29 11.18	43 10.14	2.3	4.2	0.5	6	1	267	03	0.05	0.4E+19
09 02	09:40:29.74	2	28 55.94	43 18.37	1.6	4.9	0.4	6	0	218	03	0.01	0.1E+19
09 02	10:37:24.84	2	28 56.32	43 19.93	1.5	5.0	pdc	4	2	274	04	0.05	0.3E+18
09 02	13:07:18.56	3	28 55.87	43 13.23	1.7	5.0	pdc	4	0	188	08	0.01	0.3E+18
09 02	21:19:57.43	3	28 54.49	43 13.35	3.6	5.0	pdc	3	1	319	04	0.01	0.4E+19
09 03	00:35:37.44	2	28 53.79	43 19.23	1.2	3.6	1.0	7	2	265	04	0.01	0.6E+19
09 03	06:13:29.92	2	28 57.78	43 16.47	1.0	5.0	pdc	8	2	143	02	0.04	0.4E+18
09 03	11:43:03.05	2	28 54.56	43 19.44	1.1	2.4	1.1	8	2	255	05	0.03	0.9E+19
09 03	13:42:09.57	2	28 55.48	43 19.19	2.0	3.2	0.7	5	0	240	04	0.01	0.1E+19
09 03	13:56:47.52	3	28 56.32	43 15.14	0.6	4.6	0.5	6	2	127	02	0.03	0.1E+19
09 03	16:08:16.35	2	28 55.38	43 19.53	1.7	3.0	0.8	5	0	247	05	0.01	0.4E+18
09 03	18:52:03.34	2	28 57.48	43 22.80	0.9	3.0	1.1	7	3	267	08	0.08	0.2E+19
09 03	21:46:10.05	6	29 11.15	43 05.52	8.5	5.0	pdc	4	0	300	05	0.04	0.5E+20
09 04	23:00:50.31	1	28 53.17	43 20.78	3.8	5.0	pdc	8	0	291	06	0.08	0.3E+20
09 05	01:07:39.91	2	28 55.55	43 17.74	0.7	3.7	0.8	5	0	193	04	0.00	0.3E+18
09 05	18:50:00.29	4	29 02.42	43 11.81	1.0	4.2	3.3	4	1	161	06	0.03	0.2E+18
09 05	19:39:24.25	1	28 52.13	43 30.43	2.7	5.0	pdc	5	1	316	22	0.06	0.1E+19
09 05	19:57:26.69	2	28 55.88	43 22.35	2.8	5.0	pdc	4	1	285	08	0.06	0.6E+18
09 05	21:05:36.38	1	28 52.50	43 21.41	5.0	5.0	pdc	5	0	302	07	0.06	0.9E+18
09 06	04:01:56.22	4	29 02.54	43 12.04	0.6	5.0	pdc	5	2	129	06	0.05	0.6E+18
09 06	04:14:46.26	4	29 02.40	43 12.28	0.7	6.5	1.6	8	1	126	05	0.04	0.2E+19
09 06	04:25:39.35	2	28 56.10	43 23.48	3.0	5.0	pdc	4	1	314	10	0.05	0.2E+19
09 06	04:29:05.85	4	29 01.92	43 12.39	0.9	8.3	2.2	4	2	129	04	0.01	0.5E+18
09 06	04:50:21.30	4	29 02.30	43 12.19	0.7	6.8	1.5	6	1	124	05	0.04	0.8E+18
09 06	05:03:27.20	2	28 52.48	43 20.45	5.3	5.0	pdc	4	0	303	06	0.07	0.5E+18
09 06	05:08:01.17	2	28 59.27	43 16.94	0.6	5.7	0.8	8	1	176	03	0.02	0.2E+19
09 06	05:51:03.38	4	29 02.12	43 12.56	1.2	8.4	2.1	4	2	135	05	0.02	0.5E+18
09 06	06:03:40.10	4	29 02.42	43 12.03	0.9	5.0	pdc	4	1	164	06	0.02	0.2E+18
09 06	06:41:04.44	2	29 02.29	43 12.30	0.6	6.9	1.3	8	1	126	05	0.03	0.2E+19
09 06	06:59:38.71	4	29 02.16	43 12.35	1.2	8.0	2.2	4	1	131	05	0.01	0.6E+18
09 06	07:03:42.60	4	29 02.23	43 12.18	0.7	7.1	1.4	7	2	124	05	0.03	0.4E+18
09 06	07:16:25.25	4	29 02.18	43 12.17	0.7	7.3	1.4	7	2	124	05	0.04	0.9E+18
09 06	07:49:02.06	4	29 02.61	43 12.60	0.6	5.0	pdc	6	1	145	08	0.04	0.1E+19
09 06	07:56:45.79	1	28 51.01	43 25.46	2.2	5.0	pdc	5	1	330	14	0.06	0.1E+19
09 06	11:39:58.89	1	28 49.66	43 28.36	3.2	5.0	pdc	4	1	338	19	0.08	0.1E+19
09 06	11:56:18.04	4	29 02.49	43 12.13	1.0	5.0	pdc	4	1	164	06	0.04	0.1E+18
09 06	11:59:34.55	2	28 56.23	43 18.43	1.2	4.1	0.5	5	1	223	03	0.05	0.5E+18
09 06	12:37:05.63	5	29 09.83	43 09.85	1.7	2.8	1.7	5	2	193	02	0.05	0.5E+18
09 06	19:17:09.37	2	28 59.11	43 17.83	1.2	5.0	pdc	3	1	206	03	0.02	0.8E+17
09 07	01:35:17.59	2	28 52.75	43 19.43	2.5	3.8	0.6	7	1	292	04	0.03	0.2E+19
09 07	15:12:41.07	2	28 53.55	43 19.16	1.8	3.4	0.8	5	1	269	04	0.05	0.6E+18
09 07	17:08:49.12	2	28 53.11	43 18.96	2.3	4.1	0.8	7	0	277	03	0.02	0.5E+18
09 07	17:28:41.51	2	28 53.59	43 18.31	2.0	3.7	1.3	6	0	247	02	0.01	0.2E+19
09 07	19:11:20.85	2	28 58.82	43 19.76	1.7	4.3	1.6	5	0	236	04	0.00	0.1E+19
09 07	19:14:46.70	2	28 53.21	43 18.90	1.9	3.6	1.1	6	0	274	03	0.01	0.2E+18
09 08	04:12:01.18	1	28 52.80	43 21.32	5.9	5.0	pdc	5	0	305	07	0.04	0.3E+19

09 08	15:15:45.87	5	29 11.48	43 09.47	2.6	5.0	pdc	4	1	272	04	0.10	0.5E+18
09 08	18:50:48.15	5	29 12.43	43 09.20	1.3	3.1	0.6	5	2	292	05	0.06	0.1E+19
09 08	19:10:59.93	1	28 52.82	43 23.22	4.2	5.0	pdc	7	0	302	10	0.05	0.8E+18
09 09	01:02:00.62	2	28 55.78	43 18.83	1.8	5.0	0.7	5	0	232	04	0.16	0.3E+18
09 09	02:51:47.61	2	28 58.57	43 17.28	0.6	5.1	0.6	8	2	176	02	0.04	0.2E+19
09 09	05:17:48.91	2	28 56.98	43 19.07	2.5	4.1	0.9	5	1	229	02	0.07	0.2E+19
09 09	09:40:54.11	2	28 55.63	43 19.46	1.2	4.1	1.2	4	1	243	04	0.02	0.4E+18
09 09	11:55:32.45	3	28 55.87	43 15.10	2.6	5.0	pdc	3	1	252	05	0.01	0.5E+18
09 09	17:31:39.91	3	28 56.62	43 14.55	1.1	4.6	1.0	4	1	153	06	0.02	0.8E+18
09 09	18:26:06.86	2	28 58.01	43 18.79	0.9	4.8	0.9	7	2	225	02	0.02	0.2E+19
09 09	23:23:29.17	2	28 58.16	43 21.08	1.8	3.9	0.8	7	2	291	05	0.07	0.3E+19
09 10	00:01:34.45	1	28 49.35	43 24.79	3.0	5.0	pdc	4	1	327	14	0.08	0.1E+19
09 10	08:22:00.61	5	29 11.46	43 08.25	1.7	5.0	0.6	4	2	274	06	0.23	0.2E+19
09 10	19:57:10.92	2	29 00.13	43 17.53	1.0	5.2	1.1	6	1	202	05	0.02	0.2E+19
09 10	20:21:10.97	2	28 57.68	43 16.47	0.5	4.1	0.6	8	2	111	02	0.04	0.2E+19
09 10	22:58:35.93	3	28 57.54	43 13.48	1.0	5.0	pdc	3	1	166	02	0.01	0.1E+19
09 11	01:10:26.41	2	28 55.99	43 18.50	1.7	3.3	0.9	5	0	225	03	0.01	0.1E+19
09 11	02:01:56.68	2	28 53.97	43 20.41	2.0	2.5	1.5	4	1	283	06	0.02	0.1E+19
09 11	04:52:38.89	6	29 11.51	43 05.96	6.4	5.0	pdc	5	0	301	06	0.12	0.5E+18
09 11	07:43:06.27	1	28 52.86	43 21.22	6.3	5.0	pdc	4	0	304	07	0.05	0.4E+18
09 11	11:45:31.72	3	28 56.46	43 13.28	1.6	6.9	0.8	4	2	176	01	0.06	0.9E+18
09 11	14:25:39.60	5	29 09.11	43 09.88	1.2	5.0	pdc	4	0	154	03	0.08	0.2E+18
09 11	14:30:49.51	5	29 13.08	43 07.73	9.3	5.0	pdc	4	0	303	08	0.12	0.5E+19
09 11	20:28:15.65	3	28 56.87	43 12.97	1.0	5.1	1.1	4	1	174	01	0.02	0.3E+18
09 12	02:43:02.40	3	28 54.66	43 16.64	2.2	5.0	pdc	4	0	175	03	0.01	0.2E+18
09 12	18:34:31.22	2	28 56.80	43 18.25	1.2	5.0	pdc	4	0	218	02	0.01	0.1E+18
09 13	02:26:39.15	2	28 55.52	43 23.83	1.6	5.0	pdc	7	1	283	11	0.07	0.8E+19
09 13	03:04:11.06	3	28 56.13	43 12.27	2.4	4.9	0.5	4	2	200	02	0.04	0.5E+18
09 13	09:55:22.60	2	28 55.00	43 18.10	2.7	5.0	pdc	4	0	210	04	0.01	0.5E+18
09 13	13:04:02.89	3	28 56.75	43 15.46	2.2	5.1	1.5	5	1	194	03	0.01	0.4E+18
09 13	14:04:08.74	2	28 53.06	43 18.94	2.4	3.4	0.7	6	1	279	03	0.01	0.2E+19
09 14	00:07:42.09	2	28 55.82	43 21.57	2.8	3.2	1.0	5	1	290	07	0.02	0.1E+19
09 14	01:50:00.03	2	28 57.41	43 18.14	1.2	5.0	pdc	4	0	216	01	0.01	0.2E+18
09 14	02:50:20.19	5	29 13.53	43 09.05	2.2	5.0	pdc	5	2	307	07	0.17	0.2E+19
09 14	02:58:21.38	3	28 56.84	43 14.37	0.9	3.8	0.7	6	1	091	01	0.04	0.5E+19
09 14	11:44:48.23	3	28 54.74	43 12.47	1.6	5.0	0.5	6	2	221	04	0.04	0.6E+18
09 15	03:44:12.12	2	28 59.25	43 17.34	0.7	5.0	pdc	5	2	189	03	0.02	0.3E+18
09 15	11:53:02.09	2	28 54.84	43 24.54	4.8	5.0	pdc	4	0	292	12	0.03	0.6E+18
09 15	13:25:39.19	2	28 58.37	43 16.02	0.7	3.7	0.8	5	0	136	03	0.00	0.4E+18
09 15	13:29:17.81	2	28 58.31	43 16.03	0.6	3.9	0.9	5	0	130	03	0.01	0.1E+18
09 15	13:32:35.90	2	28 53.39	43 18.40	3.2	3.2	0.6	5	1	258	02	0.01	0.8E+18
09 15	15:57:37.71	2	28 54.20	43 21.21	5.3	5.0	pdc	4	0	293	07	0.06	0.6E+18
09 15	16:44:12.78	2	28 57.54	43 18.04	0.9	5.0	pdc	4	1	233	00	0.06	0.1E+19
09 16	02:49:24.32	3	28 55.86	43 14.90	1.1	5.0	pdc	5	0	156	02	0.13	0.1E+19
09 16	04:06:27.63	5	29 13.36	43 08.40	1.3	5.0	pdc	5	2	305	08	0.16	0.3E+19
09 16	04:54:07.96	2	28 54.76	43 18.90	1.7	2.5	3.2	4	1	241	05	0.04	0.1E+18
09 16	11:34:39.36	1	28 52.02	43 25.34	7.3	5.0	pdc	6	0	312	14	0.03	0.1E+19
09 16	17:37:35.28	2	28 57.77	43 16.86	3.4	5.0	pdc	4	1	303	06	0.07	0.1E+20
09 17	00:03:20.49	1	28 54.22	43 24.34	1.6	5.0	pdc	5	2	294	12	0.05	0.1E+19
09 17	00:48:24.94	2	28 56.55	43 26.32	3.1	5.0	pdc	4	1	290	17	0.07	0.6E+19
09 17	01:08:59.72	2	28 55.70	43 20.33	1.5	4.2	2.3	4	1	255	07	0.03	0.2E+19
09 18	02:47:34.64	2	28 52.55	43 19.55	4.8	5.0	pdc	4	0	317	04	0.05	0.2E+18
09 18	03:40:16.75	2	28 58.26	43 17.52	1.3	5.0	pdc	4	0	209	07	0.00	0.1E+18
09 19	04:42:27.86	2	28 56.91	43 18.77	2.5	4.1	3.2	6	1	228	08	0.01	0.3E+18
09 19	05:18:52.95	2	28 59.26	43 17.86	1.1	4.4	0.5	7	2	213	06	0.02	0.3E+19
09 19	15:59:52.43	2	28 58.61	43 16.88	0.8	5.4	1.1	6	1	200	05	0.01	0.3E+18
09 19	20:29:03.03	1	28 51.78	43 26.50	1.4	5.0	pdc	4	2	314	16	0.09	0.7E+18
09 20	06:32:15.84	1	28 47.73	43 27.39	2.5	5.0	pdc	6	1	332	19	0.04	0.1E+19
09 20	15:40:49.79	2	28 54.55	43 20.44	1.7	2.9	1.5	4	1	269	06	0.00	0.6E+18
09 21	12:30:21.26	3	28 56.70	43 13.22	1.3	5.0	pdc	4	0	199	01	0.02	0.2E+19
09 21	12:36:42.66	1	28 54.10	43 23.85	1.5	5.0	pdc	5	2	294	11	0.05	0.8E+18
09 21	19:56:22.25	2	28 58.76	43 18.87	1.2	5.0	pdc	5	0	226	09	0.02	0.1E+18
09 22	02:31:06.08	2	28 58.05	43 16.96	8.6	5.0	pdc	4	0	334	06	0.04	0.1E+19
09 22	08:10:30.06	3	28 55.70	43 13.79	2.2	6.9	1.1	3	2	319	02	0.00	0.3E+18
09 22	12:01:31.43	2	28 59.12	43 16.79	1.4	3.8	0.7	5	1	249	04	0.01	0.5E+18
09 22	22:09:47.77	2	28 54.57	43 20.75	2.8	3.4	2.8	5	1	271	07	0.01	0.6E+18
09 23	00:07:50.03	1	28 52.98	43 21.41	2.9	5.0	pdc	5	1	312	18	0.04	0.4E+18
09 23	07:39:21.11	2	28 55.28	43 26.66	1.6	5.0	pdc	7	3	297	16	0.07	0.2E+19
09 23	10:54:24.39	2	28 57.06	43 23.86	1.3	5.0	pdc	5	3	275	13	0.07	0.4E+18
09 23	11:51:07.54	5	29 13.79	43 09.40	2.0	5.0	pdc	7	2	309	07	0.11	0.4E+20
09 23	20:17:19.02	1	28 55.34	43 16.74	7.3	5.0	pdc	4	0	312	05	0.04	0.1E+19
09 24	02:45:52.66	2	28 56.76	43 18.90	2.3	5.0	pdc	4	1	246	08	0.03	0.1E+19
09 24	08:53:56.23	2	28 58.92	43 17.26	1.8	5.5	1.1	5	1	257	05	0.01	0.1E+18
09 24	10:29:30.55	5	29 13.14	43 08.64	3.0	5.0	pdc	6	2	302	07	0.16	0.4E+19
09 25	19:46:19.67	2	28 58.32	43 18.09	1.3	5.0	pdc	4	2	216	08	0.02	0.3E+18
09 26	08:21:38.07	6	29 12.41	43 06.78	9.8	5.0	pdc	5	0	312	09	0.06	0.5E+18

09 26	12:33:22.33	2	28 57.32	43 23.52	1.9	5.0	pdc	5	1	272	13	0.07	0.2E+19
09 26	14:23:00.02	1	28 51.82	43 18.34	4.2	5.0	pdc	4	0	345	03	0.02	0.2E+19
09 26	18:50:16.00	3	28 56.22	43 15.11	1.1	4.5	0.5	8	2	160	02	0.03	0.5E+19
09 26	22:10:00.61	1	28 58.43	43 19.65	10.1	5.0	pdc	4	0	323	09	0.04	0.5E+19
09 27	04:50:27.81	5	29 11.34	43 09.20	3.3	5.2	1.5	4	1	266	04	0.03	0.7E+18
09 28	03:39:54.05	2	28 54.72	43 19.94	1.6	3.2	1.5	6	1	262	06	0.03	0.8E+18
09 28	06:07:39.87	5	29 09.77	43 10.10	2.8	5.0	pdc	5	1	272	06	0.08	0.5E+18
09 28	06:30:03.93	2	28 56.45	43 22.35	1.5	5.0	pdc	5	2	292	11	0.04	0.1E+19
09 28	10:21:19.92	6	29 15.88	43 08.14	1.7	5.0	pdc	5	3	325	12	0.15	0.8E+18
09 28	14:32:19.33	3	28 55.96	43 11.35	1.8	5.0	pdc	6	2	222	04	0.05	0.8E+19
09 28	18:17:25.55	3	28 54.52	43 10.63	3.4	5.0	pdc	4	1	294	06	0.05	0.2E+18
09 28	23:33:17.37	3	28 55.44	43 11.78	2.8	6.6	1.2	4	1	282	04	0.01	0.8E+18
09 29	00:42:21.03	2	28 56.71	43 18.20	1.5	3.9	1.4	4	1	242	07	0.02	0.2E+18
09 29	05:19:28.38	5	29 11.28	43 08.61	3.2	2.9	2.4	4	2	302	05	0.04	0.6E+18
09 29	18:39:08.76	1	28 53.82	43 23.60	1.5	5.0	pdc	6	2	295	11	0.07	0.2E+19
09 29	18:45:39.43	5	29 08.00	43 09.83	1.3	2.5	2.4	4	1	137	05	0.01	0.2E+18
09 30	00:20:29.81	3	28 56.43	43 13.56	1.3	5.3	0.5	6	2	173	00	0.04	0.3E+19
09 30	07:15:30.44	3	28 57.30	43 13.83	1.1	6.5	1.4	4	3	179	01	0.02	0.1E+18
09 30	10:20:56.03	2	28 56.80	43 19.57	1.0	5.0	pdc	5	2	239	08	0.06	0.1E+19
09 30	11:41:07.18	1	28 52.55	43 20.48	3.5	5.0	pdc	6	0	302	06	0.06	0.3E+20
09 30	11:56:14.74	1	28 51.04	43 23.80	9.7	5.0	pdc	4	0	317	12	0.06	0.4E+19
09 30	12:01:54.00	1	28 51.55	43 22.43	9.0	5.0	pdc	4	0	314	09	0.04	0.8E+19
09 30	14:30:39.25	3	28 55.75	43 13.80	2.0	4.7	0.5	8	1	310	01	0.01	0.9E+20
09 30	19:05:02.06	2	28 57.00	43 18.36	1.7	4.3	1.6	4	1	311	08	0.01	0.3E+18
09 30	21:49:07.01	1	28 52.35	43 18.47	2.8	5.0	pdc	5	0	315	03	0.02	0.2E+19
10 01	02:35:01.26	2	28 52.63	43 20.03	5.1	5.0	pdc	4	0	315	05	0.04	0.4E+18
10 01	07:07:19.30	1	28 47.11	43 27.65	2.0	5.0	pdc	6	3	334	20	0.07	0.1E+20
10 01	07:48:57.65	1	28 55.14	43 19.55	9.7	5.0	pdc	4	0	311	10	0.06	0.5E+18
10 01	10:01:51.02	2	28 58.14	43 15.56	1.2	4.7	2.2	4	1	252	04	0.00	0.2E+18
10 01	15:35:04.55	3	28 55.13	43 13.76	2.2	6.5	1.2	4	2	322	03	0.01	0.2E+19
10 01	16:01:47.54	2	28 56.33	43 18.99	1.1	3.6	1.5	5	1	254	07	0.02	0.4E+18
10 01	16:32:44.95	2	28 54.89	43 22.24	4.0	5.0	pdc	5	1	280	09	0.06	0.2E+19
10 02	05:57:33.37	3	28 57.03	43 13.07	2.2	5.6	0.6	5	0	196	01	0.01	0.2E+19
10 02	07:41:51.85	2	28 58.13	43 17.45	2.5	5.0	pdc	4	0	206	06	0.02	0.2E+20

Origin Time : GMT (hours : minutes : seconds)
REG : Region
1 Segment at 28° 50'N
2 Inside Corner
3 Segment End
4 29° 02'N
5 Segment Center
6 Other
ERH : Horizontal Error (95% confidence)
DBD : Depth Below Datum (3.22 km)
ERZ : Vertical Error (95% confidence)
P : Number of weighted *P* wave arrivals
S : Number of weighted *S* wave arrivals
MAG : Maximum Azimuthal Gap
DCS : Distance to Closest Station
RMS : Root Mean Square Travel Time Residual
pdc : Poor Depth Control

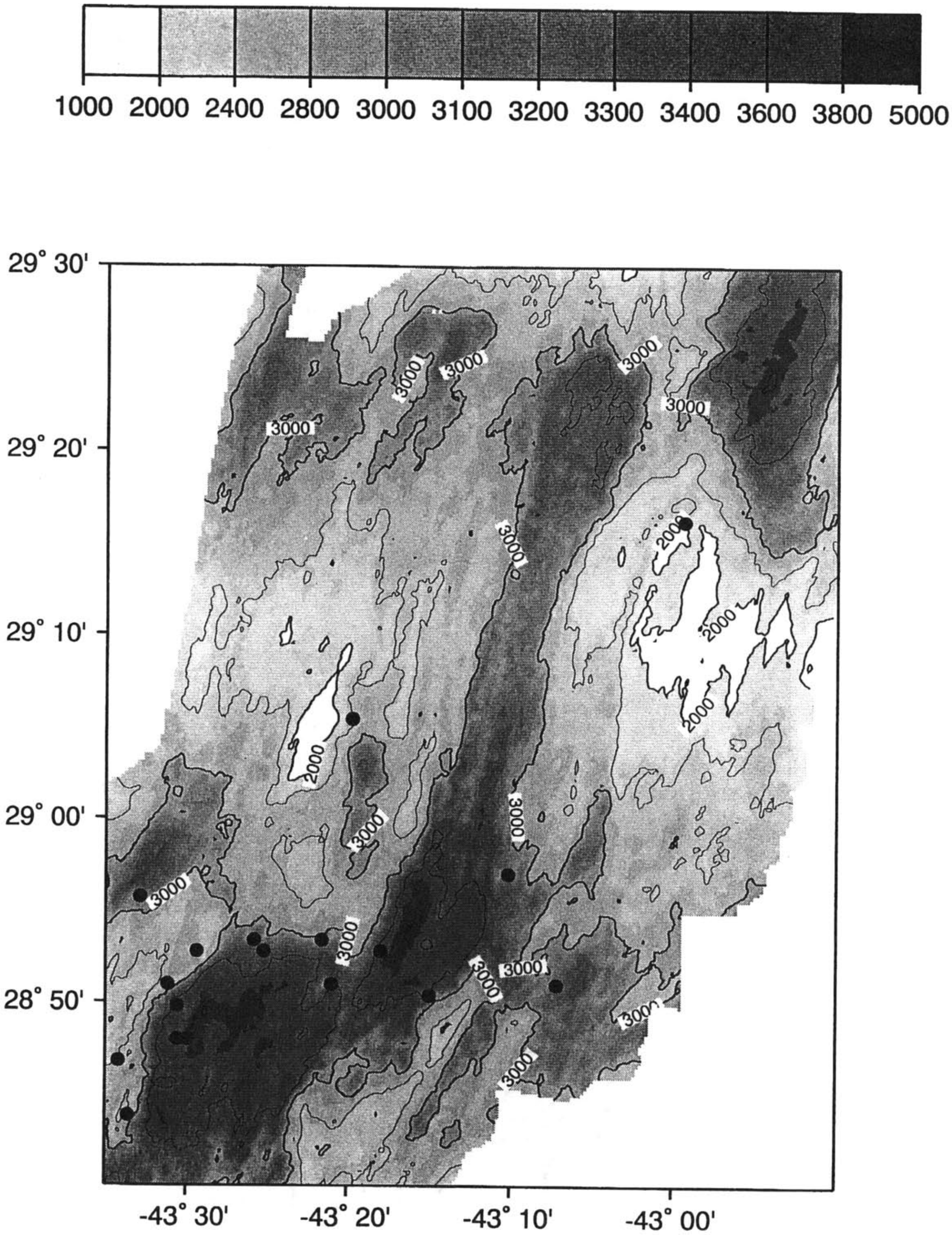
1000
2000
2400
2800
3000
3100
3200
3300
3400
3600
3800
5000
29° 30'
29° 20'
29° 10'
29° 00'
28° 50'
-43° 30'
-43° 20'
-43° 10'
-43° 00'
3000
2000

Figure 1

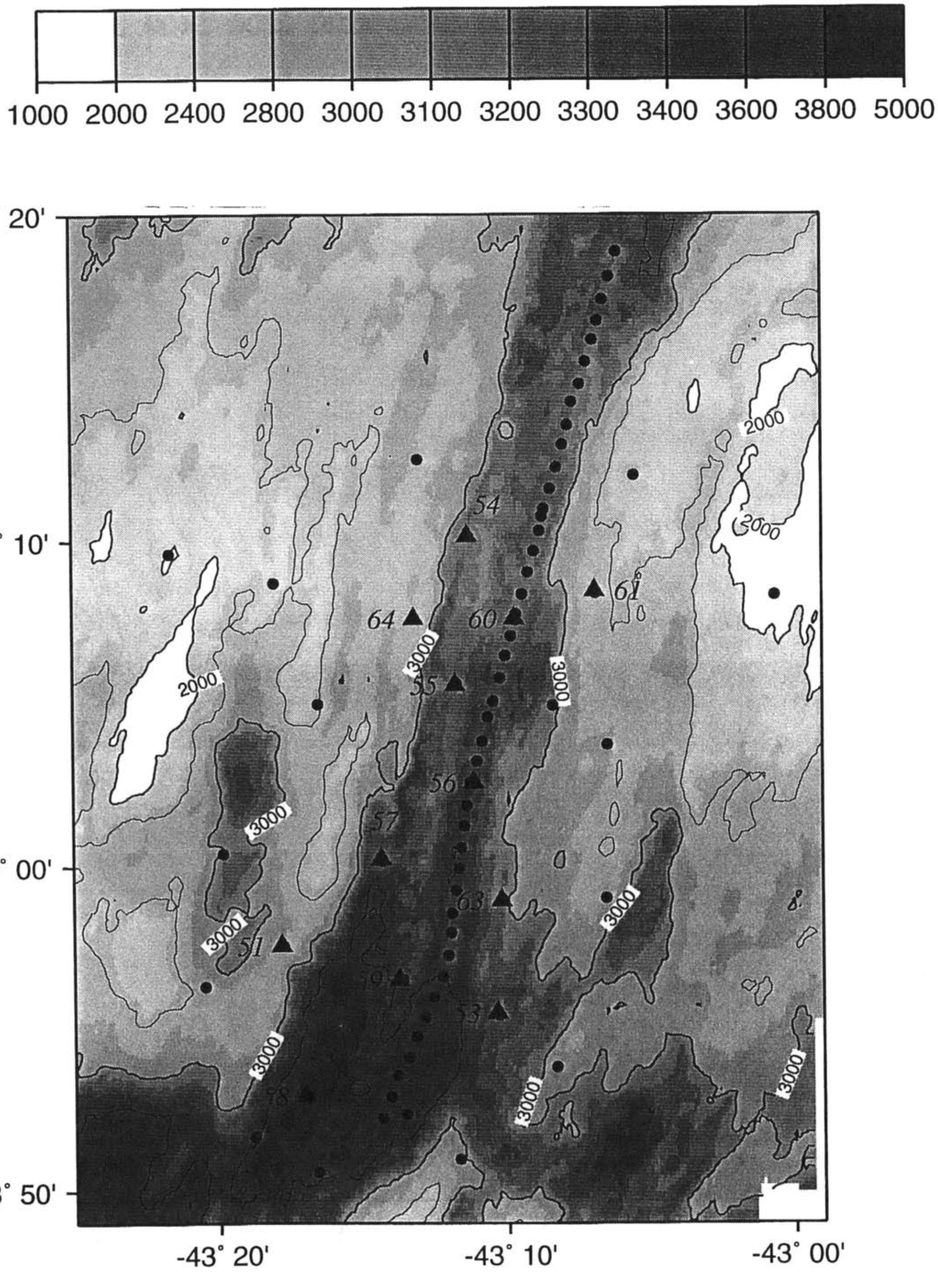
1000
2000
2400
2800
3000
3100
3200
3300
3400
3600
3800
5000
29° 20'
29° 10'
29° 00'
28° 50'
-43° 20'
-43° 10'
-43° 00'
2000
2000
2000
3000
3000
3000
3000
3000
3000
3000
3000
3000
54
61
64
60
55
56
57
63
51
59
53
58

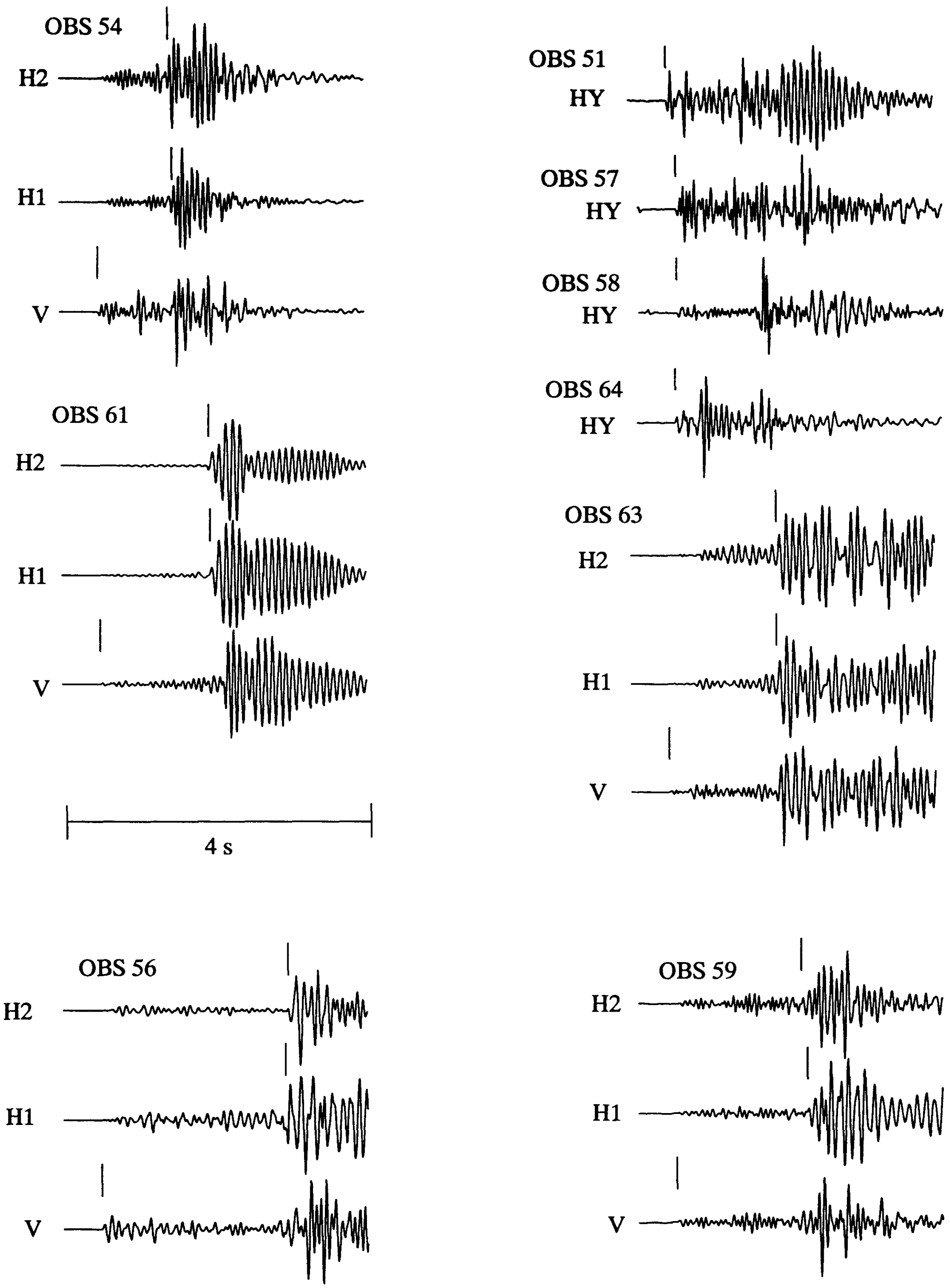
OBS 54
H2
H1
V
OBS 61
H2
H1
V
4 s
OBS 56
H2
H1
V
OBS 51
HY
OBS 57
HY
OBS 58
HY
OBS 64
HY
OBS 63
H2
H1
V
OBS 59
H2
H1
V

Figure 3

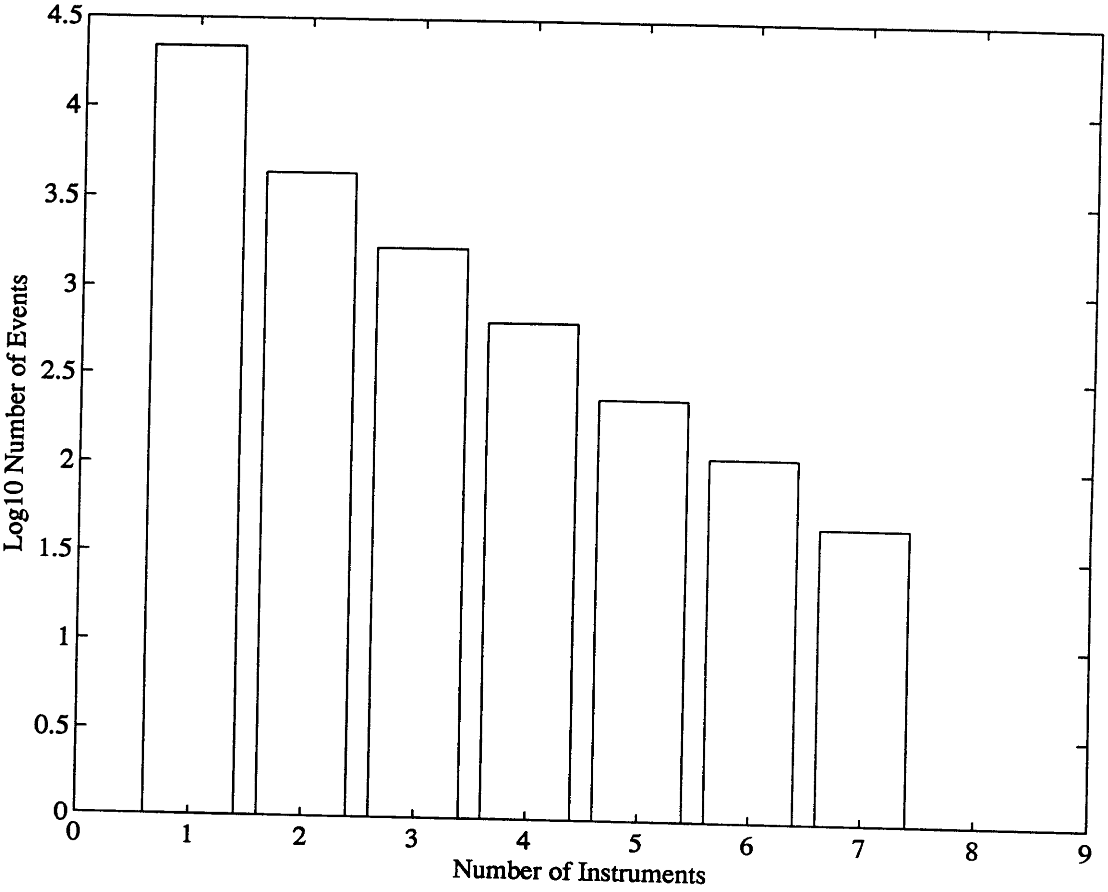
Log10 Number of Events
0
0.5
1
1.5
2
2.5
3
3.5
4
4.5
Number of Instruments
0
1
2
3
4
5
6
7
8
9

Figure 4

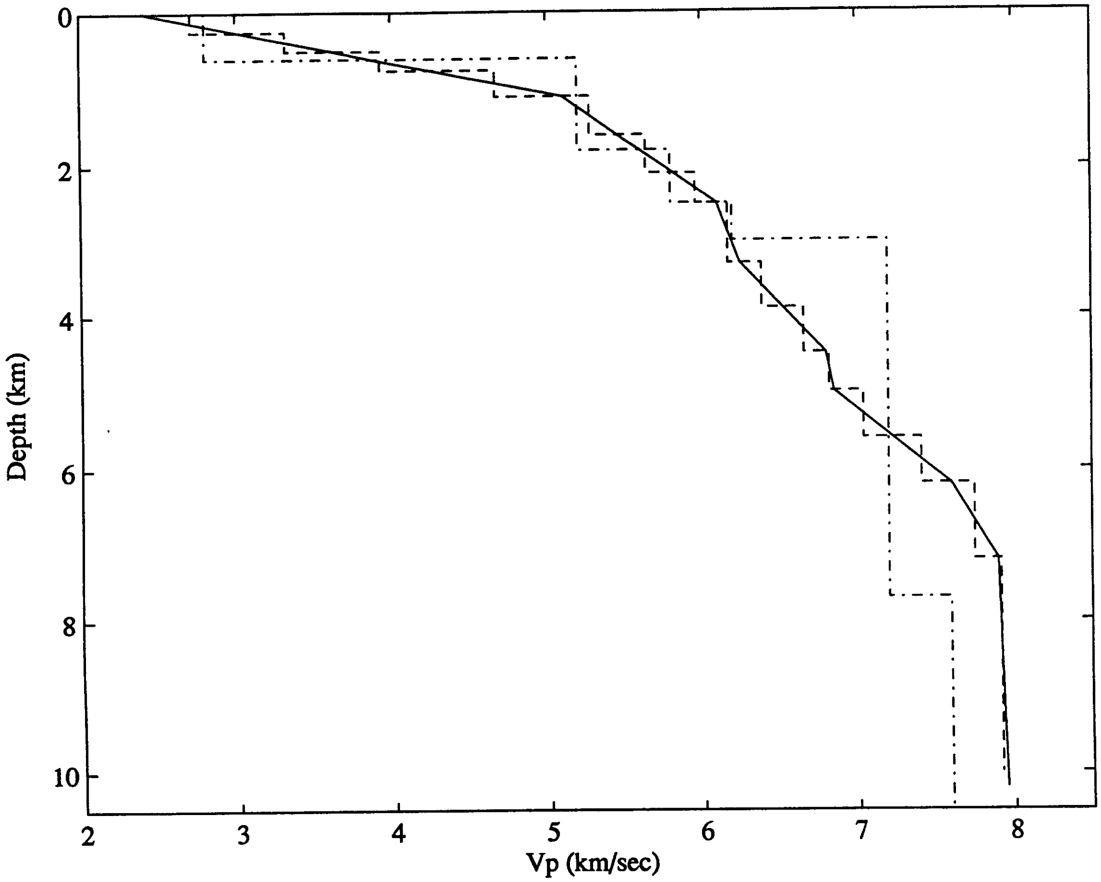

Figure 5

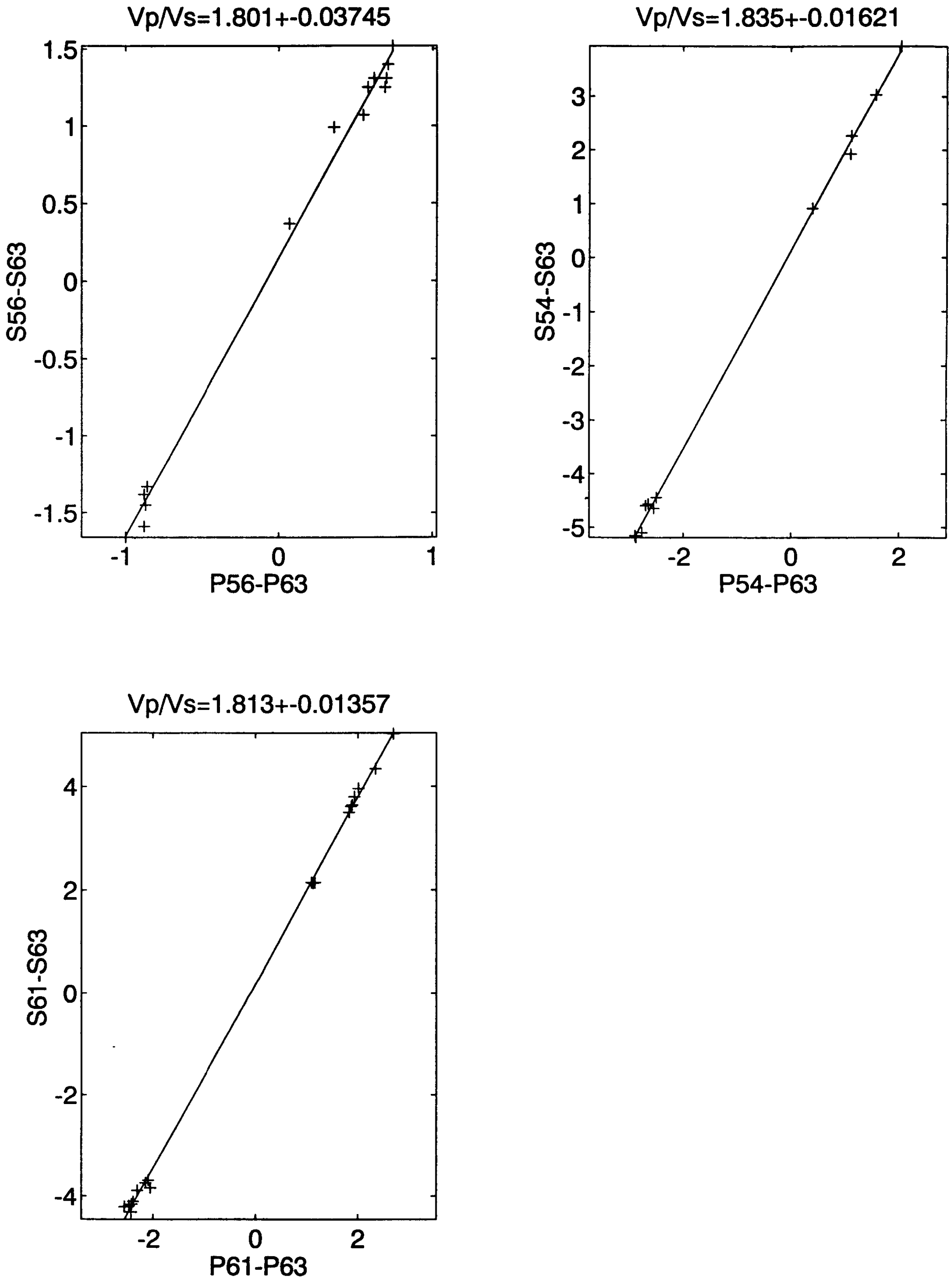
Vp/Vs=1.801+-0.03745
1.5
1
0.5
0
-0.5
-1
-1.5
S56-S63
-1
0
1
P56-P63
Vp/Vs=1.835+-0.01621
3
2
1
0
-1
-2
-3
-4
-5
S54-S63
-2
0
2
P54-P63
Vp/Vs=1.813+-0.01357
4
2
0
-2
-4
S61-S63
-2
0
2
P61-P63

Figure 6

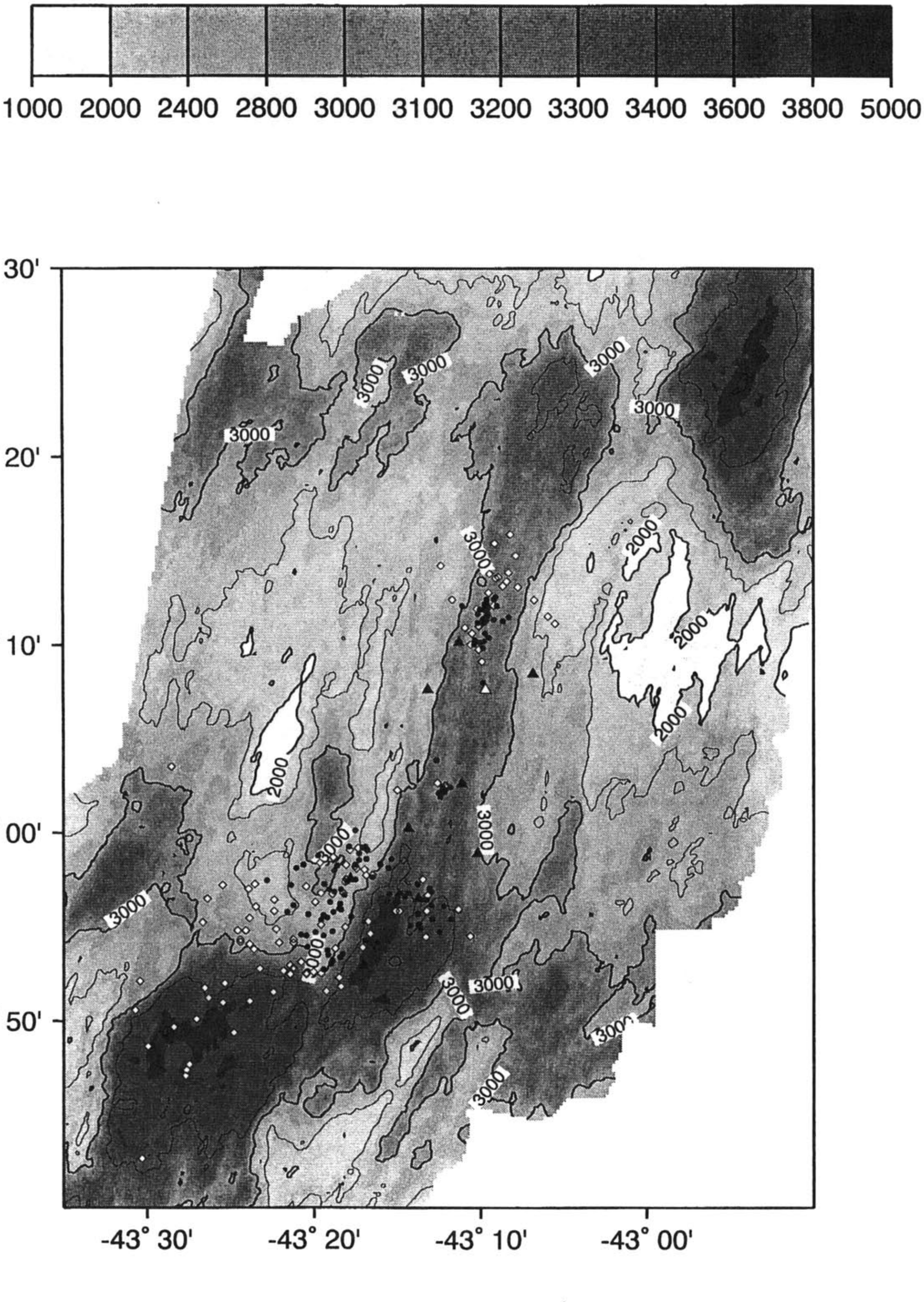
1000
2000
2400
2800
3000
3100
3200
3300
3400
3600
3800
5000
29° 30'
29° 20'
29° 10'
29° 00'
28° 50'
-43° 30'
-43° 20'
-43° 10'
-43° 00'
3000
2000

Figure 7

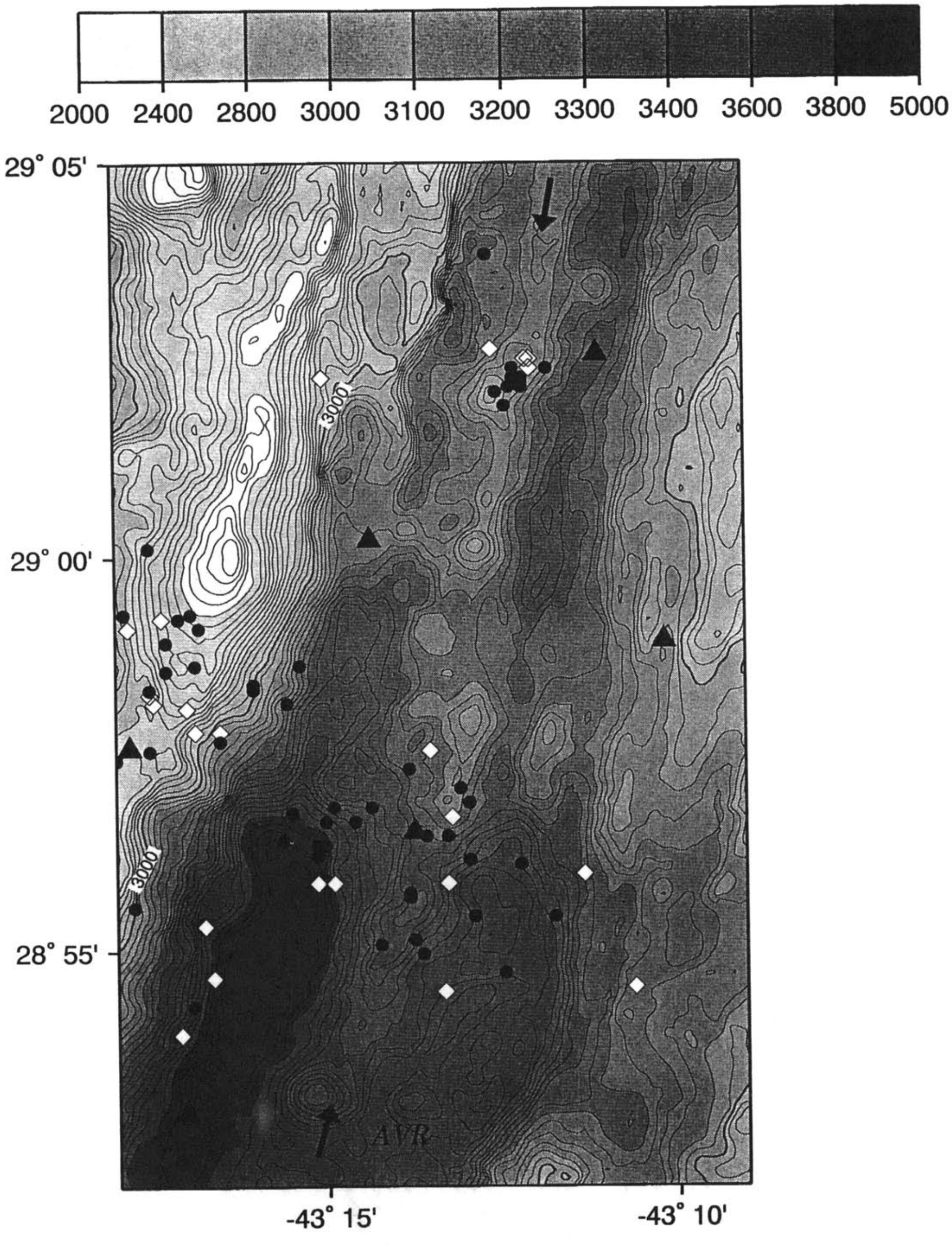
2000
2400
2800
3000
3100
3200
3300
3400
3600
3800
5000
29° 05'
29° 00'
28° 55'
3000
3000
AVR
-43° 15'
-43° 10'

Figure 8

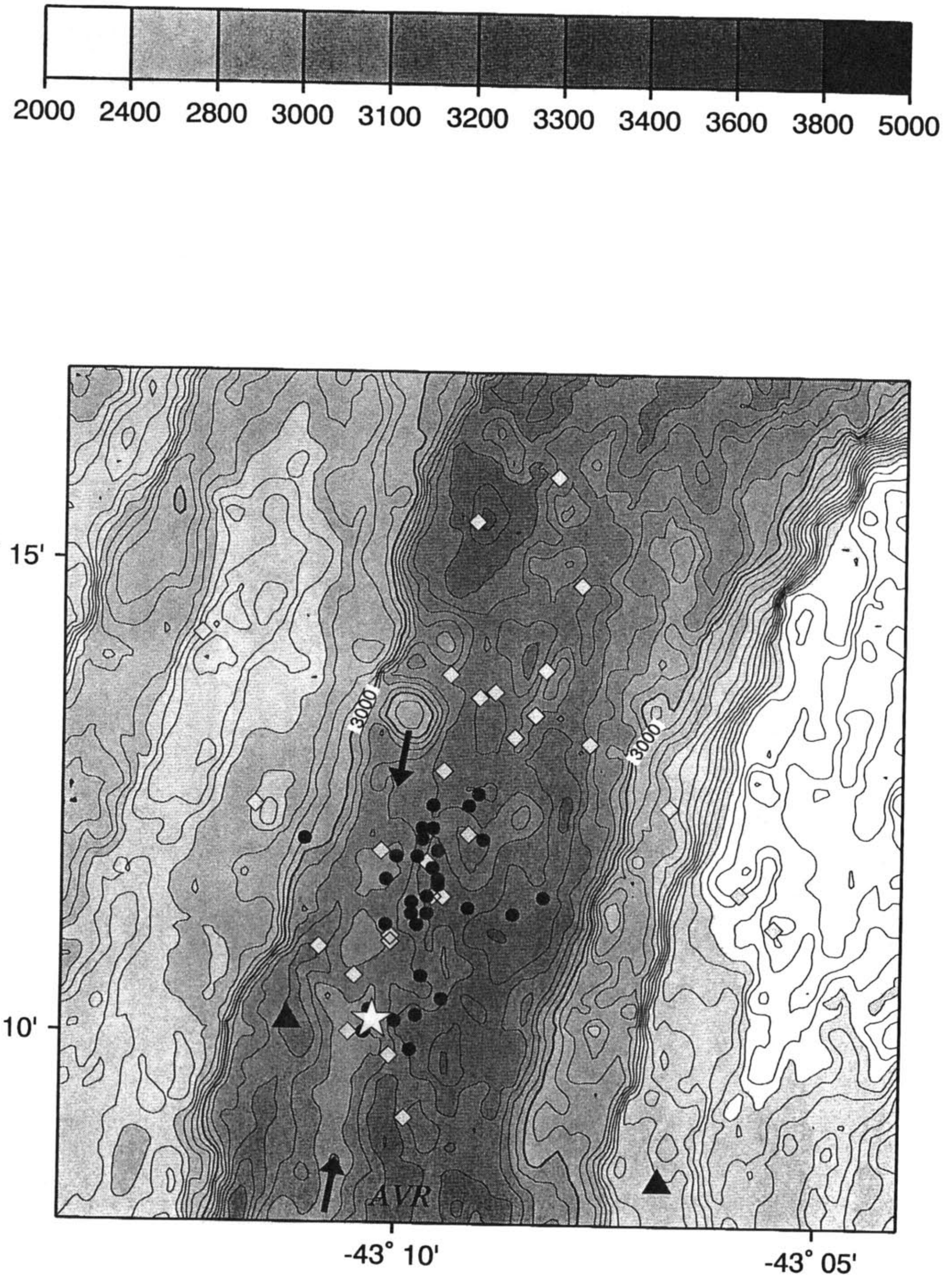
2000
2400
2800
3000
3100
3200
3300
3400
3600
3800
5000
3000
3000
AVR
29° 15'
29° 10'
-43° 10'
-43° 05'

Figure 9

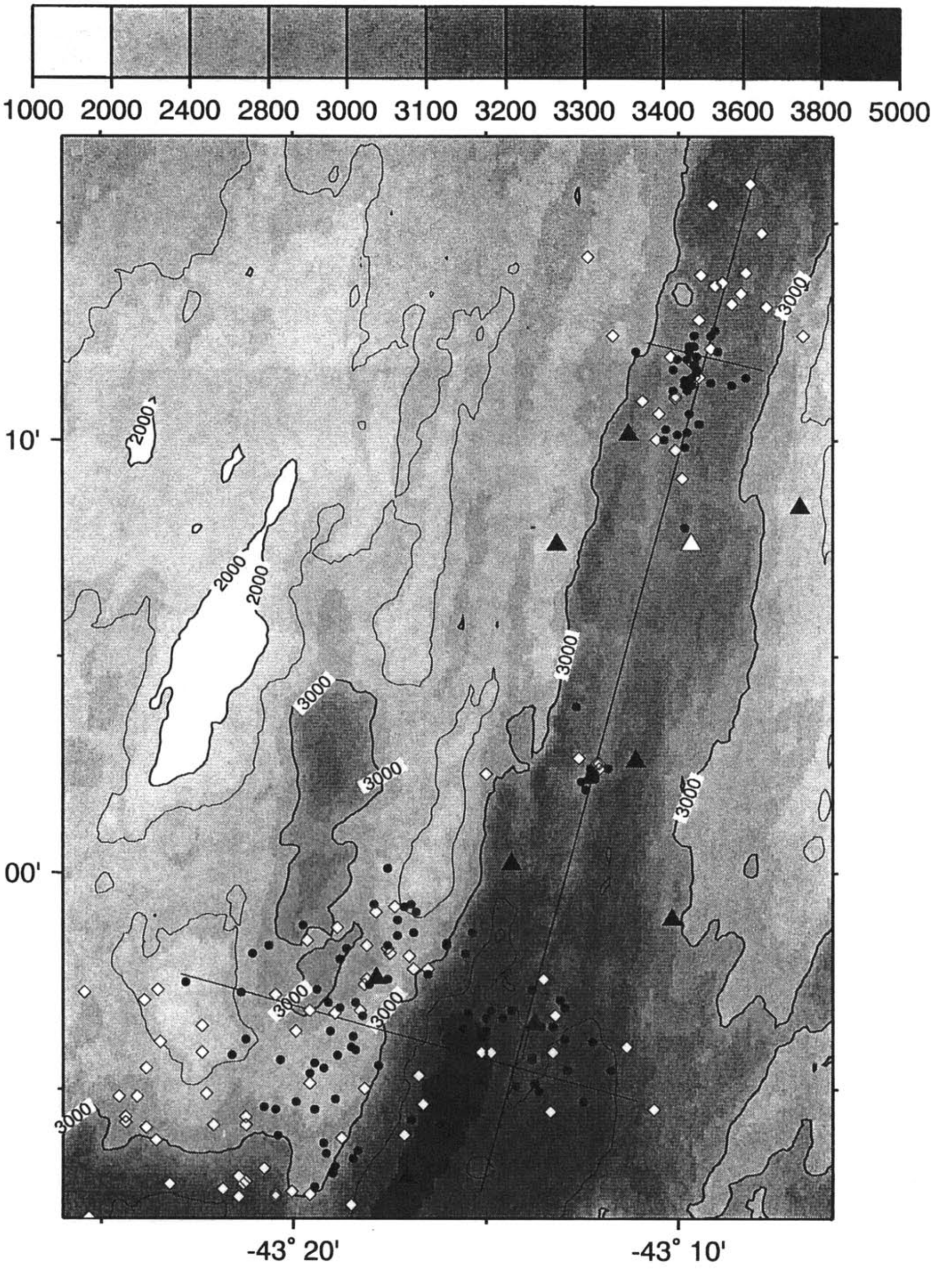
1000
2000
2400
2800
3000
3100
3200
3300
3400
3600
3800
5000
2000
2000
2000
3000
3000
3000
3000
3000
3000
3000
3000
29° 10'
29° 00'
-43° 20'
-43° 10'

Figure 10

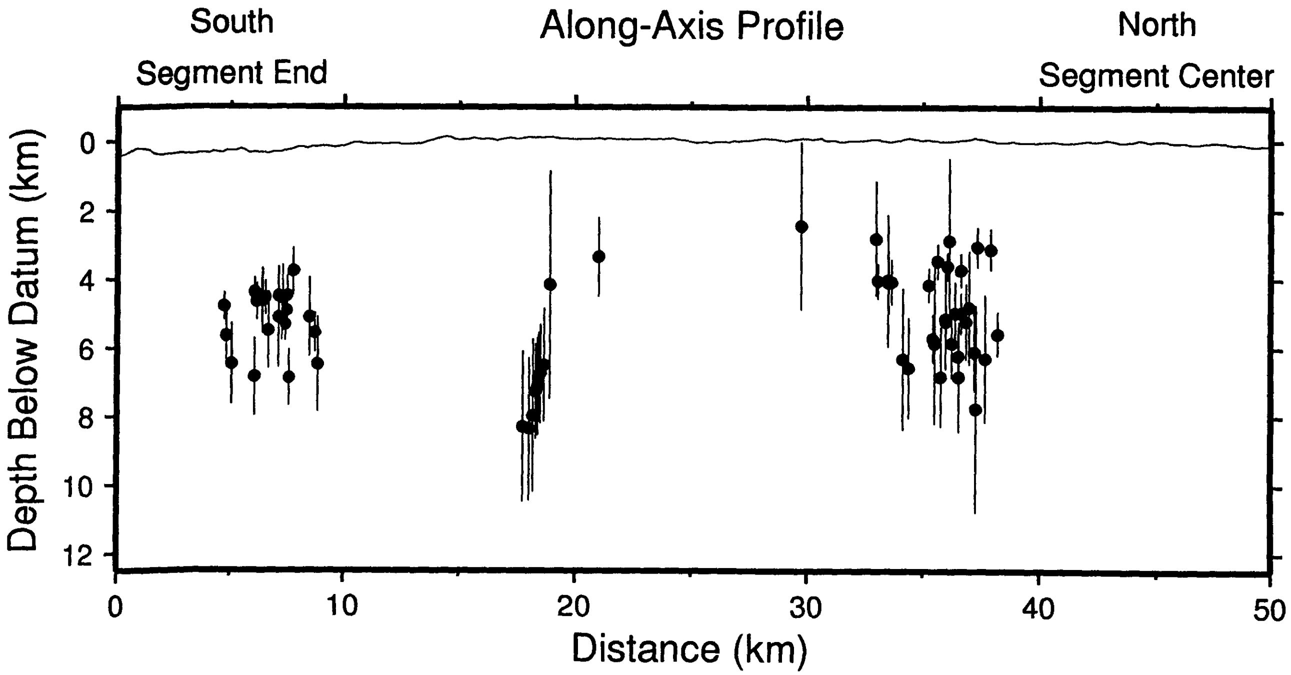
South
Segment End
Along-Axis Profile
North
Segment Center
Depth Below Datum (km)
0
2
4
6
8
10
12
0
10
20
30
40
50
Distance (km)

Figure 11

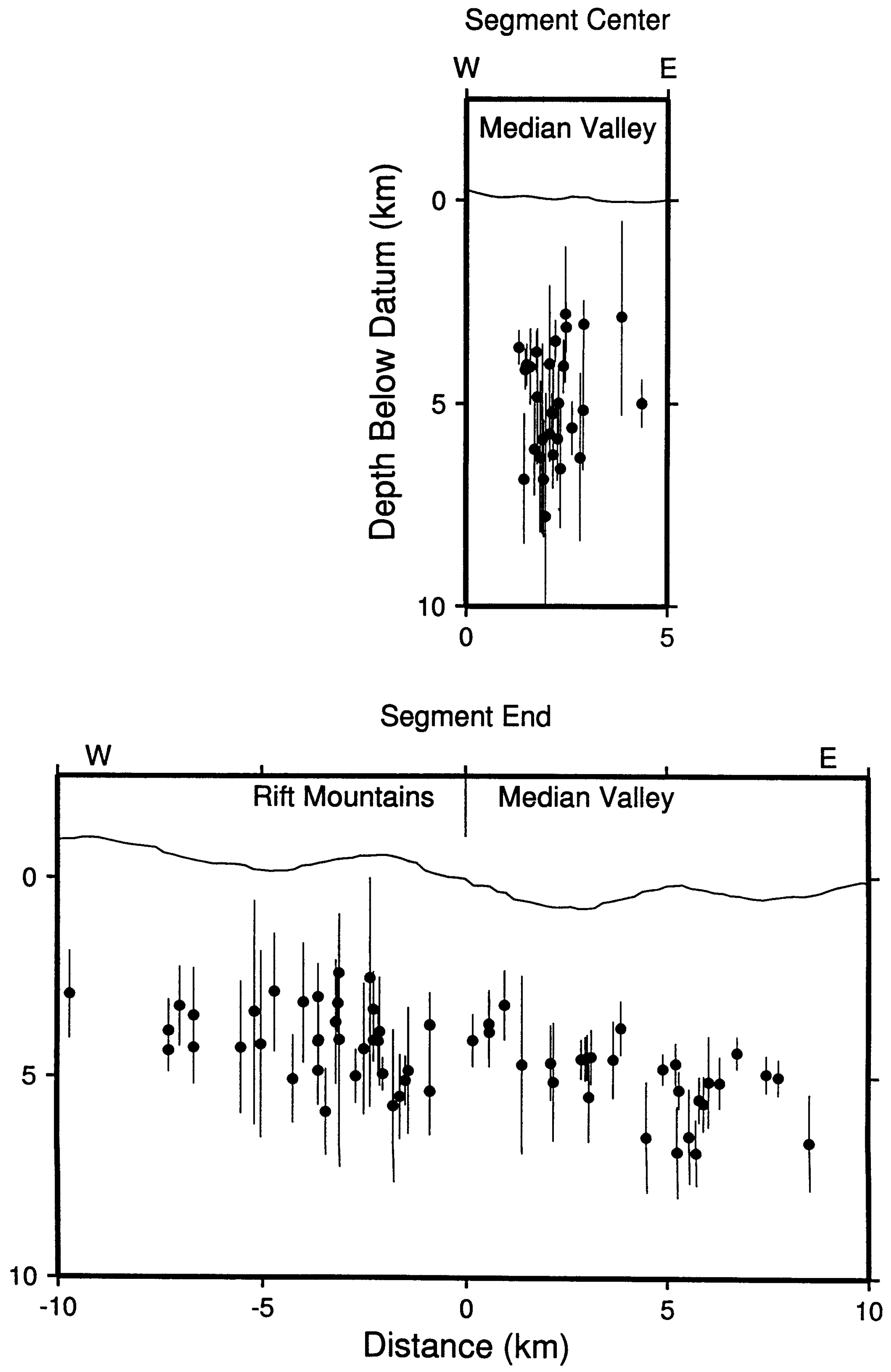
Segment Center
W
E
Median Valley
Depth Below Datum (km)
0
5
10
0
5
Segment End
W
E
Rift Mountains
Median Valley
0
5
10
-10
-5
0
5
10
Distance (km)

Figure 12

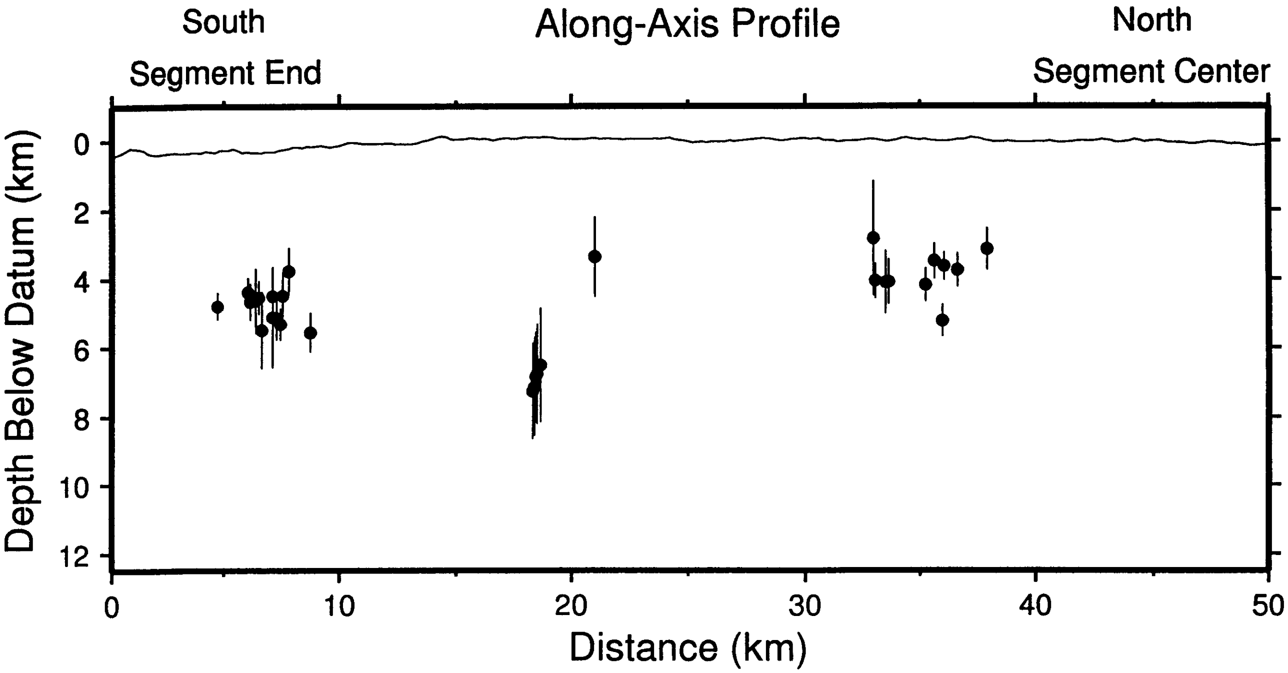
South
Segment End
Along-Axis Profile
North
Segment Center
Depth Below Datum (km)
0
2
4
6
8
10
12
0
10
20
30
40
50
Distance (km)

Figure 13

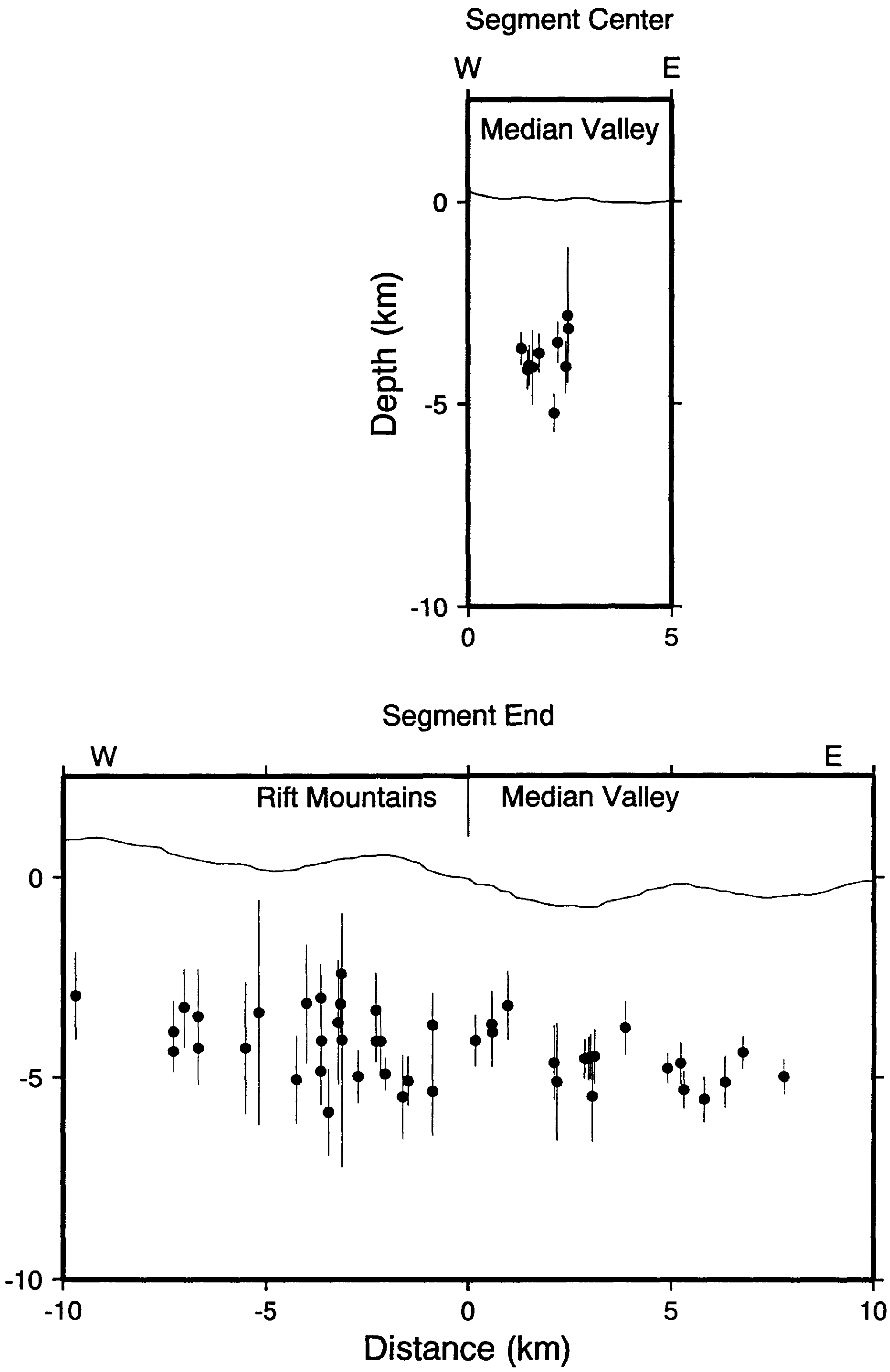
Segment Center
W
E
Median Valley
0
-5
-10
Depth (km)
0
5
Segment End
W
E
Rift Mountains
Median Valley
0
-5
-10
-10
-5
0
5
10
Distance (km)

Figure 14

354/50/270

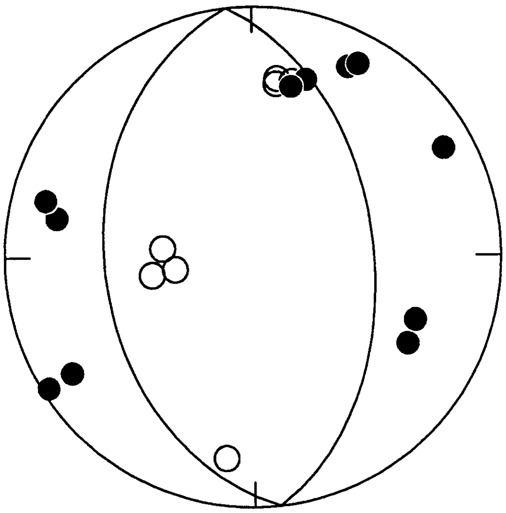

Figure 15a

165/45/37

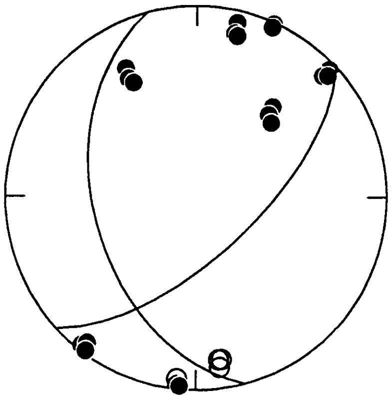

15b

165/45/327

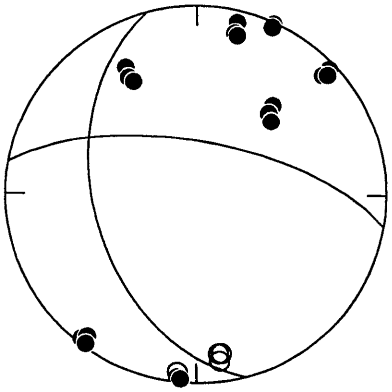

15c

29 10.19 N 43 9.79 W

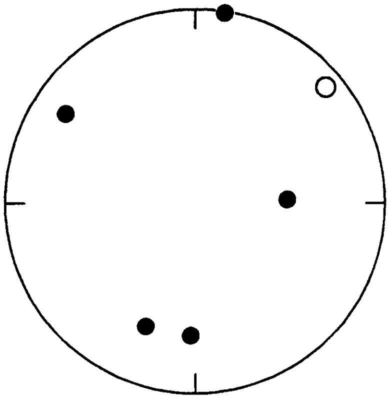

15e

29 10.02 N 43 10.40 W

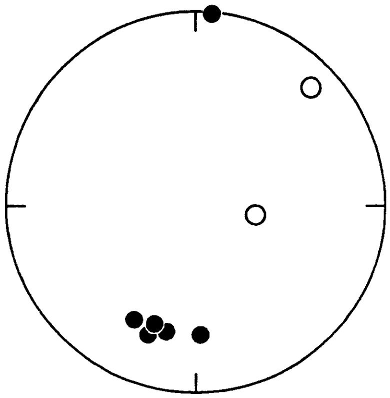

15f

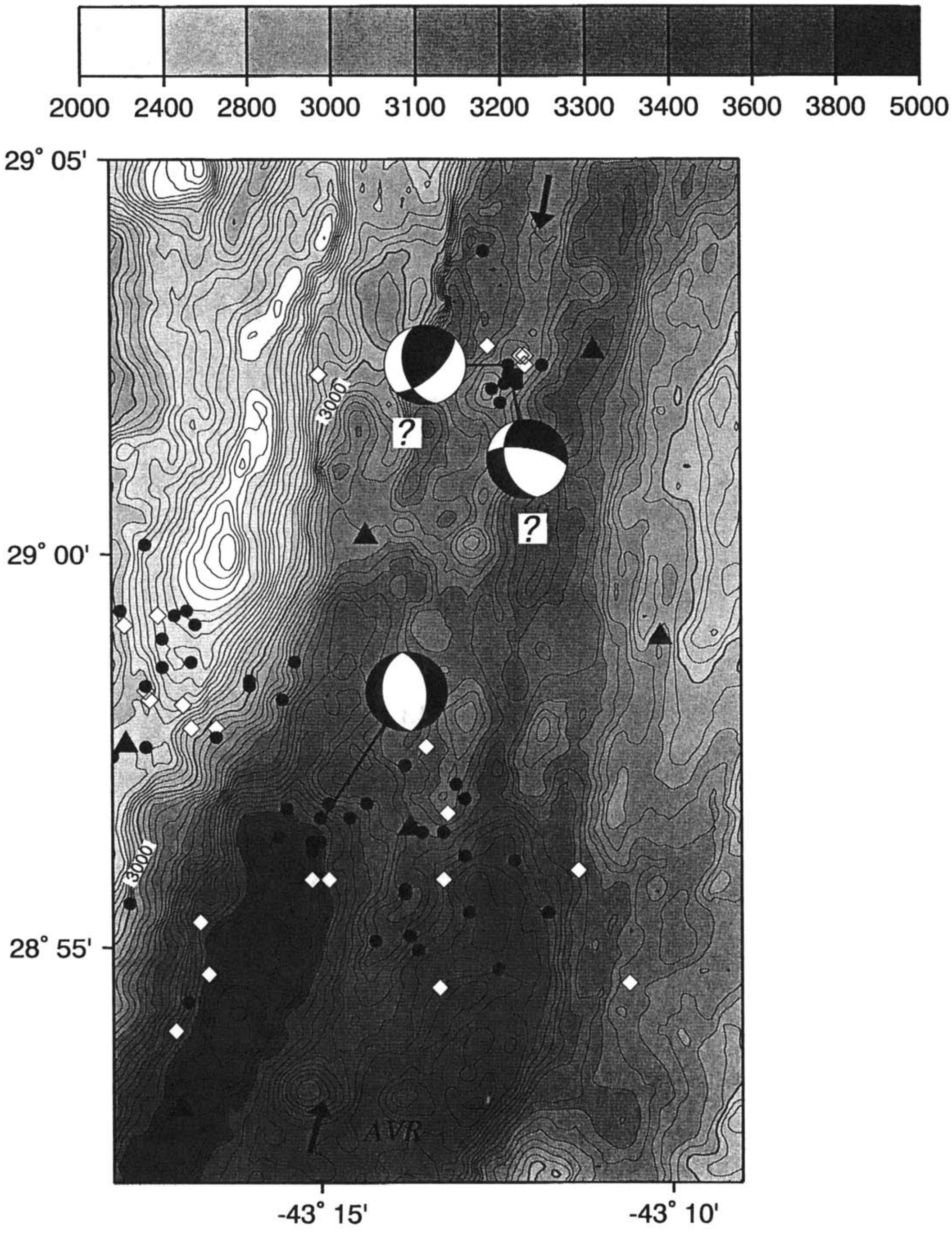
2000
2400
2800
3000
3100
3200
3300
3400
3600
3800
5000
29° 05'
29° 00'
28° 55'
-43° 15'
-43° 10'
3000
?
?
AVR

Figure 16

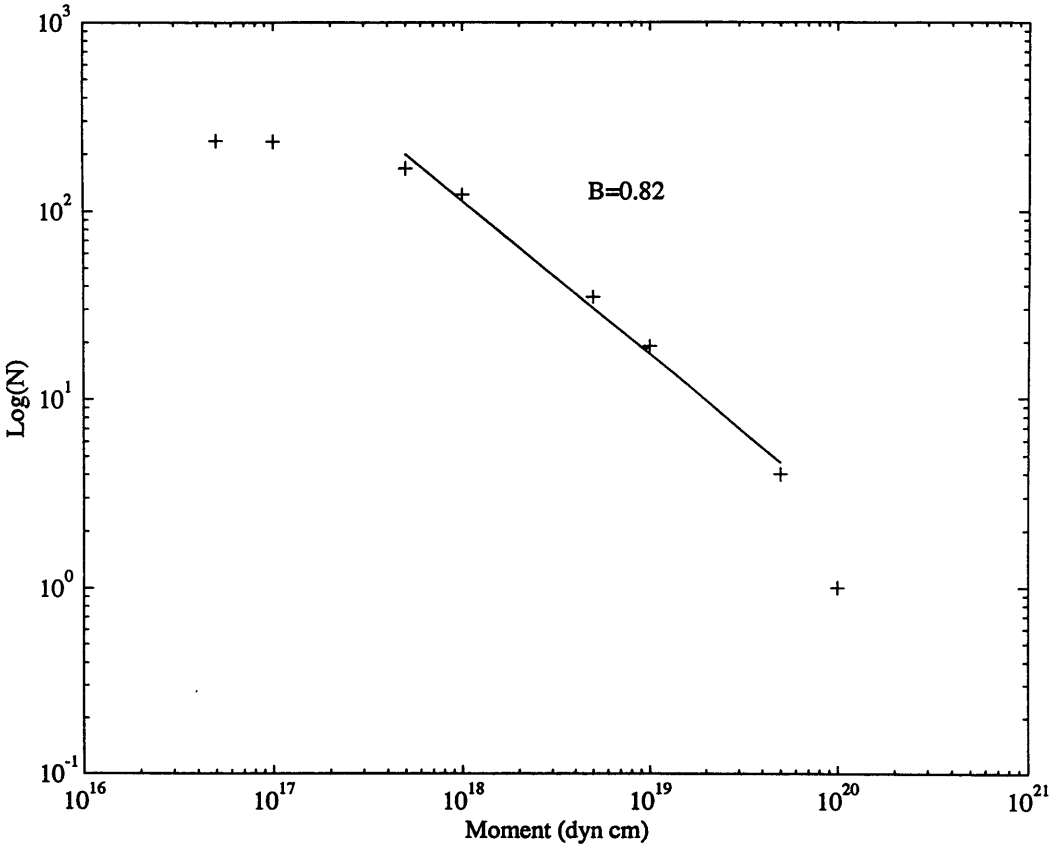
10^3
10^2
10^1
10^0
10^-1
Log(N)
B=0.82
10^16
10^17
10^18
10^19
10^20
10^21
Moment (dyn cm)

Figure 17

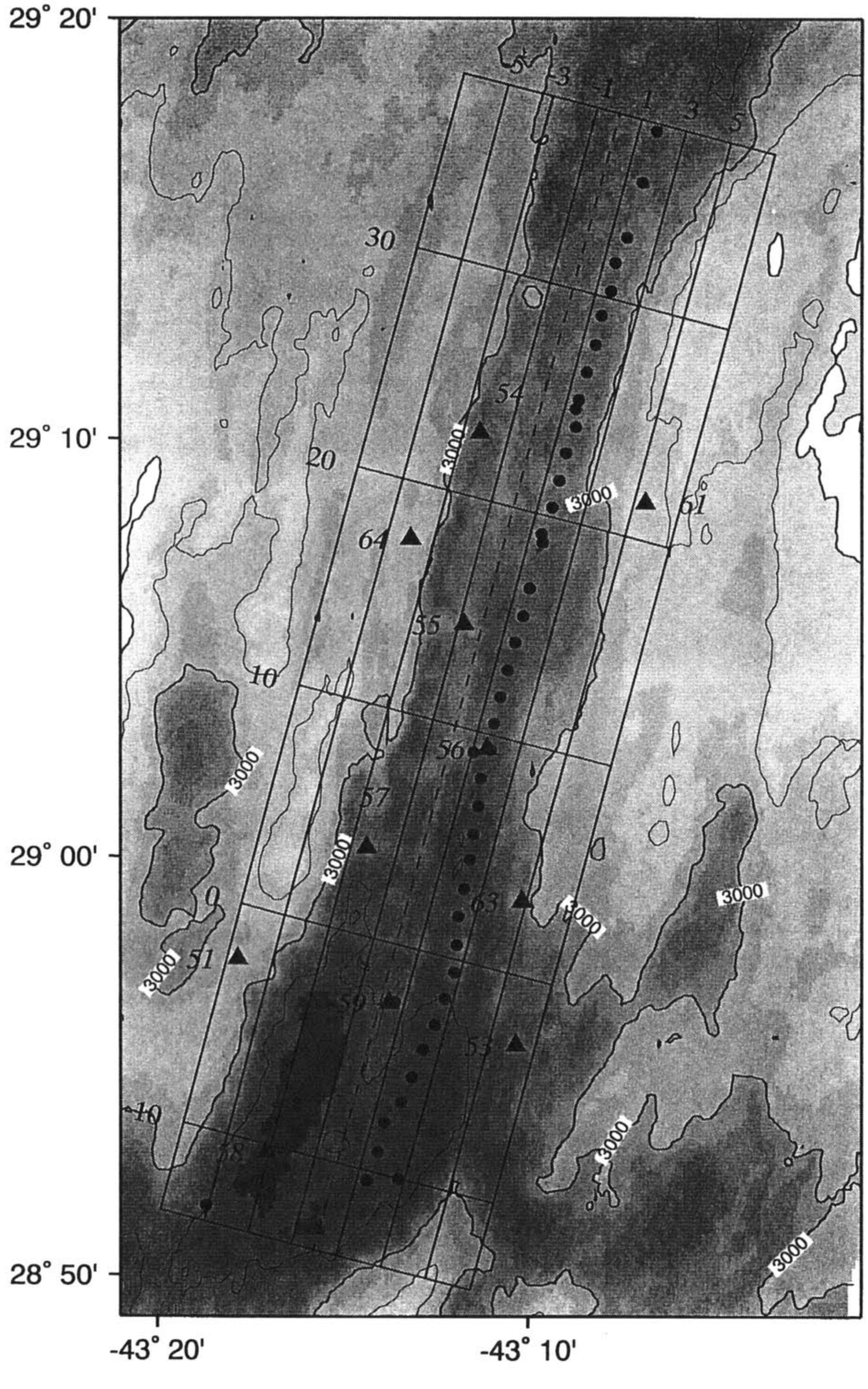
29° 20'
29° 10'
29° 00'
28° 50'
-43° 20'
-43° 10'
-5
-3
-1
1
3
5
30
20
10
0
-10
54
61
64
55
56
57
63
51
59
53
58
3000
3000
3000
3000
3000
3000
3000
3000
3000

Figure 18

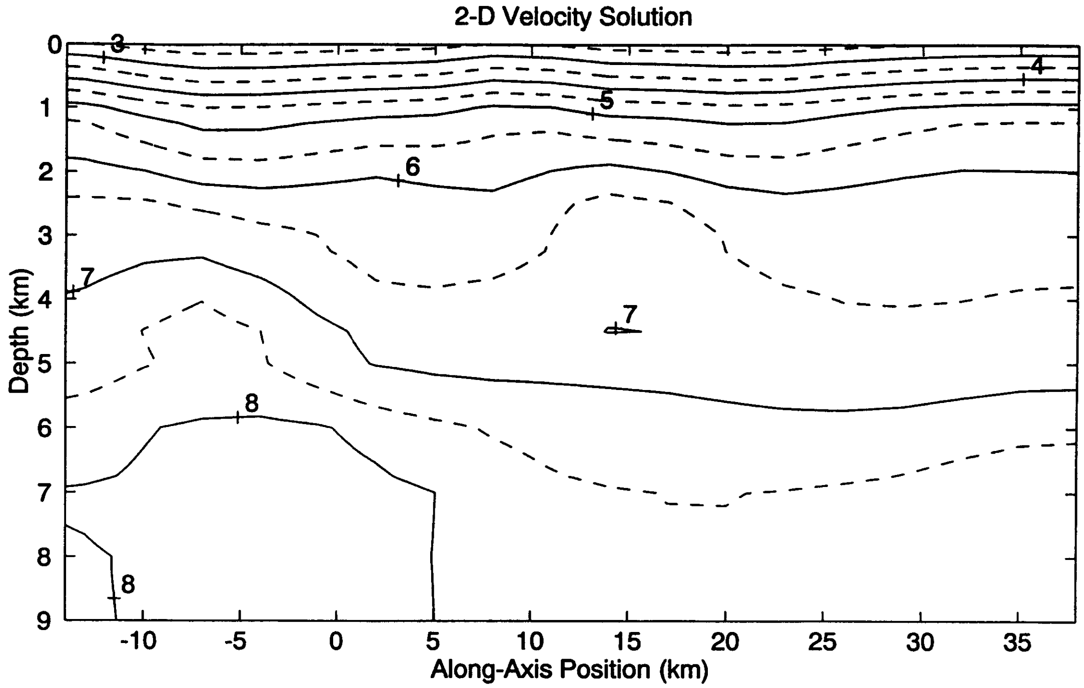
2-D Velocity Solution
Depth (km)
Along-Axis Position (km)
0
1
2
3
4
5
6
7
8
9
-10
-5
0
5
10
15
20
25
30
35
3
4
5
6
7
7
8
8

19a

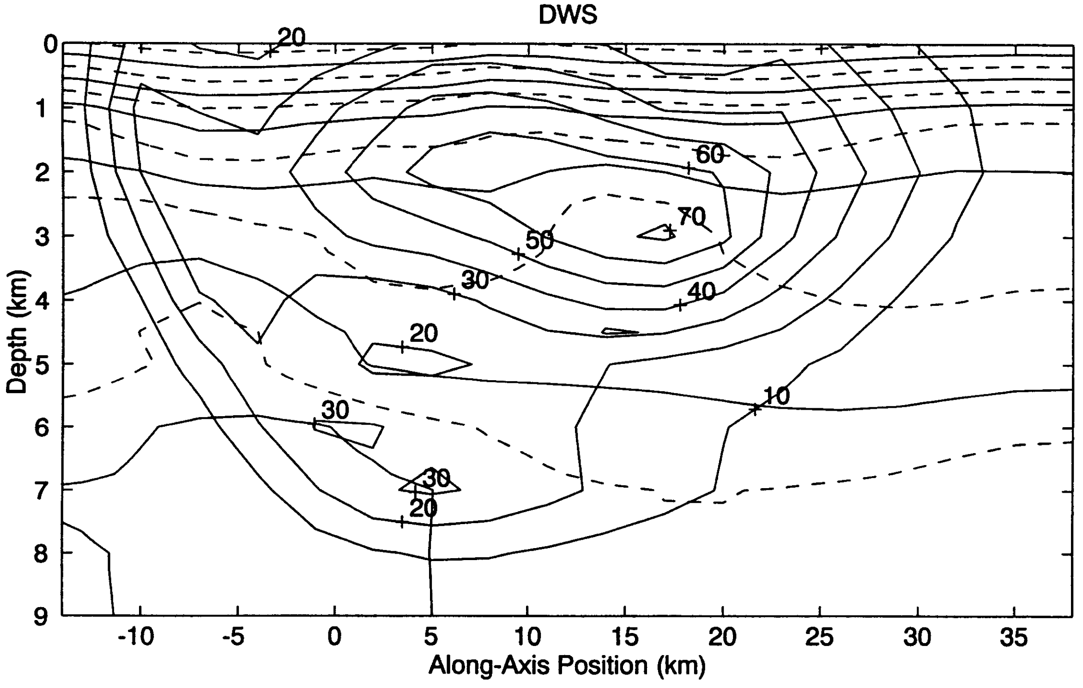
DWS
Depth (km)
Along-Axis Position (km)
0
1
2
3
4
5
6
7
8
9
-10
-5
0
5
10
15
20
25
30
35
20
60
70
50
30
40
20
10
30
30
20

19b

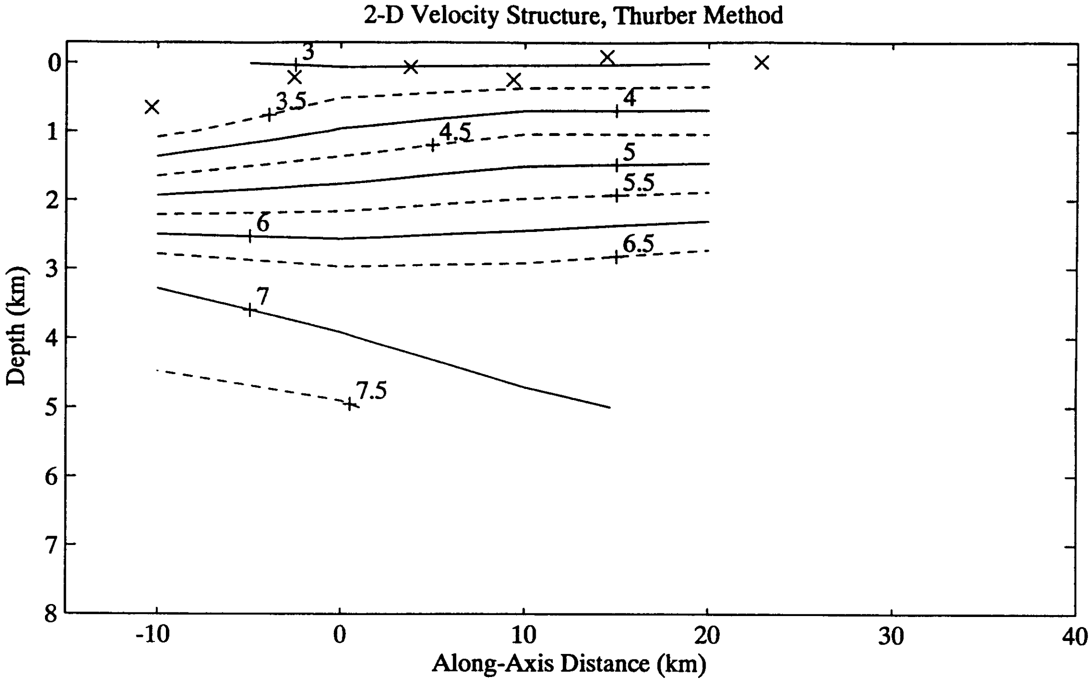
2-D Velocity Structure, Thurber Method
Depth (km)
0
1
2
3
4
5
6
7
8
-10
0
10
20
30
40
Along-Axis Distance (km)
3
3.5
4
4.5
5
5.5
6
6.5
7
7.5

Figure 20

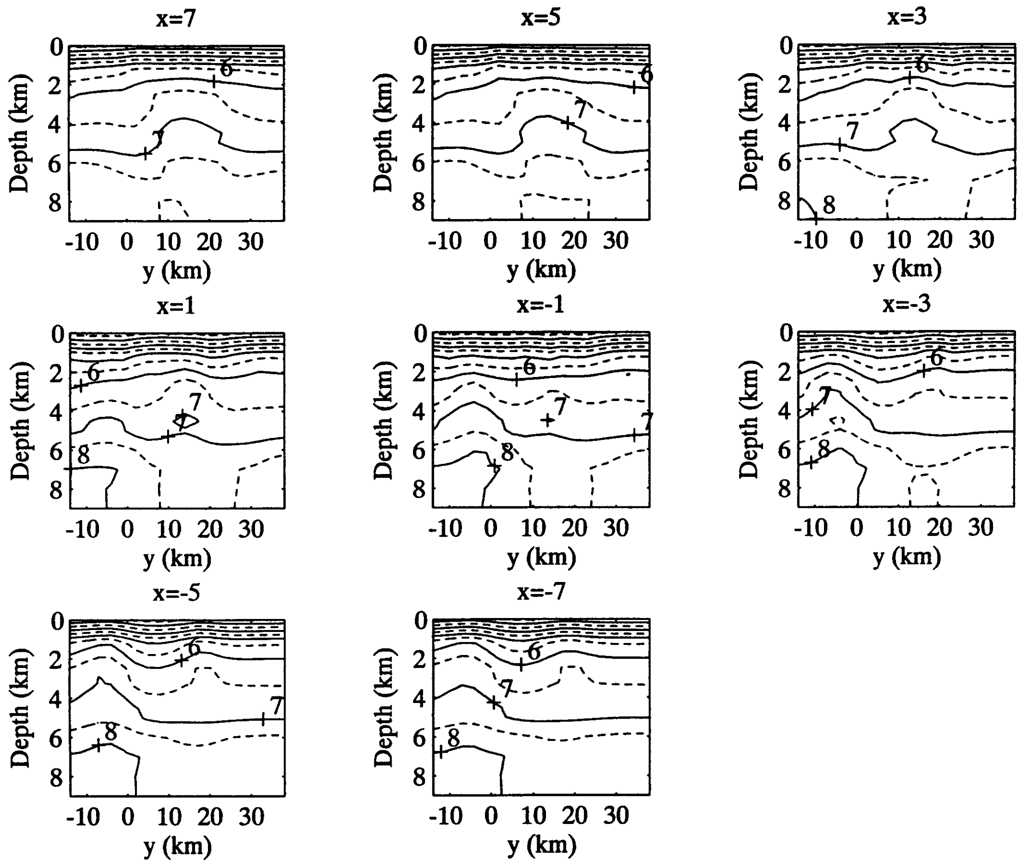

Figure 21a

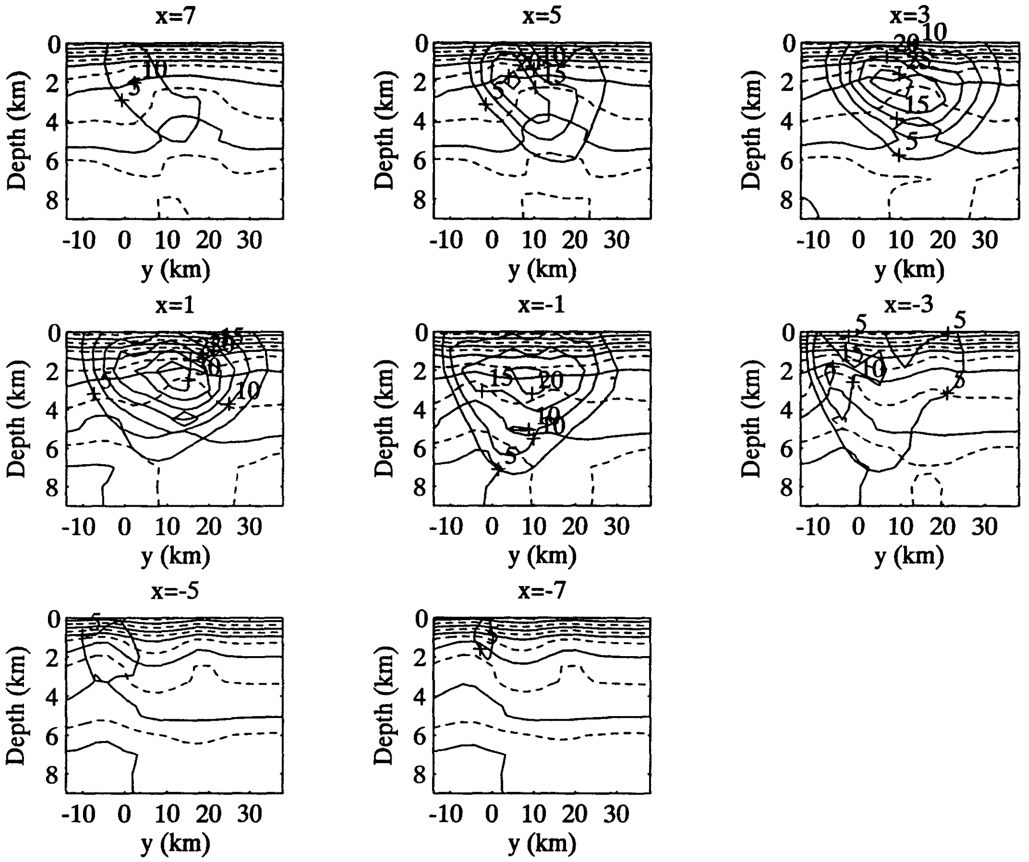

Figure 21b

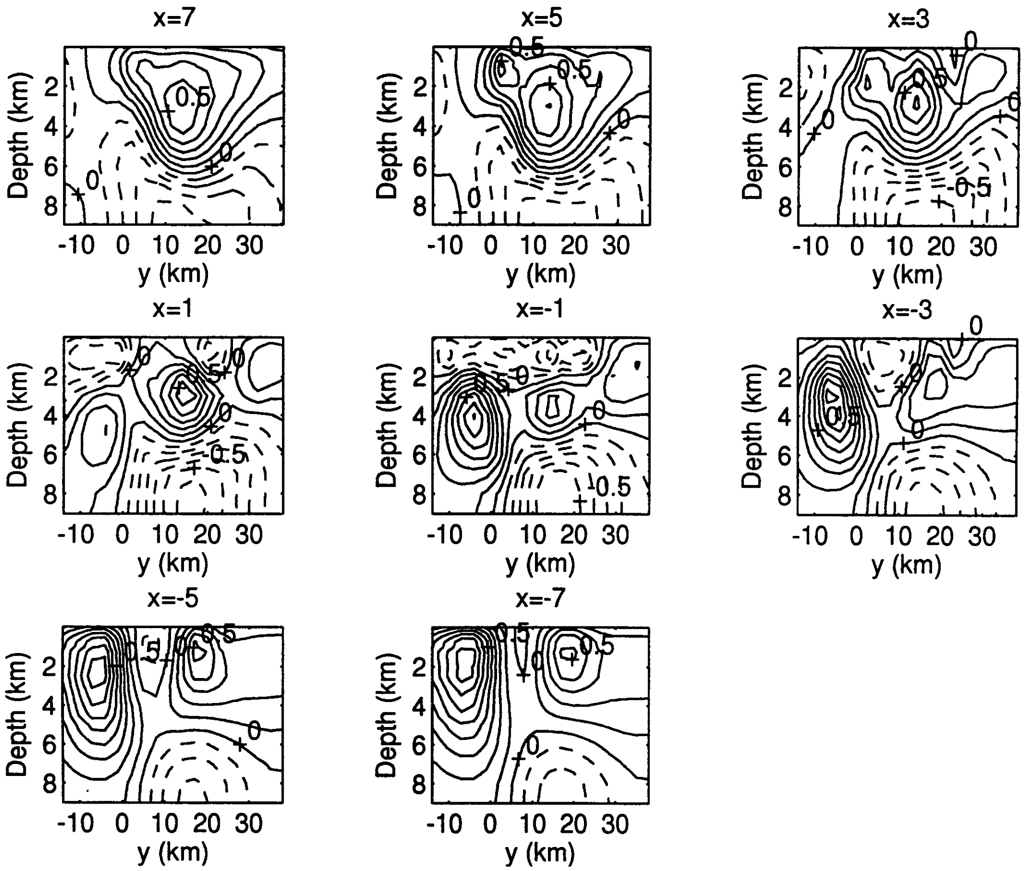

Figure 21c

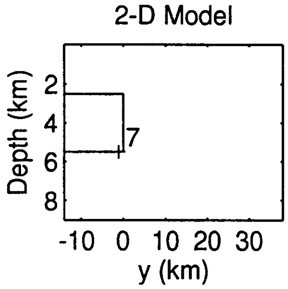

Figure 22a

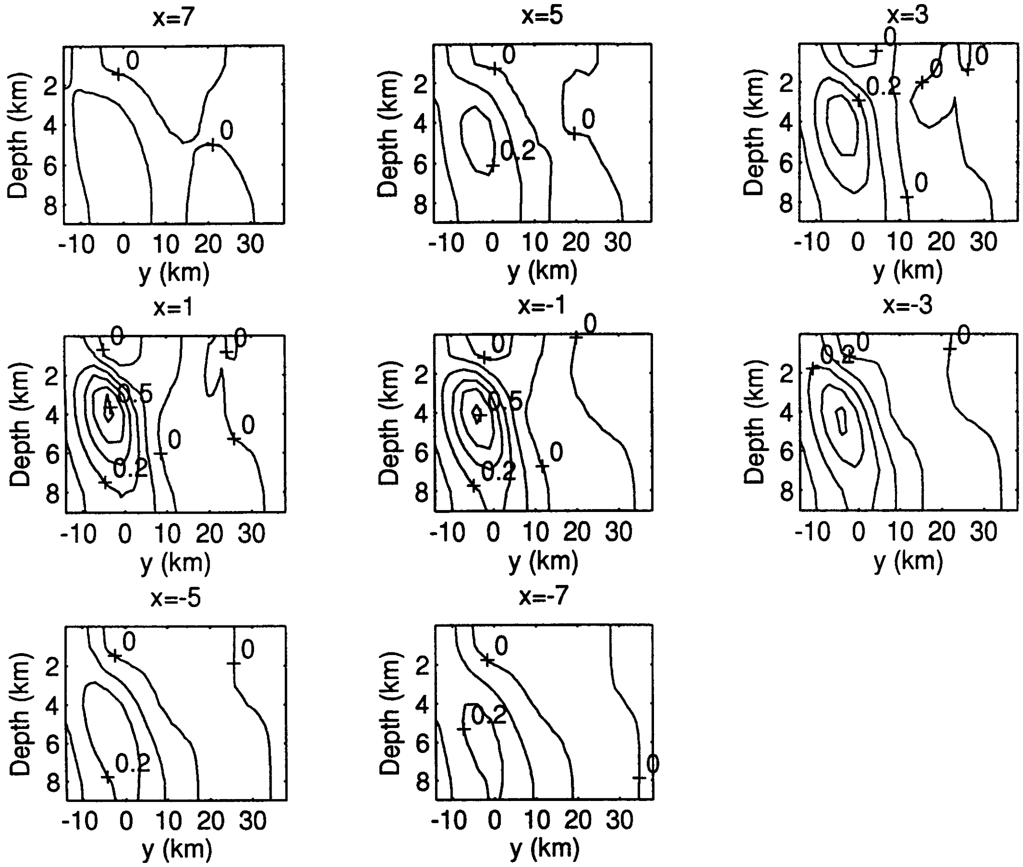

Figure 22b

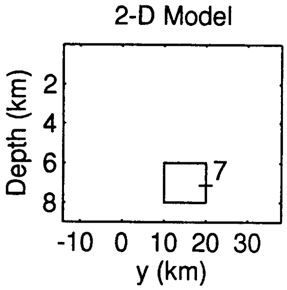

Figure 23a

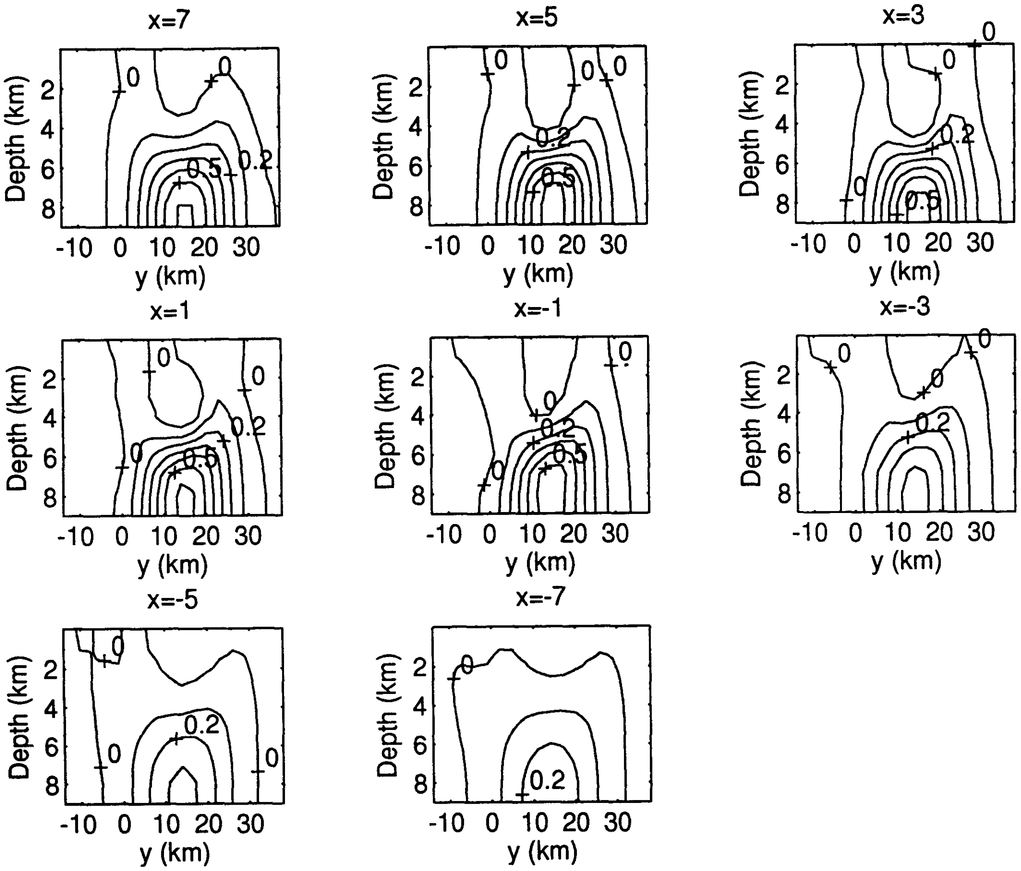

Figure 23b

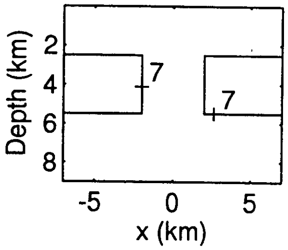

Figure 24a

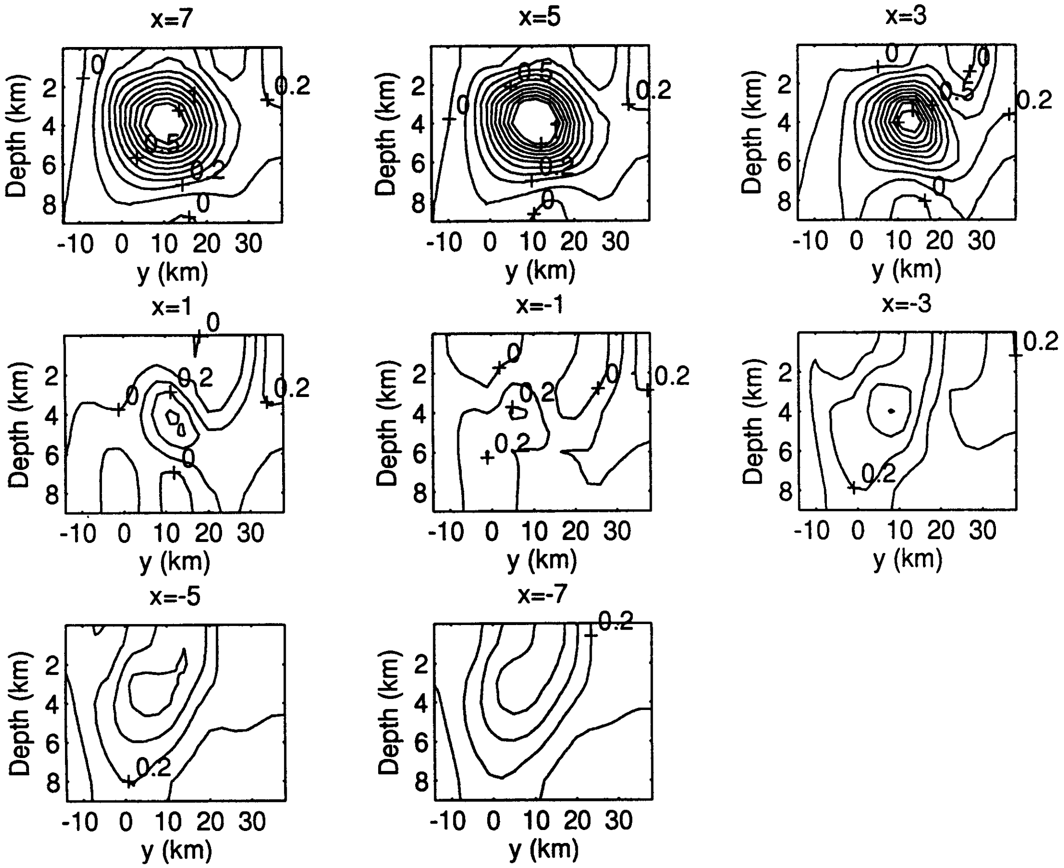

x=7

x=5

x=3

x=1

x=-1

x=-3

x=-5

x=-7

Figure 24b

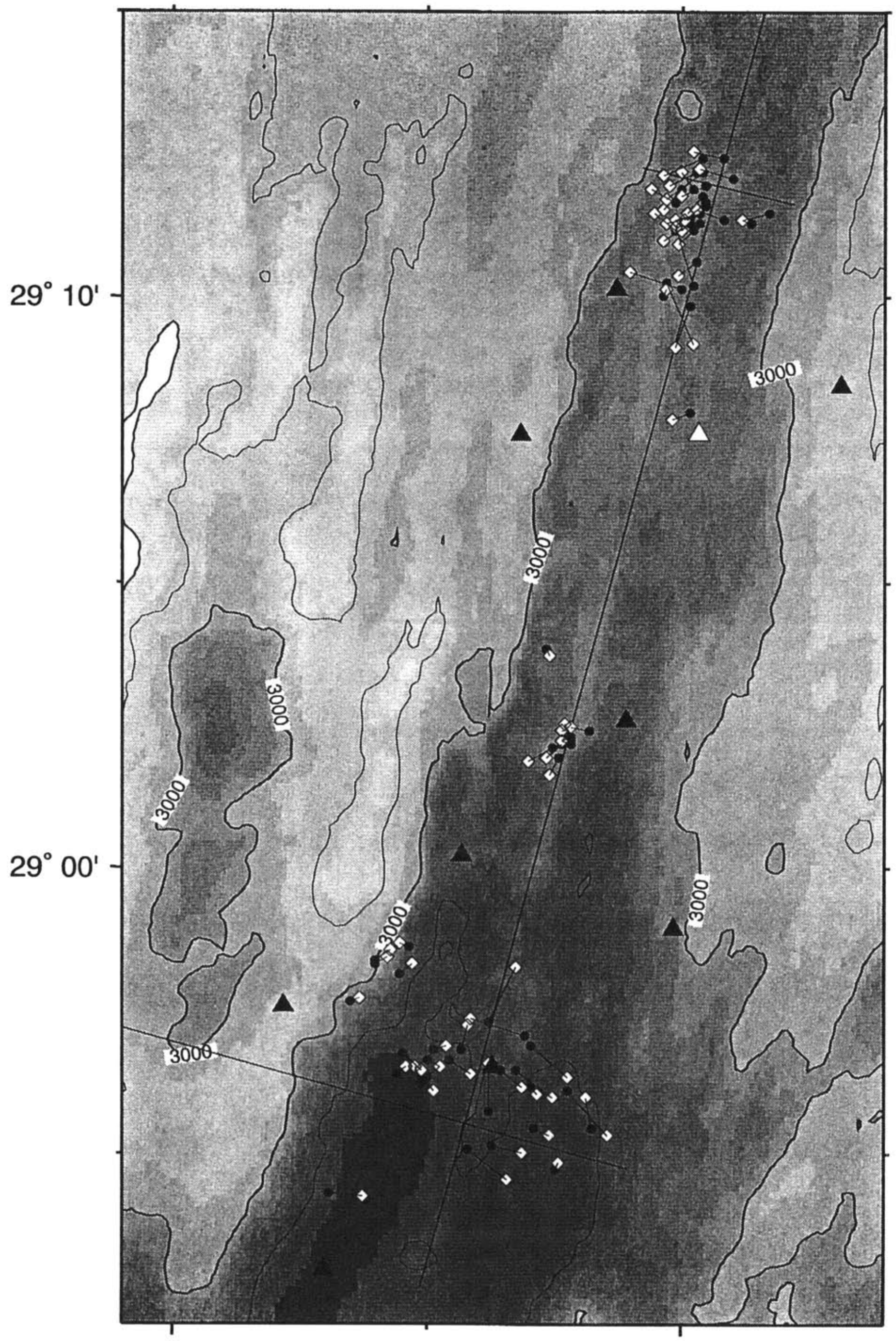

Figure 25

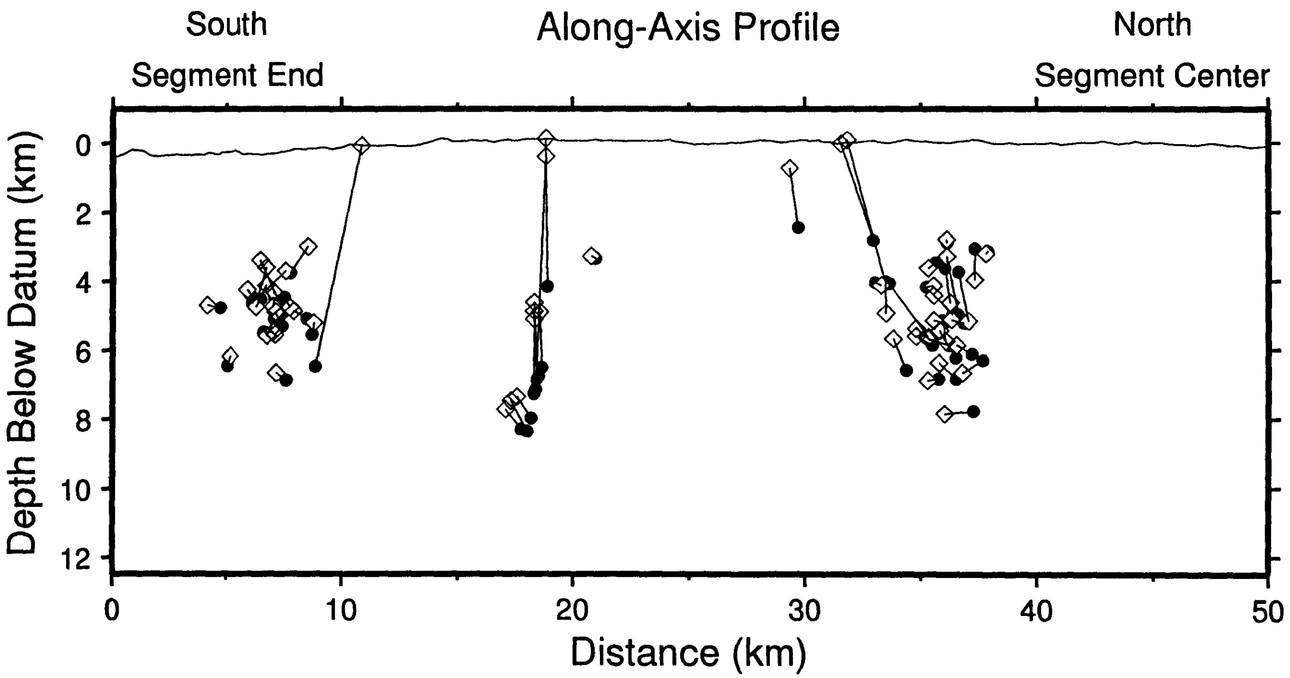
South
Segment End
Along-Axis Profile
North
Segment Center
Depth Below Datum (km)
0
2
4
6
8
10
12
0
10
20
30
40
50
Distance (km)

Figure 26a

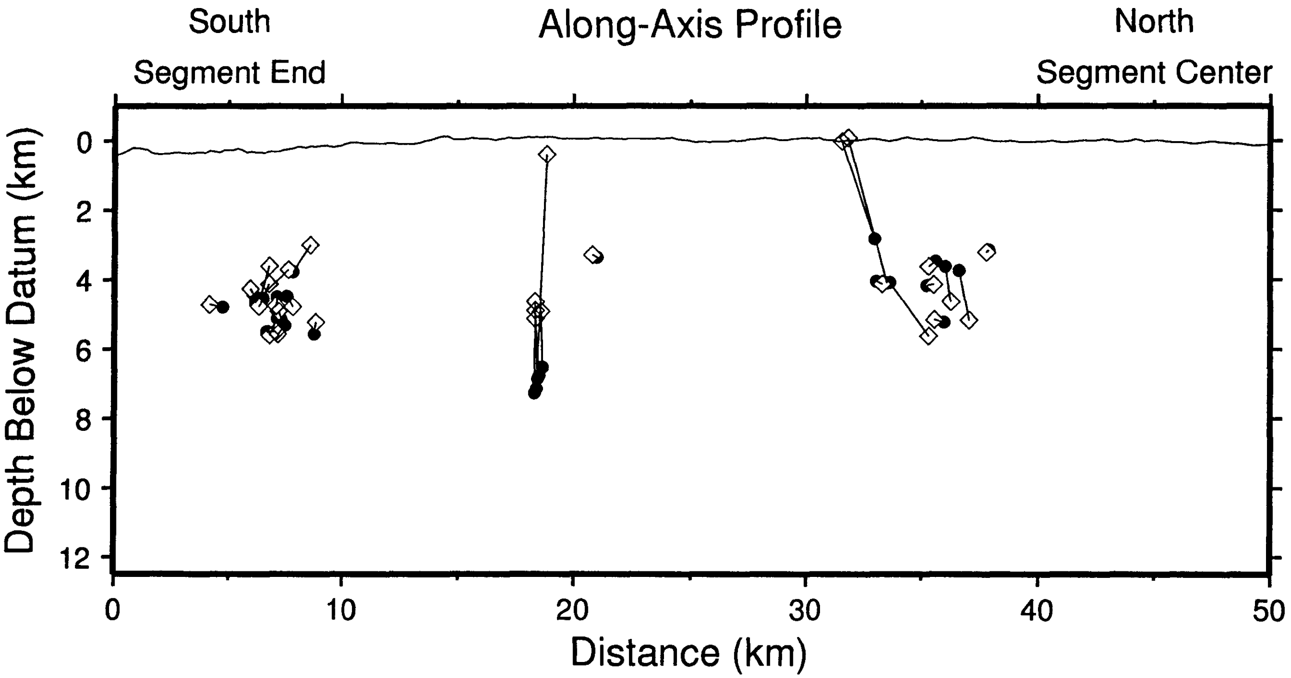
South
Segment End
Along-Axis Profile
North
Segment Center
Depth Below Datum (km)
0
2
4
6
8
10
12
0
10
20
30
40
50
Distance (km)

Figure 26b

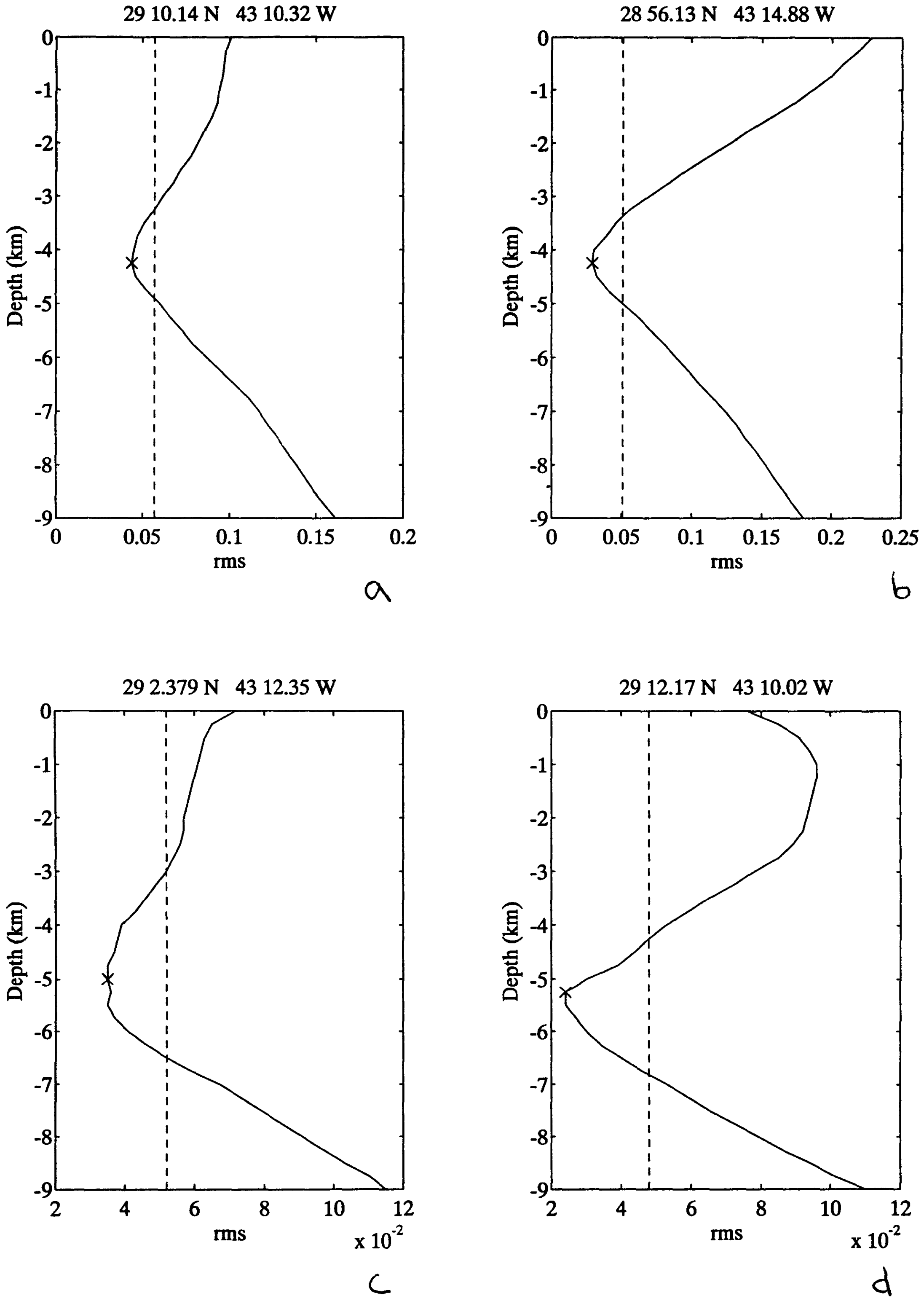
29 10.14 N   43 10.32 W
Depth (km)
0
-1
-2
-3
-4
-5
-6
-7
-8
-9
0
0.05
0.1
0.15
0.2
rms
a
28 56.13 N   43 14.88 W
Depth (km)
0
-1
-2
-3
-4
-5
-6
-7
-8
-9
0
0.05
0.1
0.15
0.2
0.25
rms
b
29 2.379 N   43 12.35 W
Depth (km)
0
-1
-2
-3
-4
-5
-6
-7
-8
-9
2
4
6
8
10
12
rms
x 10^-2
c
29 12.17 N   43 10.02 W
Depth (km)
0
-1
-2
-3
-4
-5
-6
-7
-8
-9
2
4
6
8
10
12
rms
x 10^-2
d

Figure 27

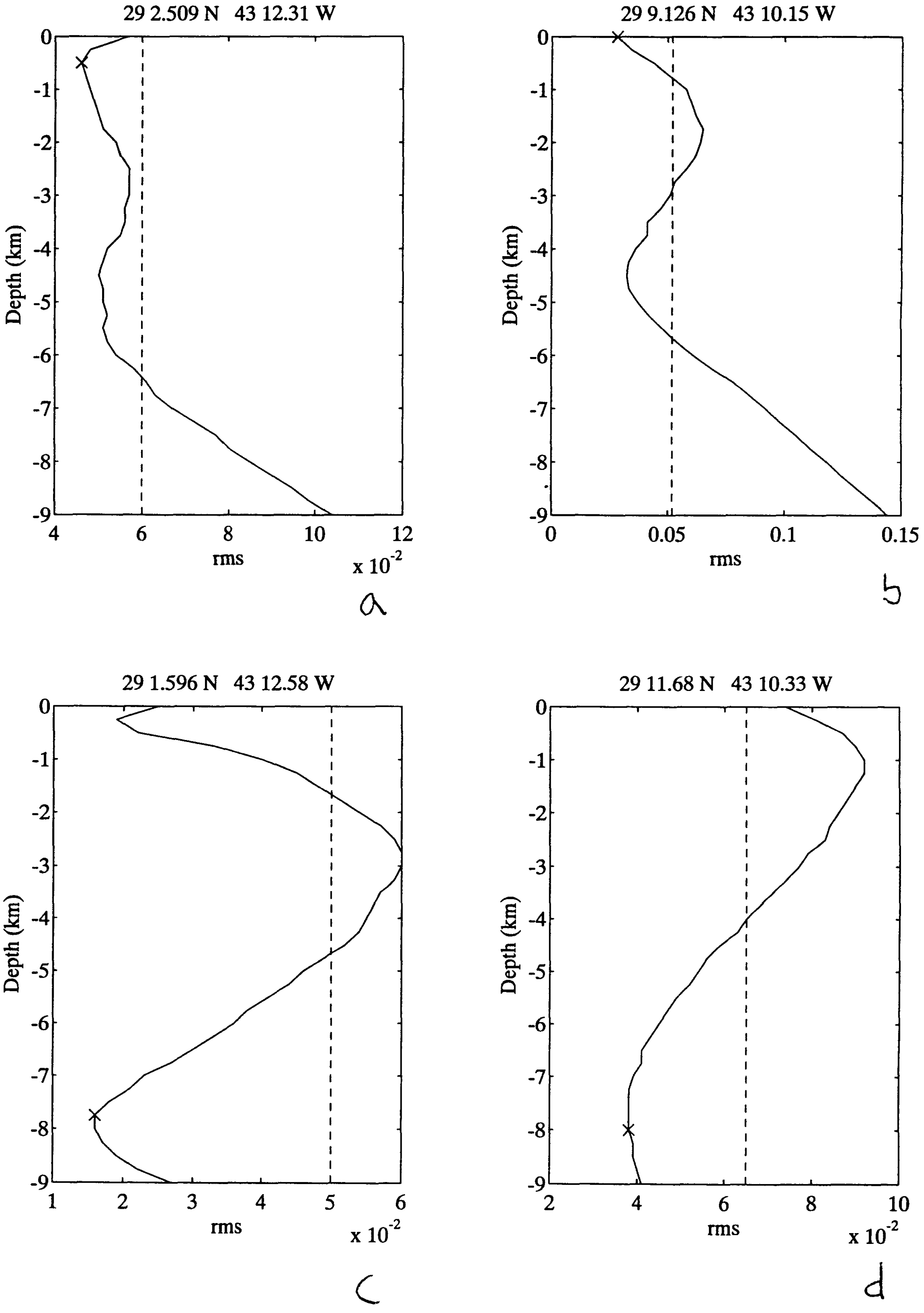

a

b

c

d

Figure 28

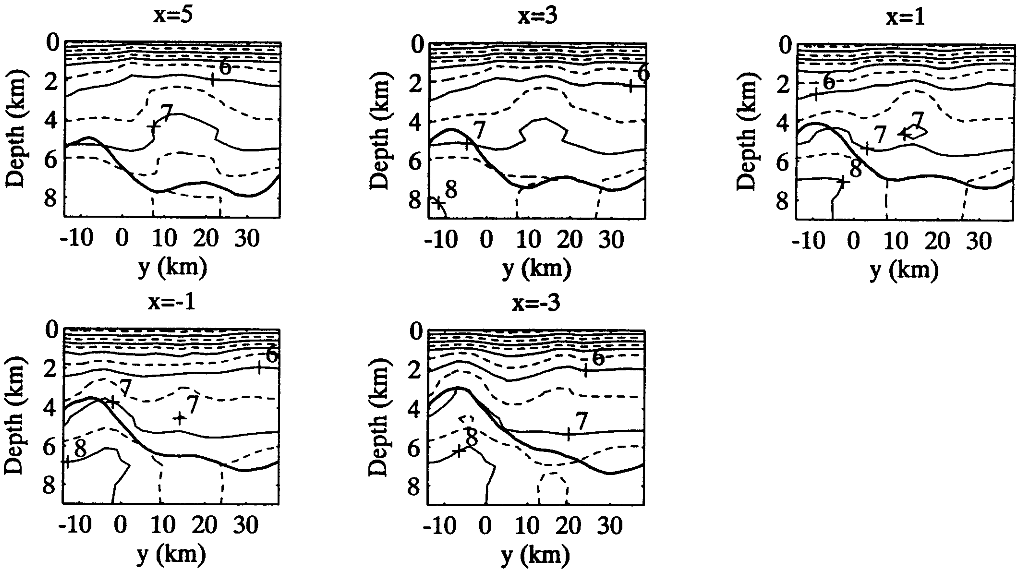

Figure 29

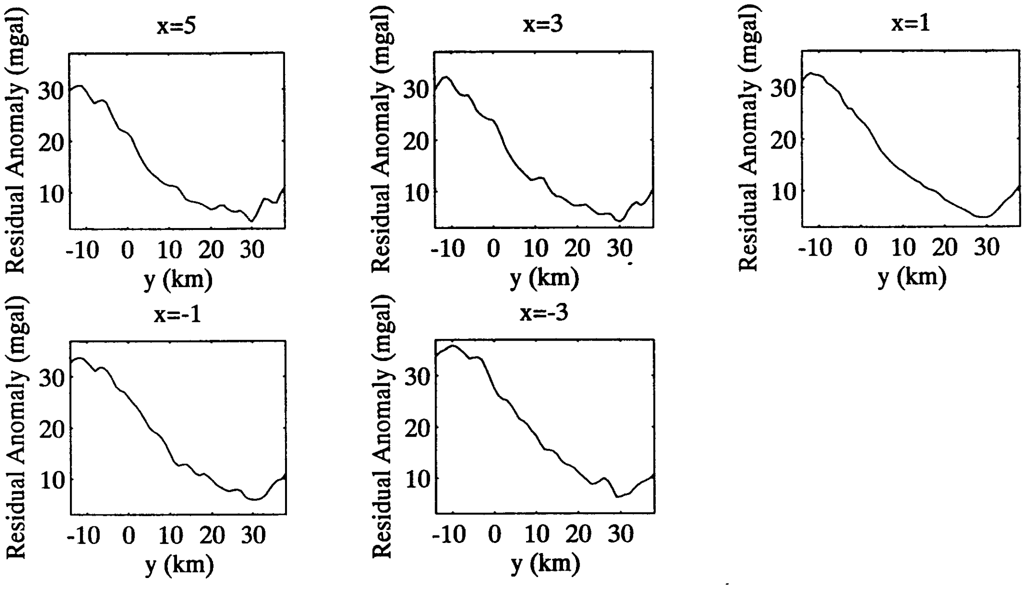

Figure 30

CONCLUSIONS

In this thesis, I have studied earthquake characteristics at mid-ocean ridges and oceanic transforms, and tectonic implications, and investigated processes at Pacific volcanoes, such as lithospheric flexure, island mass-wasting, and controls on the stratigraphy of island moats.

Chapter 1 presents evidence from gravity and deflection-of-the-vertical data that elastic plate thicknesses are remarkably low beneath seamounts of the Darwin Rise, suggesting that the Japanese and Wake seamounts formed on thermally anomalous lithosphere, such as that which is thought to exist presently beneath volcanoes of French Polynesia.

The seismic stratigraphy and quantitative flexural and sedimentation models in Chapter 2 are useful in identifying the processes that influence the Marquesas apron and make it different from that at Hawaii. Plate-flexure models require broad underplating of the crust by low density (crustal?) material to explain the depth to volcanic basement and gravity observations. While there is similar sediment supply for a given along-moat distance at both the Marquesas and Hawaii, the underfilled moat at Hawaii is apparently a consequence of greater moat volumes due to the larger size of the Hawaiian volcanoes, and possibly variations in underplating, that load the plate. The difference in sediment/edifice ratios is likely related to the larger eruption rates at Hawaii and different styles of volcano construction between Hawaii and the Marquesas. The greater sediment/edifice ratio at the Marquesas is probably typical of island chains having an archipelagic apron. Therefore, estimates of hotspot volcanism based soley on the size of volcanoes will severely underestimate the amount of erupted material.

Chapter 3 shows that some large oceanic transform earthquakes have mechanisms or locations inconsistent with simple models. Much of the anomalous earthquake activity can be associated with complex fault geometry or large structural features that apparently influence slip on the fault. Some events with unusual mechanisms occur outside of the transform fault zone and do not appear to be related to fault zone geometry. Possible additional contributors to the occurrence of anomalous earthquakes include recent changes in plate motion, differential lithospheric cooling, and the development of a zone of weakness along the fault zone, but we do not find strong evidence to confirm the influence of these processes.

Chapter 4 describes microearthquake and seismic structural characteristics along a segment at 29°N on the Mid-Atlantic Ridge. While tomographic images are supportive of a simple spreading-cell model, with higher velocities and thin crust occurring near the southern deep and lower velocities and a thickened layer 3 occurring towards the central bathymetric high, microearthquakes suggest complexities related to the small-scale variability of magmatic and hydrothermal processes. The microearthquakes in this study have rupture lengths on the order of only 100 m and therefore are sensitive to small scale variability in the influence of magmatism and hydrothermal circulation. The characteristics of large ($m_b > 4.5$) earthquakes on the MAR, in contrast, may behave more nearly in accordance with a spreading cell model because of larger rupture lengths, on the order of 10 km, that sample structure on the segment scale.

3696.37